THÈSE

En vue de l'obtention du

DOCTORAT DE L'UNIVERSITÉ DE TOULOUSE

Délivré par :

Institut National Polytechnique de Toulouse (INP Toulouse)

Discipline ou spécialité :

Surfaces Interfaces Continentales Hydrologie

Présentée et soutenue par :

M. ALI SWAIDAN

le lundi 5 février 2018

Titre :

Study of water injection with evaporation in a heterogeneous highly degraded nuclear reactor core

---

Ecole doctorale :

Sciences de l'Univers de l'Environnement et de l'Espace (SDUEE)

Unité de recherche :

Institut de Mécanique des Fluides de Toulouse (I.M.F.T.)

Directeur(s) de Thèse :

M. MICHEL QUINTARD

M. FLORIAN FICHOT

Rapporteurs :

M. FRÉDÉRIC TOPIN, AIX-MARSEILLE UNIVERSITE

M. PABLO RUBIOLO, INP GRENOBLE

Membre(s) du jury :

M. DOMINIQUE GOBIN, CNRS GIF SUR YVETTE, Président

M. FLORIAN FICHOT, CEA CADARACHE, Membre

Mme ANDREA BACHRATA, CEA CADARACHE, Membre

M. MICHEL QUINTARD, CNRS TOULOUSE, Membre

Résumé

Les accidents graves résultant de la fusion d'un coeur de réacteur nucléaire doivent être anticipés pour améliorer l'efficacité de leur mitigation. De tels accidents sont survenus à TMI-2 (1979) et à Fukushima (2011). Suite à un accident de perte de refroidissement, l'échauffement du coeur et l'oxydation de la gaine de combustible suivie d'un renoyage (injection d'eau) peuvent entraîner l'effondrement des barres de combustible et la formation d'un lit de débris dans le coeur. La vapeur produite lors du renoyage peut activer l'oxydation exothermique du Zircaloy, entraînant la fusion partielle des matériaux. Cette évolution engendre des zones à porosité réduite limitant la pénétration de l'eau et/ou des zones imperméables. Dans cette situation, l'efficacité de l'injection d'eau dans le coeur pour arrêter la progression de la dégradation et empêcher la fusion du coeur du réacteur peut être considérablement réduite.

Dans ce cadre, l'IRSN a lancé le programme PEARL visant à étudier la thermohydraulique du renoyage des lits de débris chauds entourés d'une zone plus perméable simulant la présence de zones intactes ou moins endommagées dans le coeur. Dans cette thèse, les expériences PEARL ont été modélisées et simulées avec ICARE/CATHARE pour évaluer l'évolution d'un renoyage d'un lit de débris surchauffé entouré d'un bypass de perméabilité plus grande. La thermohydraulique du processus a été analysée et l'effet de différents paramètres (géométrie, conditions aux limites) sur le comportement de renoyage a été évalué. Sous certaines conditions, l'entraînement de l'eau dans le bypass a été identifié et évalué.

Un modèle analytique a été mis au point ensuite pour étudier de façon approfondie le renoyage d'un milieu poreux hétérogène surchauffé composé de deux lits de débris de perméabilité et de porosité différentes et pour décrire l'entraînement de l'eau dans le bypass. Ce modèle calcule les principales variables caractérisant le processus de renoyage, telles que la vitesse du front de trempe, le taux de conversion eau-vapeur et le débit d'eau entraîné dans le by-pass. Il fournit de bons résultats qualitatifs et quantitatifs concernant la redistribution du débit d'eau par rapport aux résultats expérimentaux. Ce modèle a plusieurs avantages. Il est écrit sous une forme plutôt générale incluant les termes de correction de Forchheimer et les termes croisés non nuls dans l'équation de Darcy-Forchheimer généralisée. Les différentes options des équations de quantité de mouvement proposées, y compris les changements dans les corrélations et les lois de frottement interfacial, peuvent être testées facilement. La comparaison des calculs avec les résultats expérimentaux indique qu'il est nécessaire d'inclure une loi de frottement interfacial pour obtenir de bonnes prédictions.

L'extrapolation à l'échelle du réacteur est simple et des calculs ont été effectués pour évaluer l'impact des paramètres géométriques du lit de débris (granulométrie, porosité, dimensions) ainsi que les conditions thermiques et hydrauliques (température, pression, débit d'injection). Ainsi, le modèle est très utile pour estimer le temps de trempe total et la température maximale qui pourraient être atteinte dans le lit de débris à grande échelle. Cela permet d'évaluer la probabilité de réussite du renoyage d'un lit de débris chauds formé lors d'un scénario accidentel hypothétique.

Abstract

Severe accidents arising from the fusion of a nuclear reactor core must be anticipated to enhance the efficiency of their mitigation. Such accidents have occurred at TMI-2 (1979) and Fukushima (2011). Following a loss of coolant accident, core heating and oxidation of the fuel cladding followed by reflooding (injection of water) may lead to the collapse of fuel rods and formation of porous debris bed in the core. Steam produced upon reflooding may activate the exothermic oxidation of Zircaloy leading to partial melting of materials. Such evolution generates zones with reduced porosity limiting coolant penetration and/or impermeable blocked zones. In this situation, the efficiency of injecting water into the core to stop the progress of degradation and prevent the reactor core melting may be significantly reduced.

In this scope, IRSN launched PEARL program to investigate the thermal hydraulics of reflooding of hot debris beds surrounded by a more permeable zone simulating the presence of intact or less damaged zones in the core. The PEARL experiments were modeled and simulated using ICARE/CATHARE code to assess the evolution of a bottom reflooding of a superheated debris bed surrounded by a bypass of larger permeability. The thermal hydraulics of the quenching process has been analyzed and the effect of each of the initial conditions on the reflooding behavior was assessed. The effect of pressure was investigated and related to the entrainment of injected water at quench front level into the bypass.

An analytical model was then developed to investigate thoroughly the reflooding of a superheated heterogeneous porous medium, composed of two layers of contrasting permeability and porosity, and to describe the water entrainment in the bypass. This model computes the main variables characterizing the reflooding process such

as quench front velocity, water-to-steam conversion ratio, and the flow rate of water entrained in the bypass. It provides good qualitative and quantitative results for the two-phase flow redistribution as compared to experimental results. This model has several advantages. It is written in a rather general form including the Forchheimer correction terms and non-zero cross-terms in the generalized Darcy-Forchheimer momentum equation. Variations of proposed momentum equations including changes in correlations and interfacial friction laws can be tested easily and efficiently. Comparison of the calculations against experimental results indicated that it is necessary to include an interfacial friction law to obtain good predictions. This model allows performing fast evaluations of the efficiency of cooling by computing the fraction of the injected flow rate that participates in cooling. Upscaling to the reactor scale is straightforward and calculations were performed to assess the impact of geometric parameters of the debris bed (particle size, porosity, dimensions) as well as thermal hydraulic conditions (temperature, pressure, injection flow rate) on the reflooding process. Thus the model is very useful to estimate the total quenching time and the maximum temperature that could be reached by the hot debris bed at large scales. This allows assessing the probability of a successful quenching of a hot debris bed formed during a hypothetical accidental scenario.

Acknowledgments

This PhD was pursued at IRSN (Institut de Radioprotection et de Sûretées Nucléaire) in the center of Cadarache. It was financed and conducted within the context of a joint project between IRSN and EDF (Électricité de France) on severe accident studies.

I'm very grateful to my supervisor at IRSN Florian Fichot for his serious comittment, support and close flow up during the whole duration; and to my University supervisor Michel Quintard for the academic direction and whose profound knowledge and experience in the domain of porous media always made an important impact on the scientific value of my work.

I am thankful for the IRSN-SAG severe accidents division, more specifically the LEPC group. Thanks to the head of the LEPC Laboratory Renaud Meignen for reviewing my reports and to all the group members for their support whenever I needed, and for their kind hosting during the three years of the PhD making it a great and rich experience. I am and also grateful to the PEARL experimental group of IRSN for providing the experimental results and especially Nourdine Chikhi with whom I had the pleasure to collaborate and publish about PEARL tests. Thanks to Stephane Bertuzzi for his technical support in Icare-Cathare related issues. I would also like to thank the jury members for their committment and especially the reviewers for their valuable time and efforts put in reviewing my thesis.

Thanks to my friends who supported me during the PhD. And special thanks goes to my family for their endless love, encouragement, support and attendance of my defense.

This work is especially dedicated to my loving parents and to my old teachers. I also dedicate it to the memory of my friend Hassan Jaber who had always encouraged me to do a PhD but left much sooner than seeing me achieving it; and to the memory of my grandmother and grandfather who passed away during my PhD pursue.

Chapter 0

Introduction

0.1 Motivation

Cette thèse étudie le renoyage d'un lit de débris formé dans un coeur de réacteur nucléaire dégradé pendant un accident grave. Le concept de lit de débris a été introduit après l'examen post-accidentel du réacteur 2 de Three Mile Island (TMI-2). Dans la partie supérieure du noyau endommagé, une grande surface était constituée de petites particules de combustible et de segments de barres de combustible. Depuis lors, on suppose généralement que des lits de débris similaires se formeraient pendant l'injection d'eau, si les gaines de combustible sont fortement oxydées, brisées ou même ont fondu et sont devenues incapables de résister au choc thermique. La capacité de refroidissement d'un lit de débris formé dans un coeur dégradé d'un réacteur à eau pressurisée (PWR) une question cruciale pour la sûretées nucléaire. Lors d'un accident grave, l'assèchement et le réchauffement des crayons de combustible ainsi que l'oxydation de la gaine conduisent progressivement à la fragilisation des gaines et à la fusion partielle du coeur. Bien que le reformage vise à ralentir cette dégradation, le choc thermique potentiellement induit par un refroidissement rapide peut compromettre l'intégrité mécanique des crayons combustibles non revêtus et fragiliser les gaines oxydées et déclencher leur effondrement. Bien qu'il n'ait jamais été clairement démontré expérimentalement, il est communément admis que des lits de débris ,dans le coeur, sont formés à partir de la délocalisation des pastilles de combustible et des fragments de revêtement. L'étude de plusieurs échantillons provenant de l'étude post-accidentel de TMI-2 et des études expérimentales dans le but de modéliser la dégradation du coeur comme LOFT ou PBF [Akers 1994, Petti 1989] confirment ce processus de formation. Dans TMI-2, une caractéristique particulière était la présence de barres intactes entourant le lit de débris dans la partie supérieure. Cela était probablement dû au fait que les assemblages combustibles situés à la périphérie du coeur ont moins de puissance et sont moins endommagés que dans le reste du noyau. Par conséquent, ils sont susceptibles de rester intacts, tandis que les autres sont oxydés, endommagés et éventuellement effondrés. La présence d'ensembles intacts autour du lit de débris peut agir comme un by-pass pour l'eau en cas de renoyage et provoquer une limitation de la pénétration de l'eau dans le lit de débris. Afin d'étudier ce processus, les expériences PEARL ont été conçues et réalisées par l'IRSN. Les résultats ont confirmé le rôle clé de la zone plus perméable

située à la périphérie du lit de débris, avec une déviation possible de l'eau dans cette dérivation, entraînant un refroidissement plus lent du lit de débris.

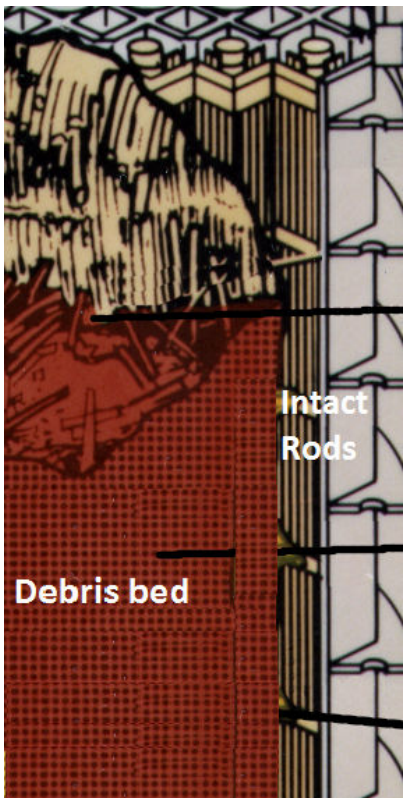

Figure 1: Zoom on the TMI-2 debris bed surrounded by intact fuel assemblies

L'objectif de cette thèse est d'étudier l'efficacité de renoyage d'un lit de débris entouré d'une zone plus perméable (by-pass) qui peut être soit des assemblages combustibles intacts, soit des débris plus grand. La problématique comporte plusieurs aspects: la caractérisation du lit et du by-pass, la modélisation d'écoulement diphasique dans un lit aux propriétés non homogènes (porosité, perméabilité) et enfin l'identification des processus-clés régissant l'efficacité de renoyage de ce milieu. La caractérisation du lit et du by-pass sort du cadre du présent travail et l'on considérera que le système peut être représenté par une géométrie simple et générique: deux cylindres concentriques, l'intérieur étant moins perméable et peut-être plus poreux. La formation de cette configuration sera expliquée dans ce chapitre. La modélisation d'écoulement diphasique suit l'approche déjà développée dans les travaux précédents de [Duval 2002, Duval 2004, Béchaud 2001, Bachrata 2012, Bachrata 2013]. Il est basé sur la méthode de prise de moyenne et les lois de fermeture empiriques pour les transferts de chaleur entre les phases et pour les termes de frottement. Les équa-

tions seront rappelées dans les chapitres suivants. La principale contribution à la modélisation dans cette thèse sera l'identification des termes de friction interfaciale nécessaires pour expliquer l'entraînement de l'eau dans le by-pass latéral observé dans les expériences PEARL. La modélisation physique simplifiée qui sera proposée dans les deux derniers chapitres est un premier pas vers un modèle générique capable d'identifier rapidement les processus qui régiraient la progression de l'eau dans le lit principal de débris et le temps de renoyage dans différentes configurations de lits de débris stratifiés verticalement.

0.2 Scénario accidentel

La description des accidents graves dans les REP est généralement classée dans les situations dans-cuve et dehors-cuve (in-vessel and ex-vessel) en fonction de la progression du corium (combustible fondu mélangé à d'autres matières). La fragmentation et la délocalisation des matériaux de base en raison du contact avec l'eau entraînent la formation de lit de débris dans le plénum inférieur de la cuve du réacteur. Avant la fusion potentielle et le déplacement du corium fondu au fond du récipient, la portée de cette thèse considère la situation dans-cuve, dans laquelle les lits de débris sont formés à l'intérieur du coeur du réacteur.

Des accidents graves résultant d'un LOCA (perte d'un accident de refroidissement) se sont survenus à l'unité 2 (TMI-2) [NSAC 1980] de Three Mile Island aux Etats-Unis, en 1979, et récemment à Fukushima, au Japon, en 2011, où 3 réacteurs ont été détruits. L'accident de Tchernobyl en 1984 a une origine différente (augmentation de la réactivité). Suite à un accident du perte de refroidissement dans un REP (réacteur à eau sous pression), le coeur du réacteur est découvert et commence à chauffer sous l'effet de la décroissance radioactive des produits de fission dans le coeur. En conséquence, cet échauffement provoquera l'évaporation du l'eau dans le coeur et diminuera le niveau d'eau dans le réacteur. Le temps requis pour l'assèchement varie en fonction de la progression de l'accident et de la conception du réacteur, mais la période standard est de deux heures à quelques heures.

Au fur et à mesure de l'évolution de l'accident, le chauffement et l'oxydation de la gaine de combustible par la vapeur de liquide de refroidissement entraînent une dégradation du coeur. Une réaction exothermique se produit donc entre la vapeur surchauffée et le zirconium de la gaine de combustible à des températures supérieures à 1700 K. La chaleur générée par cette réaction est d'environ 1.3 MJ pour 1 kilogramme de Zirconium [Coindreau 2008]. Cela provoque en outre l'augmentation de la température et le processus de dégradation du coeur. En outre, une grande quan-

tité d'hydrogène est produite et peut arriver à l'enceinte du réacteur par les soupapes de sécurité du système de refroidissement du réacteur ou par une fuite. La présence de fortes concentrations d'hydrogène qui pénètre dans l'enceinte de confinement peut provoquer une combustion explosive du mélange gazeux, où cette combustion endommagerait le confinement. L'oxydation des processus de production de métaux et d'hydrogène de base peut être trouvée dans le détail dans [Chikhi 2012].

Dans ce cas, le renoyage du coeur est l'une des options les plus courantes pour sauver la situation mais il peut provoquer un choc thermique et la fragilisation de la gaine, formant ainsi un lit de débris dans le coeur. De telles complications dans l'évolution de l'accident doivent être anticipées pour améliorer l'efficacité de son mitigation. Le concept de formation des lits de débris a été introduit par [Akers 1989] et [McCardell 1990] lors de l'examen post-accidentel de l'unité 2 (TMI-2) de Three Mile Island les USA-1979. Dans ce dernier cas, le combustible a été fragmenté en particules de taille comprise entre 1 et 5 mm ([Akers 1986], [Broughton 1989], [McCardell 1990]) en raison de la délocalisation des matériaux fondus à l'intérieur du coeur lors de la trempe des barres très chaudes. Dans de telles situations, différentes configurations de lit de débris peuvent exister, telles que la formation d'un lit de débris entouré d'une zone intacte de barres de combustible ou l'existence de zones compactes de très petites particules limitant la pénétration du liquide de refroidissement (figure 1.1). Les débris de TMI-2 étaient un mélange de phases céramiques et métalliques. Les phases céramiques sont constituées de (U, Zr) O2, et les phases métalliques sont constituées d'éléments de la barre de contrôle et des autres matériaux du coeur (Ag, Fe, Ni, Cr, etc.) plus de 80 pour cent en masse d'UO2 et une densité moyenne d'environ 8000 kg / m3 [Akers 1989]. Les densités mesurées des échantillons de débris de TMI-2 variaient de 6,32 x 10^6 g/m^3 à 8,25 x 10^6 g/m^3 ([Nagase 2012]). La densité diminue de 0,2 x 10^6 g/m^3 avec une augmentation de température de 1000 K.

Lors d'un accident menant à la fusion du coeur du réacteur, le succès du renoyage dans l'élimination de la chaleur résiduelle et l'interruption de la fusion préserve l'intégrité du coeur. Ce fut le cas dans l'accident du TMI-2 où une partie du coeur de réacteur a fondu et plusieurs tons de corium ont été trouvés au fond du coeur qui n'a pas échoué même s'il était soumis à des contraintes thermiques provoquées par la chaleur résiduelle. Il pourrait résister aux contraintes parce que le réacteur a été renfloué.

Le processus de refroidissement d'un lit de débris est plus difficile que les barres de combustible intactes en raison des températures élevées, c'est-à-dire au-dessus de 2000 K et de petits diamètres hydrauliques de quelques millimètres. La progression

ou la mitigation de l'accident repose fortement sur la stabilisation de tels lits de débris (état stable où la température du lit ne varie pas avec le temps).

Lorsque le lit de débris chauds et secs sont refroidis (refroidissement à la température de saturation par injection de l'eau) avant d'atteindre la fusion due à la chaleur de décroissance, une condition de refroidissement stable est obtenue. L'un des principaux objectifs de cette thèse est d'évaluer les chances de refroidissement un lit de débris contre la chaleur provoqué par puissance résiduelle du réacteur.

0.3 Etudes expérimentales de renoyage

La capacité de refroidissement des lits de débris a fait l'objet des études au cours des trente dernières années. Plusieurs programmes expérimentaux sur la capacité de refroidissabilité des débris ont été réalisés au cours des dernières décennies suite à l'accident du TMI, visant à déterminer la puissance maximale pouvant être extraite d'un lit de débris chauffé par le reflux de l'eau. En effet, un lit de débris non refroidissable est supposé augmenter rapidement en température, en raison de la chaleur de décroissance résiduelle, fondre et former un grand bassin de fusion qui se dilaterait même lorsqu'il est entouré d'eau et menacerait l'intégrité du cuve. De nombreuses études expérimentales et modèles théoriques ont mis l'accent sur la détermination du flux de chaleur "critique" et de la puissance volumétrique maximale pouvant être retirée de l'eau d'un lit de débris. Dans la plupart des cas, les lits de débris unidimensionnels ont été considérés comme [Lipinski 1984]. Quelques études expérimentales intéressantes d'effets bidimensionnels ont été faites en parallèle [Lee 1977, Hardee 1977]. Récemment, des effets bidimensionnels ont été étudiés dans plus de détails, expérimentalement [Décossin 2000, Atkhen 2003] ou numériquement [Mayr 1998, Béchaud 2001]. Il apparaît que la limitation du flux à contre-courant, toujours présente dans des situations unidimensionnelles, peut être évitée dans certaines configurations bidimensionnelles, conduisant à un flux de chaleur critique plus élevé. Il a également été observé que l'équilibre thermique local peut ne pas exister partout dans le lit de débris, même pour les débris chauffés recouverts d'eau à température de saturation [Atkhen 2003]. Le flux de vapeur surchauffée à travers le lit apparaît comme un processus relativement important pour refroidir les débris "secs".

D'autre part, le renoyage des lits de débris chauds a reçu moins d'attention. Des études expérimentales et des données sur le renoyage par injection du l'eau par le bas et le haut sont disponibles [Armstrong 1982, Armstrong 1981, Cho 1984, Ginsberg 1982, Ginsberg 1985, Ginsberg 1986, Tutu 1984b, Hofmann 1984, Reed 1985,

Hu 1991, Konovalikhin 2000] et quelques modèles ont été proposés [Petit 1999, Sozen 1990]. Plus récemment, la capacité de refroidissement des lits de débris a été étudiée avec des programmes expérimentaux tels que DEBRIS ([Schäfer 2006], [Rashid 2013]) chez IKE en Allemagne, et POMECO ([Nayak 2005], [Nayak 2006]) chez KTH en Suède. L'existence de différences de température entre les particules solides, l'eau et la vapeur rend la modélisation et les mesures expérimentales plus difficiles. De plus, les configurations d'écoulement sont complexes car, pour les particules à très haute température, la vapeur devient la phase de "mouillage" en raison de la présence d'un film de vapeur stable autour des particules. Ceci a été observé expérimentalement, sur des sphères simples, par [Dhir 1978] qui a proposé un modèle théorique pour le transfert de chaleur autour de sphères sous régime d'ébullition. Cependant, les résultats obtenus pour les sphères sont difficiles à appliquer aux lits de débris de particules. En raison du manque de données expérimentales sur les lits de débris réels, les modèles doivent reposer sur plusieurs hypothèses. nn Ces dernières années, PRELUDE et PEARL ([Stenne 2009], [Repetto 2011], [Repetto 2013] et [Chikhi 2015b]) ont également été lancés par l'IRSN pour étudier la thermohydraulique du processus de ré-enfouissement et développer de nouveaux modèles de renoyage et valider des modèles 2D / 3D. Le but est de prédire les conséquences du l'injection de l'eau d'un coeur de réacteur gravement endommagé où une grande partie du coeur s'est effondrée et a formé un lit de débris. Les données des expériences PEARL seront abondamment utilisées dans ce thèse.

0.4 Objectifs de la thèse

L'objectif de cette thèse est de fournir une base physique et phénoménologique pour comprendre la situation complexe qui peut résulter de l'injection forcée d'eau dans un coeur où les parties effondrées coexistent avec des zones moins endommagées. Parmi les questions importantes, l'impact de la géométrie des lits de débris est étudié, ainsi que l'impact de différentes conditions aux limites sur la trempe et la refroidissabilité des lits de débris chauds.

Après une présentation de l'approche générale suivie pour la modélisation de l'écoulement diphasique en milieu poreux, une discussion sur le choix des termes de frottement fournit une base préliminaire pour les évaluations suivantes avec des calculs numériques. Une série de tests PEARL sont calculés avec le modèle, implémenté dans ICARE / CATHARE. On montre que le modèle capture assez bien certains des phénomènes observés dans PEARL, en particulier le passage d'un front de trempe à plat (appelé 1D) à un front de trempe progressant significativement plus rapidement dans le bypass que dans le lit central (appelé comportement 2D) . Cependant,

le modèle ne permet pas de prédire avec précision le débit d'eau dans le by-pass (sa vitesse et le débit massique) et il apparaît qu'un terme de friction interfaciale supplémentaire est nécessaire pour être plus précis. Afin d'étudier plus en détail les effets de différents termes de friction, un modèle analytique est développé. Ce modèle permet d'effectuer de nombreux calculs en peu de temps. De cette étude, il confirme la nécessité d'ajouter un terme de friction interfaciale dans les équations de quantité de mouvement pour les phases liquide et gazeuse. Le modèle analytique fournit également des indications sur les effets de la géométrie du lit poreux sur la transition du comportement 1D au 2D. L'effet de la pression est également examiné. Enfin, le modèle analytique est appliqué à l'échelle du réacteur pour étudier les conditions pour lesquelles l'injection d'eau serait suffisamment efficace pour refroidir les débris et les conditions pour lesquelles une trop grande quantité d'eau est redistribuée dans le bypass et ne peut contribuer à une refroidissement efficace de le lit de débris principal.

Contents

List of Figures

List of Tables

Nomenclature

symbol	variables	units
α	void fraction	
ε	porosity	
ϕ	mass flow rate	g/s
ρ	density	kg/m^3
μ	dynamic viscosity	Pa.m/s
κ	absolute permeability	m^2
η	absolute passability	m
κ_f	relative permeability of phase f	
η_f	relative passability of phase f	
γ	conversion ratio	
ψ	relative cross-section	
C_κ	permeability contrast	
v	absolute velocity	m/s
U	superficial velocity	m/s
z	elevation in the porous medium	m
s	saturation $= 1 - \alpha$	
d_p	particles diameter	m
S	cross section area	m^2
R	radius	m
H	height	m
P	pressure	bar
T	temperature	°C
$\Delta T_f = T_f - T_{sat}$	temperature difference	°C
$\langle v_\theta \rangle^\theta$	intrinsic average velocity z-component, denoted by : v	
$\langle v_\theta \rangle$	average velocity z-component, denoted by : U	
$\langle \mathbf{v}_\theta \rangle$	average velocity vector field	

subscripts

g	gas
l	liquid
s	solid

superscripts

b	bypass
c	center
inj	injection
qf	quench front

Chapter 1

Introduction

Contents

1.1 Motivation

This thesis investigates the reflooding of a debris bed formed in a degraded nuclear reactor core. The concept of debris bed was introduced after the post-accident examination of the Three Mile Island unit 2 (TMI-2) reactor [Akers 1989, McCardell 1990]. In the top part of the damaged core a large area was made of small fuel particles and fuel rod segments. Since then, it is usually assumed that similar debris beds would form during water injection, if fuel claddings are highly oxidized, broken or even have melted away and have become unable to withstand the thermal shock. The coolability of a debris bed formed in a degraded core of a pressurized water reactor (PWR) is a crucial issue for nuclear safety. During a severe accident the dry-out and heat-up of the fuel rods together with cladding oxidation progressively lead to embrittlement of the claddings and partial melting of the core. Although reflooding aims at slowing down this degradation, the thermal shock potentially induced by a rapid cooling can compromise the mechanical integrity of unclad fuel rods and embrittled oxidized claddings and trigger their collapse. Even though it was never clearly demonstrated experimentally, it is commonly accepted that 'in-core' debris beds are formed from the resulting relocation of fuel pellets and cladding fragments. Examination of several samples coming from Three Mile Island unit 2 (TMI-2) [Akers 1989, McCardell 1990] and experimental studies with aim to model core degradation like LOFT or PBF [Akers 1994, Petti 1989] confirm this formation process. In TMI-2, a particular feature was the presence of intact rods surrounding the debris bed in the upper part. This was probably due to the fact that fuel assemblies located at the periphery of the core have less power and are less damaged than in the rest of the core. Therefore, they are likely to remain intact, while the other ones are oxidized, damaged and possibly collapsed. The presence of the intact assemblies around the debris bed may act as a by-pass for water in case of reflooding and cause a limitation of the penetration of water into the debris bed. In order to study that process, the PEARL experiments were designed and performed by IRSN. The results have confirmed the key role of the more permeable zone located at the periphery of the debris bed, with a possible deviation of water into that by-pass, resulting in a slower cooling of the debris bed. The objective of this Ph.D. thesis is to investigate the efficiency of reflooding of a debris bed surrounded by a more permeable zone (by-pass) which can be either intact fuel assemblies or larger debris. The issue involves several aspects: the characterization of the bed and by-pass, the modeling of two-phase flow in a bed with non-homogeneous properties (porosity, permeability) and finally, the identification of the key-processes governing the efficiency of reflooding of such medium. The characterization of the bed and by-pass is out of the scope of the present work and it will be considered that the system may be represented as a simple and generic geometry: two concen-

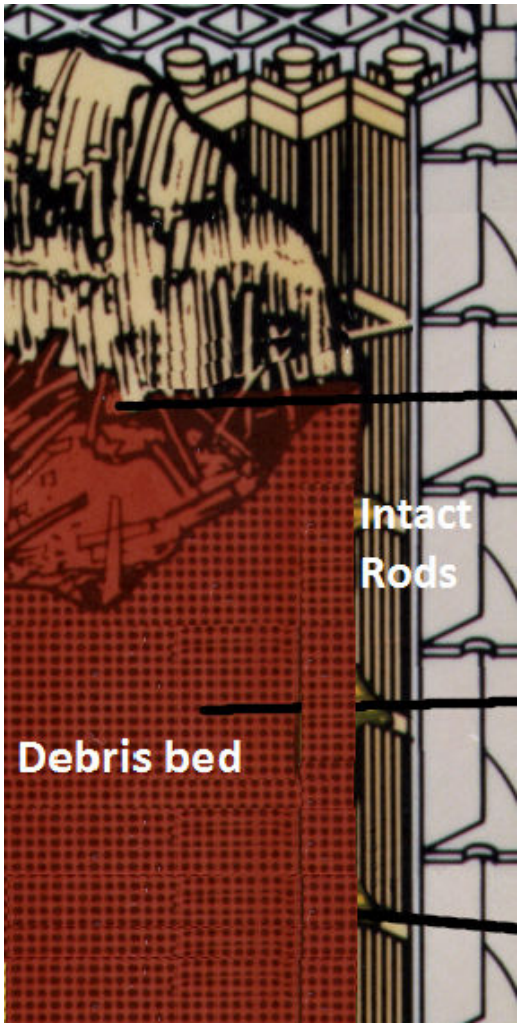

Figure 1.1: Zoom on the TMI-2 debris bed surrounded by intact fuel assemblies

tric cylinders, the inner one being less permeable and, possibly more porous. The formation of this configuration will be explained further in this chapter. The modeling of two-phase flow follows the approach already developed in previous works of [Duval 2002, Duval 2004, Béchaud 2001, Bachrata 2012, Bachrata 2013]. It is based on the volume averaging method and empirical closure laws for the heat transfers between phases and for the friction terms. The equations will be recalled in the next chapters. The main contribution to modeling in this thesis will be the identification of the interfacial friction terms that are necessary to explain the water entrainment in the lateral by-pass observed in PEARL experiments. The simplified physical modeling which will be proposed in the last two chapters is a first step towards a generic model able to identifiy quickly the processes that would govern the progression of

water in the main debris bed and the time of reflooding in different configurations of vertically-stratified debris beds.

1.2 Light Water Reactors

1.2.1 Overview

In 2016, nuclear power plants provided more than 11 percent of the world's electricity production and 13 countries relied on nuclear energy to supply at least one-quarter of their total electricity demand. With an outstanding record of 72.3 percent of its electricity production relying on nuclear power, France leads the list of the top ten countries (which are also European) and places second after the United States in the list of top Nuclear generating countries with a 384 Billion kWh (France) to 805.3 Billion kWh (US) in 2016 (Figure 1.2 lists the top ten countries by total annual production). As of April 2017, 30 countries worldwide are operating 449 nuclear reactors for electricity generation and 60 new nuclear plants are under construction in 15 countries ([NEI 2017]).

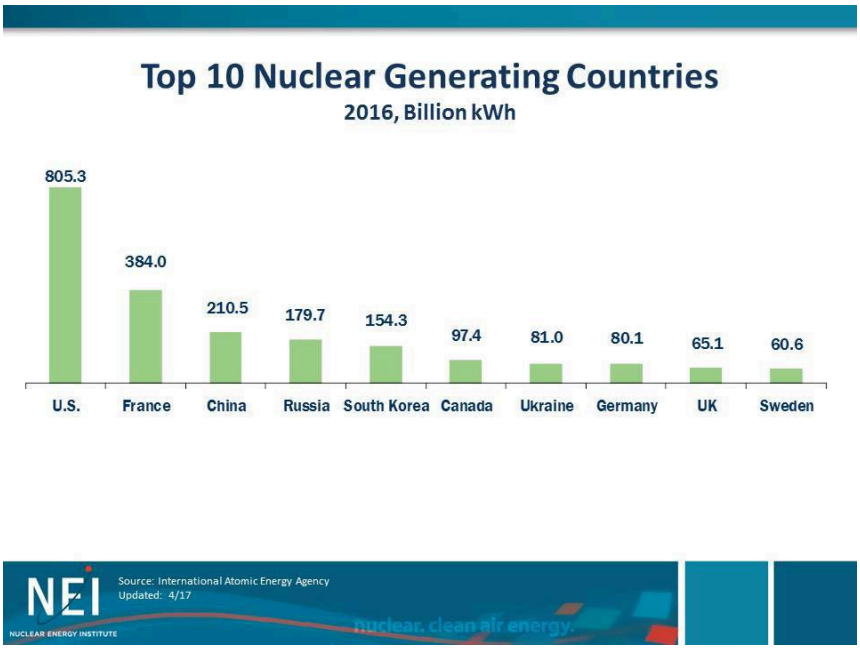

Figure 1.2: Top 10 Nuclear generating countries in 2016

The nuclear power plant is simply a thermal power plant in which the heat source is the nuclear reactor, mostly fueled by enriched Uranium. Typically, all conventional

thermal power plants produce heat in order to generate steam which drives a steam turbine connected to an electric generator which eventually produces electricity. In a nuclear reactor, heat is produced in a first circuit by chain nuclear fission reactions of the enriched Uranium atoms; this heat is then transferred to another circuit to boil water in a steam generator, and produce the steam driving a steam turbine to produce electricity.

In the electricity production process large amount of energy can be produced by small amount of fuel. Moreover, it involves the least CO2 emission, which is a major concern nowadays considering the consequences of continuous global warming. Yet, the the potential risk of nuclear energy use to the man and environment is an important concern that must to be assessed accurately in order to prevent the occurrence of accidents and mitigate it properly if it happened.

Since the beginning of comercial nuclear industry, Water-Cooled Reactors (WCRs) have played a significant role and currently account for more than 95 per cent of all operating civilian power reactors in the world. Moreover, the majority of nuclear reactors under development and construction are water-cooled.

Water Cooled Reactors (WCRs) have been the cornerstone of the nuclear industry in the 20th century. With 441 reactors operating at the end of 2015, nuclear energy had a global generating capacity of 382.9 GW(e). Five reactors were permanently shutdown, ten were connected to the grid, the highest number since 1990, and eight were started to be constructed. Near and long term growth prospects remained centered in Asia, particularly in China. Of the 68 reactors under construction, 45 were in Asia, as were 39 of the 45 reactors that were connected to the grid since 2005 [IAEA 2016]. Many of these plants were originally licensed to operate for 40 years, but through advances in knowledge, the lives of these plants are now being extended to 60 years, with a potential to operate even longer. It can be expected that WCRs will continue to play an important role in the 21st century.

Light water reactors (LWRs) are the most common WCRs worldwide and are divided into two types: Pressurized Water Reactors (PWRs), which produce steam for the turbine in separate steam generators; and Boiling Water Reactors (BWRs), which use the steam produced inside the reactor core directly in the steam turbine. All LWRs require fuel that is enriched in the fissile isotope, U-235.

1.2.2 Pressurized water reactor

Pressurized water reactors were initially designed for use in submarines. As a result of R&D works, a commercial PWR was designed and developed for nuclear power

plant applications. Eventually, several commercial PWR suppliers emerged in the USA, Germany, France and Japan. Over the past three decades, many PWRs were placed in service, accumulating thousands of reactor years of operating experience. In recent years, new generations of advanced PWR nuclear power plants have been developed, building upon the past success, as well as applying lessons learned from past operating experience. A PWR is composed of two main circuits as represented

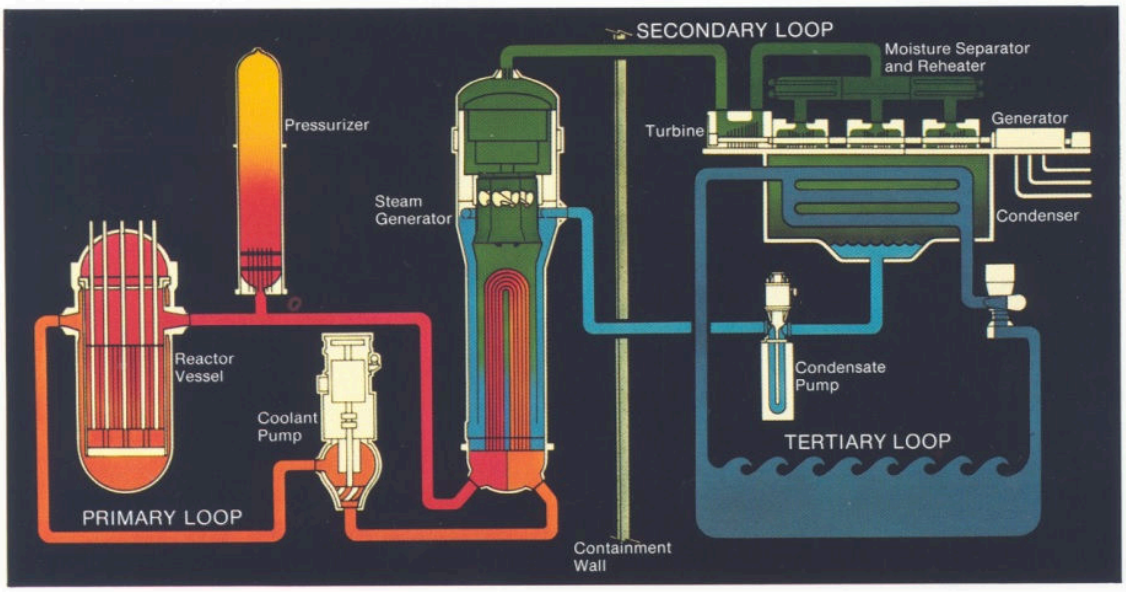

Figure 1.3: *Pressurized water reactor PWR - loops and main components, the Westinghouse design*

in Figure 1.3:

- The primary circuit which composes: the nuclear reactor core which produces the energy, a steam generator which transfers the energy from the primary circuit to the secondary circuit via steam generation profiting from the incoming heated water, a pressurizer that regulates the pressure of the primary circuit, and a pump for circulating the coolant.

- The secondary circuit to which transforms the thermal energy received from the primary circuit into mechanical and eventually electrical energy. It is composed of a turbine which converts the mechanical work driven by the steam produced into electricity, a condenser and a secondary pump. Heat is evacuated from the condenser to a cold source, usually a river or sea, or a cooling tower.

1.2.2.1 Heat generation in a nuclear reactor

In a nuclear reactor core heat is generated in a number of ways:

- The kinetic energy of fission products is converted to thermal energy when these nuclei collide with nearby atoms.
- The reactor absorbs some of the gamma rays produced during fission and converts their energy into heat.
- Heat is produced by the radioactive decay of fission products and materials that have been activated by absorption. This decay heat-source will remain for some time even after the reactor is shut down. A kilogram of uranium-235 (U-235) converted via nuclear processes releases approximately three million times more energy than a kilogram of coal burned conventionally 7.2 x 10^{13} joules per kilogram of Uranium-235 versus 2.4 x 10^{7} joules per kilogram of coal).

1.2.3 Initiating events and its categorization

Initiating events can be classified according to their frequency of occurrence (IAEA [IAEA 2002]), or in other words their probability. They can either be considered as transients, or accidents. Accidents can be further subdivided into three main categories:

- Design-Basis Accidents (DBAs): they are postulated accident that a nuclear facility must be designed and built to withstand without loss to the systems, structures, and components necessary to ensure public health and safety.
- Beyond Design-Basis Accidents (BDBAs): they are accident sequences that are possible but were not fully considered in the design process because they were judged to be too unlikely to occur.
- Severe Accidents (SAs): they are the type of accidents that may challenge the nuclear facility safety systems at a level much higher than expected.

The adopted analysis methodology for various events mainly differs in the use of diverging acceptance criteria and also in the level of conservatism in the analysis assumptions. A typical categorization for groups of initiating events was proposed by IAEA ([IAEA 2002] and [IAEA 1995]), as follows:

- Reactivity induced accidents
- Decrease of reactor coolant flow

- Increase of reactor coolant inventory
- Increase of heat removal by the secondary side
- Decrease of heat removal by the secondary side
- Decrease of reactor coolant inventory; e.g. loss of coolant accidents (LOCAs)
- Anticipated transients without SCRAM

The main interest of this Ph.D. work is to investigate the efficiency of the late injection of water into the severely damaged reactor core in case of loss of coolant accidents.

1.3 Accidental scenario

The description of severe accidents in LWRs is generally classified into in-vessel and ex-vessel situations depending on the progression of corium (molten fuel mixed other materials). In both situations, the fragmentation and relocation of core materials due to contact with water leads to the formation of particulate debris either in the reactor vessel lower plenum or in the reactor pit. Prior to the potential melting and relocation of the molten corium to the bottom of the vessel, the scope of this thesis considers the in-vessel situation, in which the hot debris beds is formed inside the core of the reactor.

1.3.1 Loss of coolant accident - LOCA

Due to the loss of coolant during a severe accident, the core gets uncovered and continues to heat up by the decay heat of the fission products in the fuel. As a result, this heating up will cause cooling water to evaporate in the core and it will decrease the water level in reactor pressure vessel. The time range for the core to dryout varies depending on the accident development and the reactor design, yet the standard period of time is from two to few hours. The decay of heat produces a continued heat up of the fuel rods and the other core materials. The fuel rod cladding is made of Zirconium material. In this situation, when the temperature is higher than 1700°C, an exothermic reaction occurs between Zirconium and the superheated steam, generating around 1.3 MJ per 1 kilogram of Zirconium. This reaction, which is a byproduct of the core heating and water evaporation, accelerates the temperature rise and the core degradation process. Besides that, large amounts of hydrogen are produced and may arrive to the reactor containment through the safety valves of

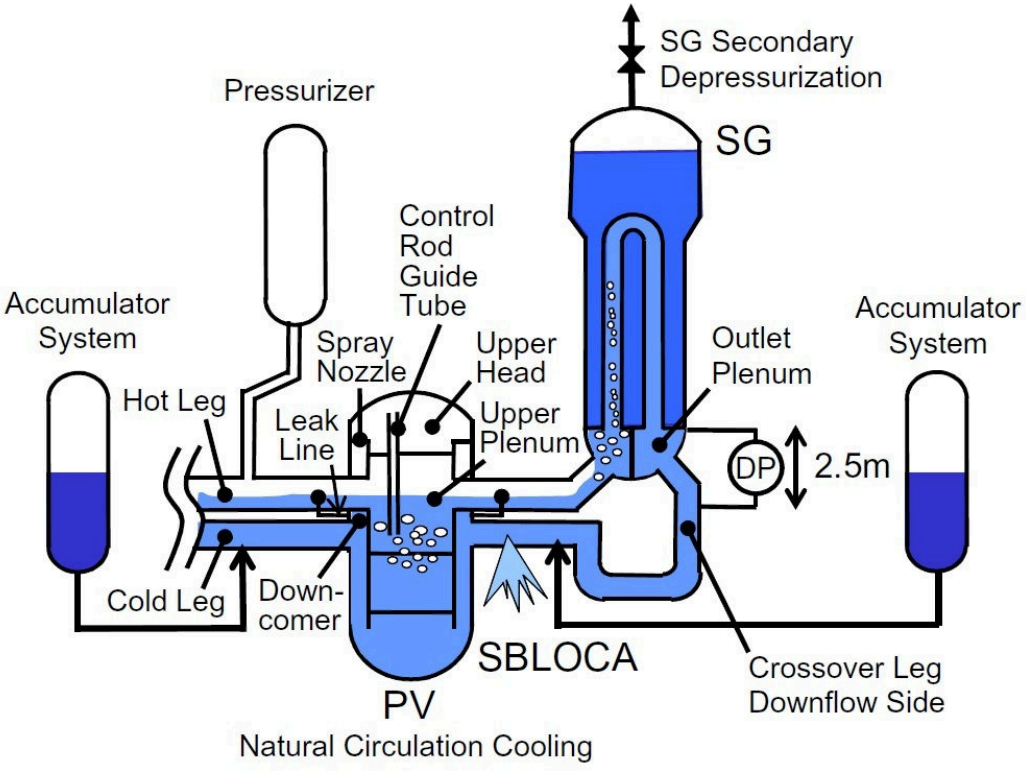

Figure 1.4: Coolant behavior during cold leg small-break LOCA with Steam-Generator depressurization in a PWR ([Takeda 2013])

the reactor cooling system or through a leak. Knowing that the reactor containment system is regarded as the 4th passive safety barrier (after the reactor vessel and primary circuit components as 3rd, fuel rods cladding as 2nd, and fuel pellets as 1st safety barrier), the failure of the containment must be avoided. Any failure of the containment would lead to catastrophic consequences in terms of radioactive release to the environment. Moreover, the presence of such high concentrations of hydrogen entering the containment can cause an explosive combustion of the gas mixture, eventually causing serious damage to the containment. Investigations of the oxidation of core metal and hydrogen generation processes can be found in details in [Sepold 2004] and [Chikhi 2012].

The Loss of Coolant Accident (LOCA), Figure 1.4, is described by a water leakage in the primary circuit of a nuclear reactor core due to a small or large pipe break. Once the leak is detected, the safety control rods, are inserted into the core to stop the fission chain reaction. The safety injection systems are then initiated to compen-

sate the loss of coolant through the breach and to ensure the long-term removal of residual heat that continues to accumulate in the core due to the radioactive decay of materials.

Since the LOCA is a design-basis accident, the safety injection systems are designed such that the accident is mitigated with causing damage to the reactor core. However, if the loss of coolant is not compensated by the safety injection systems (as what happened recently in Fukushima Daichi accident), this incident leads to the depressurization in the primary pressure. If the depressurization continues to decrease, provided the temperature in the primary circuit, and drops below the saturation pressure of water, water will then start to vaporize.

If this situation persists, the coolant in the primary circuit continues to vaporize and the reactor core gets uncovered. Due to accumulation of residual heat, the core deteriorates upon temperature increase and its safety is now under question.

Core heating and oxidation of the fuel cladding by the coolant vapor provoke core degradation and a total or partial melting of the hot fuel rods forming a corium pool that can relocate to the lower head of the reactor vessel compromising its local integrity which if failed would allow the corium to reach the concrete level which is the last confinement barrier and provoking the danger of a radioactive released to the environment.

Such an accidental scenario was considered impossible in the early times but the severe accidents that occurred in the recent decades (Three Mile Island in USA 1979) and the Fukushima accident in Japan 2011 urged the need to develop awareness and investigate to acquire a deep knowledge of the phenomenology of severe accidents in order to develop and define the means of intervention to mitigate the progression of such events.

1.3.2 Emergency core cooling systems - ECCSs

In a PWR, the mitigation of this accidental scenario is based on the ECCSs (Emergency Core Cooling Systems). They consist of one passive system and three active systems that function according on the nature and the position of the pipe break. The main purpose of the Emergency core cooling systems is to provide core cooling to minimize fuel damage following a LOCA, and to provide additional shutdown margin following a steam line break accident ([USNRC 2012a], [USNRC 2012b]).

The ECCSs (Figure 1.5) include one passive and three active systems:

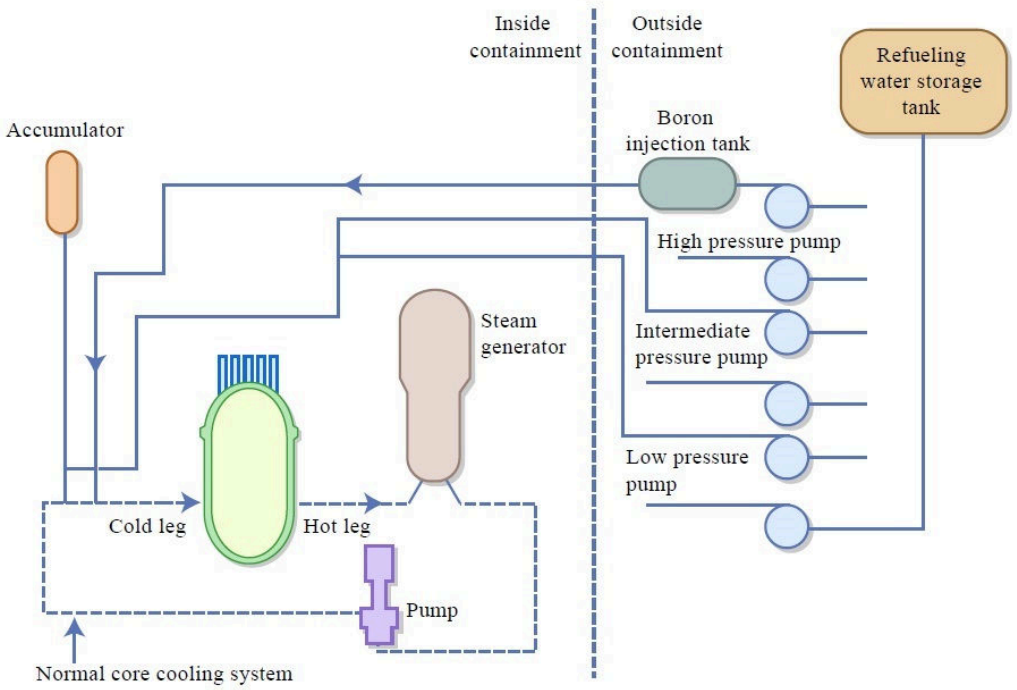

Figure 1.5: Schematic presentation of the Emergency Core Cooling Systems (ECCSs)

1. Accumulator injection system
2. High pressure injection syste (HPIS)
3. Intermediate pressure injection system (safety injection system)
4. Low pressure injection system (LPIS)

1. The cold-leg accumulators form a passive system which functions following a large LOCA. It rapidly refills the reactor vessel downcomer and bottom plenum and begins to reflood the core. The accumulator is usually two thirds full of borated water (neutron absorber) while the remaining volume is filled with nitrogen at a pressure greater than 40 bars. This boron concentration ensures that sufficient negative reactivity is added to maintain post-LOCA subcriticality.

2. The high pressure injection system (HPIS) functions following small to intermediate sized LOCAs. It is an active system which provides high pressure, low volume

safety injection and adds negative reactivity. It makes up for reactor coolant contraction by injecting water mixed with Boron (neutron absorber) into the reactor coolant system (RCS). The design pressure for this system is around 190 bars. It consists of two centrifugal charging pumps, a 3.4 m^3 boron injection tank, and a 1658 m^3 refueling water storage tank (RWST) (see Figure 1.5). The design flow rate of each pump is 560 l/s. They can deliver flow under all pressure conditions up to 190 bars, such that their discharge pressure is sufficient to provide flow to the reactor cooling system for any postulated size break upon a LOCA.

3. The intermediate pressure injection system (IPIS), also called safety injection system. It functions following a small to intermediate sized LOCAs. It is an active system which provides intermediate pressure, low volume safety injection. This system includes two safety injection pumps. For each pump, the design flow rate, design pressure, and design temperature are 1600 l/s, 117 bars, and 148°C respectively. They provide water from the RWST to the RCS in the case of a relatively small break in which the RCS pressure remains high.

4. The low pressure injection system (LPIS) is an active system which provides low pressure, high volume safety injection to complete the reflooding of the core following a LOCA, and provides a flow path and heat sink for long-term core cooling. It makes use of the Residual Heat Removal System (RHR) which composes two pumps. Their design flow rate, pressure, and temperature are 2270 l/s, 41 bars, and 200°C respectively ([Kitch 1985]). Those pumps deliver water from the RWST or the containment recirculation sump to the four cold legs of the reactor cooling system (RCS) for large RCS pipe breaks up to the design-basis LOCA.

The accumulators passive system consist of large volume tanks of borated water. The pressure in the passive system is less than that of the reactor cooling system (RCS). Following an accident, when RCS pressure decreases below tank pressure, the borated water is injected.

The (high, intermediate, and low pressure injection systems) are active systems. They consist of several pumping systems with varying discharge pressures and injection flow rates. Those systems will only start if an accident initiation signal is received. When actuated, these systems inject borated water into the reactor cooling system. After the injection phase, the residual heat removal system (RHR) provides longterm core cooling where it is aligned take water from the containment sump to cool it by circulating it through the residual heat removal heat exchangers then pumping it back to the core through the cold leg.

1.4 Debris bed in a reactor core

1.4.1 Formation

Severe accidents resulting from a LOCA (loss of coolant accident) have occurred at the Three Mile Island unit-2 (TMI-2) [NSAC 1980] in the USA, in 1979, and recently in Fukushima, Japan, in 2011, where 3 reactors were destroyed. The Chernobyl accident in 1984 has a different origin (increase of reactivity). Following a loss of coolant accident in a PWR (pressurized water reactor), the reactor core gets uncovered and starts to heat up under the effect of decay heat of the fission products in the fuel. Consequently, this warming up will cause coolant evaporation in the core and it will decrease the water level in reactor pressure vessel. The time range for the core to dryout varies relying on the progress of the accident and the reactor design, yet the standard period of time is from two to few hours. As the accident evolves, core heating and oxidation of the fuel cladding by the coolant vapor lead to core degradation. An exothermic reaction thus occurs between the superheated steam and the Zirconium of the fuel rod cladding at temperatures higher than 1700°C. The heat generated by this reaction is around 1.3 MJ per 1 kilogram of Zirconium [Coindreau 2008]. This additionally provokes the temperature rise and core degradation process. Besides that, large amount of hydrogen are produced and may arrive to the reactor containment through the safety valves of the reactor cooling system or through a leak. The presence of high concentrations of hydrogen that enters the containment can cause an explosive combustion of the gas mixture, where this combustion will damage the containment. The oxidation of core metal and hydrogen generation processes can be found details in [Chikhi 2012].

In this case, reflooding the core is one of the most common options to save the situation but it can cause a thermal shock and the embrittlement of the cladding, hence forming a configuration with particulate debris. Such complications in the evolution of the accident must be anticipated to enhance the efficiency of its mitigation. The concept of debris bed formation was introduced by [Akers 1989] and [McCardell 1990] upon the post-accident examination of the Three Mile Island unit-2 (TMI-2) that occurred in the USA-1979. In the latter accident, the fuel was fragmented to particles of size ranging between 1 to 5 mm ([Akers 1986], [Broughton 1989], [McCardell 1990]) due to the relocation of molten materials inside the core upon quenching of the very hot rods being uncovered. Figure 1.6 is a schematic representation of the core end-state of the TMI-2 unit.

In such situations different debris bed configurations might exist such as the formation of a debris bed surrounded by an intact zone of fuel rods or the existence

of compact zones of very small particles limiting the coolant penetration (Figure 1.1). The TMI-2 debris was a mixture of ceramic and metallic phases. The ceramic phases consisted of (U, Zr)O2 and/or (Zr, U)O2, and the metallic phases consisted of elements from the control rod and the other core materials (Ag, Fe, Ni, Cr, etc.) with more than 80 per cent by mass UO2 and an average density around 8000 kg/m3 [Akers 1989]. Measured densities of the TMI-2 debris samples ranged from 6.32 x 106 g/m3 to 8.25 x 106 g/m3 [Nagase 2012]. The density decreases by 0.2 x 106 g/m3 with a temperature increase of 1000 K.

During an accident leading to reactor core melting, the success of core reflooding in the removal of the residual heat and interruption of melting preserves the reactor vessel integrity where the corium is retained inside the vessel. This was the case in the TMI-2 accident where part of the reactor core melted and several tones of corium were found at the bottom of the vessel which did not fail even though it was subject to thermal stresses caused by the residual heat. It could resist the stresses because the reactor was flooded.

The process of cooling down a debris bed is more difficult than intact fuel rods due to the high temperatures i.e. above 2000 Kelvin and small hydraulic diameters of few millimeters. The progression or mitigation of the accident at this stage strongly relies upon the stabilization of such debris beds (steady state condition where temperature of the bed does not vary with time). When the hot and dry debris bed are quenched (cool down to saturation temperature by flooding with water) before reaching melting due to decay heat, a stable cooling condition is achieved. One of the major objectives of this thesis is to assess the chances of quenching such a particulate debris against heat up due to the residual heat.

1.5 Reflooding experimental studies

The reflooding models used for Loss of Coolant Accident (LOCA) are not applicable for debris bed cooling because . And as severe accident management is crucial, the question of debris coolability has to be resolved.

The coolability of debris beds has been the subject of numerous questions and studies in the last thirty years. Several experimental programs on debris coolability have been performed over the last decades following the TMI accident, aiming at determining the maximum power that can be extracted from a heated debris bed by water reflooding. Indeed a non-coolable debris bed is assumed to quickly rise in temperature, due to the residual decay heat, melt and form a large molten pool

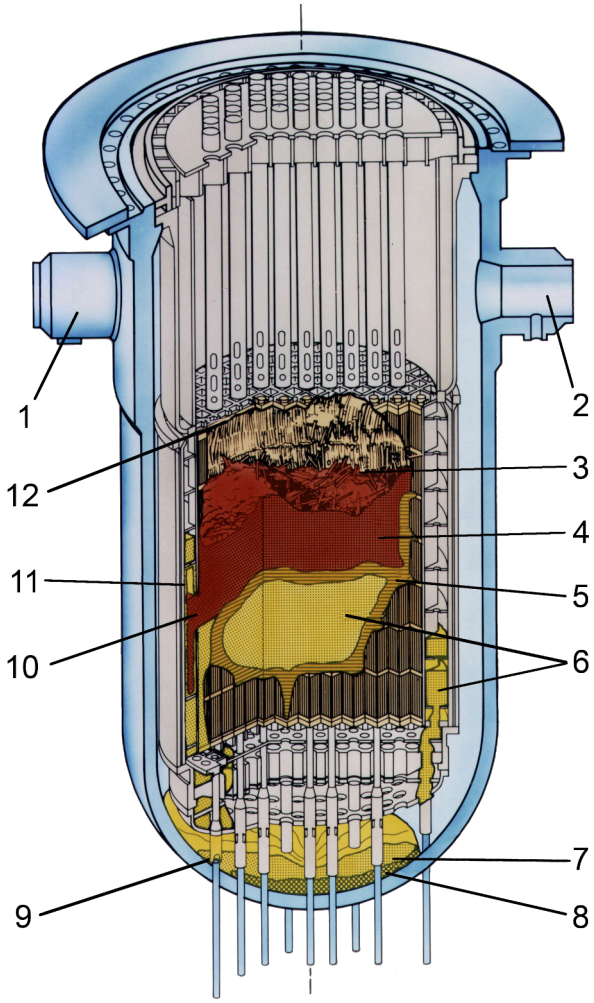

Figure 1.6: *Three Mile Island Accident, core end-state. 1.Core inlet A - 2.Core inlet B - 3.Cavity - 4.Core debris - 5.Crust - 6.Previously molten material - 7.Lower plenum debris - 8.Region depleted in Uranium - 9.Ablated in-core instrument guide - 10.Hole in baffle plate - 11.Coating of previously-molten material on bypass region interior surfaces - 12.Upper grid damaged top plate*

that would expand even when surrounded by water, and threaten the integrity of the vessel. Many experimental studies and theoretical models have focused on the determination of the "critical" heat flux and the maximum volumetric power that can be removed from a debris bed by water. In most cases, one-dimensional debris beds were considered [Lipinski 1984]. A few interesting experimental studies of two-dimensional effects were done in parallel [Lee 1977, Hardee 1977]. Recently, two-dimensional effects have been studied in more details, either experimentally [Décossin 2000, Atkhen 2003] or numerically [Mayr 1998, Béchaud 2001]. It appears

that the counter-current flow limitation, which is always present in one-dimensional situations, can be avoided in some two-dimensional configurations, leading to a higher critical heat flux. It has also been observed that local thermal equilibrium may not exist everywhere in the debris bed, even for heated debris covered by water at saturation temperature [Atkhen 2003]. The flow of overheated steam through the bed appears as a relatively important process to cool the "dry" debris.

On the other hand, the reflooding of hot debris beds has received less attention. Some experimental studies and data of top and bottom reflooding are available [Armstrong 1982, Armstrong 1981, Cho 1984, Ginsberg 1982, Ginsberg 1985, Ginsberg 1986, Tutu 1984b, Hofmann 1984, Reed 1985, Hu 1991, Konovalikhin 2000] and a few models have been proposed [Petit 1999, Sozen 1990]. More recently, debris bed coolability was investigated with experimental programs such as DEBRIS ([Schäfer 2006], [Rashid 2013]) at IKE in Germany, and POMECO ([Nayak 2005], [Nayak 2006]) at KTH in Sweden. The existence of temperature differences between the solid particles, the water and the steam makes modeling and experimental measurements more difficult. Furthermore, flow patterns are complex since, for very high temperature particles, steam becomes the "wetting" phase due to the presence of a stable steam film around the particles. This was observed experimentally, on single spheres, by [Dhir 1978] who proposed a theoretical model for heat transfer around spheres under film boiling regime. However the results obtained for spheres are difficult to apply to particle debris beds. Because of the lack of experimental data on real debris beds, models must rely on several assumptions.

In recent years, PRELUDE and PEARL ([Stenne 2009], [Repetto 2011], [Repetto 2013], and [Chikhi 2015b]) were also launched by IRSN to investigate the thermal hydraulics of the reflooding process and develop new reflooding models and to validate 2D/3D models. The aim is to predict the consequences of the water reflooding of a severely damaged reactor core where a large part of the core has collapsed and formed a debris bed. The data from PEARL experiments will be extensively used in this Ph.D. work.

1.6 Thesis objectives and outline

The objective of this thesis is to provide a physical and phenomenological basis to understand the complex process that may result from the forced injection of water into a core where fuel assemblies have collapsed and co-exist with less damaged zones. Among the important issues, the impact of the debris bed geometry is investigated, as well as the impact of different boundary conditions on the quenching

and coolablity of the hot debris. After a presentation of the general approach followed for the modeling of two-phase flow in porous medium, a discussion about the choice of friction terms gives a preliminary basis for the following assessments with numerical calculations. A series of PEARL tests are calculated numerically with the model implemented in ICARE/CATHARE. It is shown that the model captures quite well some of the phenomena observed in PEARL, in particular the transition from a flat quench front (called 1D) to a quench front progressing significantly faster in the bypass than in the central bed (called 2D behavior). However, the model fails to accurately predict the flow of water in the bypass (its velocity and the mass flow rate) and it appears that an additional interfacial friction term is necessary to be more accurate. In order to study in more details the effects of various frictions terms, an analytical model is developed. This model allows performing many calculations in a short time. From that study, it confirms the necessity to add an interfacial friction term in the momentum equations for liquid and gas phases. The analytical model also provides indications about the effects of the geometry of the porous bed on the transition from 1D to 2D behavior. The effect of pressure is also examined. Finally, the analytical model is applied at the reactor scale to investigate the conditions for which the injection of water would be efficient enough to cool the debris and the conditions for which too much water is redistributed in the bypass and cannot contribute to an efficient quenching of the main debris bed.

Chapter two presents the physical models that describe the flow in porous media. The generalization of Darcy's law is considered, the adopted model in this thesis is the Darcy-Forchheimer law with the consideration of an interfacial friction term. The physical model implemented in Icare-Cathare is then presented. In Chapter 3, PEARL tests are investigated, numerical calculations using the thermal hydraulics code Icare-Cathare are presented. The reflooding process is investigated for several tests performed at different initial and boundary conditions. The main outcomes are then analyzed, especially the entrainment behavior of water in the bypass during reflooding. An analytical model estimating the major concerning features of reflooding a two-layered debris bed with contrasting permeability is proposed in Chapter 4. Several interfacial friction laws are tested and it is shown that the generalized Darcy law does not provide good estimations of the water entrainment in the bypass, unless an interfacial friction term is added. In Chapter 5, the proposed model is implemented; PEARL and reactor-scale calculations are performed and presented. A reference configuration at the reactor-scale comparable to the situation of a formed debris system in a nuclear reactor during a severe accident is considered. The impact of several geometric parameters as well as initial and boundary conditions on the main features of the quenching process is investigated. As a consequence, the coolability chance is assessed according to those investigation as function of the varying

parameters. General conclusions drawn are then provided in Chapter 6.

Chapter 2

Porous media physical laws

This chapter presents the physical models that describe the single and two-phase flow in porous media. Generalization of Darcy's law is considered and the main interfacial friction laws found in the literature are presented. Then the physical model of two-phase flow with evaporation which is implemented in the Icare-Cathare thermal hydraulics code is presnted.

Contents

2.1 A porous medium

A porous medium is composed of a solid matrix through which interconnected cavities are distributed occupying a measurable fraction of the volume. The fluid can flow through the large cavities, called pores, in single or multi-phase form. In order to describe and characterize the porous medium, the complexity of the microscopic structure is usually avoided by studying the macroscopic physical properties, which are related to the microscopic structure. The main physical properties characterizing a porous medium are the porosity, the permeability, and the homogeneity. The porosity represents the volume fraction of the void space to the total volume, it is designated by ε. Whereas the permeability, denoted κ, is the capacity of the porous medium to transmit the fluid. The homogeneity of a porous medium is related to the absence of local variations of macroscopic properties, like the permeability, on scales comparable to the size of the porous medium. Typically, the naturally formed porous media possesses some in-homogeneity. Yet, the medium can be regarded as homogeneous if the magnitude of the local variations have negligible impact on the macroscopic properties at a larger scale.

The resolution of the conservation equations at the pore scale is necessary in order to form the tools to perform simulations of fluid flows in a porous medium. This macroscopic approach is usually limited to certain calculation domains. This study is concerned in the two phase flow of water and steam in a debris bed. For such large systems, at large scales, the porous medium can be considered as a continuum such that the flow characteristics are continuous. This macroscopic approach describes the medium by its macroscopic properties but it is restricted to the validity of the considered correlations. The debris bed under consideration composes two coaxial cylindrical debris layers each of which is regarded as a homogeneous porous medium. We regard a porous medium as homogeneous with respect to a given process and a given averaging volume when the effective transport coefficients in the volume averaged transport equations are independent of position.

2.2 On the modeling of flow

The modeling of flow in porous media is mathematically very complex and it involves many approximations. The main existing methodologies are the pore-scale numerical approach and the macroscopic continuum approach. In the pore-scale numerical approach, the porous medium is described in detail applying the relevant physics of flow at pore-scale level, which is not often accessible. Various numerical methods like finite volume and finite difference may be implemented to find the solution. This approach is that the closest to the analytical solution and the most direct one that

describes the physical situation. However, it requires a detailed description at the pore-scale level which makes it very complex and hard to implement thus increasing the computational cost massively. That is why its current use is still limited to simple flow processes in porous media and/or small volumes.

In the macroscopic approach, the porous medium is treated as a continuum and all the complexities of the microscopic pore structure are grouped into effective transport terms, such as permeability. Semi-empirical equations are usually employed in this approach such as Darcy's law or Ergun's equation. The advantage of this approach is that it is simpler and easier to implement with lower computational cost. It has less convergences difficulties than the pore-scale approach but the disadvantage is that it can not describe in detail the physics at the pore level so it is less capable than the macroscopic approach in dealing with time-dependent transient situations.

2.3 Up-scaling method: volume averaging

Following the macroscopic approach for modeling of flow in porous media, up-scaling methods are implemented to make the connection between the physics of the flow in porous media at small scales and the macroscopic scale. Several methods exist in the literature, such as the homogenization method ([Mei 2010], [Bensoussan 1978], [Sanchez-Palencia 1982],[Bourgeat 1984], [Mei 1991], [Wodie 1991], [Balhoff 2010]) and the volume averaging volume method ([Quintard 1994b], [Quintard 1994c], [Quintard 1994d], [Quintard 1994e], [Quintard 1994f], [Whitaker 1999]).

The volume averaging method is a synthesis between the stochastic method and the homogenization method. The concept was originally introduced making use of the stochastic method stochastic ([Matheron 1965]) and multi-scale homogenization. The use of the method of volume averaging in the modeling of transfer phenomena in porous media dates back to about fifty years ([Marle 1967], [Whitaker 1967]). In 1967, Whitaker demonstrated the volume averaging theorem and applied it to study the diffusion-dispersion problem in a porous media. In the same year, [Anderson 1967] applied this method to describe the flows in fluidised beds while [Slattery 1967] employed it to study the flow of visco-elastic fluids through porous media.

Upscaling methodologies are beyond the scope of this thesis. However, in order to clarify the definitions and models used, we define the volume averaging standards. The transport equations used are obtained by the method of volume averaging. This method was developed for single-phase flow and later extended to two-phase flow in porous media by several authors ([Whitaker 1986b], [Whitaker 1986a],

[Whitaker 1994], [Whitaker 1996], [Chella 1998], [Lasseux 1996], [Lasseux 2008], [Lasseux 2011]). This technique can be implemented to derive the continuum equations for multiphase systems.

In other words, the pore-scale information, including the valid equations that can be spatially smoothed and the boundary conditions, is used to derive local volume averaged equations which are valid everywhere in the porous medium. And eventually providing estimations of the effective physical properties which are clear relations between the pore-scale structure and the macroscopic description.

2.3.1 Representative elementary volume

The system under study is composed of three phases (liquid, gas, solid) designated by (β, γ, σ) respectively. It is represented in (Figure 2.1) where the macroscopic quantities are characterized by length L and the representative elementary volume, over which the averaging technique is applied, is identified by V. The characteristic lengths of the phases β, γ, and σ are denoted l_β, l_γ, and l_σ respectively.

The method of volume averaging is applicable whenever the characteristic lengths are constrained by the assumption of separation of scales ([Whitaker 1969], [Whitaker 1986b]):

$$l_{\beta,\gamma,\sigma} \ll r_0 \ll L \tag{2.1}$$

where r_0 represents the radius of the representative elementary volume V. The averaging technique is then applied over this volume to spatially smooth the pore-scale equations.

In our work, L will be typical of the heterogeneity length scale. We assume that we have a separation of scales that allow to introduce a macro-scale (or Darcy-scale) description with effective terms having spatial variations.

2.3.2 The macro-scale description

Proceeding the analysis of the two-phase flow in a porous medium, the quantities associated with each phase are identified by its respective subscript. The interfacial area between two phases λ and θ is defined by A_{λ_θ}, whereas $A_{\lambda e}$ identifies the area of entrances and exits of the λ-phase in the macroscopic system.

For each quantity ϕ_β in the β-phase, the superficial average is given by:

$$\langle \phi_\beta \rangle = \frac{1}{V} \int_{V_\beta} \phi_\beta dV \tag{2.2}$$

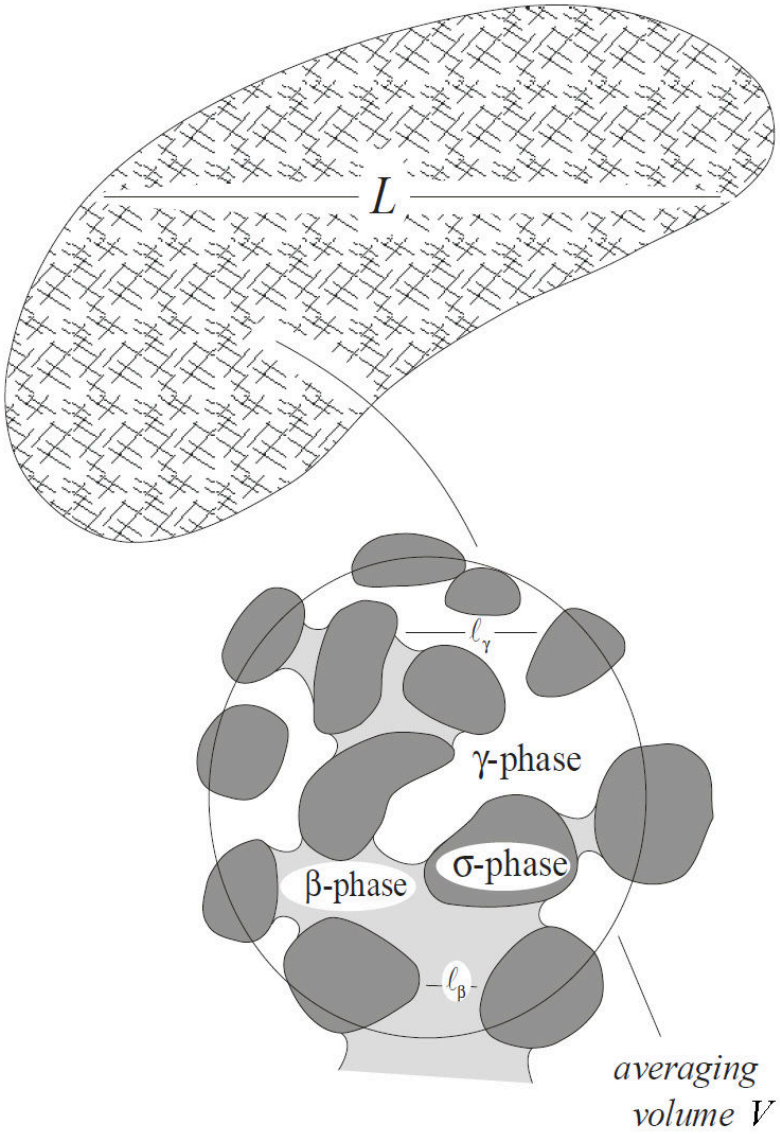

Figure 2.1: Solid - Liquid - Gas phases in a porous medium

where V_β represents the partition occupied by the β-phase in the representative elementary volume V.

However, when ϕ_β is a constant ${\phi_\beta}^o$, $\langle\phi_\beta\rangle = \varepsilon^\beta {\phi_\beta}^o$. Due to this fact, the so called

intrinsic average is prefered and it is defined by:

$$\langle \phi_\beta \rangle^\beta = \frac{1}{V_\beta} \int_{V_\beta} \phi_\beta dV \tag{2.3}$$

which gives $\langle \phi_\beta \rangle^\beta = {\phi_\beta}^o$ in the case of a constant ϕ_β.

The volume fraction ε_β of the β-phase is defined by:

$$\varepsilon_\beta = \frac{V_\beta}{V} \tag{2.4}$$

it relates the superficial average and the intrinsic average by:

$$\langle \phi_\beta \rangle = \varepsilon_\beta \langle \phi_\beta \rangle^\beta \tag{2.5}$$

Following Gray's decomposition [Gray 1975], each quantity ϕ_β can be written in terms of its intrinsic average and a spatial fluctuation term as:

$$\phi_\beta = \langle \phi_\beta \rangle^\beta + \widetilde{\phi}_\beta \tag{2.6}$$

This decomposition was then adopted by many authors on porous media physics. By definition the average of the spatial fluctuation is null:

$$\langle \widetilde{\phi}_\beta \rangle = 0 \tag{2.7}$$

which is an approximate sense following the assumption of separation of scales.

The decomposition replaces the local functions by the volume averaged quantities and its fluctuation which can be treated later in closure problems. For instance, writing the spatial decomposition of a scalar function ϕ_γ and the velocity vector $\vec{v}_\gamma$ in the gas-phase:

$$\phi_\gamma = \langle \phi_\gamma \rangle^\gamma + \widetilde{\phi}_\gamma \tag{2.8}$$

$$\vec{v}_\gamma = \langle \vec{v}_\gamma \rangle^\gamma + \widetilde{\vec{v}}_\gamma \tag{2.9}$$

Then the phase averaging operator applied on the product of two quantities ϕ_γ and $\vec{v}_\gamma$ can be defined as:

$$\langle \vec{v}_\gamma \phi_\gamma \rangle = \langle \langle \vec{v}_\gamma \rangle^\gamma \langle \phi_\gamma \rangle^\gamma + \widetilde{\vec{v}}_\gamma \langle \phi_\gamma \rangle^\gamma + \langle \vec{v}_\gamma \rangle^\gamma \widetilde{\phi}_\gamma + \widetilde{\vec{v}}_\gamma \widetilde{\phi}_\gamma \rangle \tag{2.10}$$

Furthermore, according to ([Whitaker 1999]) (Whitaker 1985), considering the constraint:

$$\frac{r_0^2}{L^2} \ll 1 \tag{2.11}$$

it simplifies to:

$$\langle \vec{v}_\gamma \phi_\gamma \rangle = \varepsilon_\gamma \langle \vec{v}_\gamma \rangle^\gamma \langle \phi_\gamma \rangle^\gamma + \langle \widetilde{\vec{v}}_\gamma \widetilde{\phi}_\gamma \rangle \tag{2.12}$$

Whenever applying the volume averaging method to the equations governing the two-phase flow, one often encounters averages of gradients, divergences and partial time derivatives of a quantity ϕ_β. However, it is more interesting to obtain the terms resembling those differential operators applied on the phase-averaged terms. For instance, using the spatial averaging theorem, the superficial average of the gradient of ϕ_β is written as:

$$\langle \nabla \phi_\beta \rangle = \nabla \langle \phi_\beta \rangle + \frac{1}{V} \int_{A_{\beta\sigma}} \vec{n}_{\beta\sigma} \phi_\beta dA + \frac{1}{V} \int_{A_{\beta\gamma}} \vec{n}_{\beta\gamma} \phi_\beta dA \tag{2.13}$$

where $\vec{n}_{\beta k}$ is the normal unit vector to the $A_{\beta k}$ interfacial area between the β and k phases.

Similarly, the average of the divergence of a vectorial quantity $\vec{v}_\beta$ can be written as:

$$\langle \nabla . \vec{v}_\beta \rangle = \nabla . \langle \vec{v}_\beta \rangle + \frac{1}{V} \int_{A_{\beta\sigma}} \vec{n}_{\beta\sigma} . \vec{v}_\beta dA + \frac{1}{V} \int_{A_{\beta\gamma}} \vec{n}_{\beta\gamma} . \vec{v}_\beta dA \tag{2.14}$$

Whereas the superficial average of a partial time derivative of ϕ_β is treated using Reynolds transport theorem and written as:

$$\langle \frac{\partial}{\partial t} \phi_\beta \rangle = \frac{\partial}{\partial t} \langle \phi_\beta \rangle - \frac{1}{V} \int_{A_{\beta\sigma}} \vec{n}_{\beta\sigma} . \vec{w}_{\beta\sigma} \phi_\beta dA - \frac{1}{V} \int_{A_{\beta\gamma}} \vec{n}_{\beta\gamma} . \vec{w}_{\beta\gamma} \phi_\beta dA \tag{2.15}$$

with $\vec{w}_{\beta\theta}$ being the velocity of the β-θ interface.

Applying this scaling-up technique to the pore-scale transport equations, the volume averaged form is obtained and it includes averaged quantities and spatial fluctuations. The closure problems are then written based on the governing equations for the spatial fluctuations. This process will eventually provide estimations of the effective properties which link the pore-scale structure and the macroscopic description.

Each spatial fluctuation $\widetilde{\phi_\beta}$ is often related to averaged quantities through mapping

variables which are obtained by solving the pore-scale problems, named closure problems. If this kind of representation can be achieved, then the fluctuations in the averaged equations can be replaced in order to obtain a closed form of macro-scale equations. The macro-scale equations required for the modeling of our problems are briefly discussed in the next section.

2.4 Single phase flow

2.4.1 Darcy's law and flow regimes

Single phase flows are usually characterized by non-dimensional numbers, one of which is the Reynolds number which is defined as the ratio of the inertial to viscous forces and is given by:

$$Re = \frac{\rho\, v\, l}{\mu} \tag{2.16}$$

where ρ is the mass density of the fluid, l is a characteristic length of the flow system, v is a characteristic speed of the flow and μ is the dynamic viscosity of the fluid. However, when the fluid is flowing through a porous medium the Reynolds number is written in a different form to take into account the complex structure of the medium at pore-scale, by redefining the characteristic length l and the velocity v.

For a single phase flow in a porous medium of porosity ε and a measurable superficial or filtration velocity $\langle v \rangle$, the Reynolds number can be defined as:

$$Re = \frac{d_{st}\, \rho\, \langle v \rangle}{\mu\, (1 - \varepsilon)} \tag{2.17}$$

where d_{st} is the Sauter diameter of the particles defined by:

$$d_{st} = \frac{6\, V_{particle}}{A_{particle}} \tag{2.18}$$

This definition was adopted by several authors in nuclear engineering ([Li 2012a], [Li 2012b]), and chemical engineering domains ([Saez 1986a], [Saez 1986b]). For a porous medium composing particles with full sphericity d_{st} is simply equal to the particles diameter d_p. For simplicity, we denote the superficial velocity $\langle v \rangle$ by U. The Reynolds number for a single phase flow in a porous medium can be then defined as:

$$Re = \frac{d_{st}\, \rho\, U}{\mu\, (1 - \varepsilon)} \tag{2.19}$$

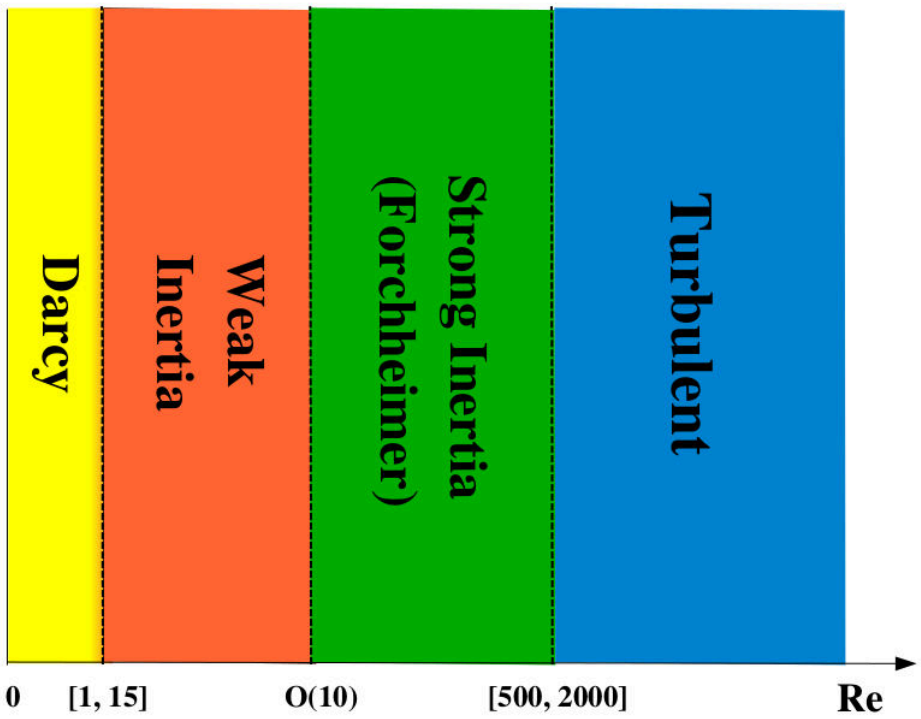

Figure 2.2: Flow regimes in porous media

In 1856 Henry Darcy conducted column experiments, in the French city Dijon, that lead to the proposed physical law describing the flow through sands. Since then, it has been generalized to a variety of situations and is by far the most widely-used model for single-phase flow through porous media. Darcy's law became the basic equation describing the flow of single phase through a saturated porous medium. Darcy's experiments showed that there is a linear relation between the fluid flow rate and the pressure gradient in the porous medium [Darcy 1856] where the linear proportionality factor represents the resistance to the flow. [LeRosen 1942] observed later on that this law was restricted to laminar (viscous) flow, at relatively low Reynolds number (creeping regime). This law assumes the dominance of viscous forces over inertial forces in porous media; hence, inertial forces were neglected. [Nutting 1930] suggested to replace that proportionality factor by ratio of the viscosity of fluid μ to another constant k, now known as the permeability. Thus for a one-directional steady state flow of an in-compressible Newtonian fluid through a horizontal porous medium, Darcy law can be written as:

$$U = -\frac{k \bigtriangledown P}{\mu} \tag{2.20}$$

where U (m/s) is the Darcy or filtration velocity, k (m^2) is the intrinsic permeability of the porous medium, μ (Pa.s) the fluid viscousity, and ∇P (Pa/m) the macroscopic pressure gradient.

It can be formally derived by the homogenization of steady Stokes flow, this development can be found in [Sanchez-Palencia 1982]. For a 3-dimensional flow, using the notations and definitions introduced in the previous section, this relation can be written in vector form as:

$$\langle \mathbf{v}_\beta \rangle \;=\; -\frac{\mathbf{K}}{\mu_\beta} \cdot \left(\nabla \langle p_\beta \rangle^\beta \;-\; \rho_\beta \mathbf{g} \right) \tag{2.21}$$

where $\mathbf{K}$ is the intrinsic permeability tensor characterizing the porous medium, $\mathbf{g}$ is the gravitational acceleration, (p_β, ρ_β, μ_β) are the pressure, density, and dynamic viscosity of the fluid respectively.

The flow regimes in porous media can be classified according to [Skjetne 1999a] into four main regimes, depending on the Reynolds number, as illustrated in Figure 2.2:

- Creeping flow regime (also called Darcy regime where Darcy's equation applies)
- Weak inertia regime (transitional regime into non-Darcian flow)
- Strong inertia regime (Forchheimer equation)
- Turbulent regime

In the creeping flow regime Darcy's equation applies, this regime corresponds to flows at low Reynolds number. After experimental and numerical investigations, several authors have proposed a limit for this regime where inertial effects start to appear. This limit is the onset of the non-Darcian flow regime, the proposed values range between Re = 1 to 15. The typical values provided experimentally were: 1 by [Tek 1957], 2 by [Wright 1968], 5 by [De Vries 1979], between 1 and 10 by [Dybbs 1984]. Other numerical studies suggested a range of 5 to 13 ([Stark 1972], [Coulaud 1986], and [Coulaud 1988]).

The deviation from Darcy's law starts with a transitional regime called the weak inertia regime, the onset ranges between Re = 1 to 15. In this regime the flow is described by a corrected Darcy law where the correction term is generally cubic in fluid velocity. This deviation from Darcy's law was investigated numerically

(by [Barrère 1990] and [Mei 1991]) and derived analytically by [Wodie 1991] for homogeneous isotropic and periodic porous media using double scale homogenization method. It was later extended to anisotropic porous media by [Firdaouss 1995] and [Firdaouss 1997]. This equation with a cubic velocity term was derived for both macroscopic and microscopic scales and the existence of the weak inertia regime was later confirmed by numerically by [Rasoloarijaona 1994] and experimentally by [Skjetne 1999b].

At higher flow rates, higher Reynolds numbers, the dominance of the inertial term increases and the fluid flow in porous media is approximately described by the Forchheimer equation which is a correction to Darcy's law such the the correction term is quadratic in velocity. More about the governing equations of fluid flow in weak and strong inertia regimes is presented in the next section.

2.4.2 Inertial flows

The deviation from Darcy's law is caused by inertial effects. Several researchers described the non-linear relationship between the pressure gradient and the velocity of the flow following different approaches which can be identified and are discussed in the literature. More information is included in the books ([Scheidegger 1974] and [Hannoura 1981]). Based on empirical models, certain theories were developed to explain the non-linear effects in porous media flows. Dimensional analysis and other theoretical considerations form the basis for those theories ([Dupuit 1863], [Forchheimer 1901], and [Ward 1964]) which can be classified into groups of models.

This generalization of Darcy's law has been the subject of many experimental and theoretical investigations. Various approaches have been developed and analyzed in order to provide a physical or theoretical basis for the Forchheimer law derivation such as: dimensional analysis by [Ward 1964], experimental study by [MacDonald 1979], averaging methods by [Irmay 1958], and variational principles by [Knupp 1995]. More recently, several authors ([Giorgi 1997], [Mei 1991], and [Wodie 1991]) have employed the mathematical technique of two-scale homogenization ([Wodie 1991], [Dupuit 1863]) to derive the Forchheimer law from the Navier-Stokes equation.

When the flow rate is high, Darcy's law was proven inadequate to describe fluid flow. For that reason, [Forchheimer 1901] proposed in 1901 a correction to the Darcy's law. In a homogeneous medium, for a single phase θ, the Darcy-Forchheimer law relates the gradient of the intrinsic phase-averaged pressure $\nabla\langle p_\theta\rangle^\theta$, where p_θ is the pore-scale pressure field, to the average velocity (filtration velocity), $\langle \mathbf{v}_\theta\rangle$, where $\mathbf{v}_\theta$ is the

pore-scale velocity field, as:

$$\langle \mathbf{v}_\theta \rangle \;=\; -\frac{\mathbf{K}}{\mu_\theta} \cdot (\nabla \langle p_\theta \rangle^\theta \;-\; \rho_\theta \mathbf{g}) - \; \mathbf{F}(\langle \mathbf{v}_\theta \rangle).\langle \mathbf{v}_\theta \rangle \tag{2.22}$$

where $\mathbf{K}$ is the intrinsic permeability tensor of the medium, $\mathbf{g}$ is the grauitational acceleration, (p_θ, ρ_θ, μ_θ) are the pressure, density, and dynamic viscosity of the θ-phase, and $\mathbf{F}$ is the Forchheimer correction tensor. A discussion on the estimation of the inertial contribution for particle debris beds can be found in [Clavier 2015b].

Forchheimer proposed that the correction term depends upon the flow velocity up through a polynomial expression up to a power m. The one-dimensional form of the equation can be written as:

$$-\frac{\partial P_\theta}{\partial z} = a\, U_\theta + b\, U_\theta^m \tag{2.23}$$

where m is close to 2. For simplicity we donte by P_θ and U_θ the average pressure and the z-component of the velocity average. Forchheimer also proposed that the pressure loss can be written as a polynomial to the order 3 in velocity:

$$-\frac{\partial P_\theta}{\partial z} = a\, U_\theta + b\, U_\theta^2 + c\, U_\theta^3 \tag{2.24}$$

where a, b, and c are constants. Lot of research works (e.g. [Ergun 1952], [Tek 1957], and [Geertsma 1974]), were conducted to obtain correlations for those constants as function of the microscopic and macroscopic properties such as particle diameter, porosity, viscosity. Forchheimer equation, was then given by:

$$-\frac{\partial P}{\partial z} = \frac{\mu}{K_f}\, U + \beta_f\, \rho\, U^2 \tag{2.25}$$

where K_f is the Forchheimer permeability [m^2] which is the same permeability κ defined in Darcy's law, and β_f is the coefficient of inertial resistance [m^{-1}], or the coefficient of high-velocity (non-Darcian) flows, or as it is known today by the turbulence or the beta factor. This signifies the transition to inertial regimes, the main reason behind this phenomena is the conversion of kinetic energy into internal energy by work done against the viscous stress, known as viscous dissipation.

Several correlations for estimating the beta factor as a function of porosity and permeability are available in the literature. Scheidegger summarized the theoretical research works in ([Scheidegger 1953] and [Scheidegger 1974]). Later on, [Li 2001]

summarized the empirical correlations based on experiments performed on a variety of porous media and fluids, and proposed a methodology to choose among the different correlations for estimating the Forchheimer coefficient. Table 2.1 summarizes most of the correlations found in the literature.

Source	Correlation
[Ergun 1952]	$\beta_f = 4.36 \times 10^3 \, {K_f}^{-0.5} \, \varepsilon^{-1.5}$
[Janicek 1955]	$\beta_f = 5.55 \times 10^9 \, {K_f}^{-1.25} \, \varepsilon^{-0.75}$
[Tek 1962]	$\beta_f = 2.33 \times 10^{10} \, {K_f}^{-1.2}$
[Geertsma 1974]	$\beta_f = 4.85 \times 10^4 \, {K_f}^{-0.5} \, \varepsilon^{-0.55}$
[Pascal 1980]	$\beta_f = 1.45 \times 10^{12} \, {K_f}^{-1.176}$
[Jones 1987]	$\beta_f = 6.15 \times 10^{10} \, {K_f}^{-1.55}$
[Coles 1998]	$\beta_f = 1.07 \times 10^{12} \, {K_f}^{0.449} \, \varepsilon^{-1.88}$
[Li 2001]	$\beta_f = 3.51 \times 10^8 \, {K_f}^{-1} \, \varepsilon^{-1}$
[Aminian 2007]	$\beta_f = 10^{10.264} \, {K_f}^{-0.85}$

Table 2.1: Correlations for the beta-factor

This form of the Forchheimer equation (Eq. 2.25) was proposed by different authors ([Chauveteau 1967], [Muskat 1937], [Skjetne 1999a]). Written in this form, the Forchheimer equation may describe the flow in porous media for the Darcy regime, the strong inertia regime as well as the weak inertia transitional regime between them. Yet, the flow description is more accurate when the cubic velocity term is included in the latter regime. In this form, the pressure loss can be considered as a sum of a viscous term and an inertial term; in other words, viscous and kinetic energy losses. The dominance of either terms simply follows the flow regime where the viscous term dominates in the Darcy regime and the inertial term in the Forchheimer regime.

This two-scale technique is simple and mathematically rigorous ([Chen 2001]). In a periodic porous medium, it averages the detailed microscopic equations and yields simpler macroscopic equations by scaling the microscopic equations by the ratio ε of two length scales associated with the microscopic and macroscopic phenomena. However, the homogenization analysis in ([Mei 1991] and [Wodie 1991]) suggested, in the isotropic case, a cubic velocity term as a nonlinear correction to Darcy's law due to inertial effects. This isn't in agreement with experiments of [MacDonald 1979] and the averaging method by [Irmay 1958], which showed that the correction term should be quadratic. [Giorgi 1997] later linearized Navier-Stokes equation too recover the quadratic velocity term. [Chen 2001] also derived the Forchheimer law using the theory of homogenization directly from the Navier tokes equation following the same way as ([Mei 1991], and [Wodie 1991]) but they changed the choice of power of ε which led to the absence of microscopic inertial effects in the first order approximation of the Navier-Stokes. They rather had the microscopic inertial effects reflected in the first order approximation and the outcome of their approach was a quadratic non linear correction instead.

2.5 Two phase flow

2.5.1 Darcy-Forchheimer law

The change of scale for Stokes flow equation and continuity has already been investigated leading to Darcy's law ([Whitaker 1996]). Similar to single-phase flows, the Darcy-Forchheimer equations for two-phase flows are obtained by adding the Forchheimer correction ([Forchheimer 1901]) to the generalized Darcy law in order to include non-linear velocity terms. This law was obtained basically by studying steady state flow conditions, but it is commonly implemented to study transient flows.

For a (liquid-gas) two-phase flow system, the macroscopic momentum equations describing inertial two-phase flows in porous media were obtained theoretically by [Lasseux 2008]. They are written in the following structure:

$$\langle \mathbf{v}_l \rangle = -\frac{\mathbf{K_{ll}}}{\mu_l} \cdot (\nabla \langle p_l \rangle^l - \rho_l \mathbf{g}) - \mathbf{F_{ll}} \cdot \langle \mathbf{v}_l \rangle + \mathbf{K_{lg}} \cdot \langle \mathbf{v}_g \rangle - \mathbf{F_{lg}} \cdot \langle \mathbf{v}_g \rangle \tag{2.26}$$

$$\langle \mathbf{v}_g \rangle = -\frac{\mathbf{K_{gg}}}{\mu_g} \cdot (\nabla \langle p_g \rangle^g - \rho_g \mathbf{g}) - \mathbf{F_{gg}} \cdot \langle \mathbf{v}_g \rangle + \mathbf{K_{gl}} \cdot \langle \mathbf{v}_l \rangle - \mathbf{F_{gl}} \cdot \langle \mathbf{v}_l \rangle \tag{2.27}$$

This developed form of the equations include 8 unknown tensor terms:

$\mathbf{K}_{ll}$ and $\mathbf{K}_{gg}$ are the permeability tensors. They represent the viscous dissipation inside each fluid phase due to the interaction with the solid matrix.
$\mathbf{K}_{lg}$ and $\mathbf{K}_{gl}$ are the viscous coupling tensors. They represent the viscous drag at the liquid-gas interface.
In quasi-static conditions, the $\mathbf{K}_{ij}$ tensors are mainly described by the void fraction, the geometry of the porous medium, and the structure of the flow at pore scale ([Clavier 2015b]).

$\mathbf{F}_{ll}$ and $\mathbf{F}_{gg}$ are the inertial correction tensors and they represent the inertial effects inside each fluid phase.
$\mathbf{F}_{lg}$ and $\mathbf{F}_{gl}$ are the inertial coupling correction tensors. They represent the inertial momentum transfer through the interface between fluid phases. The two latter tensors are the ones in which the aforementioned interfacial friction laws can be embedded.
$\mathbf{F}_{ij}$ tensors generally depend on the void fraction, the porous medium geometry, and the structure of the flow at pore scale but also on the liquid and gas velocities $\langle \mathbf{v}_l \rangle$ and $\langle \mathbf{v}_g \rangle$.

To simplify the nomenclature, in the scalar form, we introduce the notations:

$$\langle v_\theta \rangle = U_\theta \tag{2.28}$$

$$\langle p_\theta \rangle^\theta = P_\theta \tag{2.29}$$

In the z-direction $\langle v_\theta \rangle$, or as denoted U_θ, is the z-component of the average velocity vector field $\langle \mathbf{v}_\theta \rangle$. And the one-dimensional system of equations for liquid-gas two phase system can be rather written in the general form:

$$-\partial P_g/\partial z = \rho_g g + a_g U_g + b_g {U_g}^2 + c_g U_g U_l + d_g U_l + e_g {U_l}^2 \tag{2.30}$$

$$-\partial P_l/\partial z = \rho_l g + a_l U_l + b_l {U_l}^2 + c_l U_l U_g + d_l U_g + e_l {U_g}^2 \tag{2.31}$$

In which the superficial velocity U_θ of the phase θ is related to the intrinsic average velocity $\langle v_\theta \rangle^\theta$ in a porous medium of porosity ε by:

$$U_\theta = \varepsilon s_\theta \langle v_\theta \rangle^\theta \tag{2.32}$$

with s_θ the θ-phase saturation, directly related to the void fraction α in case of (liquid-gas) systems. The saturation of the liquid phase is (1-α) and that for the gas phase is simply (α)

The benefit of writing the system of equations in this general form is that it allows to embed any form of the pressure drop equation or any interfacial friction law, quadratic in the phases velocities, which is the case for the interfacial friction laws present in the literature ([Tung 1988], [Schulenberg 1987], [Schmidt 2007]), [Clavier 2015b]. Those approaches will be presented in the last section.

However, if the tensors $\mathbf{K}$ and $\mathbf{F}$ are assumed diagonal and the inertial and viscous cross-terms are null ($\mathbf{K}_{ij}$=0, $\mathbf{F}_{ij}$=0 for i≠j), then only the intrinsic inertial ($\mathbf{F_{ll}}$, $\mathbf{F_{gg}}$) and viscous terms ($\mathbf{K_{ll}}$, $\mathbf{K_{gg}}$) are included. The one-dimensional form in the vertical direction thus renders Ergun's law ([Ergun 1952]). For the two-phase flow in a porous medium, the Darcy-Forchheimer equation for each phase θ is is further generalized to include the relative permeability κ_θ and the relative passability η_θ. For the two-phase flow (liquid, gas) system, the equations are written as:

$$-\frac{\partial P_g}{\partial z} = \rho_g g + \frac{\mu_g}{\kappa\kappa_g} U_g + \frac{\rho_g}{\eta\eta_g} {U_g}^2 \tag{2.33}$$

$$-\frac{\partial P_l}{\partial z} = \rho_l g + \frac{\mu_l}{\kappa\kappa_l} U_l + \frac{\rho_l}{\eta\eta_l} {U_l}^2 \tag{2.34}$$

where κ and η represent the intrinsic permeability and passability of the medium. The linear and quadratic velocity terms in the right hand side of those equations represent the viscous and kinetic energy losses per unit length respectively.

For spherical particles, combining this law with Kozeny-Carman equation [Carman 1937], the permeability and passability are obtained correlated to the particles diameter d_p and the porosity ε of the bed as follows:

$$\kappa = \frac{\varepsilon^3 {d_p}^2}{180(1-\varepsilon)^2} \qquad and \qquad \eta = \frac{\varepsilon^3 d_p}{1.75(1-\varepsilon)} \tag{2.35}$$

2.5.2 Relative permeability and passability

The relative permeability and passability approach is based on the generalization of Darcy-Forchheimer equation in the form:

$$-\frac{\partial P_\theta}{\partial z} = \rho_\theta g + \frac{\mu_\theta}{\kappa\kappa_\theta} U_\theta + \frac{\rho_\theta}{\eta\eta_\theta} {U_\theta}^2 \tag{2.36}$$

where κ_θ and η_θ are respectively the relative permeability and the relative passability of the phase θ. θ being either liquid or gas. In this classical approach there are four unknown terms: κ_l, η_l, κ_g, and η_g. Those terms are generally non-linear functions of, at least, the saturation of the phases. Several authors (Lipinski [Lipinski 1982], Saez and Carbonnell [Saez 1985]) suggested that the relative permeability and passability of each fluid must be equal. Other authors (Lipinski [Lipinski 1981]), Turland and Moore [Turland 1982], Schulenberg and Muller [Schulenberg 1984]) considered that the relative permeabilities κ_l and κ_g can be obtained in the viscous regime where inertial forces are negligible compared to viscous forces, whereas the relative passabilities which resemble the inertial factors measured experimentally.

κ_θ and η_θ have been also determined for spherical particles according to different correlations. A widely used and rather classical relations for a two-phase (liquid-gas) system was proposed by [Brooks 1966] to define relative permeability and relative passability of each phase as follows:

$$\kappa_l = (1-\alpha)^{n\kappa} \qquad and \qquad \eta_l = (1-\alpha)^{n\eta} \tag{2.37}$$

$$\kappa_g = \alpha^{n\kappa} \qquad and \qquad \eta_g = \alpha^{n\eta} \tag{2.38}$$

where $\alpha = S_g$ is the void fraction and the subscripts (l, g) refer to the phases (liquid, gas).

This classical formulation was cited many times in the literature by several authors ([Lipinski 1984], [Reed 1982] and [Hu 1991]) who proposed different sets of the exponents $n\kappa$ and $n\eta$. A different formulation was later proposed by [Fourar 2000] in which the relative permeability is equal to the relative passability for the same fluid phase and where the gas phase relative permeability and passability not only depended on the void fraction but also on the viscosities of liquid and gas.

Table 2.2 lists the main correlations defining relative permeability and passability that are found in the literature for porous media. s is the saturation of the liquid phase and s_e is the effective saturation defined as:

$$s = 1-\alpha \qquad and \qquad s_e = \frac{s-s_r}{1-s_r} \tag{2.39}$$

where s_r is the residual saturation of water.

Fourar and Lenormand [Fourar 1998] proposed a simple model based on experiments

Correlation	κ_l	κ_g	η_l	η_g
Lipinski 1982	s^3	$(1-s_e)^3$	s^3	$(1-s_e)^3$
Saez 1985	${s_e}^{2.13}$	$(1-s)^{1.8}$	${s_e}^{2.13}$	$(1-s)^{1.8}$
Reed 1982	s^3	$(1-s)^3$	s^5	$(1-s)^5$
Hu 1991	s^3	$(1-s)^3$	s^6	$(1-s)^6$
Lipinski 1981	s^3	$(1-s_e)^3$	${s_e}^5$	$(1-s_e)^5$
Turland 1982	s^3	$1-s$	${s_e}^4$	$(1-s)^2$
Schulenberg	${s_e}^3$	$(1-s_e)^3$	${s_e}^5$	$(1-s_e)^6$ for $s_e 0.68$
1984				$0.1(1-s_e)$ for $s_e > 0.68$

Table 2.2: Relative permeability and passability correlations

performed without inertial effects. This simple model takes into account the viscous coupling between the fluids and writes the relative permeabilities as follows:

$$\kappa_l = (3-s)\frac{s^2}{2} \tag{2.40}$$

and

$$\kappa_g = (1-s)^3 + \frac{3}{2}\frac{\mu_g}{\mu_l}s(1-s)(2-s) \tag{2.41}$$

Fourar and Lenormand [Fourar 2000] later modelled the relative passability assuming the relative permeability is given by the latter viscous model. The relative passabilities are then compared to the inertial factor terms and determined by:

$$\eta_l = \frac{\Gamma X^2}{1+\Gamma X^2+f(X)} \tag{2.42}$$

$$\eta_g = \frac{1}{1+\Gamma X^2+f(X)} \tag{2.43}$$

where,

$$X = \frac{\kappa_l}{\kappa_g} \tag{2.44}$$

$$f(X) = 11.58X^{1.53} \tag{2.45}$$

$$\Gamma = \frac{\rho_l {\mu_g}^2}{\rho_g {\mu_l}^2} \tag{2.46}$$

However, this model was proposed for porous media flows through rock fractures rather than particulate debris beds.

2.5.3 Interfacial friction laws

The two phase friction models found in the literature are generally based on Ergunâs law ([Ergun 1952]). This law was proposed for single phase flow through porous media and was later extended to two phase flows by introducing relative permeabilities and passabilities described in the previous section. In the presented classical models of [Lipinski 1984], Reed [Reed 1982], and [Hu 1991], the interfacial friction was not considered explicitly. They considered the interfacial friction between steam and water in the relative friction contributions of those phases with the solid particles. This is not sufficient especially in the situations where this water-steam interfacial friction plays a significant role.

Thus, there is a need for an interfacial friction term. This has also been shown by [Schulenberg 1987] and [Buck 2001]. The experimental measurements of pressure loss in debris bed have demonstrated that the classical friction laws of [Lipinski 1984], Reed [Reed 1982], and [Hu 1991], not including explicitly interfacial friction terms, could not well predict the pressure drops . Hence, including an interfacial friction term such as that defined by the Schulenberg-Muller or Tung and Dhir friction laws, could enhance the results and at least reproduce the behavior qualitatively.

2.5.3.1 Schulenberg-Muller

Including an interfacial friction law in the momentum equations introduces some cross-terms to the Darcy-Forchheimer equations. A convenient law that is often used in thermal-hydraulics codes to study this type of flow in porous media is the Schulenberg-Muller law ([Schulenberg 1984]). The authors correlated their data based on experimental results of debris bed bottom reflooding tests and deduced an equation for the interfacial friction from the measured pressure drop in the bed. It will be considered in this study to produce the results and it is defined as follows:

$$-\frac{\partial P_g}{\partial z} = \rho_g g + \frac{\mu_g}{\kappa\kappa_g} U_g + \frac{\rho_g}{\eta\eta_g} {U_g}^2 + \frac{F_i}{\alpha} \tag{2.47}$$

$$-\frac{\partial P_l}{\partial z} = \rho_l g + \frac{\mu_l}{\kappa\kappa_l} U_l + \frac{\rho_l}{\eta\eta_l} {U_l}^2 - \frac{F_i}{1-\alpha} \tag{2.48}$$

where F_i represents the interfacial drag force defined by:

$$F_i = 350\,(1-\alpha)^7\,\alpha\,\frac{\rho_l K}{\eta\sigma}\,(\rho_l - \rho_g)\,g\,(\frac{U_g}{\alpha} - \frac{U_l}{1-\alpha})^2 \tag{2.49}$$

with σ being the surface tension.

They adopted Brooks and Correy relations ([Brooks 1966]) for the liquid phase relative permeability and passability with:

$$\kappa_l = (1-\alpha)^3 \qquad and \qquad \eta_l = (1-\alpha)^5 \tag{2.50}$$

whereas for the gas phase, they assumed a relative permeability of $\kappa_g = \alpha^3$ and deduced the corresponding relative passability η_g to be:

$$\eta_g = 0.1\,\alpha^4 \ : \ \alpha \leqslant 0.3 \qquad and \qquad \alpha^6 \ : \ \alpha > 0.3 \tag{2.51}$$

F_i can be written in the form:

$$F_i = f(\alpha)\,(\frac{U_g}{\alpha} - \frac{U_l}{1-\alpha})^2 \tag{2.52}$$

where

$$f(\alpha) = 350\,(1-\alpha)^7\,\alpha\,\frac{\rho_l K}{\eta\sigma}\,(\rho_l - \rho_g)\,g \tag{2.53}$$

Eq. 2.52 is developed in terms of the liquid and gas velocities as follows:

$$F_i = \frac{f}{\alpha^2}{U_g}^2 + \frac{f}{(1-\alpha)^2}{U_l}^2 - \frac{2f}{\alpha(1-\alpha)}\,U_g\,U_l \tag{2.54}$$

Writing Eq.s 2.47 and with the interfacial friction term F_i developed in this form falls into the proposed general one dimensional form of Darcy Forchheimer law presented in Eq.s 2.30 and 2.31. The latter will form the basis of the proposed analytical model in Chapter 4.

2.5.3.2 Tung-Dhir

A different approach was proposed by Tung and Dhir [Tung 1988] based on visual observation in air-water experiments. They classified the flow patterns into three different flow regimes: bubbly, slug, and annular flow regime. Those regimes were distinguished according to the void fraction as shown in Figure 2.3. They considered that each two successive flow regimes are separated by a transition regime. For each flow regime and transition particle fluids friction and interfacial friction are derived from geometric considerations.

They compared their model with the measured pressure gradient and they found a

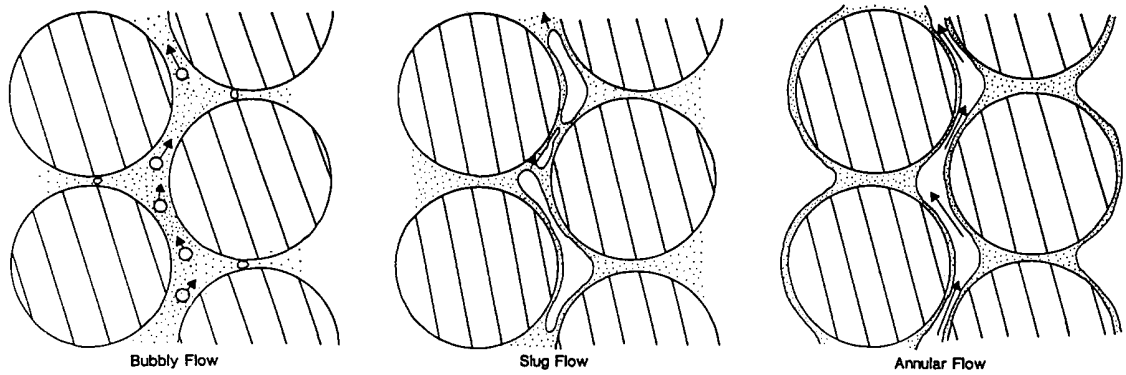

Figure 2.3: Sketches of flow patterns in different flow regimes

good agreement with the experiment. However, they compared their model with the experiments which are performed with relatively large particles diameter.

Similar to Schulenberg-Muller model, Tung and Dhir [Tung 1988] proposed the following term F_i to describe the interfacial friction between water and steam:

$$F_i = C_1 \frac{\mu_l}{{D_b}^2}(1-\alpha)(\frac{U_g}{\alpha} - \frac{U_l}{1-\alpha}) + C_2 \frac{((1-\alpha)\rho_l + \alpha\rho_g)}{D_b \varepsilon}(1-\alpha)^2(\frac{U_g}{\alpha} - \frac{U_l}{1-\alpha})^2 \quad (2.55)$$

where C_1 and C_2 are functions of the void fraction. D_b is the bubble diameter, it is given by:

$$D_b = 1.35\sqrt{\frac{\sigma}{g(\rho_l - \rho_g)}} \quad (2.56)$$

F_i can be written in the form:

$$F_i = f_1(\alpha)\,(\frac{U_g}{\alpha} - \frac{U_l}{1-\alpha}) + f_2(\alpha)\,(\frac{U_g}{\alpha} - \frac{U_l}{1-\alpha})^2 \quad (2.57)$$

where $f_1(\alpha)$ and $f_2(\alpha)$) are defined by:

$$f_1(\alpha) = C_1 \frac{\mu_l}{{D_b}^2 \varepsilon}(1-\alpha) \quad (2.58)$$

and

$$f_2(\alpha) = C_2(\frac{\rho_l(1-\alpha) + \rho_g \alpha}{D_b \varepsilon})(1-\alpha)^2 \quad (2.59)$$

The interfacial friction term F_i can be regrouped and written as:

$$F_i = \frac{f_1}{\alpha} U_g - \frac{f_1}{1-\alpha} U_l + \frac{f_2}{\alpha^2} {U_g}^2 + \frac{f_2}{(1-\alpha)^2} {U_l}^2 - \frac{2f_2}{\alpha(1-\alpha)} U_g U_l \tag{2.60}$$

In a similar manner as the Schulenberg-Muller, this allows to embedd the Tung-Dhir interfacial friction term in the Darcy Forchheimer Eq.s 2.30 and 2.31.

2.5.3.3 Clavier

In the initiative for achieving an accurate assessment of the coolability of a debris bed, [Clavier 2017] proposed a new model for pressure losses in two-phase flows through homogeneous porous media. The model is based on the theoretical development of the Darcy Forchheimer model by [Lasseux 2008] in the form presented in Eq. 2.26 and Eq. 2.27. In the latter model, each momentum equation included eight terms corresponding to the viscous and inertial friction in liquid and gas phases, and interfacial friction between the phases.

[Clavier 2015b] provided an analytic formulation of each of the 8 terms. They have been derived in accordance with an original experimental database collected at the IRSN CALIDE facility. The database contains pressure drop measurements, average velocities and void fractions. The new model has then been validated against the experimental data for various liquid and gas Reynolds numbers up to several hundreds. It has been also compared to the models which are often used in the severe-accident codes, which are based on a generalization of the Ergun law for multi-phase flows. The comparison showed that the new proposed model gives a better prediction both for the pressure drop and for the void fraction. An implementation of this model as an interfacial friction law into the analytical model proposed in this thesis will be presented in Chapter 4.

In the vertical direction, the one dimensional form of the macroscopic momentum equations presented earlier (2.26 and Eq. 2.27) is written as:

$$\langle v_l \rangle = -\frac{K_{ll}}{\mu_l} \left(\frac{\partial \langle p_l \rangle^l}{\partial z} + \rho_l g \right) - F_{ll} \langle v_l \rangle + K_{lg} \langle v_g \rangle - F_{lg} \langle v_g \rangle \tag{2.61}$$

$$\langle v_g \rangle = -\frac{K_{gg}}{\mu_g} \left(\frac{\partial \langle p_g \rangle^g}{\partial z} + \rho_g g \right) - F_{gg} \langle v_g \rangle + K_{gl} \langle v_l \rangle - F_{gl} \langle v_l \rangle \tag{2.62}$$

Analytical expressions were identified for the 8 terms associated to those momentum equations. They were defined as follows:

- terms associated to the liquid phase:

$$K_{ll} = \kappa \left(1-\alpha\right)^3 \qquad K_{lg} = k_{lg} \frac{\mu_g}{\mu_l} \frac{\left(1-\alpha\right)^2}{\alpha}$$

$$F_{ll} = \frac{\rho_l}{\mu_l} \frac{\kappa}{\eta} \left\langle v_l \right\rangle \qquad F_{lg} = K_{lg} \frac{\alpha^3}{\alpha^3 + \left(1-\alpha\right)^n}$$

- terms associated to the gas phase:

$$K_{gg} = \kappa \alpha^4 \qquad K_{gl} = \frac{\mu_l}{\mu_g} \frac{K_{gg} K_{lg}}{K_{ll}}$$

$$F_{gg} = \frac{\rho_g}{\mu_g} \frac{\kappa}{\eta} \left\langle v_g \right\rangle \qquad F_{gl} = f_{lg} \alpha^6$$

Here, the permeability κ and the passability η were defined by Ergun correlations as:

$$K = \frac{d^2 \varepsilon^3}{181 \left(1-\varepsilon\right)^2} \qquad \eta = \frac{d \varepsilon^3}{1.63 \left(1-\varepsilon\right)}$$

The terms are then regrouped and written in the form of Darcy Forchheimer Eq.s 2.30 and 2.31.

The predictions of this model were compared against experimental data. The comparison demonstrated its predictability within the whole investigated range of liquid A significant improvement in the description of multi-phase flows in particle beds is represented by this model as compared to the existing models. Moreover, similar to the indications of the proposed models describing the interfacial friction, the cross-terms included in this model associated to the friction between the two phases were also shown to play an important role.

2.6 Two phase flow with phase change: (Icare-Cathare physical model)

2.6.1 Momentum balance equations

The friction forces on the fluid phases are taken into account by using the classical extension of Darcy's law to two-phase flows via introducing the Forchheimer correction terms. This means that viscous and inertial drag forces are calculated with relative permeabilities and passabilities coefficients, depending mainly on the void fraction. There is no explicit interfacial drag force between the liquid and gas phases. This may be a lack in the model, as it was demonstrated by [Schulenberg 1987] and by [Buck 2001], but there does not appear to be a satisfactory correlation available in the literature. The form of the momentum equation for a two-phase flow in a porous medium is still a matter of investigations.

In the calculations presented in this thesis, the momentum balance equations have a rather classical form, as follows:

$$\begin{aligned}&\alpha\langle\rho_g\rangle^g\left(\frac{\partial\langle\mathbf{v}_g\rangle^g}{\partial t}+\langle\mathbf{v}_g\rangle^g.\nabla\langle\mathbf{v}_g\rangle^g\right)=-\alpha\nabla\langle p_g\rangle^g+\alpha\langle\rho_g\rangle^g\mathbf{g}\\&-\varepsilon\alpha^2\left(\frac{\mu_g}{\kappa\kappa_g}\langle\mathbf{v}_g\rangle^g+\varepsilon\alpha\frac{\langle\rho_g\rangle^g}{\eta\eta_g}\langle\mathbf{v}_g\rangle^g\left|\langle\mathbf{v}_g\rangle^g\right|\right)\end{aligned}\tag{2.63}$$

$$\begin{aligned}&(1-\alpha)\langle\rho_l\rangle^\ell\left(\frac{\partial\langle\mathbf{v}_\ell\rangle^\ell}{\partial t}+\langle\mathbf{v}_\ell\rangle^\ell.\nabla\langle\mathbf{v}_\ell\rangle^\ell\right)=-(1-\alpha)\nabla\langle p_\ell\rangle^\ell\\&+(1-\alpha)\langle\rho_l\rangle^\ell\mathbf{g}-\varepsilon(1-\alpha)^2\left(\frac{\mu_l}{\kappa\kappa_l}\langle\mathbf{v}_\ell\rangle^\ell+\varepsilon(1-\alpha)\frac{\langle\rho_l\rangle^\ell}{\eta\eta_l}\langle\mathbf{v}_\ell\rangle^\ell\left|\langle\mathbf{v}_\ell\rangle^\ell\right|\right)\end{aligned}\tag{2.64}$$

In these equations, $\langle p_\beta\rangle^\beta$, $\langle\rho_\beta\rangle^\beta$, μ_β and $\langle\mathbf{v}_\beta\rangle^\beta$ are respectively the average pressure, density, dynamic viscosity and velocity of the β-phase ($\beta = g, l$). These variables are defined as volume averages over a representative volume including all phases (however, for each phase, averaging is made only over the fraction of volume occupied by the phase). In the calculations presented, the capillary effect is negligible because of the relatively large size of the particles.

2.6.2 Energy balance equations

Macroscopic energy conservation equations of the three phases are obtained by averaging the local energy conservation equations ([Duval 2004], [Duval 2002], [Quintard 1997]). In this method, local thermal non-equilibrium between the three phases is considered. For further details on the averaging process, the reader may refer to [Quintard 2000], [Quintard 1994a]. The complete set of closure problems is presented in [Duval 2002].

The averaged equations are simplified following [Petit 1999, Bachrata 2013], where heat transfers occurring in the porous medium are expressed according to temperature differences between the phase temperature and the saturation temperature. The expression of the heat transfer terms exhibits explicitly the thermal exchanges between fluid phase and solid phase ($Q_{f\beta}$), fluid phase and interface (Q_{β}), solid phase and interface (Q_{fi}).

$$Q_{\beta} = h_{\beta i}\left(\langle T_{\beta}\rangle^{\beta} - T_{sat}\right) \tag{2.65}$$

$$Q_{f\beta} = h_{s\beta}\left(\langle T_{s}\rangle^{s} - \langle T_{\beta}\rangle^{\beta}\right) \tag{2.66}$$

$h_{f\beta}$, $h_{\beta i}$ are the heat transfer coefficients. The resulting macroscopic energy conservation equations are expressed as follows:

- gas phase:

$$\begin{aligned}&\frac{\partial\left(\alpha\varepsilon\langle\rho_g\rangle^g\langle h_g\rangle^g\right)}{\partial t} + \nabla\cdot\left(\alpha\varepsilon\langle\rho_g\rangle^g\langle\mathbf{v}_g\rangle^g\langle\mathbf{v}_g\rangle^g\langle h_g\rangle^g\right)\\ &= \nabla\cdot\left(\mathbf{K}_g^*.\nabla\langle T_g\rangle^g\right) + \dot{m}_g h_g^{sat} + Q_{fg} + Q_{gi}\end{aligned} \tag{2.67}$$

- liquid phase:

$$\begin{aligned}&\frac{\partial\left((1-\alpha)\,\varepsilon\langle\rho_l\rangle^{\ell}\langle h_l\rangle^{\ell}\right)}{\partial t} + \nabla\cdot\left((1-\alpha)\,\varepsilon\langle\rho_l\rangle^{\ell}\langle\mathbf{v}_{\ell}\rangle^{\ell}\langle h_l\rangle^{\ell}\right)\\ &= \nabla\cdot\left(\mathbf{K}_l^*.\nabla\langle T_l\rangle^{\ell}\right) + \dot{m}_{\ell}\, h_l^{sat} + Q_{fl} + Q_{li}\end{aligned} \tag{2.68}$$

- solid phase:

$$\frac{\partial\left((1-\varepsilon)\,\langle\rho_s\rangle^s\langle h_s\rangle^s\right)}{\partial t} = \nabla\cdot\left(\mathbf{K}_s^*.\nabla\langle T_s\rangle^s\right) - Q_{fl} - Q_{fg} - Q_{fi} + \varpi_s \tag{2.69}$$

In these equations, $\langle h_\beta \rangle^\beta$ and $\langle T_\beta \rangle^\beta$ are the macroscopic enthalpy and the temperature of the β-phase respectively ($\beta = g, l, s$ for the gas, the liquid and the solid phases respectively). $\mathbf{K}^*_\beta$ is the effective thermal diffusion tensor and ϖ_s is the heat deposited deposited in the solid phase.

The phase change rate, which is obtained by adding the three phase equations and neglecting diffusion terms, is then given by the relation:

$$\dot{m}_g = \frac{Q_{fi} - Q_{gi} - Q_{li}}{h_g^{sat} - h_l^{sat}} \tag{2.70}$$

2.7 On the consideration of Darcy-Forchheimer law

The generalized Darcy-Forchheimer models are now widely adopted as a standard approach in nuclear safety studies [Naik 1982], [Schmidt 2007], [Burger 2006], chemical engineering [Saez 1986b] and petroleum engineering [Fourar 2000]. However, those models often fail to provide a correct representation of the pressure drop, void fraction, and velocity relationships, and particularly for debris beds as it has been recently indicated by [Chikhi 2016].

The source of such failure may root back to two main reasons. The first one is based on the current knowledge of upscaling multi-phase flows in porous media. During the last decades, lot of investigations were made to provide theoretical analysis of high velocity single phase flows in porous media. The results showed that that there exists some flow regimes which can not be described correctly by a quadratic Forchheimer correction to Darcy's law. Namely, the weak inertia regime which is needed described better by a cubic velocity correction term. The different flow regimes may be observed experimentally. This has been illustrated by [Clavier 2015a] in their experimental study on single phase pressure drops in a nuclear debris beds. However, it was observed that using the classical quadratic Forchheimer law, the results were fair. In a recent study, [Clavier 2017] mentioned that results for a debris bed composed of several mm to cm particles were good up to a 10% appoximation. Such investigations of the multi-phase flows are still lacking. In addition to its simplicity, that is one main reason why the generalized Darcy Forchheimer model has been implemented extensively.

The other reason that may lead to the incorrectness is the lack of experimental data related to this type of flow. Moreover, there are technical difficulties when attempting to perform online measurements of the pressure drop, phases velocities and

saturation which are essential keys for the validation of the two-phase flow pressure drop models. Such measurements in dynamic systems are difficult, especially for void fractions. In an experimental investigation on the two-phase water-oil flow in a stratified heterogeneous porous medium, [Bertin 1990] implemented a gamma-ray absorption technique to measure the saturation of one or several phases. They used an Americium 241 radioactive source emitting gamma rays at 59.6 keV. However, for the water-steam two-phase flow, the situation may become more complex due to the possible evaportation of water. When addressing coolability of debris beds, phase change often takes place. The complex dynamics of this phenomena increases the technical difficulty of online saturation measurements. That explains the lack of experimental data in the literature. Few relevant experimental data were presented three decades ago by [Tutu 1984a], [Tutu 1984b], [Lipinski 1984], and [Hu 1991].

For the discussion presented here above and in the previous sections, in the absence of a valid and better approach, and because of its simplicity and extensive use for nuclear safety analysis, the generalized Darcy Forchheimer model is considered in this thesis.

Chapter 3

Numerical simulations of reflooding a heterogeneous hot debris bed

In this chapter, numerical simulations of reflooding a hot debris bed composing two coaxial cylindrical layers with contrasting permeability will be presented. The thermalhydraulics coupled code Icare-Cathare will be used to carry out the calculations. Most of the results obtained in this chapter were published in a paper ([Chikhi 2017]) in the Annals of Nuclear Energy.

Contents

3.1 Preliminary calculations with Icare-Cathare

3.1.1 Two-Layered debris bed with different particle size

Upon a severe nuclear accident leading to the degradation of the nuclear reactor core, a heterogeneous hot debris bed is likely to form as described in Chapter 1. Considering the presence of compact zones of lower permeability in the center of the formed debris bed, a study concerned in the effect of geometry and the particles size of the system is performed to assess the effect of each on the coolability in such situations. In preliminary calculations, different sets of simulations of reflooding a hot debris bed were performed using Icare-Cathare thermal-hydraulics code. The aim of those calculations was to investigate the effect of the diameter of the central compact zone and its particles size on the overall coolability condition of the debris system. Figure 3.1 is a schematic representation of a debris bed of length $L2$=1 m and external radius R_{ext}=0.5 m. It is composed of particles of diameter D_p. This debris bed surrounds the compact zone which itself is another debris bed of length $L1$=0.6 m, radius R_{cz}, and composed of particles of diameter d_p smaller than D_p. The dimensions considered for this cylindrical debris bed are comparable to the dimensions of a debris bed formed inside a nuclear reactor core upon a severe accident leading to partial core melting, such as the TMI-2 accident.

Firstly, two sets of calculations corresponding to different compact-zone-to-debris bed thickness ratios of ($R_{cz}/R_{ext} = 0.2$ and 0.8). Each configuration included different particle diameter contrast with d_p and D_p ranging between 1mm and 8mm. A maximum ratio of $D_p/d_p = 2$ is considered for those preliminary calculations. This assumption is based on a study on nuclear fuel rod defragmentation performed by Coindreau et al. [Coindreau 2013]. They demonstrated that the formed debris beds were composed of particles with sizes ranging between 1mm and 4mm and a maximum ratio of $D_p/d_p = 2$. They also demonstrated that the particles size my even vary within a narrower range depending on several factors such as: initial debris temperature, nuclear fuel burn-up rate, etc.

In those preliminary calculations 20x30 meshes were considered in cylindrical geometry (RxZ). The beds were simulated by 20x20 RxZ meshes. Several meshes were left empty below and above the debris system. The empty meshes below the beds allow the uniform distribution of the injected water before entering the debris bed. Thus allowing the process of flow radial redirection to occur naturally due to permeability contrast and other potentially affecting mechanisms like evaporation.

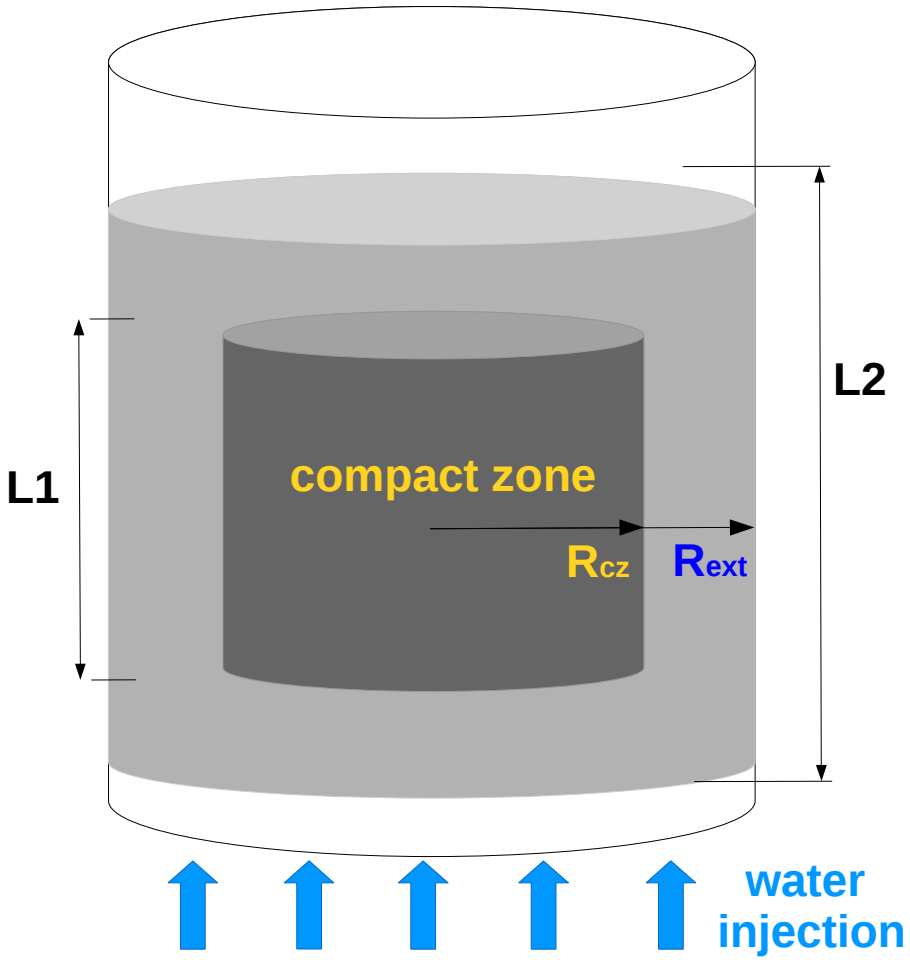

Figure 3.1: Reflooding a hot debris bed with compact central zone

Initial conditions

The porosity of the debris bed formed in TMI-2 was determined by Akers et al. [Akers 1986] to vary within a range of [0.35 - 0.55]. For moderately irradiated nuclear fuel, an average value of 0.4 is usually used for safety analysis (Burger et al. [Burger 2006]). The hot debris bed under study is composed of stainless steel particles, it has a uniform porosity $\varepsilon = 0.4$ (which is a typical value for a debris bed composed of spherical particles) and a uniform initial temperature set to $T_i = 673$K (400°C). A constant volumetric power deposition of 150 W/kg is induced during the reflooding process to simulate the heating effect due to residual power described by the decay heat produced by radioactive elements present in the nuclear reactor core in such an accidental scenario.

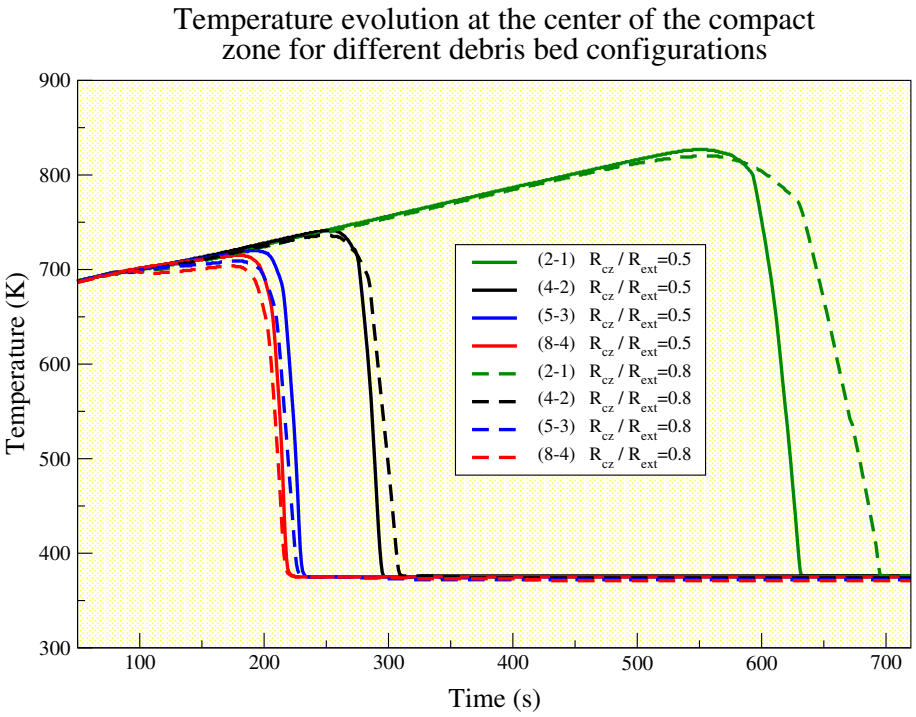

Figure 3.2: Temperature evolution T(K) at the center of the debris system for different configurations. Name of the test: (D_p-d_p) R_{cz}/R_{ext}=x

Boundary conditions

The reflooding is assumed to be at atmospheric pressure (P= 1bar, pressure imposed at the outlet). Reflooding is performed from the bottom by injecting water at temperature 343 K (70°C, close to water boiling point in order to obtain evaporation during the reflooding). The flow rate of water injection is 1560 g/s and the velocity at the inlet is 0.002 m/s (or 2 mm/s). At the outlet, the fluid can flow out freely and a zero gradient is imposed for all transported quantities. A friction factor is also imposed there to prevent any reverse flow.

3.1.1.1 Observations and discussion

Figure 3.2 represents the temperature evolution at the center of the compact zone for different diameters of the compact zone (ratio to the total radius R_{cz}/R_{ext} = 0.5 dashed-lines and 0.8 solid lines) and for different configurations (changing the particles diameter in both debris zones). Figure 3.3 represents the temperature evolution at the top of the compact zone. Each test is named according to its configuration as (D_p-d_p) R_{cz}/R_{ext}=x. We observe that the increase in the width of

the compact zone delays the quenching process where the calculated temperatures remain high for a longer period than the configuration with smaller compact zone.

Moreover, the maximum temperature rise $\triangle T_{max}$ beyond the initial system temperature and the total quenching duration were calculated for each case and they are represented in the bar diagram in Figure 3.4. The quenching duration is defined by the instant at which the temperature at each and every point in debris bed drops and reaches thermal equilibrium with the injected water. The notation (D_p, d_p, D_p) is used to abbreviate the name of the test based on its particles diameter. And the star (*) refers to the debris bed configuration with larger central compact zone: $R_{cz}/R_{ext} = 0.8$.

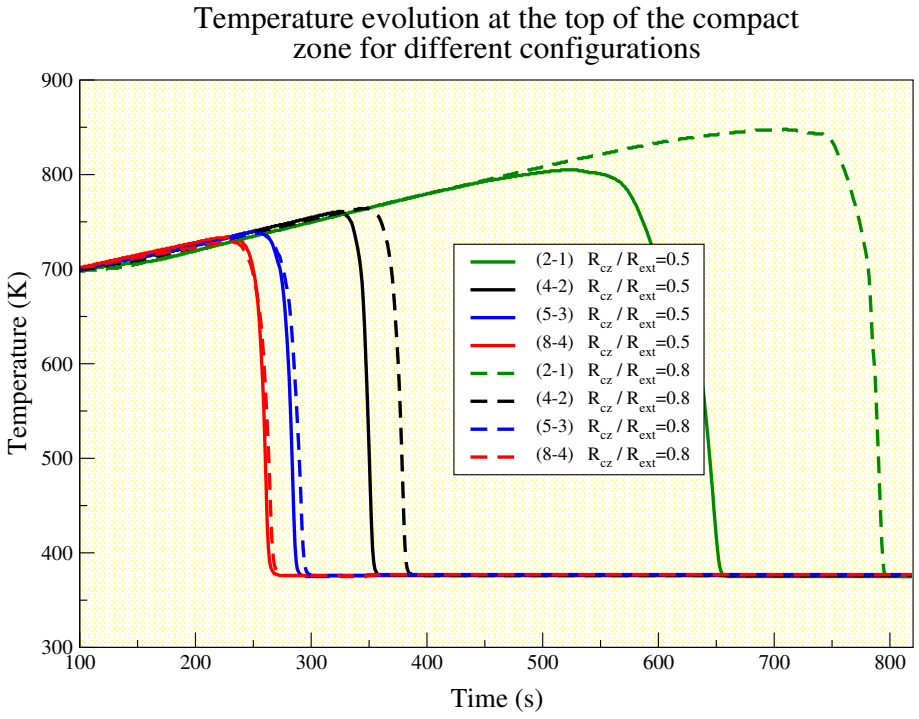

Figure 3.3: Temperature evolution T(K) at the top of central compact zone for different configurations. Name of the test: (D_p-d_p) R_{cz}/R_{ext}=x

As observed in the figures and the bar diagram, the configurations with larger particles diameter were quenched faster (t_q(8-4-8)=270s < t_q(2-1-2)=656s for configuration $R_{cz}/R_{ext} = 0.5$ and t_q(8-4-8)*=275s < t_q(2-1-2)*=796s for configuration $R_{cz}/R_{ext} = 0.8$). On the other hand, concerning the size of the central compact zone, we observe that for a smaller compact zone, the total quenching takes places

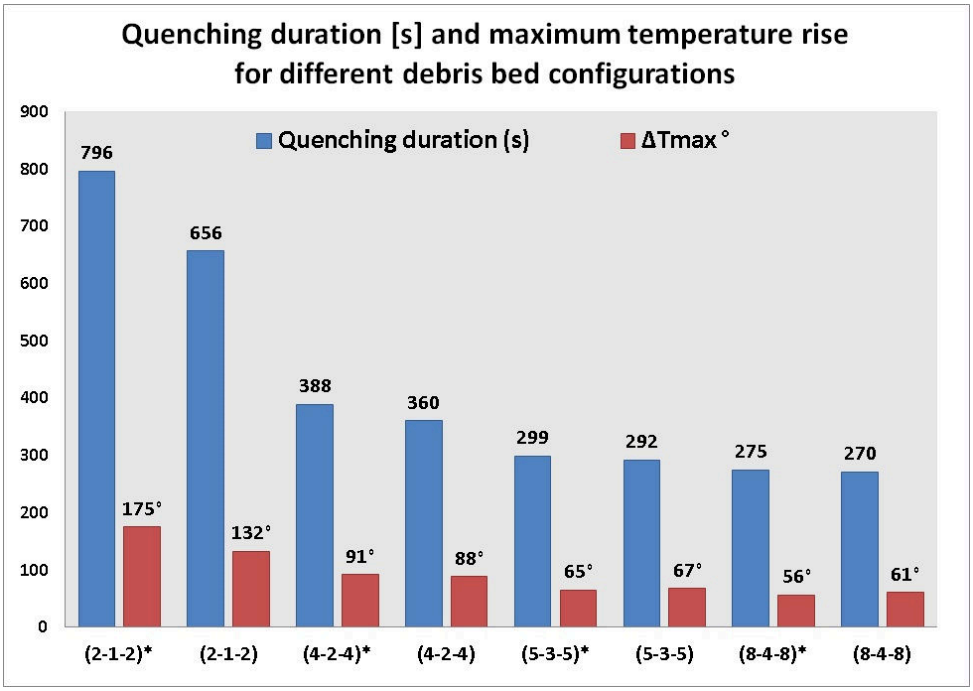

Figure 3.4: Effect of compact zone geometry on quenching duration and maximum temperature rise

earlier than the configuration with larger compact zones. A similar interpretation comparing the maximum temperature rise can be made since $\triangle T_{max}$ is directly related to the total quenching duration. For smaller temperature rise $\triangle T_{max}$ the quenching process occurs faster and vice versa. Moreover, we observe that for larger particles, both the quenching duration and the maximum temperature tend to a lower limit, and that the size of the compact zone doesn't have the same influence on the reflooding behavior as for smaller particles (Figure 3.4).

3.1.2 Effect of a bypass

Secondly, another set of calculations is performed to investigate the effect of a highly permeable bypass surrounding the debris bed. Such a configuration is considered to simulate the presence of fuel rod zones that remained intact during the severe accident leading to partial melting and formation of the debris bed in the nuclear reactor core. Similar to the previous calculations, the debris bed and the central compact zone are considered to possess a porosity ($\varepsilon = 0.4$), a uniform initial temperature $T_i = 673K$, and a constant volumetric power deposition of 150 W/kg. The bypass (when present) has a larger porosity (ε_b=0.55), internal radius

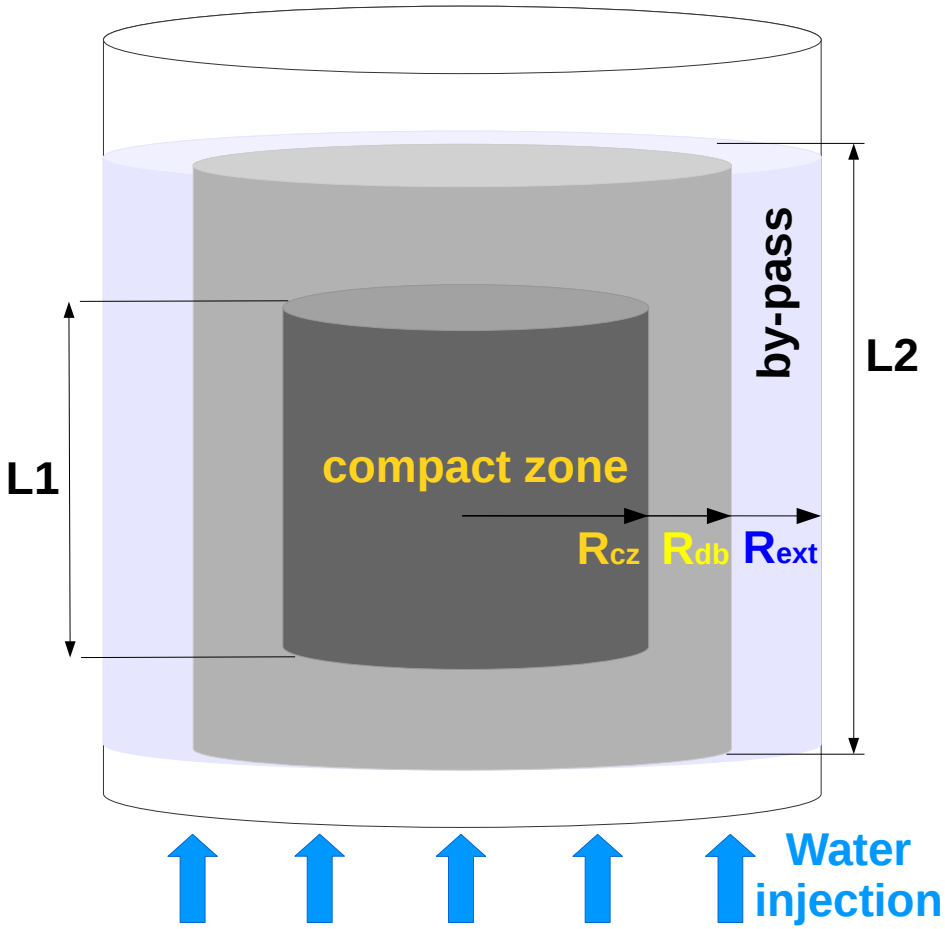

Figure 3.5: Reflooding a hot debris bed centered by a compact zone and surrounded by a by-pass of larger permeability

R_{db}=0.8R_{ext}. It is composed of larger particles (D_{bp}=20mm), thus it is 450 times more permeable than the debris bed and 1850 times more than the central compact zone if the latter beds were composed of smaller particles with (D_p=2mm and d_p=1mm). Figure 3.5 is a schematic representation of the debris bed system surrounded by a bypass lateral layer. Three calculations noted as (2-1-2), (4-2-4) and (2-1-2)-bypass are performed and presented. The debris bed is L_1=1m long and has an external radius R_{ext} where as the compact zone in the center is half the debris bed by length and radius (L_1=0.5m and R_{cz}=R_{ext}/2=0.25m, thus it is quarter the debris bed by cross-section and one-eighth by volume. Figure 3.6 represents the temperature evolution at the center and above the compact zone (r,z)=(0m,0.8m) and (0m,1.2m), where the debris bed bottom is positioned at $z = 0.3m$. The initial and boundary conditions are the same considered for the previous calculations

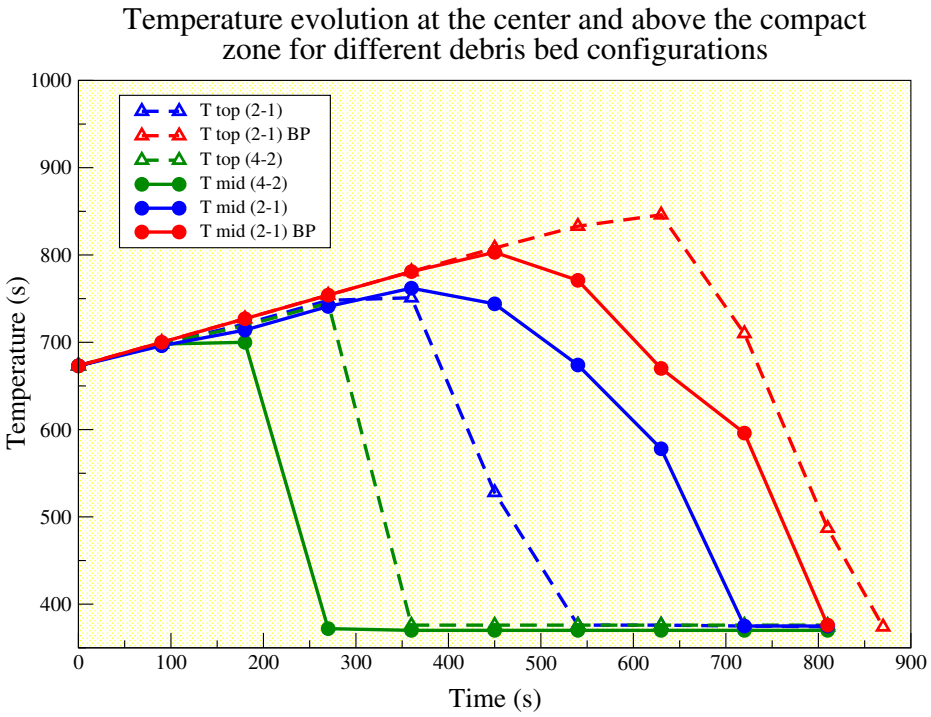

Figure 3.6: Temperature evolution T(K) for different debris configurations

presented previously.

3.1.2.1 Observations and discussion

The first observation infers a deduction similar to that made in the previous section where the increase of the particles size facilitates the cooling process as the total quenching is achieved in the '(4-2-4)' configuration before the others. On the other hand, in the presence of the bypass, case '(2-1-2)-BP' as compared to '(2-1-2)', the reflooding process changed drastically. The quenching duration was extended by 140s and the maximum temperature rise was increased by 100 degrees. Moreover, the reflooding behavior has changed in '(2-1-2)-BP' as the top of bed was quenched rather earlier than the central compact bed. This behavior is opposite to what was observed for the no-bypass cases where the quench front propagates successively along the central channel in the vertical direction. This behavior is observed more clearly in the 2D temperature field graphs represented in Figure 3.7. In the presence of a highly permeable bypass, the injected water had a preferential path leaving the inner debris bed and the central compact bed unquenched for a longer duration as compared to the case with no bypass at the periphery. In such situations, the

efficiency of the reflooding process decreases as a larger percentage of the injected flow rate is directed into the bypass and progressing towards the top of the debris system leaving the central part uncovered while accumulating heat under the effect of residual heat and thus questioning the coolability of the bed.

3.1.3 Perspectives

Simulations of reflooding a hot debris bed including a central compact zone showed that both the quenching duration and the maximum temperature rise decrease and tend to a lower limit as the beds particles size increase (considering the criterion $D_p/d_p = 2$). Whereas, when the particles diameter is smaller, the quenching duration and the maximum temperature rise increase and are expected to be unbounded. For smaller particles beds, the contact surface between the fluid and the solid increases. This enhances the heat transfer but on the other hand, the friction increases and resists the fluid flow. This leads to the delay of the quenching duration and consequently achieving higher temperature rise beyond the initial bed temperature. The diameter of the central compact zone has a significant effect on the reflooding process. For larger compact zone, the time required for total quenching and the maximum temperature achieved increased unless the particles were larger than 8mm in diameter.

In the aim of cooling the heat-accumulating hot debris bed, coolant is in injected into the whole cross section of the debris system. However, the presence of intact zones (bypass) surrounding a hot debris bed formed upon a severe accident in a nuclear reactor core, lead to the significant diversion of the injected coolant flow into the periphery. This is mostly observed when the bypass is highly permeable as compared to the debris bed. In such a configuration, the time required to achieve a total quenching of the hot debris bed is extended. This delay of quenching may compromise the coolability of the hot debris which also depends on the initial thermal state of the bed. If for instance the formed debris bed resulting from a severe accident was being uncovered and heated up to high temperatures, the reflooding process in the presence of a highly permeable bypass may result in a high temperature rise of some zones in the hot debris bed. Further heating of those certain zones may compromise the coolability chances because they could reach the melting point, if the coolant didn't succeed to penetrate into those zones. It is therefore a major concern to investigate thoroughly the effect of the bypass on the reflooding process, estimate the limitations, and define the factors that describe the coolability chances of the debris bed.

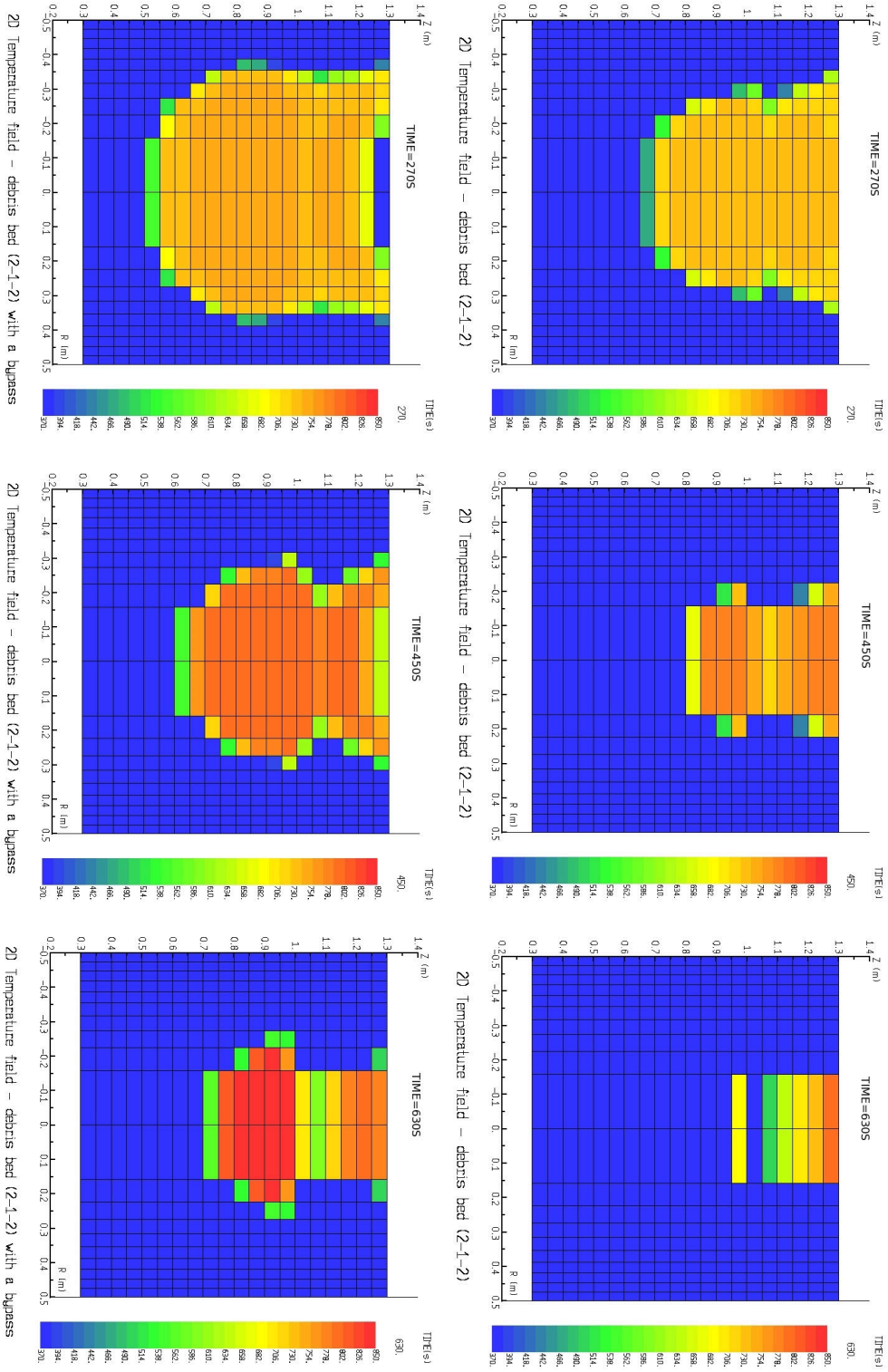

Figure 3.7: 2D temperature fields at different instants during reflooding - behavoir in presence of bypass

3.2 Numerical simulations of PEARL tests with Icare-Cathare

3.2.1 PEARL tests

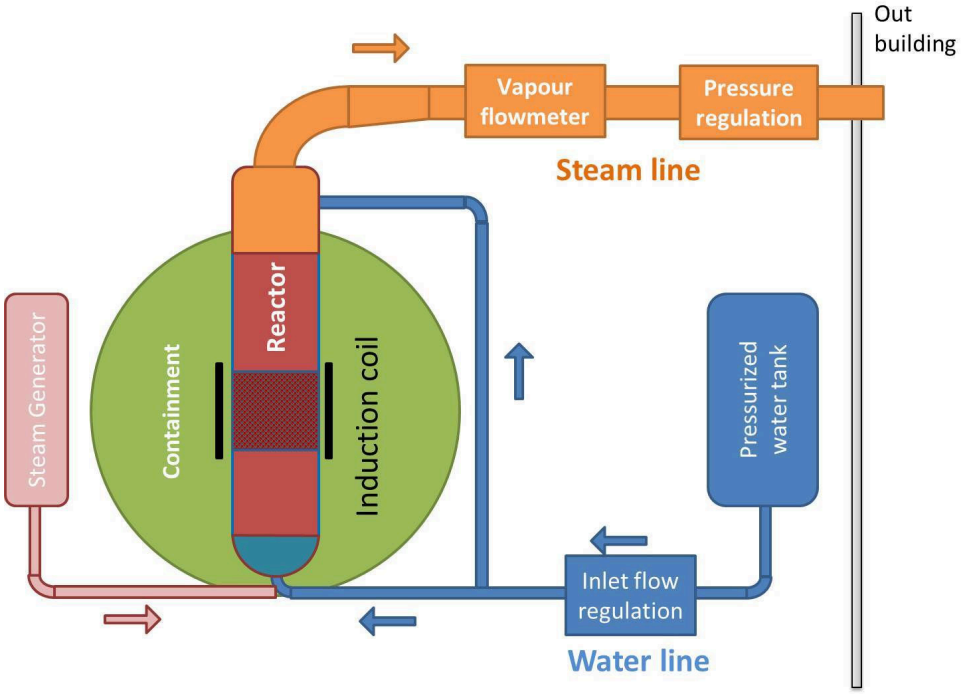

Figure 3.8: Schematic view of PEARL facility

Severe accidents management is essential to maintain the safety and prevent drastic consequences. The question of debris coolability has to be resolved in such a way that the mitigation of accidental scenario leading to debris bed formations must be mastered. For those reasons the IRSN (Institut de Radioprotection et de Sûretées Nucléaire), has launched the experimental program PEARL (Programme Expérimental Analytique sur le Renoyage de Lits de débris) to investigate the thermal hydraulics of the debris bed reflooding process. The aim is to predict the consequences of the water reflooding of a severely damaged reactor core where a large part of the core has collapsed and formed a debris bed.

In the PEARL facility, the debris bed, 500 mm in height and 450 mm in diameter, was made of 4 mm stainless steel balls surrounded by a 45 mm-thick bypass filled with 8 mm quartz balls. In the first set of experiments, bottom-reflood tests have been

successfully conducted under pressures (1-2-3-5 bar) with water injection velocities (2-5-10 m/h) and initial temperatures (150-400-700 °C). The system is a large-scale debris bed, it contained 360 kg of stainless steel spherical particles, and it was heated by an induction coil surrounding the debris as shown in figure 3.8 which is a schematic representation of the PEARL facility. The induction process resembles a volumetric heat source whose deposition power is 150 W/kg. This power deposition simulates the decay heat (residual power) in the real accidental scenario in a nuclear reactor core. The matrix of the investigated reflooding tests that were performed at the PEARL facility is listed in Table 5.1. This experiment conducted at IRSN was the first of its kind at such scale. A specific instrumentation has been developed to measure the debris bed temperature, pressure drop inside the bed and the steam flow rate during the reflooding ([Chikhi 2015a], [Chikhi 2015b]). It allows measuring the progression of water within the bed and the timing of quenching. It also provides the conversion ratio corresponding to the ratio of the outlet steam flow rate produced to the water injection flow rate. One specific feature of the PEARL facility is the presence of a lateral by-pass in order to simulate the presence of non-damaged zones at the periphery of the bed. This by-pass induces flow patterns which differ significantly from previously observed patterns in the PRELUDE 1D experiment ([Repetto 2013]).

The debris bed is equipped with K-type thermocouples,1 mm diameter, located in the bed pores at different elevations, radial, and angular positions. 62 Thermocouples were used, their positions are shown in Figure 3.9. The steam temperature is also measured at the top of the debris bed and in the outlet steam line. Absolute pressure is measured at the top of the test section. The water injection flow rate is measured by a Coriolis flow meter and controlled by an electro-pneumatic valve. The steam flow rate is measured with an Annubar flow meter. This flow meter consists in an absolute and a differential pressure sensor, and converts a pressure drop into fluid velocity. The tests were done at atmospheric pressure (1 bar) and other tests at higher pressures (2, 3, and 5 bars) to assess the effect of pressure on the behavior of reflooding and total quenching duration. Reflooding was performed with bottom water injection at different injection velocities (2, 5, and 10 m/hr). The uncertainties associated to the measurents are: ± 0.02 bars for the pressure measurements, ± 7.5°C, and ± 6 g/s for the mass flow rate measurements. Other uncertainties may rise due to the positioning of the thermocouples; the thermocouples position plays the main role in determining the position of the quench front and eventually the quenching velocity. The PEARL experimental measurements are thoroughly reported in IRSN technical reports ([Chikhi 2015a]).

In a hypothetical severe accident, the dry reactor core continues to warm up due to

the residual heat being released by the decay of radioactive fission products, to simulate this heat generation volumetric power deposition by conduction is maintained during reflooding. Its effect is more visible on the test with low initial temperature and low coolant injection velocity. The PEARL facility (Figure 3.8) has been designed to simulate large scale debris bed reflooding under pressure. The debris bed is supported by a bed made of 8mm quartz balls and positioned in a quartz tube. It is heated by an induction coil linked to a high frequency generator. The quartz tube is placed in a stainless steel sealed containment (up to 10 bar). Water enters the test section by the bottom or the top from a pressurized water tank. In the water injection line, the water flow rate is measured with a Coriolis flow meter and regulated by a electro-pneumatic valve. The steam, generated by reflooding, flows from the test section outlet at the top through a heated steam line equipped with a steam flow meter (Annubar flow meter). The steam line is ended by a pneumatic valve which regulates the pressure in the test section. This line is temperature-controlled so that condensation of steam is avoided inside.

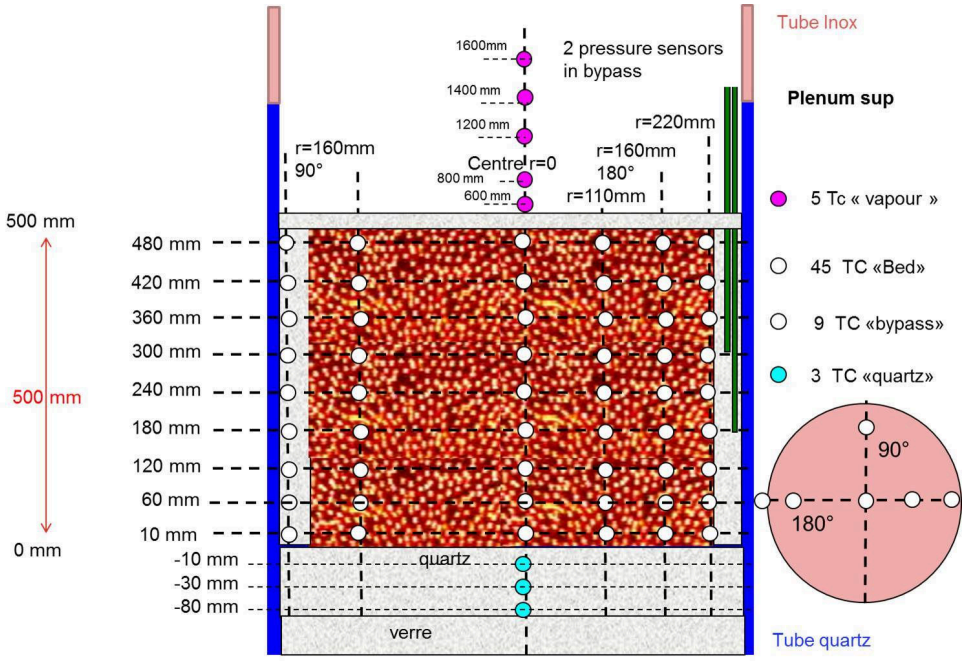

Figure 3.9: PEARL test section and thermocouples positions

First, the whole system is pressurized to the target pressure. Nitrogen was used to avoid any interaction between air and hydrogen (which can be produced by steel balls oxidation during the tests). Using the induction coil, the bed is heated from room temperature up to 150°C. Simultaneously, steam is injected through the bed

Table 3.1: PEARL Tests

PEARL test	Initial temperature (°C)	Injection velocity (m/hr)	Power deposit (W/kg)	Pressure (bar)	Flooding mode
PA0	150	5	150	1	Bottom
PA1	400	5	150	1	Bottom
PA2	700	5	150	1	Bottom
PA4	400	2	150	1	Bottom
PA5	400	10	150	1	Bottom
P22	700	5	150	2	Bottom
P32	700	5	150	3	Bottom
P51	700	5	150	5	Bottom

and the bypass and maintained until the initiation of reflooding by water injection from the bottom. When the bed temperature has reached 150°C, the furnace is stopped, the bed temperature stabilizes and the bypass temperature increases up to the saturation temperature. Then, a second heat-up phase is started to achieve the target temperature for the test (initial temperatures for each test are listed Table 5.1). The bed temperature is stabilized and water is injected from the pressurized water tank. The power deposit by induction is restarted when water reached the bottom of the bed and it is maintained during the reflood to simulate the residual heat in the reactor case.

3.2.2 Use of PEARL results in this thesis

This thesis benifited from the experimental results of PEARL tests obtained by the experimental team at IRSN. The author of this thesis recieved the experimental results tabulated in excel files. It corresponded to the temperature, pressure, and flow measurements. Data processing of those results were done in the framework of the thesis to obtain specific results and study the behavior of reflooding. The modeling of the PEARL tests in Icare-Cathare was done based on the geometry described in the technical report provided by the experimental team ([Chikhi 2015a]). All the results presented in the thesis, with the mention "Calculation" are either obtained by the author. The results with the mention "Experimental" are obtained by processing the experimental data which were provided by the experimental PEARL team.

3.2.3 Meshing and initialization

The system is discretized in cylindrical geometry where it is meshed into (34 x 28). Icare-Cathare solves the equations applying a cylindrical symmetry, the meshing considered is thus (Z x R) = (34x14) meshes as shown in Fig. 3.10.

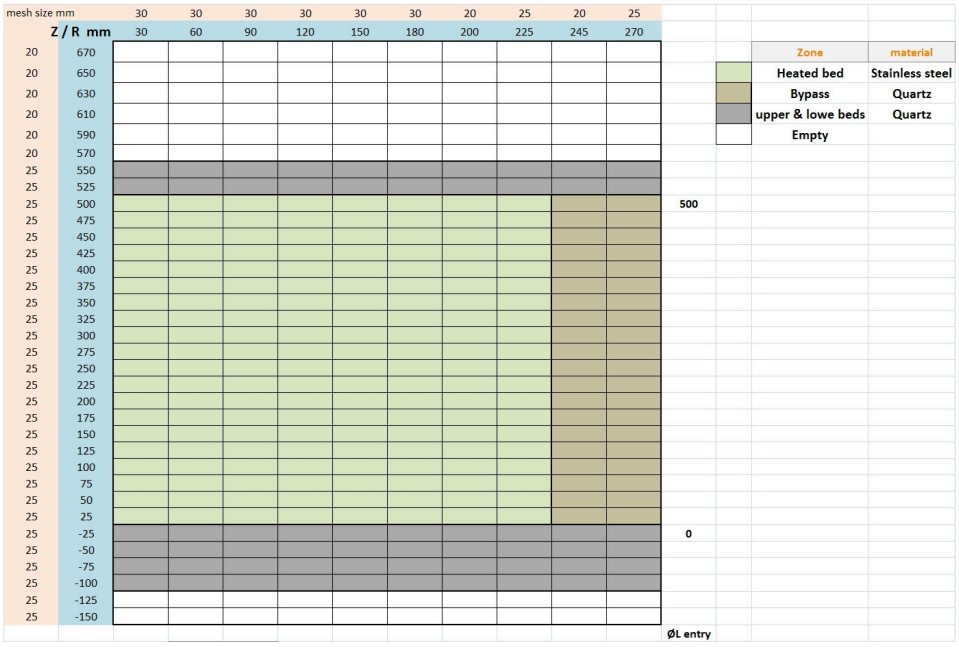

Figure 3.10: Schematic representation of PEARL meshing in cylindrical coordinates

The 50cm high central debris bed (in light green), composed of 4 mm stainless steel balls, was decomposed into three main zones. The outer diameter is 22.5 cm and porosity=0.4. It was surrounded by a 4.5 cm thick bypass composed of quartz balls (in brown) of diameter=8 mm and porosity around 0.4 - 0.42. Quartz beds were also placed above and below the debris beds (in grey color). They have the same properties as the bypass and their heights are 10 cm (bottom layer) and 5 cm (top layer). 26 meshes in vertical direction were allocated to the debris system including the top and bottom layers. At the inlet, 2 empty meshes were placed below the debris system to ensure proper and uniform injection of water into the bottom layer rather than imposing a specific flow rate at the inlet of each mesh. Above the debris system, 6 empty meshes were placed. In the debris system, Icare-Cathare solves the conservation equations developed for two-phase flow in porous media and assuming local non-thermal equilibrium, as described in the Chapter 2. In the empty meshes, the fluid flow is described by Navier-Stokes equations.

However, the height of the quartz bed at the top (5 cm) was not measured and not listed in the technical report of the experiment It was an estimation provided by the experimental team. No thermocouples were positioned there to provide temperature readings either. Such a recording is important to better describe quantitatively and qualitatively the expected penetration of water into that permeable zone and having it quenched earlier than the neighboring zone below it composed of hot stainless steel (bed top).

In the PEARL tests the temperature of the debris was measured by thermocouples places at 6 different axes as shown in Figure 3.9. At each axis, 9 thermocouples were positioned at different elevations. In order to impose the same initial energy of the debris system as accurate as possible in the simulations, an axial average of the initial temperature reading was imposed for each axis. So in the Icare-Cathare calculations, the debris system was decomposed into different coaxial layers (or zones) whose initial temperature was provided according to the average of 9 thermocouples readings in that axis. However considering the uncertainty of the thermocouples readings ($\pm$7.5 degrees), the initial energy provided in the calculations based on the thermocouples tolerates an overall uncertainty ranging between 8% and 15%. For instance, it is 9.7% for the PA2 test.

It is worth mentioning here that the thermocouple listings of the support quartz bed below was not clear, and that there was NO temperature readings in the upper quartz bed. That increases the uncertainty on the total initial energy of the system and the behavior of reflooding in those zones.

The PEARL setup composed a long support bed of glass balls, but this bed was not simulated as it is longer than the debris beds which are the main focus for reflooding The time-zero is set to the instant where injected water arrives at the bottom of the stainless steel debris bed, that point is also considered the elevation-zero as shown in the schematic representation (Fig.3.10).

In the experiment, as a consequence of the first heating phase by steam, the glass balls support bed remain heated over a long period as compared to the total duration of the debris bed quenching. From the point of view of the author, this is a drawback of the experimental conduct. The debris bed system is said to be quenched via bottom reflooding by water injection at 30°C. However, due to the heat remaining in the glass support bed, water arrives at the heated stainless steel central bed at saturation temperature 100°C over a certain period (221s for PA2) after which it declines gradually to 30°C. That is seen in the thermocouples readings in the

quartz support bed (which were not listed in a clear form in the technical report). For the simulation, water was initially injected at saturation temperature and the liquid temperature profile was made up to simulate the transition of having water again at 30°C after quenching the glass bed. That input concering water injection relied upon the thermocouples readings and it had increased the uncertainty on the duration of the quenching process.

The initial and boundary conditions for the Icare-Cathare calculations are described as follows:

Initial conditions
The temperature of the debris layers is provided by the thermocouples readings as stated before.

Boundary conditions
A constant volumetric power deposition of 150 W/kg is induced during the reflooding process to simulate the heating effect due to residual power described by the decay heat produced by radioactive elements present in the nuclear reactor core in such an accidental scenario. In the experiment it is deposited in the stainless steel debris bed. This is equivalent to an energy source of 0.684 MW/m^3 considering a stainless steel debris layer of density 7600 kg/m^3 and 0.4 porosity.

The reflooding is assumed to be done either at atmospheric pressure (P=1 bar) or at higher pressures according to each test. The provided pressure is imposed at the outlet of the system.

At the inlet, water injection flow rate is imposed at each mesh, given the injection velocity for each test and also the water temperature.

At the lateral boundary, a thin layer of quartz is placed to simulate the thermal isolation as in PEARL tests. In the calculations, it was designed as a 10mm-thick layer having the same temperature as the bypass and a low heat transfer coefficient. A reasonable heat exchange was also tested in the preliminary calculations but it didn't show a significant effect. So it was later decided to have a weak heat exchange with the surroundings to simulate the thermal isolation.

At the outlet, the fluid can flow out freely and a zero gradient is imposed for all transported quantities. A friction factor is also imposed there to prevent any reverse flow.

3.2.4 Convergence studies: numerical sensitivity

3.2.4.1 Radial meshing

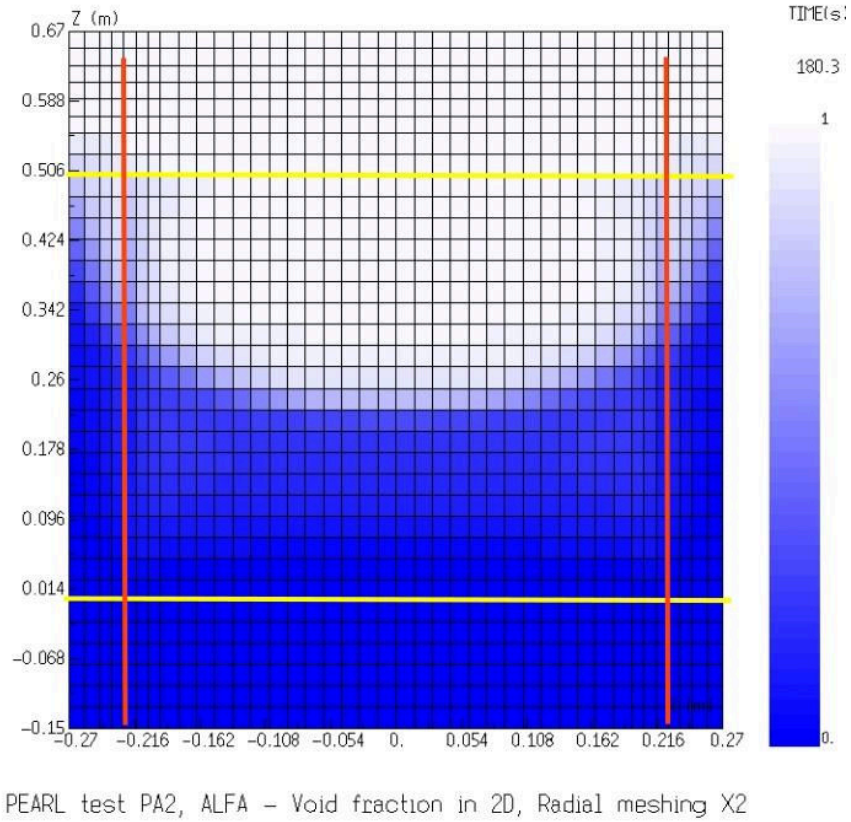

Figure 3.11: Void fraction 2D field for doubled radial meshes - PA2 test

The number of radial meshes is doubled from 20 to 40 (as shown in the void fraction 2D field in Figure 3.11) to investigate the accuracy of the solution on the meshing considered. The stainless steel debris bed is situated between the yellow horizontal lines, whereas the bypass zone is situated radially beyond the orange lines. Comparing it to the reference calculation (shown in Figure 3.12) for the 2D field of void fraction obtained by doubling the radial meshing at the same instant of time, shows insignificant difference.

Figures 3.13 and 3.14 represents two radial profiles, at a specific instant, of the steam upward velocity and the debris temperature taken at two different elevations (z=0.25 middle of the bed, and z=0.64 m at the top outlet) to investigate more

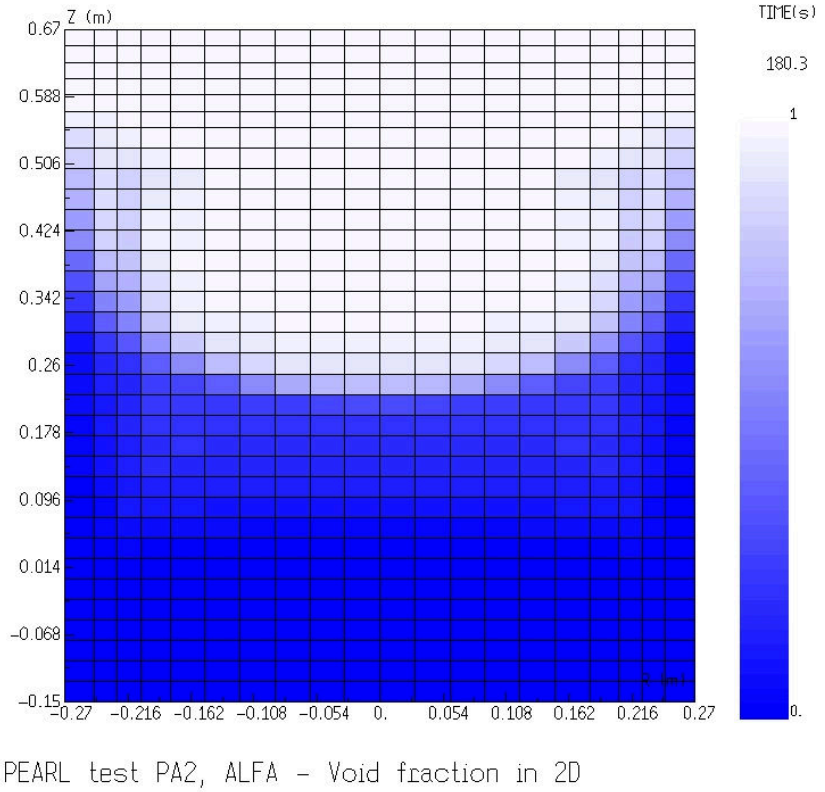

Figure 3.12: Void fraction 2D field, reference - PA2 test

thoroughly the effect of increasing the number of meshes in radial direction as compared to the reference calculation. Those figures are produced by post-processing the Icare-Cathare calculations. The curves in Red correspond to the calculation with doubled radial meshes while the Blue ones represent the reference. It is clear that the difference is insignificant and in some cases the curves perfectly overlay.

Figures 3.18, 3.19, and 3.20 also show that the total steam flow rate (red curve) is just smoother than the reference calculation (black curve). For the flow rates in the central debris bed and the bypass, slight difference is observed except a little extension of the steam production. The presented comparison indicates that the radial meshing initially considered is good enough to produce a reliable result. It has to be noted that the maximum number of meshes for each calculation in Icare-Cathare is restricted to 1000 meshes in total and to 50 radial meshes at most.

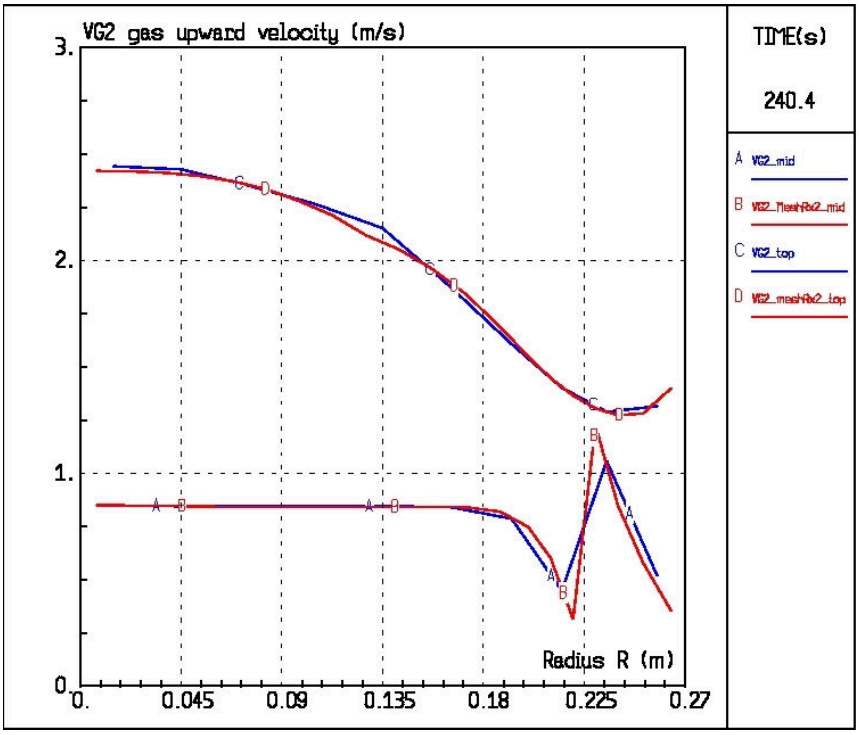

Figure 3.13: Radial profiles of steam upward velocity 'VG2(r,z)' at two different elevations z=0.25m and z=0.64m, comparison of doubled radial meshes (Red) against reference calculation (Blue) - PA2 test. A:VG2(r,z=0.25m); B:VG2(r,z=0.25m) doubled meshing; C:VG2(r,z=0.64m); D:VG2(r,z=0.64m) doubled meshing

3.2.4.2 Axial meshing

In a similar attempt, the number of axial (vertical) meshes was doubled from 34 to 68 (as shown in the void fraction 2D field in Figure 3.15) in order to provide a clearer view of some vertical profiles at specific instants during the simulation and check the effect of the vertical meshing on the main results of the calculations. The stainless steel debris bed is situated between the yellow horizontal lines, whereas the bypass zone is situated radially beyond the orange lines. As compared to the reference calculation (Figure 3.11), the 2D field of void fraction (Figure 3.15), obtained at the same instant of time, shows insignificant difference.

Figures 3.16 and 3.17 represents three axial profiles, at a specific instant, of the steam upward velocity and the debris temperature taken at three different radial positions (in the center r=0, in the middle r=0.16 m, and in the bypass r=0.25 m) to investigate more thoroughly the effect of increasing the number of meshes in radial

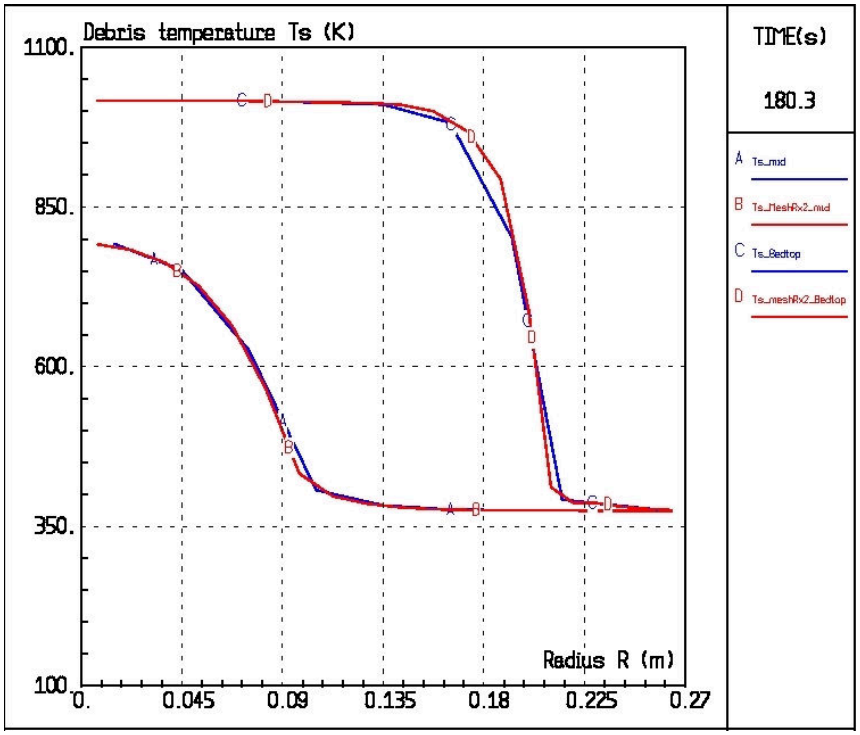

Figure 3.14: Radial profiles of debris temperature 'Ts(r,z)' at two different elevations z=0.25m and z=0.64m, comparison of doubled radial meshes (Red) against reference calculation (Blue) - PA2 test. A:Ts(r,z=0.25m); B:Ts(r,z=0.25m) doubled meshing; C:Ts(r,z=0.64m); D:Ts(r,z=0.64m) doubled meshing

direction as compared to the reference calculation. The curves in Red correspond to the calculation with doubled axial meshes while the Blue ones represent the reference. The difference is not significant for the center and the bypass yet a relatively slight is seen for profiles at the middle.

In the figures 3.18, 3.19, and 3.20 the effect of the axial meshing on the steam production is relatively small. Comparing to the reference calculation, the total steam flow rate (green curve) is smoother than the reference (black curve). For the flow rates in the central bed and the bypass, a slight difference is seen compared to the reference calculation. Those presented figures indicate that the axial meshing initially considered is also good enough to produce a reliable result. The oscillations appearing in those grahs represent the arrival of the quench fron at each axial mesh. The frequency of the oscillations increase when the number of meshes increase.

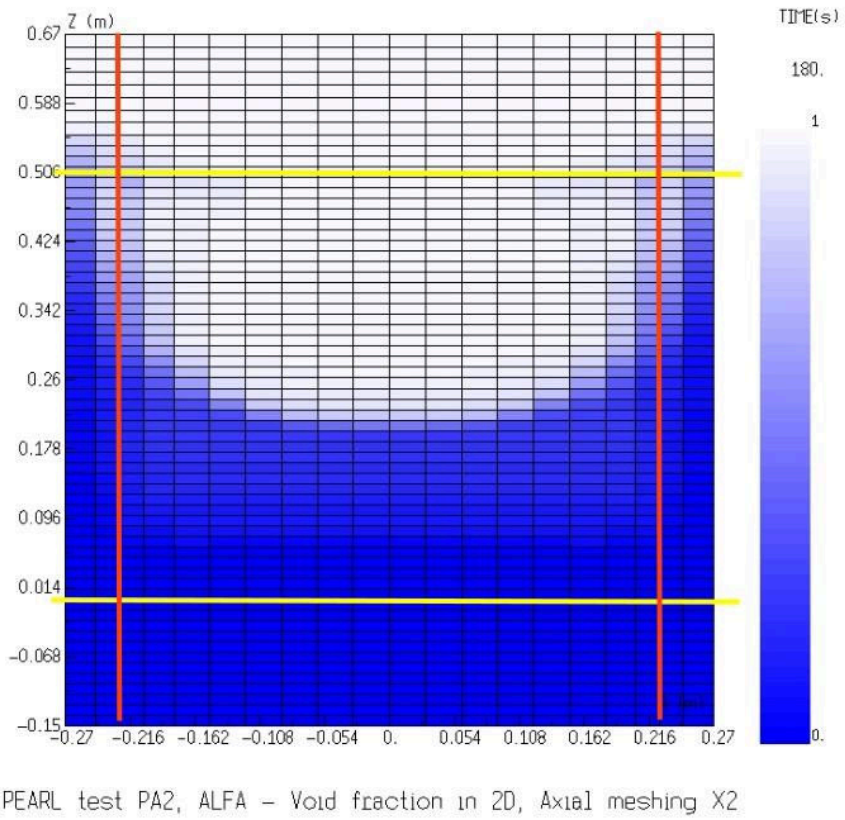

Figure 3.15: Void fraction 2D field for doubled axial meshes - PA2 test

3.2.4.3 Icare-Cathare guidelines

When defining the descritization, it is highly recommended to avoid jumps between the lengths of two neighboring meshes. For the calculations of small scale experiments, an average mesh length of about 5 to 10 cm seems to be a satisfactory choice. When needed, a local reduction to 2.5 cm may be done, but, in any case, any shorter length must be prohibited. Conversely, in the zones where no special physical phenomenon has to be accurately reproduced (no heat-up, no relocation), the axial meshes may be enlarged, but they must never exceed 20 cm. For reactor calculations, an average length of about 15 to 25 cm seems to be a satisfactory choice. ([Drai 2010]).

3.2.4.4 Finer meshing in Bypass - wall effect

As shown in the experimental study by Tung and Dhir [Tung 1988], in such debris

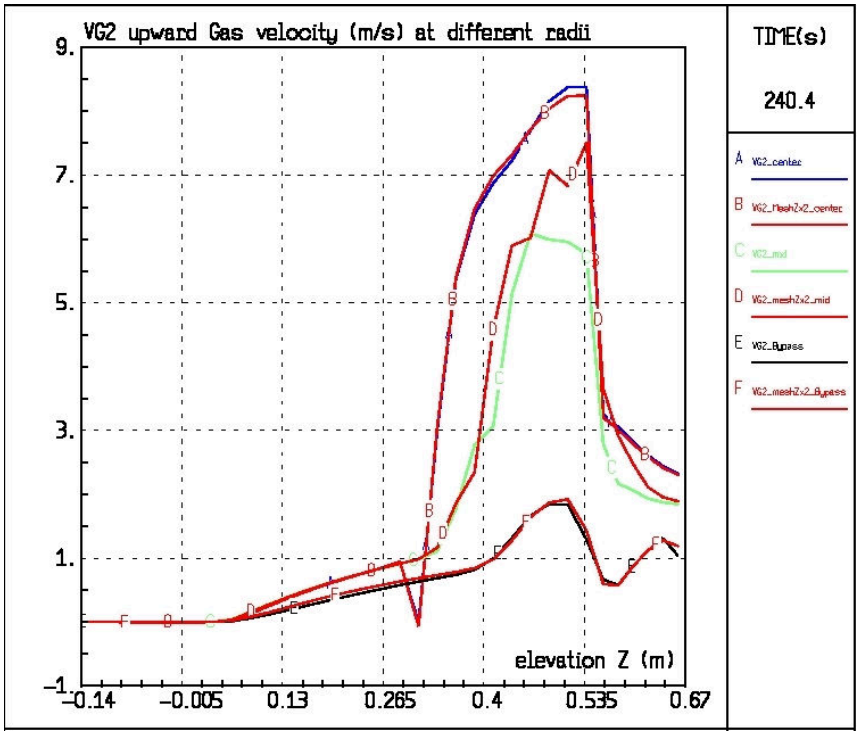

Figure 3.16: Steam velocity axial profiles 'VG2(r,z)' at three different radii (center, mid, bypass) r=(0m, 0.16m, 0.25m), comparison of doubled axial meshes (Red curves B,D,F), against reference calculation (curves A,C,E) - PA2 test. A:VG2(r=0m,z); B:VG2(r=0m,z) doubled meshing; C:VG2(r=0.16m,z); D:VG2(r=0.16m,z) doubled meshing; E:VG2(r=0.25m,z); F:VG2(r=0.25m,z) doubled meshing

beds configurations there exists a thin region near the wall (rim) where the permeability is larger, this so called "wall effect" case appears naturally when cylindrical debris beds are composed of spherical balls. To investigate the effect of such a configuration, a calculation was done with finer meshes inside the bypass and a very thin mesh at the rim where the porosity is larger to simulate the "wall effect" that could result from the increased permeability in that zone where it was suspected to enhance the water entrainment into the bypass. Another calculation with increased number of meshes (4 in the bypass) was also carried out.

However, the results showed no significant difference from the reference calculation, and water entrainment in the bypass was not enhanced. Figure 3.20 represents a comparison of the steam flow rate calculated with finer meshing in the bypass zone. But both cases showed no significant difference from the reference calculation. This seems to indicate that the structure of the flow, with an accumulation of water in the bypass, (see Figure 3.12), does not depend on the conditions at the wall but is

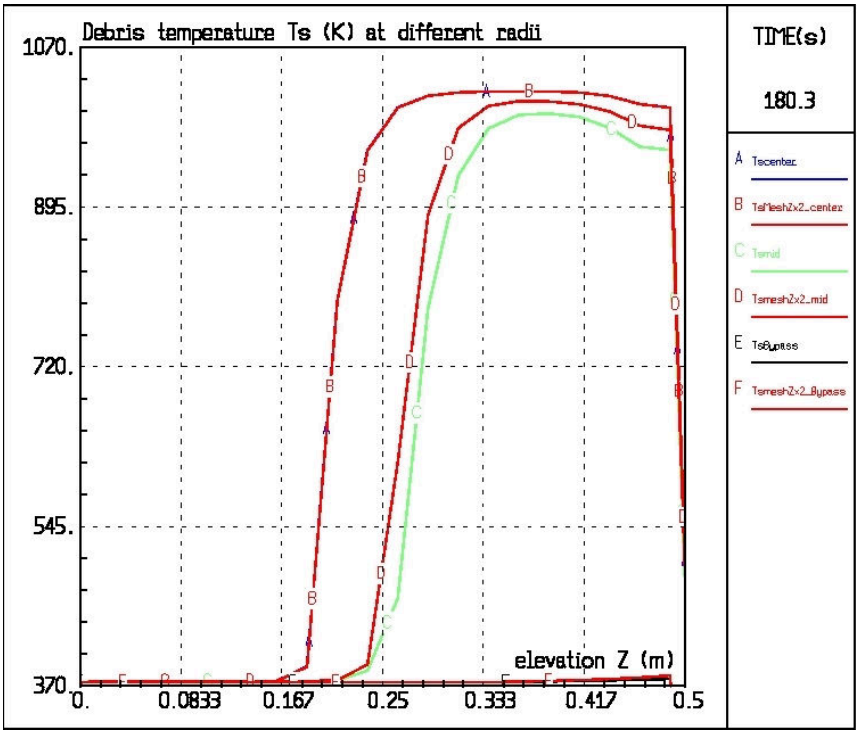

Figure 3.17: Debris temperature axial profiles 'Ts(r,z)' at three different radii (center, mid, bypass) r=(0m, 0.16m, 0.25m), comparison of doubled axial meshes (Red curves B,D,F), against reference calculation (curves A,C,E) - PA2 test. A:Ts(r=0m,z); B:Ts(r=0m,z) doubled meshing; C:Ts(r=0.16m,z); D:Ts(r=0.16m,z) doubled meshing; E:Ts(r=0.25m,z); F:Ts(r=0.25m,z) doubled meshing

more related to the large scale redistribution occurring between the center and the bypass.

For the configuration and process under study, the considered meshing does not appear to present a big issue as it was tested by doubling the number of meshes in the radial and vertical direction. Moreover, the physical process occurring involves water entering fully saturated into the hot debris bed and exiting in steam form, and the two-phase flow zone is rather thin. The quench front in the center is thin and could be contained within 3 meshes as shown in the void fraction 2D fields.

3.2.5 Power deposition and extraction

The system is cooled by injecting water from the bottom. Upon the arrival of water at the experimental bed, heating starts and energy deposition is simulated by a vol-

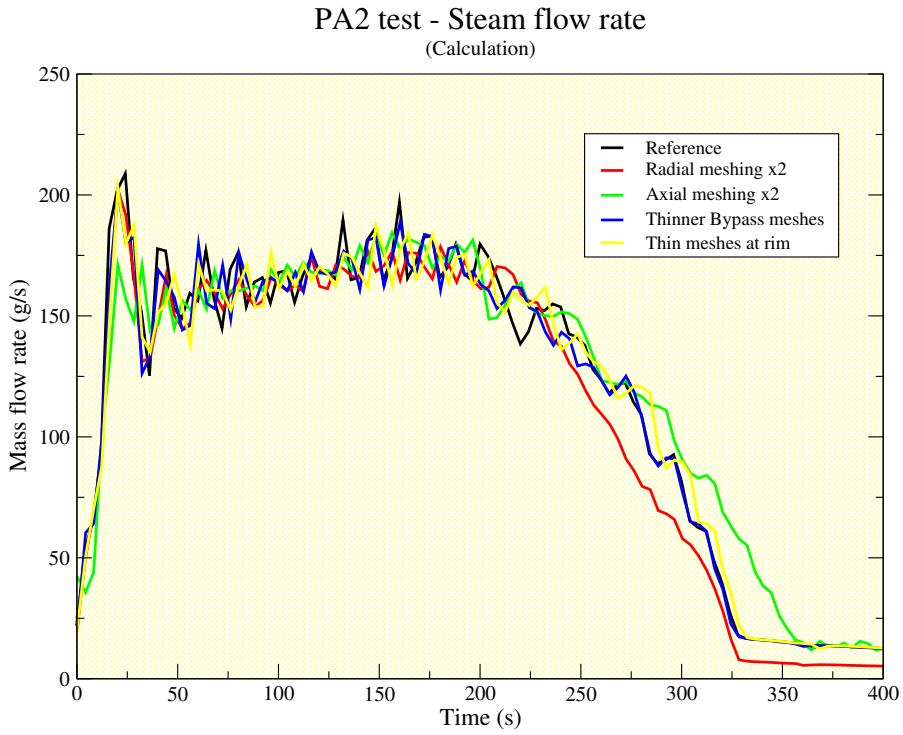

Figure 3.18: Impact of meshing on the steam flow rate

Table 3.2: Reflooding time, maximum temperature, and steam production. A comparison of the calculations against experimental results ([Chikhi 2015a])

Test	Reflooding time (s) Exp - Calc	Bed max. Temperature (°C) Exp - Calc	Steam production (kg) Exp - Calc
PA0	108 - 150	173 - 181	11 - 11
PA1	240 - 186	447 - 440	31 -30
PA2	490 - 338	790 - 763	59 - 51
PA4	440 - 545	490 - 541	44 - 42
PA5	185 - 146	430 - 428	28 - 26
P22	341 - 301	745 - 754	52 - 45
P32	257 - 269	739 - 752	X - 43
P51	224 - 263	732 - 749	44 - 41

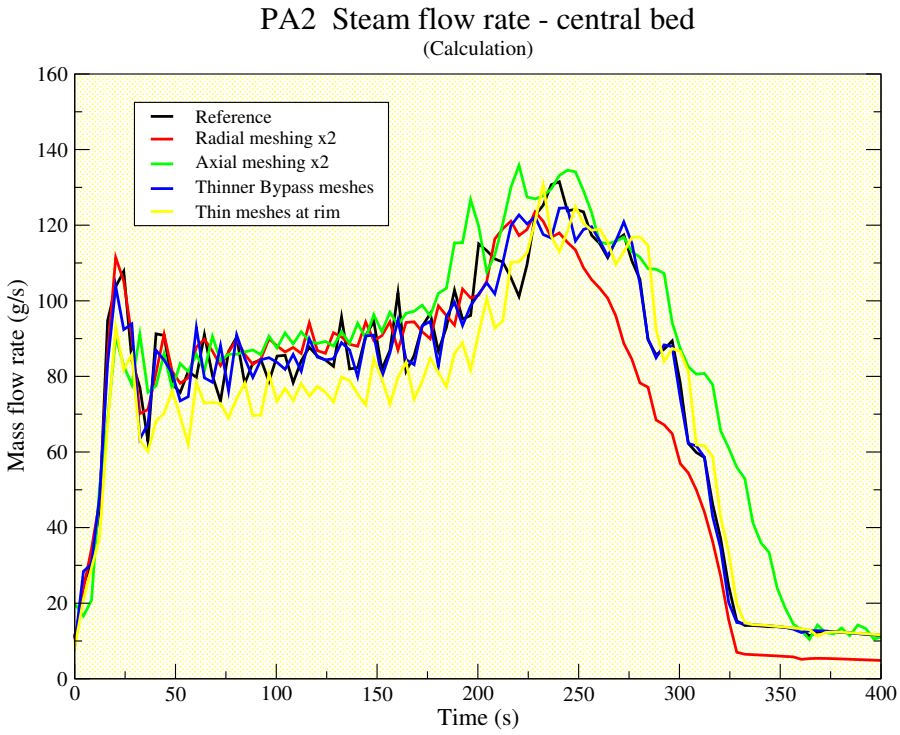

Figure 3.19: Impact of meshing on the steam flow rate - central bed

umetric heat source applied homogeneously (Power=150W/kg) on the stainless steel experimental bed. In the simulation of the reflood, the produced steam was exiting the beds super-heated and carrying a significant portion of the energy extracted by the fluid. However, in the experiment, almost all of the energy extracted from the hot bed was used to vaporize the water. A comparison of the outlet steam temperatures as calculated and measured in experiments is found in the appendix A.1. The temperatures are always higher in the calculations indicating that the steam is exiting carrying more energy than what was recorded experimentally. Due to this fact, the steam production calculated in the simulations is expected to be less than what was recorded in the experiment above the beds.

Figure 3.21 represents the energy extracted from the system by the steam being produced, for both experimental and calculation results. The energy carried by steam consists of two portions: the energy of vaporization and a smaller portion accounting for the superheating of steam. It is calculated as follows:

$$E_{total} = E_{produced} + E_{superheat} \tag{3.1}$$

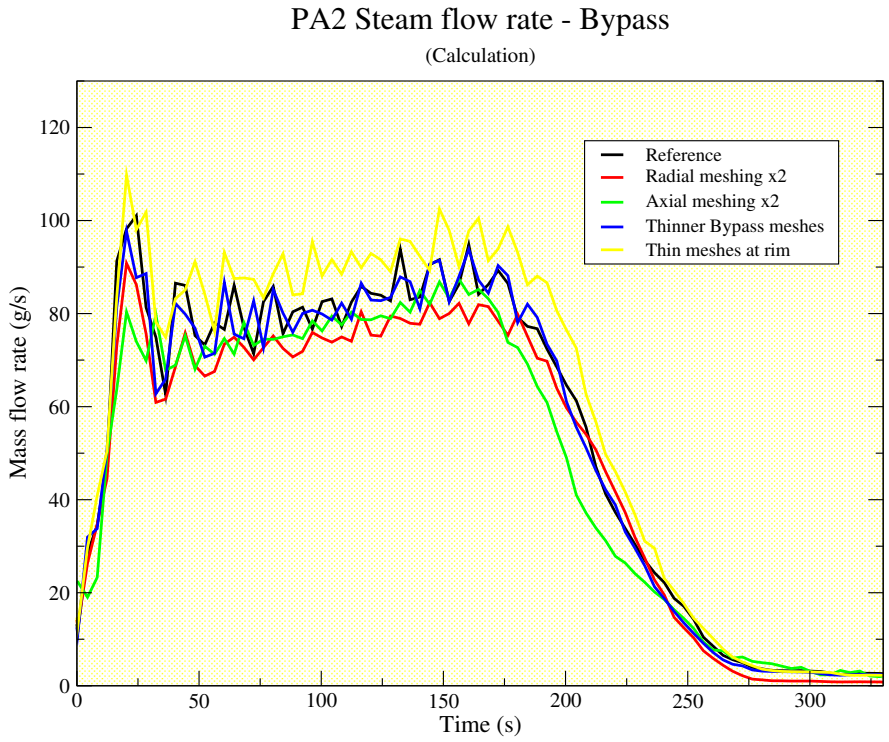

Figure 3.20: Impact of meshing on the steam flow rate - bypass

with

$$E_{superheat} = \int \alpha \, \varepsilon \, \Phi_v \, c_p (T_g - T_{sat}) \, dt \tag{3.2}$$

$$E_{produced} = \int \alpha \, \varepsilon \, \Phi_v \, \triangle H_{vap} \, dt \tag{3.3}$$

where: Φ_v = steam flow rate, ε = porosity, and $\triangle H_{vap}$ = enthalpy of vaporization.

The maximum temperatures reached were good agreement. the mass of steam produced results were also in good agreement except for the tests with high initial temperature where the mass of accumulated steam was always less in the calculations than the experiment. the first reasoning was provided above where the gas was shown to exit superheated in the calculations and thus carrying more energy that was rather used to evaporate more water in the experiments. for those situations the largest discrepancy in reflooding time was seen where the calculations resulted in faster quenching (shorter reflooding times).

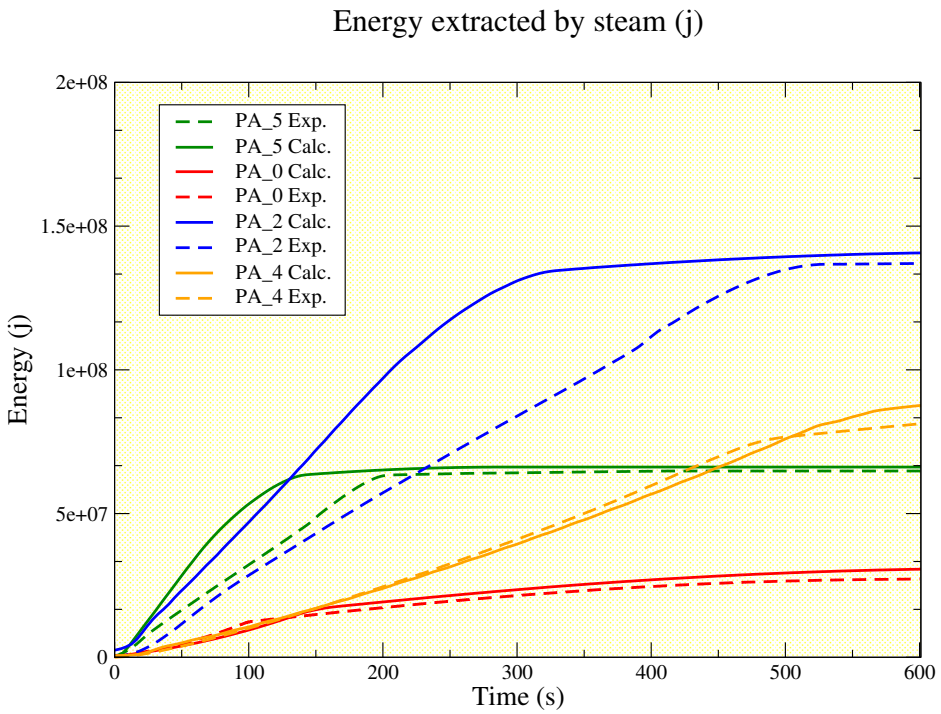

Figure 3.21: Energy of steam produced (J)

3.2.6 Interpretation and comparison against experiments

3.2.6.1 Steam flow rate

Tests at atmospheric pressure

Flow rates of the steam generated upon cooling of the debris beds are calculated at the exit line downstream. Figure 3.22 represents the evolution of the mass flow rates of steam produced by the tests performed at atmospheric pressure.

For the tests with low injection velocity (PA4 : 2m/hr) and low initial temperature (PA0 : 150°C) as well as (PA1) test, the steam flow rate showed a continous yet slowly rising until quenching took place. Whereas the other tests with higher initial temperature (PA2 : 700°C) and higher injection veclotity (PA5 : 10m/hr), show a steam flow rate with a first strong peak followed by constant rate then a final peak which appears before the complete quenching debris bed. In some cases, the steam production recorded in the experiment (Figure 3.23) is larger than the one calculated in the simulation. This can be explained by observing that, in the numerical simulations, the produced steam leaves the beds with a significant superheat (up to 15% of

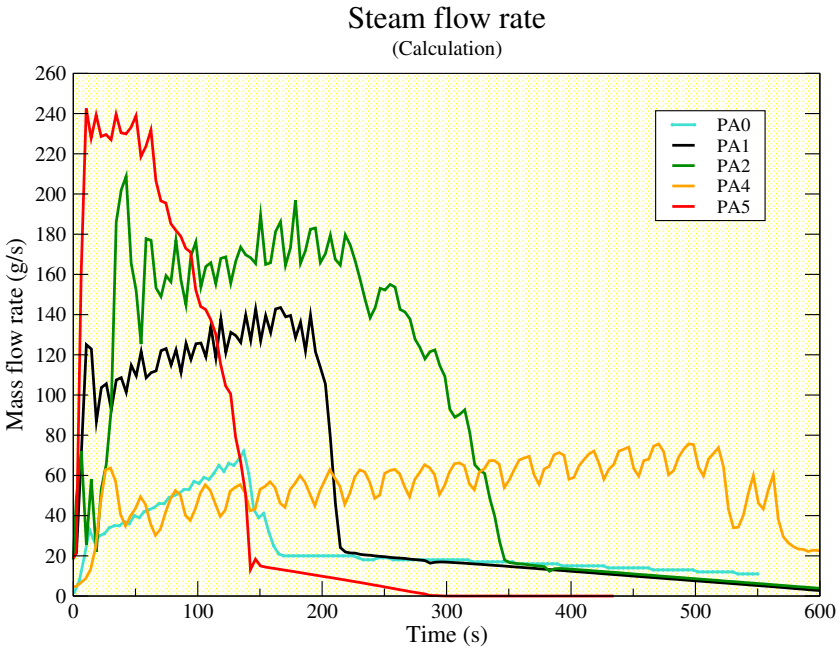

Figure 3.22: Calculated steam flow rates (g/s) for PEARL tests at atmospheric pressure

the energy extracted by the fluid) whereas almost all of the energy extracted in the experiment was used to evaporate water and the measured superheat of steam was low. In PA2 and PA5 tests, a similar behavior was observed. A first peak followed by a constant flow and then a second peak before achieving the total quenching. Among the others, those tests were performed at 700°C and highest injection velocity 5m/hr and 10m/hr respectively. The first recoreded peak correspond to the first strong thrust of steam through the bypass, it happens upon the evaporation of water water entering into the hot debris bed. Following that, a constant steam production was recorded during the quasi-steady quenching of the hot debris. Another peak, was also recorded right before achieving the total quenching.

If the contributions of the steam flow rate exiting the main bed and the flow exiting the bypass are drawn separately (Figure 3.24), a peak is observed in the center at the end of quenching. The evolution of the water-to-steam conversion rates as calculated by Icare-Cathare and the experimental measurements are represented in Figure 3.25 and Figure 3.26 respectively. It ranged between 20% and 70%, the maximum conversion rate was recorded in the tests which had the longest reflooding duration:

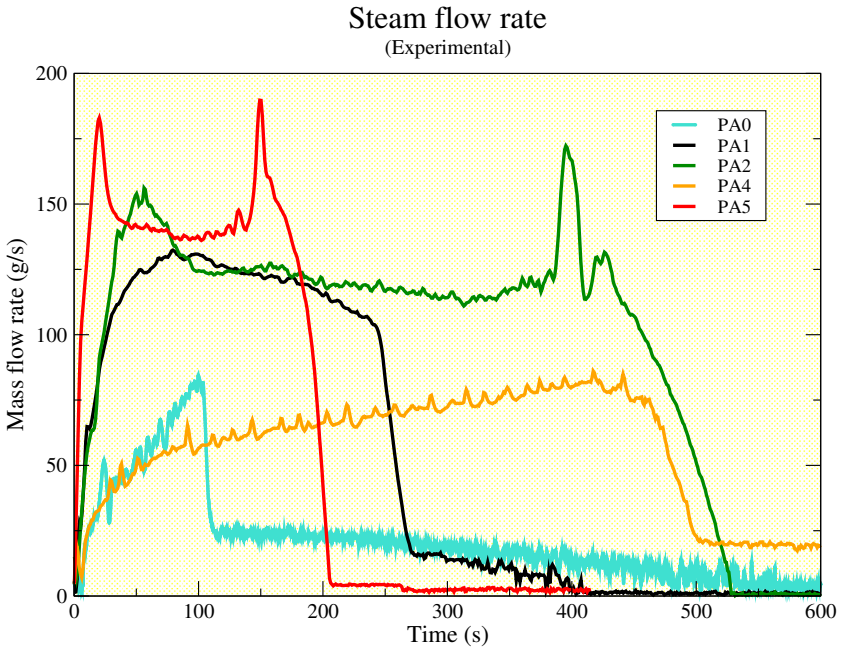

Figure 3.23: Measured steam flow rates (g/s) in PEARL tests at atmospheric pressure

PA2 with the highest initial temperature 700°C (i.e more energy to be extracted and thus a longer reflooding interval) and PA4 with lowest injection velocity of 2 m/hr (i.e slower propagation of the quench front and thus extending the reflooding interval). Whereas the lowest conversion ratio were registered in PA0 test (lowest initial temperature 150°C) and PA5 (highest injection velocity 10 m/hr).

Tests at higher pressure

Tests PA2, P22 and P32 were performed under the same thermal-hydraulic conditions except being differently pressurized under 1 bar, 2 bar and 3 bars respectively. The steam flow rate evolution for those test is represented in Figure 3.27. In the P22 test the first peak recorded by the PA2 test is seen whereas in P32 it is proceeded by a slightly higher one before having a smaller one coincident with the first peak of PA2 and P22. The flow rates then oscillate slightly around 160 g/s forming a plateau until the end where they decline yet masking the second peak that was recorded in the experimental measurements and which itself corresponds to a significant flow of steam out of the beds at the central zone. The duration of steam production which corresponds to the quenching duration is reduced, it decreases with increasing pres-

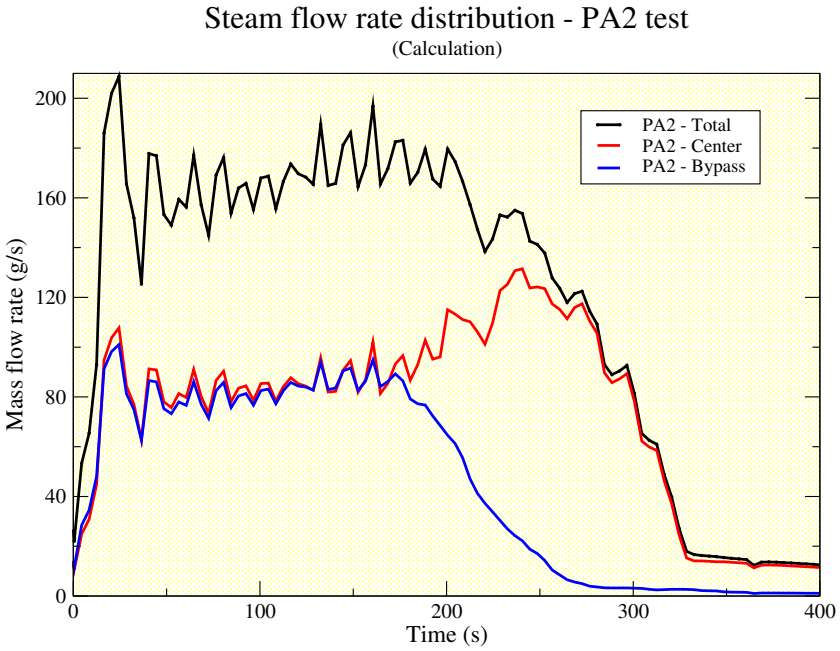

Figure 3.24: Calculated PA2 Steam flow rate (g/s): distribution between heated bed and bypass

sure. However, at the highest tested pressures, 3 bars and 5 bars, the reduction in the quenching duration is limited.

3.2.6.2 Quench front velocity

Tests at atmospheric pressure

Temperature readings corresponding to the thermocouples positioned at each 60mm in the different vertical axes were obtained in the Icare-Cathare V2 calculations of the PEARL tests. Following the same method as Tung and Dhir for processing the thermocouples readings in the experiments, the quench front velocities are calculated where the quenching front position is determined as that corresponding to temperature drop to few degrees above the saturation temperature. Table 3.3 lists the results along the central axis (R=0mm) and in the bypass (R=250mm). The ratio of the central quench front velocity to that in the bypass provides an idea about the shape of the quench front propagating through the beds; lower values indicate a curved quench front whereas values close to 1 correspond to at front propagation. Two different quenching behaviors were distinguished, the flat 1-D and the curved

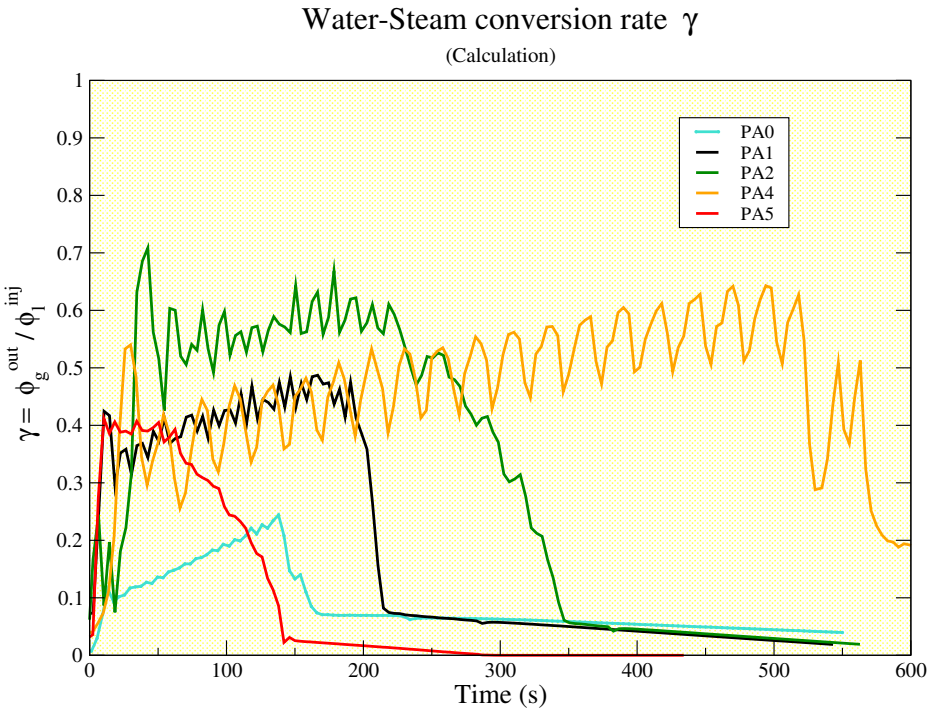

Figure 3.25: Conversion ratio - Icare-Cathare Calculation

Table 3.3: Calculated quench front velocities: central bed, bypass, and their ratio

Quench front velocity (mm/s)	Center R=0mm	Bypass R=250mm	ratio Center/Bypass (%)
PA0	3.63	NA	NA
PA1	2.51	2.8	89.6
PA2	1.51	3.54	11.4
PA4	0.89	0.90	98.3
PA5	3.28	13.46	24.4
P22	1.86	2.02	92.1
P32	1.9	1.95	97.4
P51	1.92	1.93	99.5

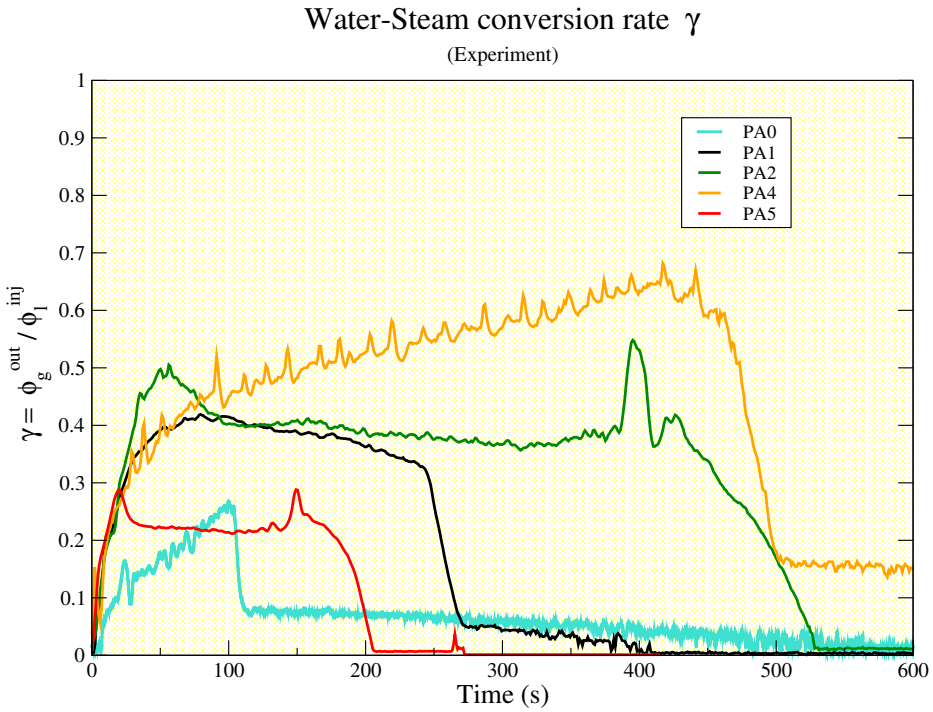

Figure 3.26: Conversion ratio - Experimental measurements

2-D. For the tests performed at low injection velocity (PA4 : 2m/hr) and low initial temperature (PA0 : 150°C), the quench front was very flat with a particular 98.3% ratio of the quench front velocity in the center with respect to the bypass in PA4 test where the heated debris bed and the bypass were approximately quenched at the same time.

In contrast, for the tests at higher initial temperature (PA2 : 700°C) and higher injection velocities (PA5 : 10m/hr) the bypass was quenched much faster than the experimental bed. The quench front is more curved (Figure 3.28), and water had a preferential flow path through the bypass leaving the hot debris bed dry for a longer time. This behavior allows water to accumulate above the top of the bed yet not causing a top quenching but a slighter decrease in the temperature of the top of the bed is seen earlier to that at lower altitudes in the dry part for the axis (R=220mm).

Tests at higher pressure

Increasing the pressure had a significant effect on the reflooding behavior in the beds. Tests PA2, P22, P32 and P51 were performed under same conditions but

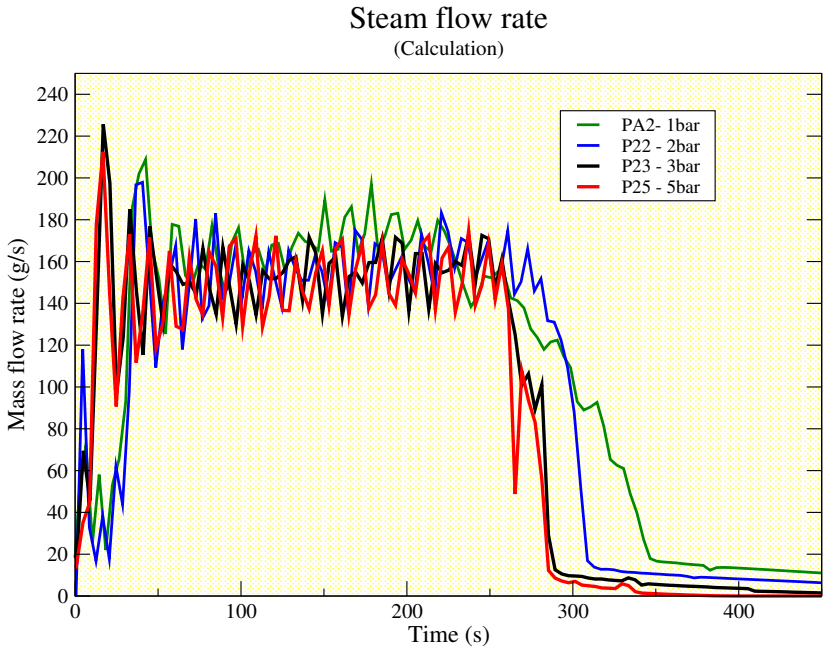

Figure 3.27: Calculated steam flow rates (g/s) for PEARL tests at different pressure

with different pressures: 1bar, 2bar, 3bar and 5bar respectively. The quench front velocity in the central axis (R=0) was increased from VQF = 1.51mm/s at 1bar to VQF = 1.92mm/s at 5bar. Whereas the quench front velocity in the bypass declined from VQF-bypass = 3.5mm/s at 1bar to VQF-bypass = 1.93mm/s at 5bar. A radical change in the shape of quench front is observed in Figure 3.28 where it transformed gradually from a curved shape in PA2 (P=1bar) test to a very flat one in P32 (P=3bar) in which the quench front velocity in the center and the bypass were almost equal. There is no significant change between 3bar and 5bar. That could be also described in numbers as listed in Table 3.3, where the ratio of VQF center/bypass tends to 1 (it varies from 0.11 to 0.99).

Figures 3.29 and 3.30 represent a comparison between the calculations and experimental results for the quench front velocities in the bypass and the central hot bed. In the center the velocities are comparable in most of the tests whereas in the bypass it is always found that the calculated quench front velocity is slower than that measured in the experiments. It indicates that there is larger entrainment of water into the bypass in the experiments. This is consistent with having faster quenching in some of the calculations where a portion of the liquid flow rate that was experimen-

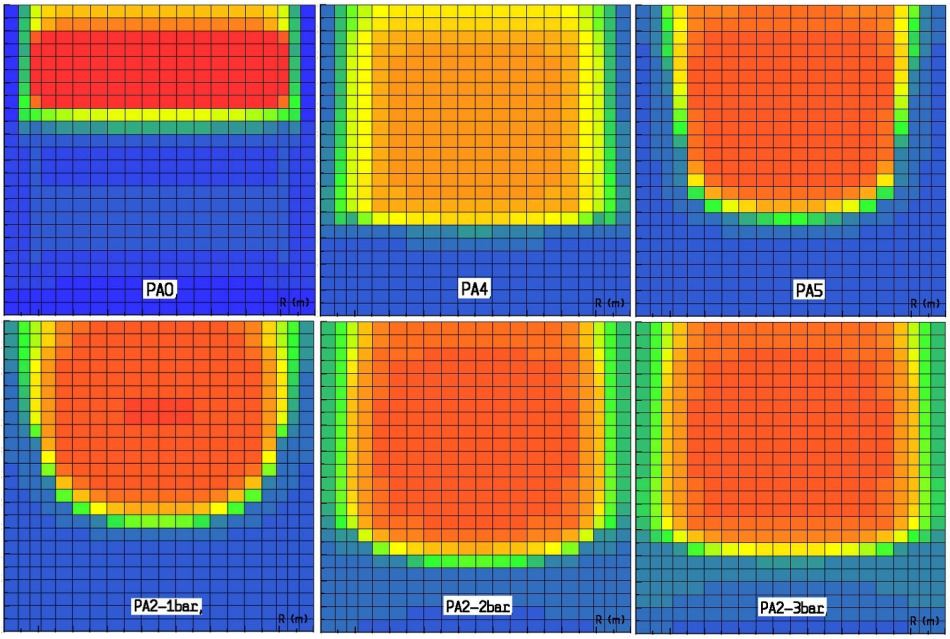

Figure 3.28: Calculated 2D temperature fields; comparison of 1D (flat) and 2D (curved) quench fronts

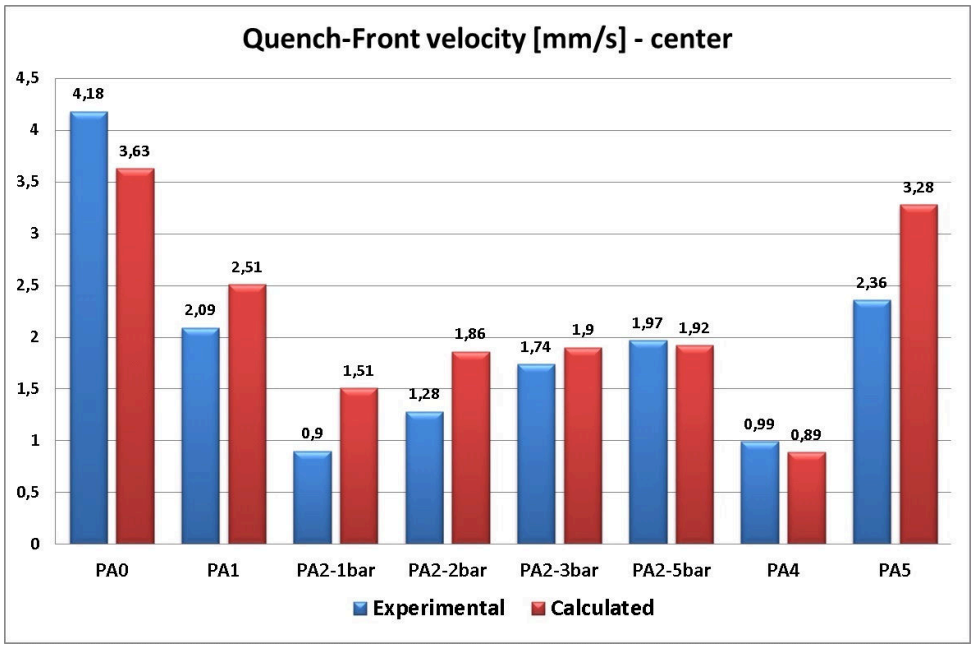

Figure 3.29: Quench front velocities in the central bed - Calculations Vs Experiments

tally entrained into the bypass is used for cooling the heated bed in the calculation,

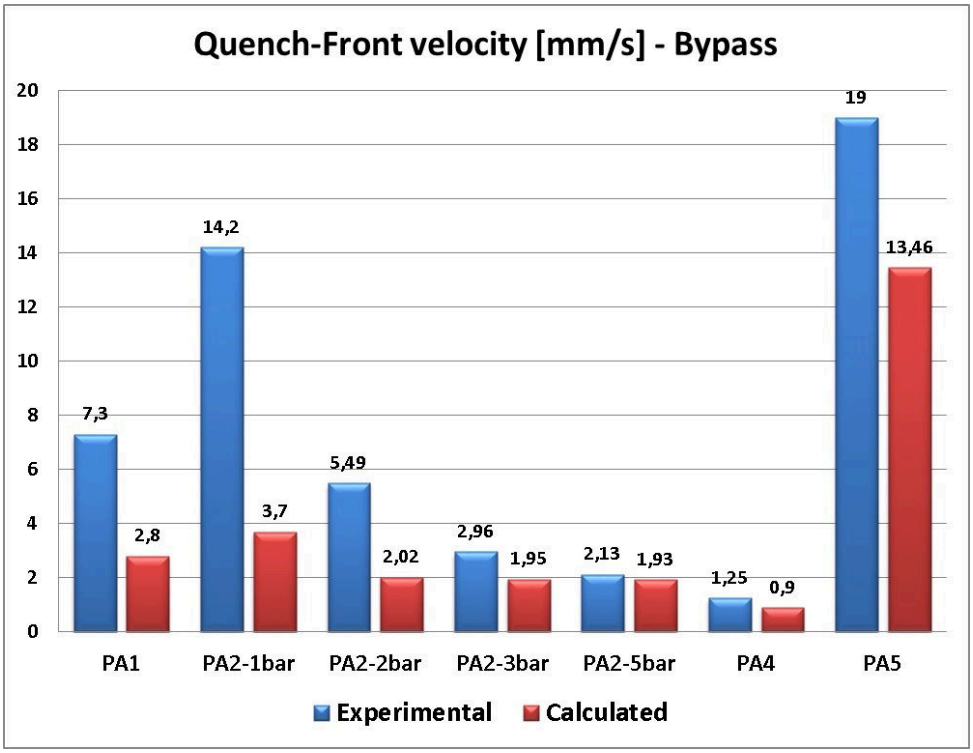

Figure 3.30: Quench front velocities in the bypass - Calculations Vs Experiments

resulting in earlier quenching. Sensitivity calculations are presented later to identify the source of such discrepancies.

3.2.7 Reflooding and water entrainment in the bypass

3.2.7.1 Effect of injection velocity and initial temperature

Injection velocity effect has been explored comparing the reflooding time among the tests PA4, PA1 and PA5 performed under same pressure and initial temperature (1bar, 400°C) being cooled by injecting water at velocities: 2 m/h, 5 m/h and 10 m/h respectively. Figure 3.31 illustrates this effect.

Similar to what was deduced from the experimental results, increasing the injection flow rate of water helps in reducing the time needed for reflooding only up to a certain limit beyond which higher injection rates may no longer speed up the cooling process, i.e the efficiency of reflooding becomes limited as injection rate increases. Checking the quench front velocity in the bypass, it is clearly observed that the water injection velocity has a great effect on VQF as it increased dramatically from VQF-

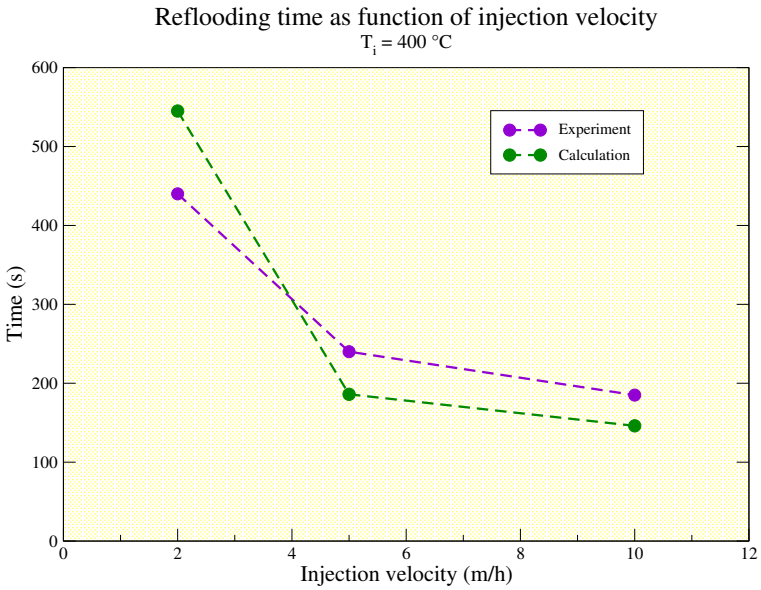

Figure 3.31: Effect of injection velocity on reflooding time

bypass,PA4=0.89mm/s in test (PA4 : Vinj=2m/h) to VQF-bypass,PA5=13.46mm/s in test (PA5 : Vinj=10m/h). Water arriving at higher velocities at the bottom of the hot debris bed experience a larger entrainment force due to the pressure gradient induced by vaporization and the difference in permeability between the center and the bypass. Being entrained by steam, water arriving from the bottom is then forced into a preferential path through the bypass. This behavior is clearly observed in the 2D illustration of steam and water velocity vector fields for PA5 test (Figure 3.32). The yellow line corresponds to the quench front level while the green line designates the upper limit of the two-phase flow zone, or in other words the level reached by water in the bypass for a 2D quenching process. This was clearly observed as water proceeded up to an elevation of z=370mm while the quench front level was still below z=10mm.

At the quench front level, steam flows radially towards the bypass entraining the arriving water into the bypass which indeed possesses a smaller pressure drop than the central heated bed during the beginning of reflooding since it is composed of larger balls of diameter dp=8mm (i.e. higher permeability and passability) in contrast to 4mm balls in the central bed inside. Water is then accelerated through the bypass, flows at a velocity higher than the injection velocity (VQF-bypass(PA5) = 13.46mm/s $>$ Vinj(PA5) = 6.94mm/s in debris) and starts to accumulate above the beds.

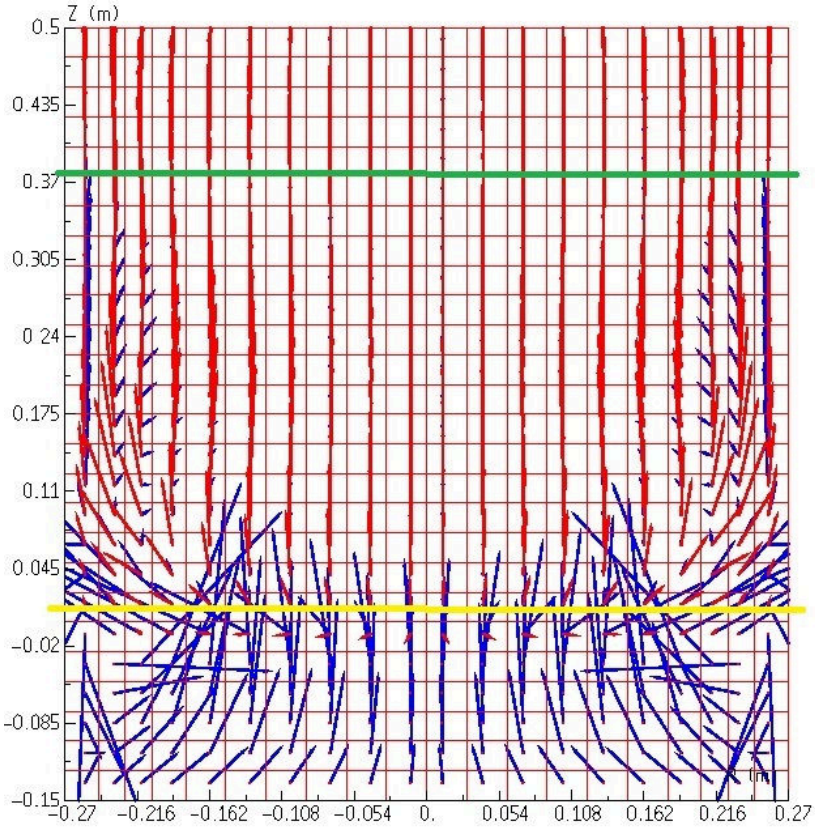

Figure 3.32: PA5 test, water (blue) and steam (red) 2D velocity vector fields. Scale: 1m $\mapsto$ 1m/s and $v_g = 650 v_l$

An illustration of the evolution of the 2D velocity vector fields for steam and liquid in the PA2 test (Ti = 700°C) is presented in Figure 3.35.
At the first instants of reflooding, water arrives at level z=0 (bottom of the hot central bed), the penetration attempt into the hot bed is resisted by a strong steam flow generated by the vaporization of large portions of this incoming flow of water. This is mainly associated to the test with a 2D curved quench front propagation. In those situations water is driven into the bypass forced by the strong radial flow of steam at the quench front level. Below the quench front, a recirculation is observed where some portion of water diverted into the bypass which could not advance updwards falls down and flows back to the center as shown in the graphs.

Pressure in the bypass is less than that in the less permeable and hot center. Upon water evaporation in the center, the steam flow is directed radially towards the bypass imposing a preferential path for water, a process we refer to as 'water en-

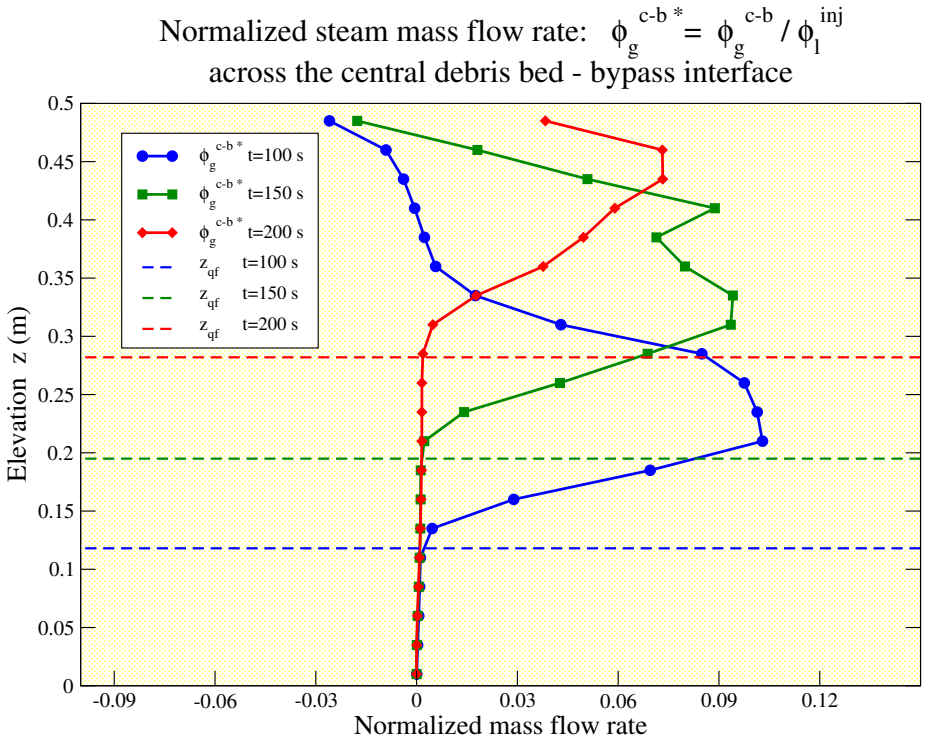

Figure 3.33: Vertical profiles of normalized steam flow rate acorss the center-bypass interface, at different instants during reflooding (Calculation)

trainment'. Figure 3.33 represents the vertical profiles of the normalized steam flow rate ϕ_g^{c-b*} entering from the center into the bypass (+ve direction) at different instants of time. We observe that steam flows radially into the bypass above the quench front level z_{qf}. At later instants during the reflooding process, the quench front level progresses towards the upper part of the bed, the steam exit path becomes shorter and larger portions of the steam flow rate leave through the top of the central debris bed rather than the bypass. This behavior was detected in the Icare-Cathare calculations but could not be measured in the experiment. In Figure 3.24 we clearly observed the decrease of steam flow rate earlier than the central bed). The void fraction was progressively decreasing in the bypass since water level there was increasing due to entrainment. Figure 3.33 also shows a decaying amplitude of the radial flow of steam into the bypass at later instants (i.e. at higher elevations in the bed). This curved quench front propagation could be also observed in the evolution of 2D temperature fields and steam vector fields in Figure 3.39.

Figure 3.34 represents the vertical profiles of the normalized water flow rate ϕ_l^{c-b*} entering from the center into the bypass (+ve direction) at different instants of time.

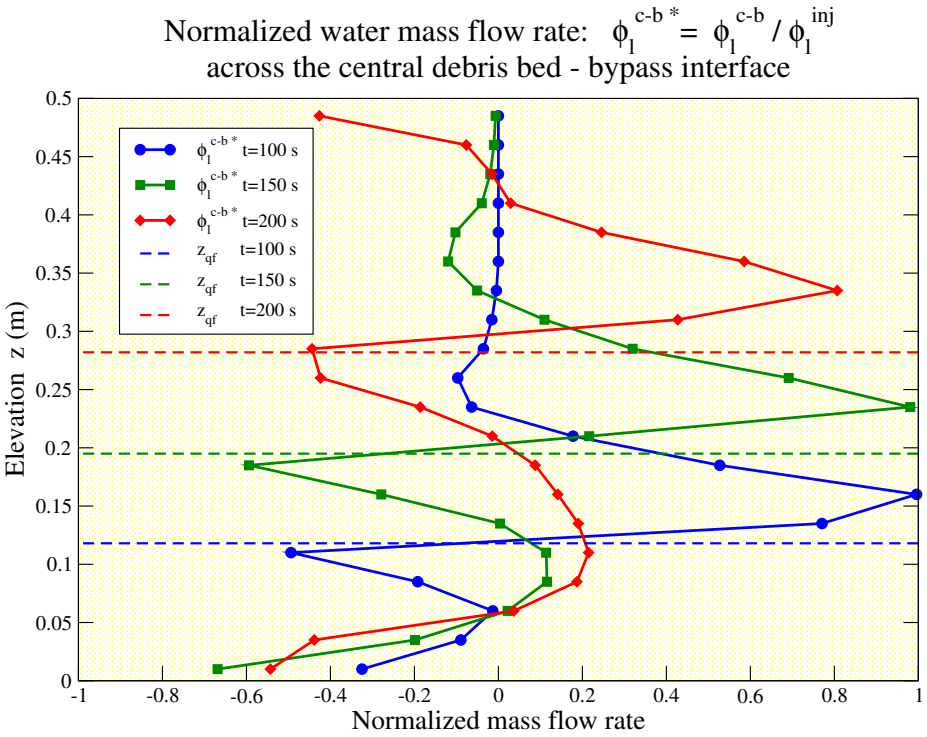

Figure 3.34: Vertical profiles of normalized water flow rate from the center to bypass, at different instants during reflooding (Calculation)

Driven by the steam flow, water flows radially into the bypass at the quench front level. A small reverse flow to the center is also observed similar to the behavior shown in the 2D velocity vector fields in Figure 3.35. Figure 3.36 shows both steam and water radial flow rates across the interface between the center and the bypass, at one instant of time. In this figure, the normalized steam flow rate (ϕ_g^{c-b*}) is scaled by 10 because it was relatively small. We clearly observe the dragging effect of steam flow on water entrainment in the bypass where the peak of radial flow rate of water coincides with the start of radial flow of steam into the bypass.

On the other hand, to explore the effect of the initial temperature on the reflooding process, tests PA0, PA1 and PA2 are considered. Performed under same pressure and injection velocity (P = 1bar, Vinj= 5m/h), the experimental central beds were heated up to 150°C, 400°C, and 700°C respectively. It is straight forward to expect that the quench front velocity in the experimental bed decreases (see Table 3.2) with increasing the initial temperature where the initial energy to be extracted by cooling becomes larger. Nevertheless, the quench front velocity in the bypass increases for higher initial temperatures (VQF-bypass(PA2)=3.56mm/s while VQF-bypass(PA1)

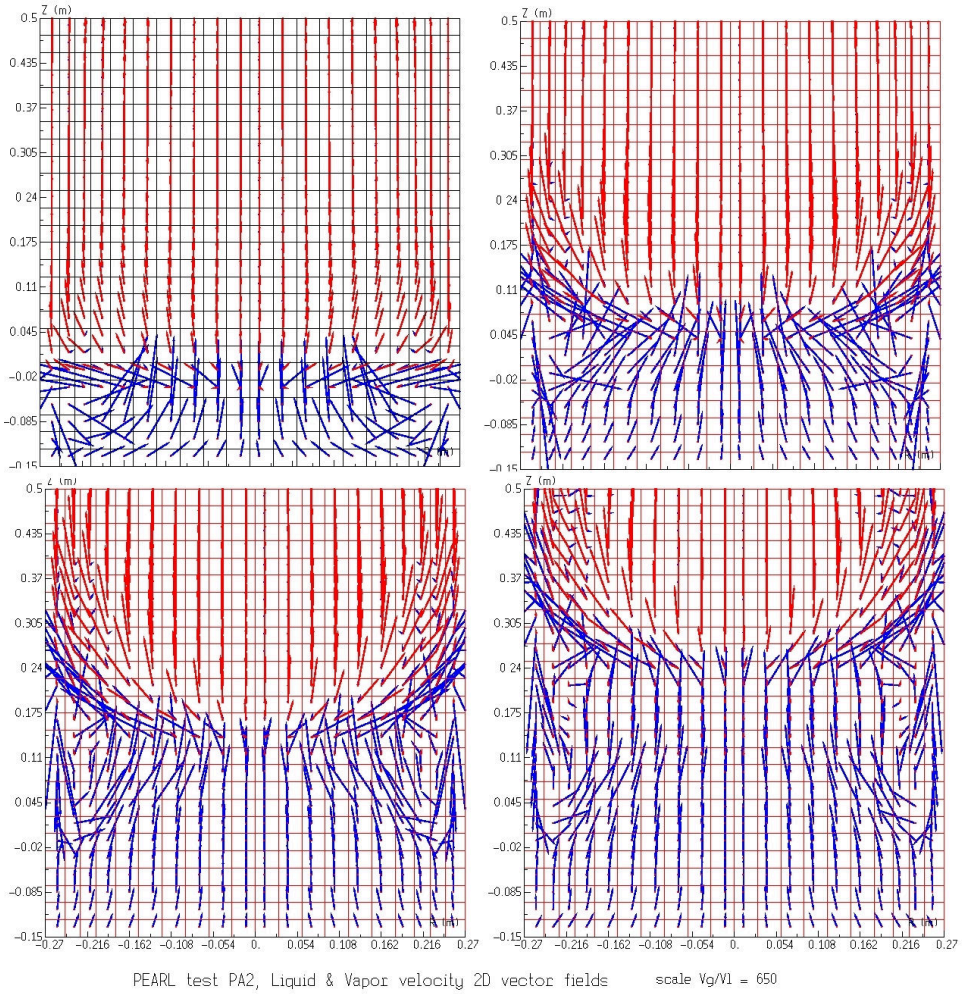

Figure 3.35: PA2 test, water (blue) and steam (red) 2D velocity vector fields. Scale: 1m $\mapsto$ 1m/s and $v_g = 650 v_l$

=2.8mm/s) in agreement with the behavior observed in the experiments. A similar behavior of dragging water into the bypass is seen in the test PA5 with high injection rate.

3.2.7.2 Effect of pressure

Similar to the experimental results, as the pressure increases the reflooding time was consistently reduced (Figure 3.37). The 2D temperature field evolution Figure 3.28 confirmed the effect of increasing pressure on the quench front propagation which becomes more flat and almost 1D under highest pressure. Generally speaking,

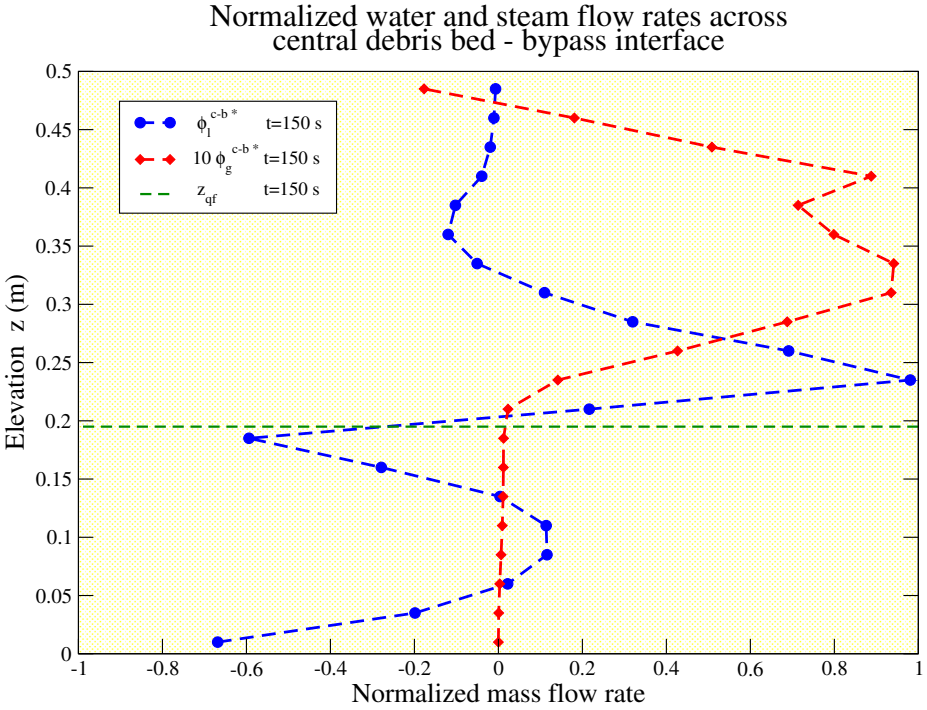

Figure 3.36: Vertical profiles of normalized water and steam flow rates from the center to bypass, at different instants during reflooding (Calculation)

increasing the pressure reduces the pressure gradient in the central bed and the bypass, which leads to the reduction of water entrainment into the bypass.

Figure 3.38 represents the calculated radial pressure difference between the center (r=0,z) and the bypass (r=0.25,z) at different elevations in the debris system.

$$\Delta P(z) \;=\; P^{c}(z) \;-\; P^{b}(z) \;=\; P(r=0,z) \;-\; P(r=0.25,z) \tag{3.4}$$

The solid lines correspond to PA2 test (at 1 bar) while the dashed lines correspond to P32 test (at 3 bars). It shows that, at a certain elevation, upon the arrival of the quench front, the vaporization of water induces a radial pressure gradient which provokes the radial flow of steam flow outwards at the quench front level. The radial pressure difference is calculated at the elevations 120 mm, 240 mm, and 360 mm. For the test at higher pressure, P32 at 3 bars, this radial gradient is significantly smaller (smaller peaks) and the effect is shorter (narrower range) summing up to a smaller integral of the force driving steam and water in radial direction at the quench front level. Another observation is that the peaks recorded at the same elevation

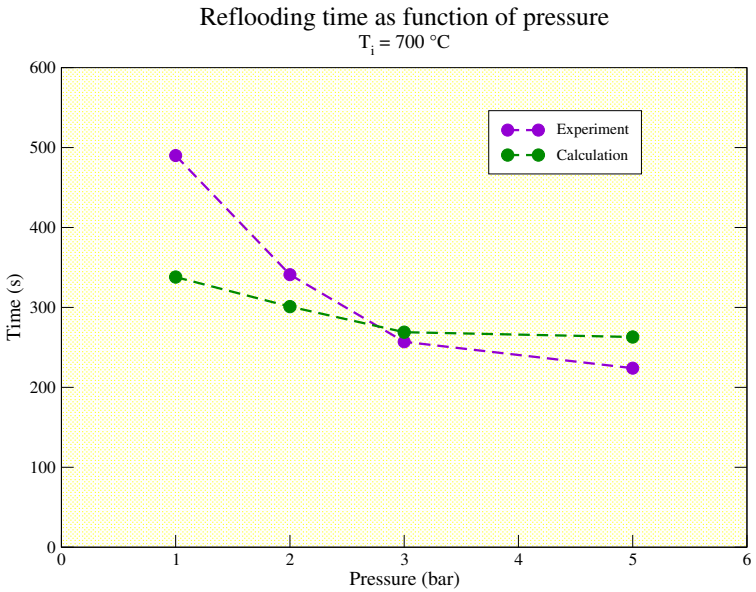

Figure 3.37: Effect of pressure on reflooding time

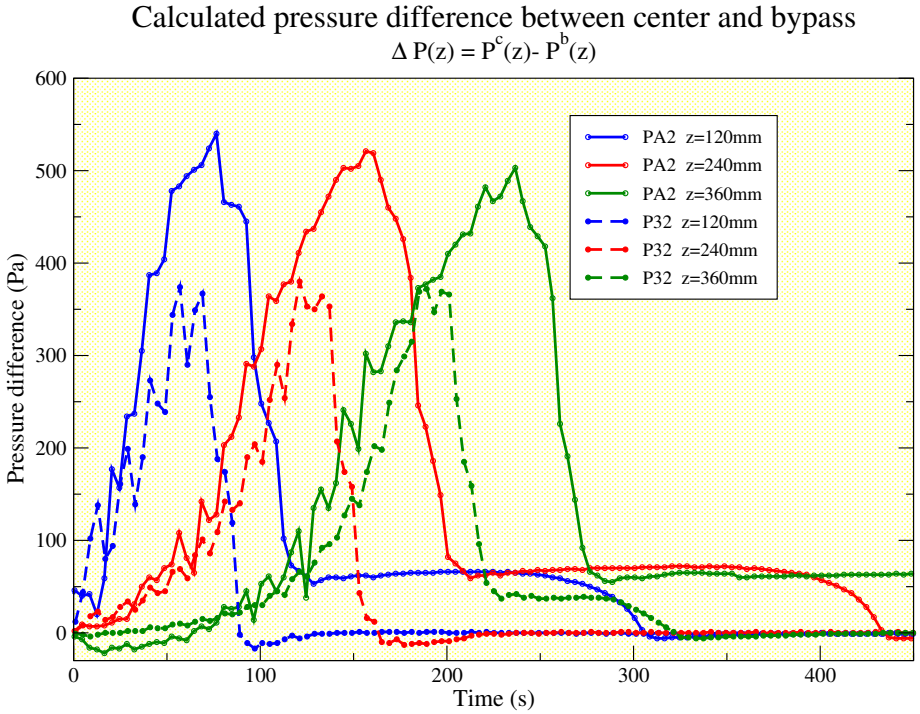

Figure 3.38: pressure difference different elevations

for P32 test occur before those of PA2 indicating that it has been quenched earlier. This is in agreement with the experimental and calculation results that proved the faster quenching when the pressure is higher.

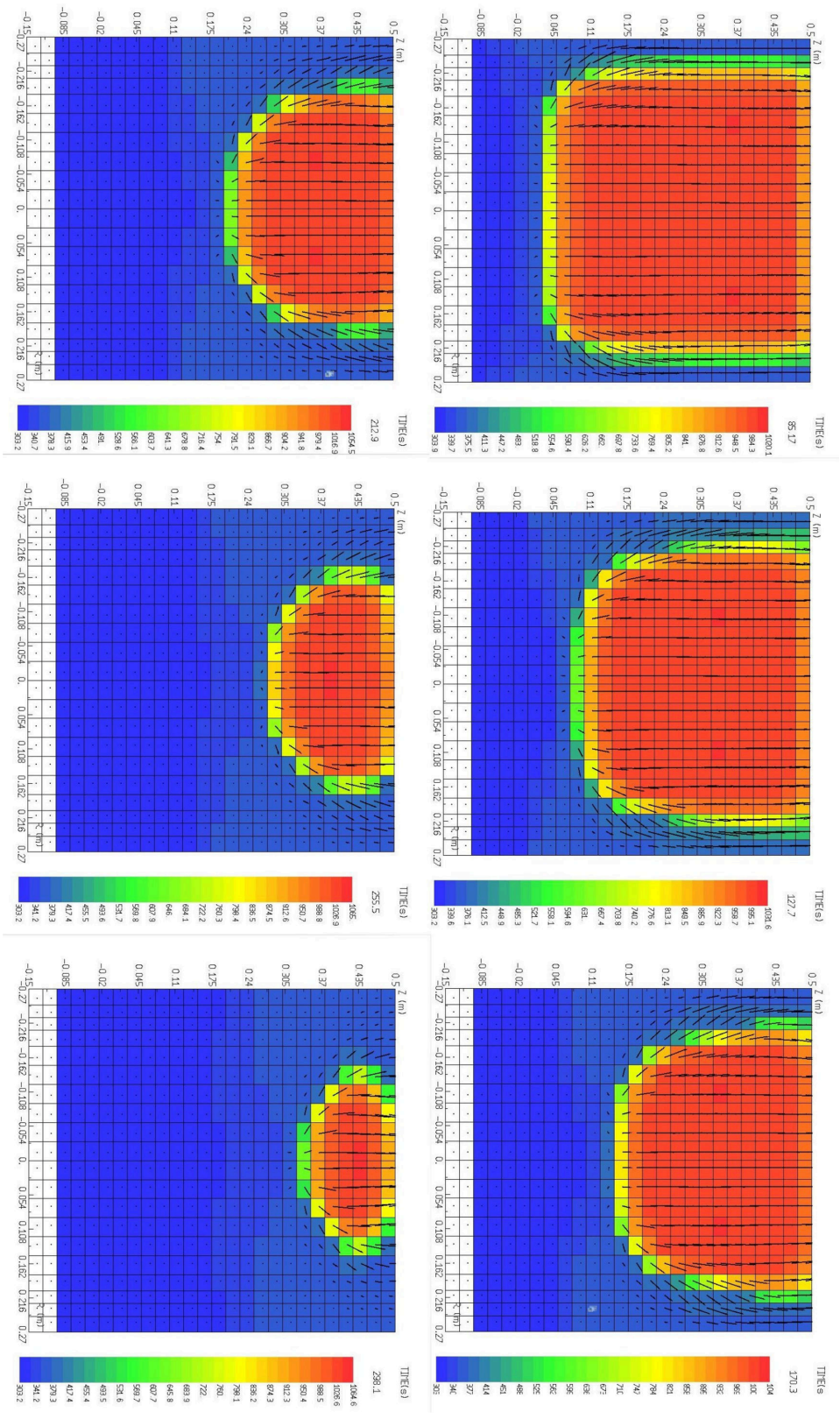

Figure 3.39: Evolution of 2D temperature and steam vector fields (black vectors) - PA2 (Icare-Cathare Calculation)

3.2.8 Sensitivity calculations to permeability correlations and differencing schemes

Some discrepancies in the entrained liquid velocity in the bypass, and mass of steam produced were observed after comparing the calculations against the experimental results of PEARL tests. In order to enclose the sources of those discrepancies some sensitivity calculations (meshing, geometrical effects, boundary conditions, differencing schemes) were performed and are presented in this section.

3.2.8.1 Exponents of relative permeability and relative passability correlations

In the reference calculation, the relative permeability and relative passability adapted the Fourar formulation [Fourar 2000]. It is the default option in the ICARE-CATHARE code where an assumption has been made setting the relative permeability equal to the relative passability for each fluid phase β as follows:

$$\kappa_{r\beta} = \eta_{r\beta} \tag{3.5}$$

Knowing that the relative permeability for liquid and gas was defined, according to [Fourar 2000], as:

$$\kappa_{rl} = \eta_{rl} = \frac{\alpha^2(3-\alpha)}{2}(1-\alpha) \tag{3.6}$$

and

$$\kappa_{rg} = \eta_{rg} = \alpha^3 + \frac{3\mu_l}{2\mu_g}\alpha(1-\alpha)(1+\alpha) \tag{3.7}$$

Two other calculations were done using the BROOKS ([Brooks 1966]) option corresponding to the classical formulation where the relative permeabilities and passabilities are defiend as:

$$\kappa_{rl} = (1-\alpha)^{nk} \tag{3.8}$$

$$\eta_{rl} = (1-\alpha)^{np} \tag{3.9}$$

$$\kappa_{rg} = (\alpha)^{nk} \tag{3.10}$$

$$\eta_{rg} = (\alpha)^{np} \tag{3.11}$$

Those calculations corresponded to the set (nk, np)=(3, 3) following [Brooks 1966], and (nk, np)=(3, 5) following [Reed 1982].

However, no significant change in the major results (e.g steam flow rate, reflooding time, maximum temperature reached) was seen. At this point, it is worth mentioning that, in the momentum equations for liquid and gas, the relative permeability and relative passability were in fact defined up to the orders (nk-1) and (np-1) respectively, and multiplied by an additional void fraction term, for the gas, and saturation term, for the liquid, to compensate for the order in the momentum equation. This is only correct if the "BROOKS" correlation was assumed for this Icare-Cathare calculation. Otherwise, if the option was kept as default, FOURAR, the relative permeability and relative passability are thus wrongly defined where an additional void fraction and a saturation term will be appearing in the denominator of the kinetic and viscous energy losses terms in the momentum equations. Yet, it didn't result in significant changes when adjusted.

3.2.8.2 Fluxes computation across the neighboring meshes

The numerical scheme used in Icare-Cathare is the staggered cell. In this scheme, some variables are defined at the center of the cell (such as pressure, temperature, saturation, porosity, density, ...) and others such as fluid velocities are defined at the boundaries with the neighboring cells. The fluids fluxes across the cells are computed by solving the momentum equations. The momentum equations terms embed the void fraction α that need to be determined at the boundaries of the neighboring cells. It is computed according to one of the criteria listed below:

- Donor cell (or upwind): in which the void fraction across the boundary between two neighboring cells is taken equal to that in the cell with larger gas velocity.
- Centered (or weighted mean): in which the void fraction across the cells boundaries is calculated as a weighted mean of the two cells void fractions with the volume of each cell being the corresponding weight.

On the other hand, the absolute permeability and passability are determined at the boundary by applying a harmonic mean combining their values in the two neighboring cells. For instance, the harmonic mean of a variable X is defined by the following relation:

$$\bar{X} = \frac{2.X_{above}.X_{below}}{X_{above} + X_{below}} \tag{3.12}$$

In the momentum equations, the terms of kinetic and viscous energy losses were

considered to investigate different ways of calculating the flux across the neighboring cells boundaries. The existing form of those terms in the Icare-Cathare model was written as:

$$\begin{aligned} &-(\varepsilon\alpha)_{centered}\left(\frac{\mu_g.(\alpha)_{centered}}{\bar{K}.(k_{rg})_{centered}.(\alpha)_{upwind}}.\langle v_g\rangle^g\right) \\ &+(\varepsilon\alpha)^2_{centered}\left(\frac{\langle\rho_g\rangle^g.(\alpha)_{centered}}{\bar{\eta}.(\eta_{rg})_{centered}.(\alpha)_{upwind}}\langle v_g\rangle^g|\langle v_g\rangle^g|\right) \end{aligned} \tag{3.13}$$

The terms $(\varepsilon\alpha)_{centered}$ and $(\varepsilon\alpha)^2_{centered}$ present on the left hand outside of the brackets were kept unchanged as "centered" (or weighted) since they were assumed as a by-product of the volume averaging method. The absolute permeability and passability were calculated using a harmonic mean. The main changes were applied to the void fraction terms and two other configurations were tested according to the following formulations:

- Case .1

$$\begin{aligned} &-(\varepsilon\alpha)_{centered}\left(\frac{\mu_g.(\alpha)_{upwind}}{\bar{K}.(k_{rg})_{upwind}.(\alpha)_{upwind}}.\langle v_g\rangle^g\right) \\ &+(\varepsilon\alpha)^2_{centered}\left(\frac{\langle\rho_g\rangle^g.(\alpha)_{upwind}}{\bar{\eta}.(\eta_{rg})_{upwind}.(\alpha)_{upwind}}\langle v_g\rangle^g|\langle v_g\rangle^g|\right) \end{aligned} \tag{3.14}$$

- Case .2

$$\begin{aligned} &-(\varepsilon\alpha)_{centered}\left(\frac{\mu_g.(\alpha)_{upwind}}{\bar{K}.(k_{rg})_{centered}.(\alpha)_{upwind}}.\langle v_g\rangle^g\right) \\ &+(\varepsilon\alpha)^2_{centered}\left(\frac{\langle\rho_g\rangle^g.(\alpha)_{upwind}}{\bar{\eta}.(\eta_{rg})_{centered}.(\alpha)_{upwind}}\langle v_g\rangle^g|\langle v_g\rangle^g|\right) \end{aligned} \tag{3.15}$$

Calculations showed that the scheme defined in Case.1 was not suitable and couldn't achieve convergence. The calculation was automatically terminated after few seconds. On the other hand, the scheme defined in Case.2 worked properly but it didn't show a significant change from the reference calculation (based on Eq. 3.13).

3.2.9 Limitations and uncertainties

3.2.9.1 Meshing

The maximum number of meshes for each calculation in Icare-Cathare is restricted to 1000 meshes in total and to 50 radial meshes at most. All the tries to overcome

those restrictions failed due to technical problems because of the way this restriction is defined in this coupled code.

3.2.9.2 Injected water temperature

The thermocouple listings of the support quartz bed below was not clear, and that there was NO temperature readings in the upper quartz bed. That increases the uncertainty on the total initial energy of the system and the behavior of reflooding in those zones.

The calculations didn't include the long support bed of glass balls whose length and physical properties such as porosity was not indicated in the technical document of the experiments. As a consequence of heating the whole system by steam in the first heating phase, the glass bed stored enough energy to increase the temperature of the injected water from 30°C to saturation temperature for a significant period during the reflooding process whose time=0 was set when water level has reached the bottom of the hot stainless-steel bed after it has already crossed the relatively long glass bed and the quartz support bed.

The injected water temperature profile was set following the temperature recordings of thermocouples in the quartz support bed which were not indicated clearly. The temperature in the support quartz bed below the hot debris bed was set up to the thermocouples readings in the experiments. In particular, for PA2 test, the measurements showed that the injected water is arriving at that level at saturation temperature (close to 100°C or 373 K) for a period of ∼220s before decreasing to the initial injection temperature of 303 K (30°C). The uncertainty in making up this temperature profile together with the uncertainty associated to linking the water injection temperature directly to the temperature records in the quartz bed both affect the overall reflooding process and particularly the total reflooding time.

3.2.9.3 Initial energy of the system - initial temperatures

The precise prediction of the initial energy of the system is important in order to well predict the produced steam flow rate and the reflooding duration. The initial energy of the debris is determined by the thermocouples readings in the experiments. Several sources of uncertainty over the initial energy exist. The thermocouples readings are accurate up to 7.5 K degrees. Moreover, there is an uncertainty associated to positioning of thermocouples in the test section and their distribution on the different zones in the simulation (which was done with care to minimize the error). Those

uncertainties built up to around 8 to 15 % on the initial energy of the debris beds system, excluding the upper quartz bed. The thickness, porosity, and temperature of the quartz top layer was not specified in the experiment reporting. The role of this top layer is not negligible in the tests at high temperature or high injection flow rate. In such tests, entrainment of water into the bypass takes place. When this entrained water reaches the top layer, it may flow radially to the center and may participate in cooling the top of the hot central bed.

This lack of information restricted the good prediction of the thermal hydraulic behavior in that zone which is important as the penetration of bypass water entrained into the central zone may also confront with the hot steam flowing upwards, and thus resulting in more steam production and lower steam temperature at the outlet as in the experiment. Moreover, the video records of the experiments show that this top quartz bed was not stable. The particles in that zone were shaking strongly and were put into short vertical oscillations due to water boiling. In the experiments, this behavior could facilitate the water penetration into that zone.

Attempting to reproduce that latter effect, a calculation of PA2 test was done such that a 15% portion of the water injection rate was injected above the top quartz bed. This injected portion will later fall into that zone due to gravity. The percentage of this portion corresponded to the difference of water entrainment flow rate between the calculations and the experiment. However, this attempt did not show great success as the effect of this injection on the total mass and temperature of steam produced was not significant.

3.2.9.4 Effect of interfacial drag correlation

In another alternative to enhance the calculations accuracy, the Schulenberg-Muller interfacial friction law was imposed in the momentum equations. This friction law is highly non-linear in void fraction (α^7). That for instance, represented a difficulty for Icare-Cathare. The calculations crashed because reaching convergence during the initialization was not feasible. The source of the error leading to the crash was the divergence of the void fraction out of the possible range, in the early steps of the calculations.

3.3 Discussion and conclusions

The models of two-phase flow in porous media are able to represent the main features of the flows observed in the PEARL experiments. The heat extracted by water, the

rate of steam production, the quench front velocity (both in the main debris bed and in the by-pass) and the total quenching time are well predicted by the calculations in general. However, there is a difference on the behavior of water entrainment in the bypass in the 2D cases. The calculations predict a lower entrainment than what is observed experimentally. This results in a faster quench front velocity in the debris bed (because more water is available) and in a smaller mass of steam produced (because about 15% of the energy is extracted by steam superheat, whereas in the experiment this energy is converted into additional steam). Preliminary sensitivity tests on the interfacial friction correlation did not show a significant effect on the global behavior. Uncertainties and limitations were defined and described, then sensitivity calculations were performed to define the sources of such a discrepancy which was generally present in the tests performed at high initial temperatures and high water injection rate. In other words, comparing to the experimental results, some differences in the thermal hydraulic behavior were seen in the tests where the quench front progresses in 2D. Whereas in the 1D tests, the calculations showed better qualitative and quantitative consistency with the experiments. PEARL tests provided new experimental data about the reflooding of a severely damaged reactor core, numerical simulations of those test were presented and showed good agreement with the experiments. The damaged part of the core is represented by a bed of stainless steel spheres which are heated in order to simulate residual power generated by the decay of radioactive material in the reactor core. This debris bed is surrounded by an area representing a less damaged zone, such as remaining intact fuel assemblies. The scale of the experiment is approximately 1/8th of the reactor scale. One of the main results featured in PEARL is the effect of water entrainment which occurs under some conditions and affects the timing of quenching as well as the temperature of steam at the outlet. From the experimental data and the calculations, it appears that the upwards progression of entrained water into the bypass depends on a threshold value of the axial pressure gradient generated in the debris bed by the intense flow of steam. Below this threshold, the progression of the quench front is uniform across the section and the situation is 1D. Above this threshold, water submitted to a large pressure gradient is able to move at a faster velocity than the injection velocity, in the bypass region. This leads to an accumulation of water above the debris bed before its complete quenching. Quantitative values of the thresholds can be deduced from the PEARL tests. Considering the intermediate test PA1 (T=400°C, V=5m/h and P=1bar) at the median initial temperature and injection velocity, the entrainment of water in the bypass appears: if the temperature or the injection velocity is increased (PA2 and PA5 tests respectively), and it disappears if the temperature or the injection velocity is decreased (PA0 and PA4 tests respectively). The effect of pressure has been investigated. In the PA2 test (T=700°C, V=5m/h and P=1bar), the entrainment of water occurs and a curved

quench front propagation is observed. This phenomena is attenuated as the pressure is increased as it was shown in the tests P22 (P=2bar), P32 (P=3bar) and P51 (P=5bar). Above P=3bar, the progression of the quench front is one dimensional and homogeneous in the experimental and in the bypass. According to these results, the exact values of the thresholds could not be yet exactly identified (neither from the experimental data nor from the calculations) because it depends on several coupled parameters: the injection velocity, the maximum temperature in the debris bed, the pressure, and the aspect ratio of the bed and by-pass. But the existence of two different reflooding situations, the 1D and the 2D, is clear from the experiment and is confirmed by the calculations. This will be further investigated to formulate the criterion. Those are important parameters to evaluate the consequences of accident management by injection of water in the core. The 1D reflood is more efficient because all the water is devoted to cool down the debris whereas some of the water is diverted into the bypass and accumulated at the top of the bed for 2D reflood. However, the presence of water on top of the debris bed before complete quenching leads to decrease the temperature of steam above the bed which is a good point for the integrity of the top part of the vessel and of the hot leg of the primary circuit.

Chapter 4

An analytical model of flow redistribution in a two-layered porous medium with contrasting permeability

In this chapter, an analytical model is proposed to describe the bottom reflooding of a vertically stratified debris bed composed of two concentric cylindrical layers of contrasting thickness and permeability, the outer layer being more permeable. The proposed model and most of the results contained in this chapter were published and presented at the *International Symposium of Computational Heat and Mass Transfer. Napoli, 2017.* ([Swaidan 2017]).

Contents

4.1 Objectives

In the previous chapter, an investigation of PEARL experimental results and comparison against Icare-Cathare thermal hydraulics code calculations was presented. The physical models implemented in Icare-Cathare were verified and validated. For reactor scale configurations the calculations identified some non-coolable situations with small particles (few mm diameter) and high initial temperature (around 1500°C) where the quenching duration was extended to around 20 minutes while some zones of the debris were still uncovered and accumulating heat. Moreover, in order to obtain the results and describe the main features of each PEARL test, the calculations and post processing were time consuming and there was a need to perform sensitivity studies with a faster computation tool. This was the motivation to develop an analytical model to describe the reflooding process of such a system of debris layers with contrasting permeability. This physical situation involves a strong evaporation of water in the particulate bed, leading to high-velocity flow of steam. That has been investigated by several authors until recently ([Tutu 1984b], [Atkhen 2003], [Chikhi 2015b]).

The investigation is concerned in the two phase flow in a particle bed stratified vertically. It is a porous medium composed of two concentric cylindrical layers of contrasting thickness and permeability, the central one being less permeable and less porous. The analytical model is developed to predict the behavior of water in the lateral layer (bypass) of larger permeability and porosity representing the case of bottom reflooding of a hot debris bed surrounded by an intact zone in a degraded nuclear reactor core during an accidental scenario. The redistribution of water and steam into the bypass is investigated in several steps in order to evaluate the pressure gradient which can be generated downstream of the quench front. Considering a set of mass and energy balance equations, taken over frames of reference moving at the quench front velocity, allows estimating the water-to-steam conversion ratio and the quench front velocity. The velocity of water in the bypass, which is shown to be the unique solution of a system of two equations (mass conservation and momentum conservation) is then computed and consequently the flow rates of water and steam downstream. The results are then compared to PEARL bottom reflooding experimental tests ([Chikhi 2015b] and [Chikhi 2017]).

It is a simplified investigation to explore the behavior of water entrainment into a

bypass of larger permeability and porosity surrounding a central bed of debris. In the first approach the redistribution of a single phase flow into the more permeable bypass at the periphery will be investigated, simulations with Icare-Cathare will be presented and the derived analytical model will be compared against those calculations. This investigation of the steady-state steam flow aims to produce results upon which some assumptions considered in the investigation of the two-phase (water and steam) flow are based. In the second approach, the two-phase flow will be studied and the analytical two-phase flow redistribution model will be derived to describe the entrainment behavior of water into the bypass. This simplified analytical model will form a tool to perform fast calculations of two phase flow redistribution in such a system of porous layers with different thickness, porosity and permeability and assess the condition for water entrainment. It will also allow testing different correlations in the variations of the momentum equations for porous media such as relative permeability and passability correlations and interfacial friction laws.

4.2 Steam flow redistribution

4.2.1 Debris bed and flow system

The system under study is a two-layered debris bed of cylindrical geometry, it is composed of a central part with smaller particles surrounded by a lateral part (bypass) with larger particles and hence larger permeability.

Steam is injected into the hot debris bed system from the bottom. The steam temperature is set equal to that of the bed in such a way that the processes are isothermal; no heat exchange and no phase change would take place in this system. This ensures decoupling the heat exchanges effect from the investigated behavior. Steam is only injected into the central bed whereas the flow into the bypass is blocked by a compact non-porous zone in order to assess the redistribution behavior of the injected steam across the porous layers. The main reason behind this choice is to simulate only the production of steam in the central hot layer.

Figure 4.2 is a schematic representation of the debris beds system, the central bed has a radius R^c=0.225m whereas the more permeable bypass had a radial thickness of 0.045m making the total radius of the system R^{ext}=0.27m. The total height is typically H=0.5m. The geometry of the debris system adopts the configuration of the PEARL tests conducted at IRSN. The particles in the center have a fixed diameter d_p^c=4mm whereas the more permeable bypass was composed of particles of larger diameter, typically d_p^b=8mm when not mentioned. The steam is set to flow into the center since the aim of this study is to investigate the redistribution

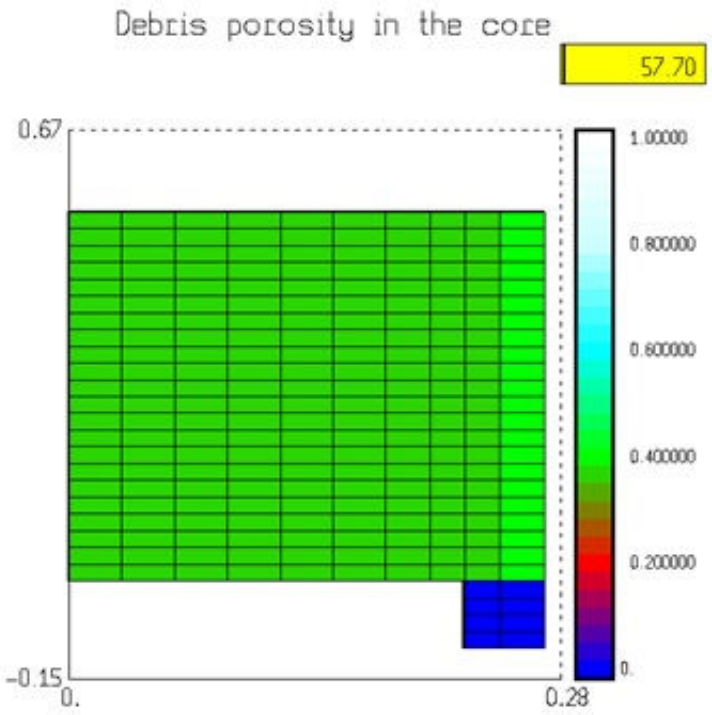

Figure 4.1: Schematic representation of the meshing and porosity in the code calculations - cylindrical geometry

of steam flow from the center to the more permeable bypass. Figure 4.1 represents the meshing of the debris bed system in the Icare-Cathare code calculations. It is meshed in cylindrical coordinates (10 radial meshes and 34 axial meshes with the debris bed containing 20 axial meshes of 25mm height providing a resolution up to 12.5mm, whereas the radial meshes vary between 20mm and 30mm). A blocked zone of reduced porosity is constructed below the bypass to block the flow and force it to enter only through the center. The pressure at the outlet downstream is set to 1bar and the temperature at the lateral boundaries is set equal to the bed temperature to dismiss any heat exchange with the surroundings.

4.2.2 Icare-Cathare calculations of flow redistribution

The radial redistribution occurs along the elevation up to a certain height at which the driving force of this flow diversion towards the bypass has significantly decreased. It corresponds to the elevation at which the radial steam flow rate into the bypass is almost null and the pressure in the center is approximately equal to that in the bypass. This height over which steam flow redistribution occurs is noted H_d (Figure

4.2).

$$\phi_g^{r\,c\to b}(z = H_d) \approx 0 \tag{4.1}$$

where $\phi_g^{r\,c\to b}(z)$ represents the integral steam flow rate redistributed radially, from the central layer to the bypass, up to an elevation z.

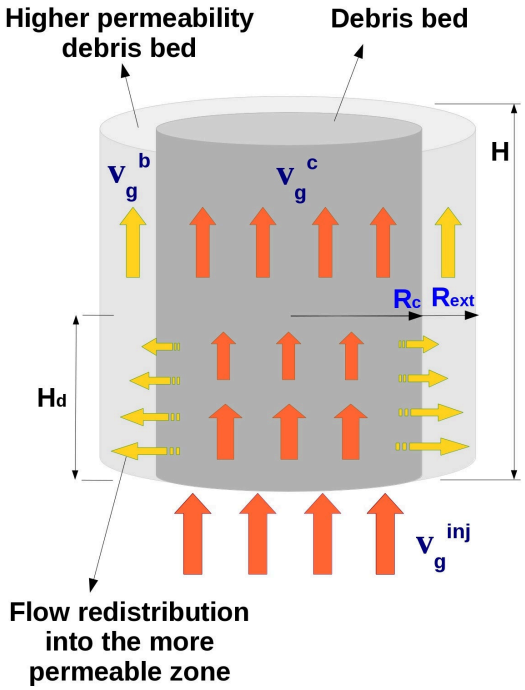

Figure 4.2: Flow redistribution in a debris bed system

4.2.2.1 Effect of injection velocity

The injection velocity of steam and respectively the flow rate is varied from 0.01 m/s to 3 m/s to assess its effect on the flow behavior conserving the same geometry of the debris system and its temperature. The elevation at which the bypass pressure $P_b = P(z, r = R^b)$ becomes approximately equal to that in the center $P_c = P(z, r = 0)$ corresponds to the height over which steam stops flowing radially from the center to the bypass. This is observed in Figure 4.3 which represent this pressure difference variation over the elevation, normalized by the pressure difference at the debris bed entrance which is the maximum for each case. A zoomed version this figure is found

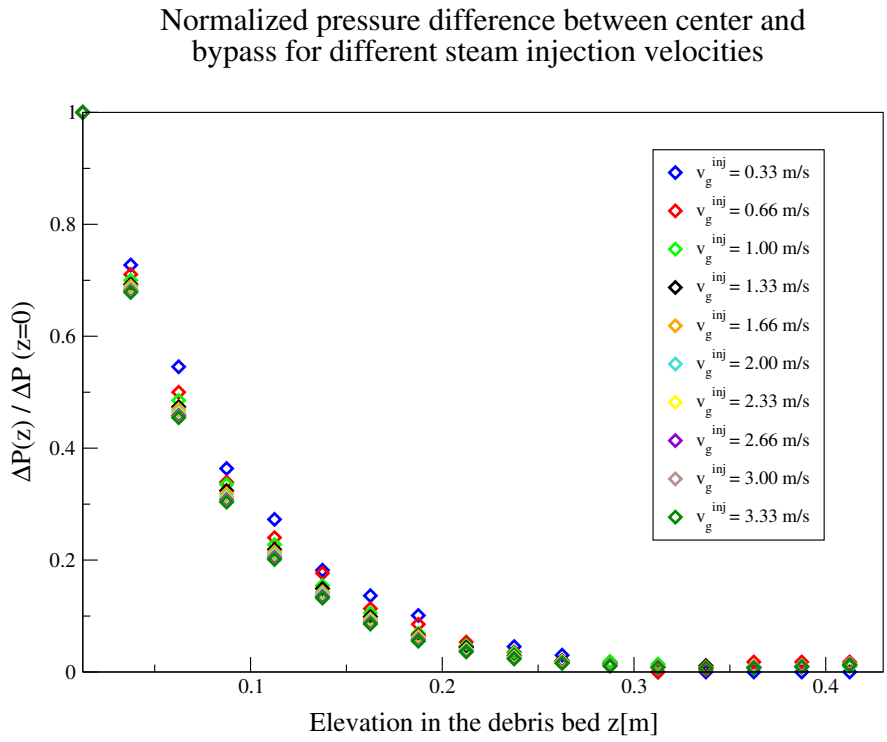

Figure 4.3: Normalized pressure difference as function of elevation for different injection velocities

in the appendix A.1.

$$R^b = \frac{R^{ext} + R^c}{2} \tag{4.2}$$

$$\Delta P(z) = P_c(z) - P_b(z) \tag{4.3}$$

However, as the flow redistribution is the major concern, the radial steam flow rate is more relevant than the radial pressure difference across the debris system. Figure 4.4 shows the distribution of this radial steam flow rate from the center into the bypass, normalized by the injected steam flow rate. The redistribution height H_d is almost constant in this case (considering a resolution of $1.25 \times 10^{-2} m$) for different steam injection flow rates. Figure 4.5 is a zoom-in version of Figure 4.4 showing the gradual decrease of the radial flow rate and the local minimum corresponding to height H_d. Beyond this point, approaching the bed top to exit of the porous medium, a negligible portion ($< 10^{-3}$) of the normalized flow rate is oppositely diverted to the center. This issue is purely numerical because of the existence of a discontinuity at the top of the debris bed. The porous bed is composed of two layers of different permeability where porous media laws apply, and right above it

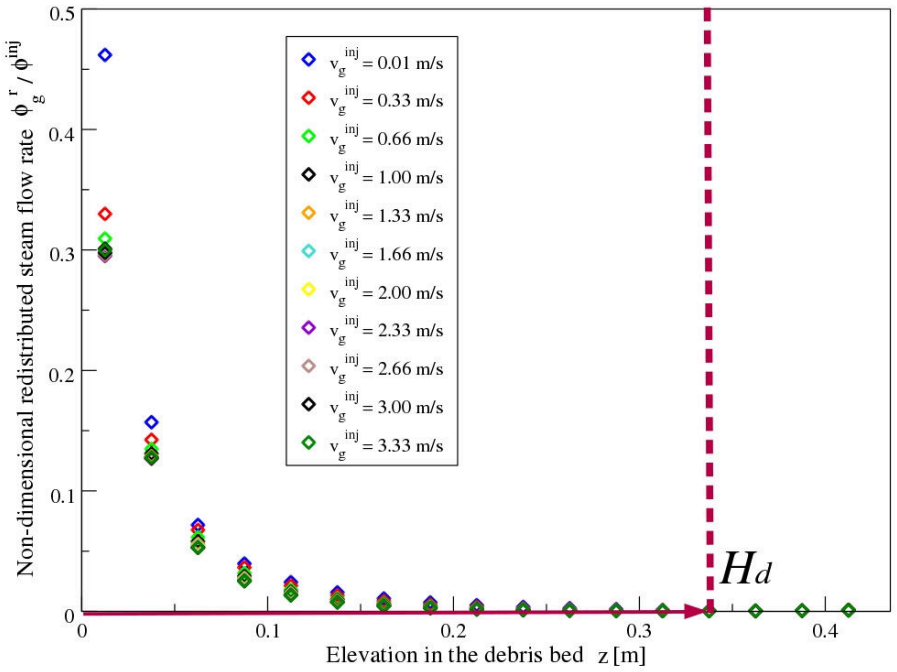

Figure 4.4: Non-dimensional redistributed steam flow rate as function of elevation for different injection velocities

there is an empty layer where the flow is described by Navier Stokes equations. This imposes a negligible diversion of steam flow back to the center just below the bed top.

The steam radial flow rate redistributed into the bypass is also calculated for different injection velocities and total heights H of the debris beds system, the graphical results show that the redistribution height H_d changes when the bed height H changes yet it varies slightly when varying the injection flow rate in each case as shown in Fig. 4.4, Fig.4.6 and Fig.4.8. In the case of a debris bed system with height H=0.5m the redistribution height was $H_d \approx$0.33m.

Figure 4.10 represents the variation of the pressure difference between the central debris bed and the bypass as function of steam injection rate. It has a parabolic shape and the correlation rather follows a 2nd order polynomial with a very strong regression ($R^2 \approx 1$).

This suggests that the contrasting-permeability two-layered homogeneous

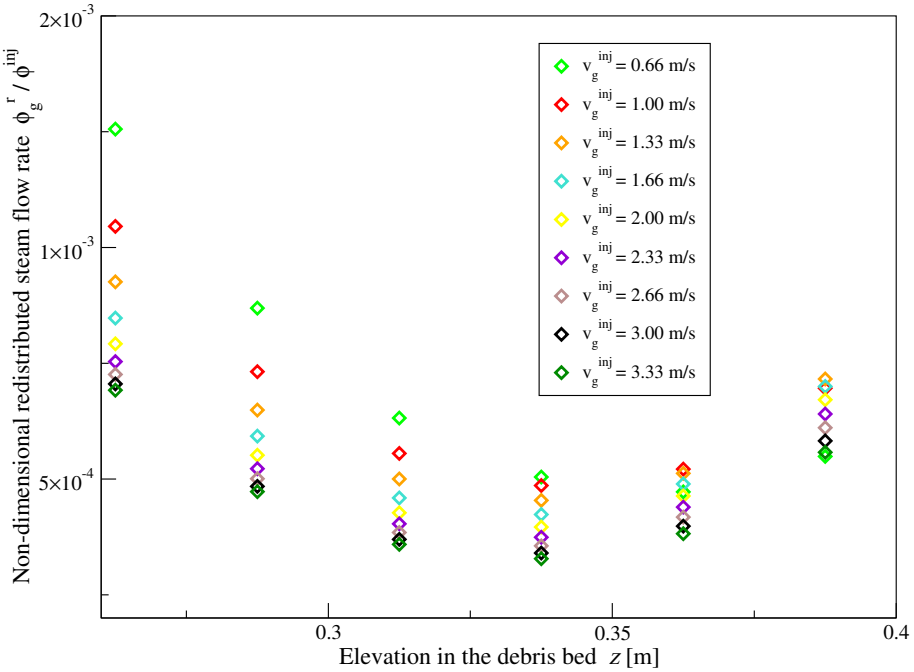

Figure 4.5: Non-dimensional redistributed steam flow rate as function of elevation for different injection velocities (zoom-in)

porous medium is acting as a single-layered porous medium possessing an equivalent permeability and equivalent passability.

The radial pressure drop equations are quadratic in velocity and have the parabolic form:

$$\triangle P = A(v_g^{inj})^2 + Bv_g^{inj} + \varepsilon \tag{4.4}$$

where ε is a negligible compared to the other terms. This finding is analogous to the results presented in Lake and Hirasaki [Lake 1981] on dispersion in a two and multi-layered porous medium where under certain conditions the medium behaves as if it were single-layered.

Other sets of Icare-Cathare single-phase flow calculations were done to investigate the effect of the system temperature and the passability contrast between central and lateral bed on the redistribution of injected steam into the bypass. The flow redistribution occurs quickly (few seconds in those cases) and the system reaches

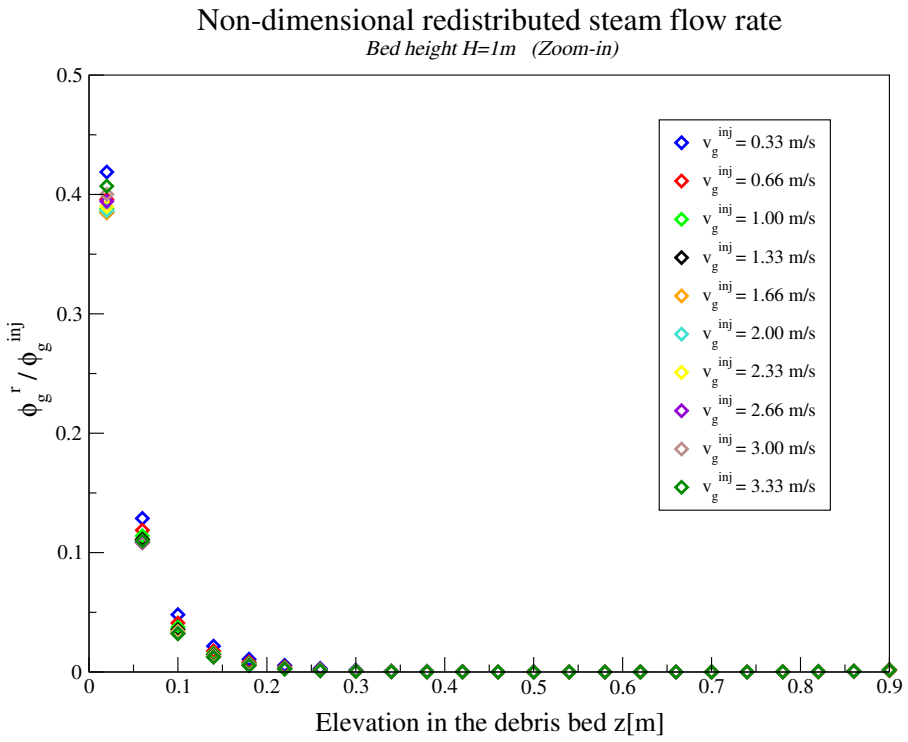

Figure 4.6: Non-dimensional redistributed steam flow rate as function of elevation for different injection velocities, H=1m

a steady state. The outcomes of those calculations are presented and discussed separately in the following paragraphs.

4.2.2.2 Contrast in passability between the central and lateral beds

In each case the passability of the lateral bed (bypass) is changed by varying the particles diameter while keeping it fixed in the central bed. This will also change the permeability contrast which depends on the particles diameter as well. The results presented in Figure 4.11 show that the redistribution height is almost independent of the passability contrast among the central and lateral layer of the debris bed provided the bypass is more permeable than the center. On the other hand, when the center is more permeable, H_d has increased. This was expected as the flow is then less driven towards the less permeable bypass.

Figure 4.11 represents the radial flow rate of redistributed steam as function of center-to-bypass passability ratios which are directly linked to the particles diameter by:

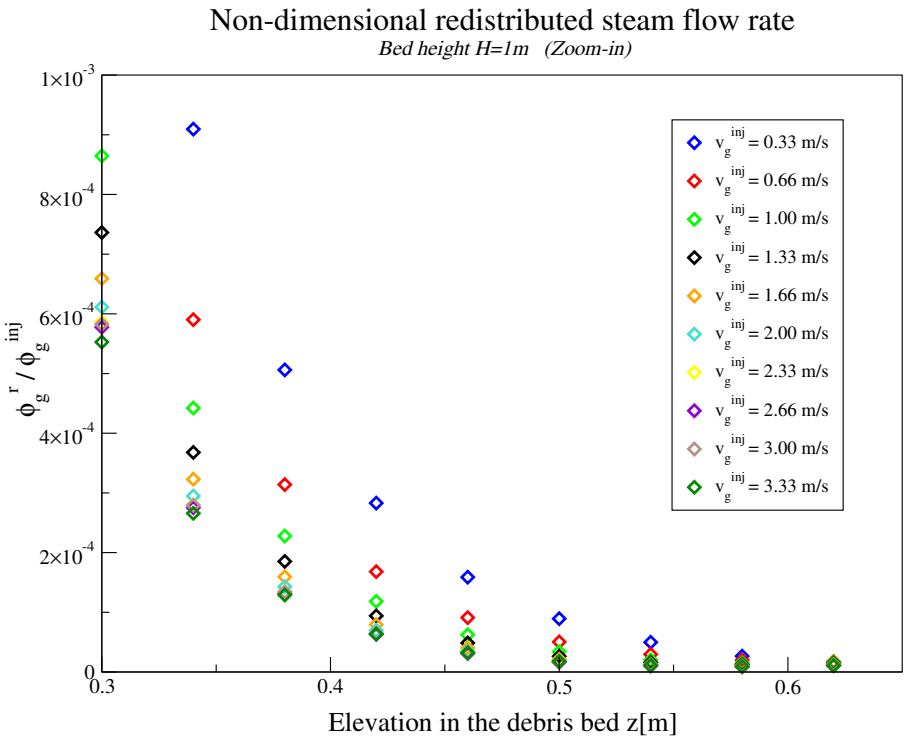

Figure 4.7: Non-dimensional redistributed steam flow rate as function of elevation for different injection velocities, H=1m (zoom-in)

$$\eta^q = \frac{d_p^q \, \varepsilon^{q3}}{1.75(1-\varepsilon^q)} \tag{4.5}$$

where the subscript q refers to the medium (c for center, b for bypass) ε^q is the porosity of the medium q.

4.2.2.3 Conclusion

To finish the sensitivity studies, the effect of the temperature of the injected steam and debris bed system on H_d, the height of flow redistribution into the bypass, was investigated. Calculations at different temperatures ranging between 200°C and 800°C were performed. The steam injection temperature was fixed equal to the debris temperature in each case to avoid pressure variations due heat redistribution as the steam flows through the beds. It is observed as shown in Figure 4.12 that H_d varies slightly if the temperature is changed.

That concludes that when varying one of the initial or boundary condition: tem-

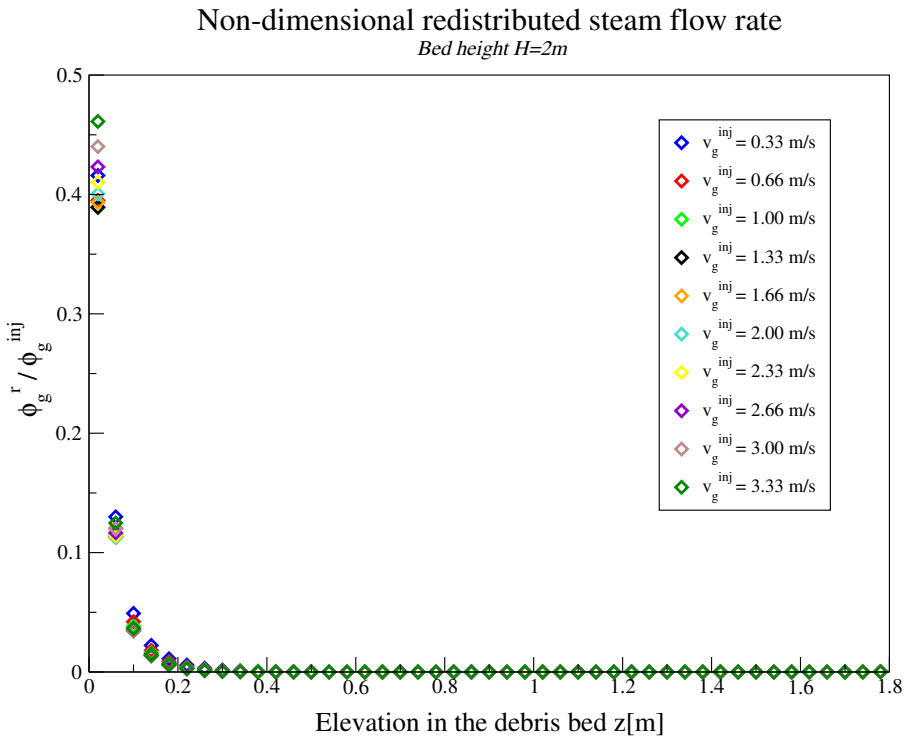

Figure 4.8: Non-dimensional redistributed steam flow rate as function of elevation for different injection velocities, H=2m

perature, pressure, injection rate, or contrast in the permeability among the debris layers, there exists a length up to which the flow redistribution occurs from the central layer to the more permeable lateral layer. This length H_d is almost constant when varying one of those conditions whereas it is rather dependent on the geometry of the system. It is also important to notice that:

the radial redistribution occurs mainly in the first two thirds of H_d where the already redistributed flow rate into the bypass is almost equal to the total redistribution.

This can be formulated as:

$$\int_{z=0}^{z=2/3H_d} \phi_g^{r\,cb}(z)dz \;>\; 0.95 \;\times\; \int_{z=0}^{H_d} \phi_g^{r\,cb}(z)dz \tag{4.6}$$

4.2.3 Analytical model of redistribution into the bypass

The single phase steam flow in the debris bed and its redistribution into the more permeable zone is modeled in a simple procedure explained in what follows. Firstly,

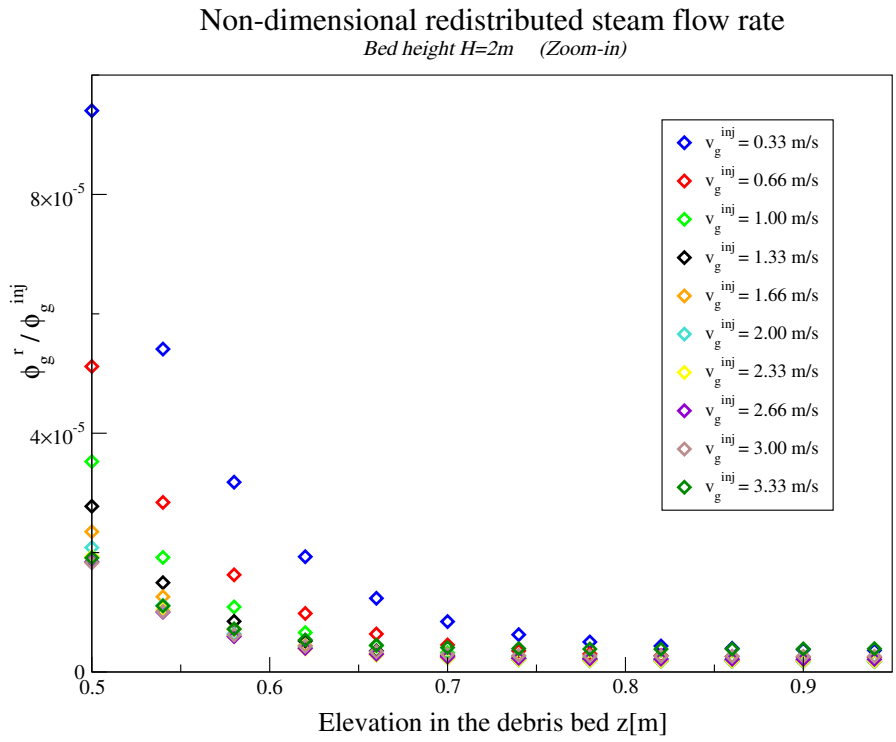

Figure 4.9: Non-dimensional redistributed steam flow rate as function of elevation for different injection velocities, H=2m (zoom-in)

mass balance equation is written between two levels z_0 at injection and z_1=H_d as shown in Figure 4.2. Recalling that steam is only injected into the central bed, the mass balance of this single phase steady state flow writes:

$$\varepsilon^o \rho_g v_g^{inj} S^c = \varepsilon^c \rho_g v_g^c S^c + \varepsilon^b \rho_g v_g^b S^b \tag{4.7}$$

where ε^o is the porosity at the entrance below the debris bed, v_g^{inj} is the steam injection velocity, (ε^c, S^c, v_g^c) and (ε^b, S^b, v_g^b) are respectively the porosity, cross-section and steam velocities exiting the center and the bypass at $z_1 = H_d$.

Defining the porosity-cross-section contrast of the bypass and the central bed by the parameter:

$$\xi = \frac{\varepsilon^b S^b}{\varepsilon^c S^c} = \frac{1}{F_\varepsilon F_S} \tag{4.8}$$

where

$$F_\varepsilon = \frac{\varepsilon^c}{\varepsilon^b} \qquad (porosity\ contrast) \tag{4.9}$$

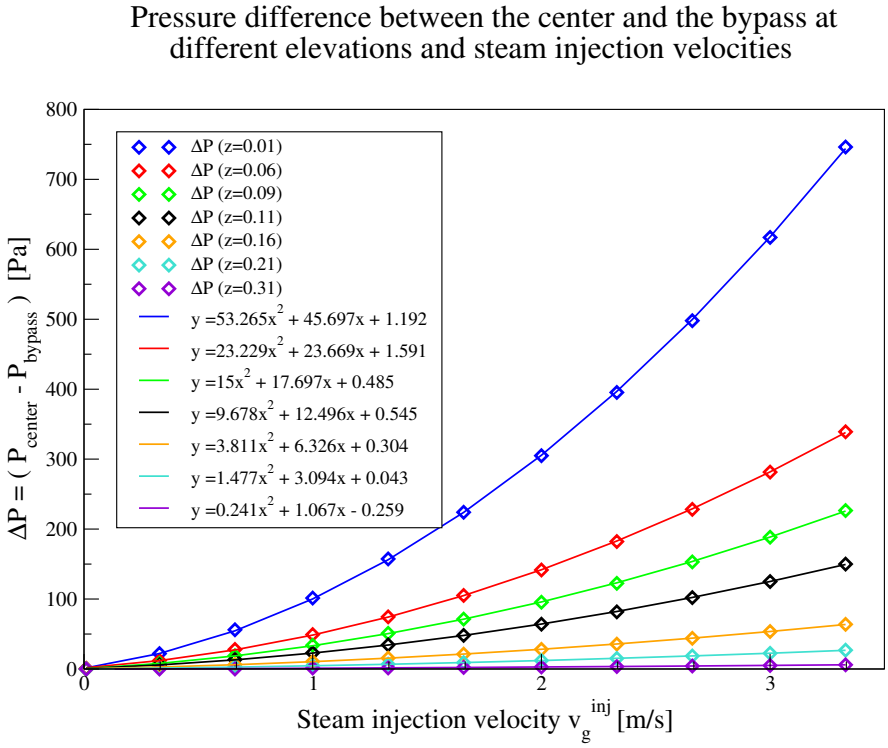

Figure 4.10: Pressure difference between the center and the bypass at different elevations for different injection velocities

and

$$F_S = \frac{S^c}{S^b} \qquad (cross - section\ contrast) \tag{4.10}$$

This allows writing v_g^c in Eq. 4.7 as a function of v_g^b, v_g^{inj} and ξ in the following form:

$$v_g^c = -v_g^b \xi + v_g^{inj} \frac{\varepsilon^o}{\varepsilon^c} \tag{4.11}$$

The Darcy-Forchheimer equation for this single phase steam flow in porous media is written as:

$$-\frac{dP_g}{dz} = \rho_g g + \frac{\mu_g}{\kappa} U_g + \frac{\rho_g}{\eta} U_g^2 \tag{4.12}$$

We consider the approximate equality of pressure in radial direction above the redistribution level H_d, an assumption that has been confirmed by the Icare-Cathare calculations presented above (see Fig. 4.3). So we may assume the pressure equality above that level and this allows writing the relation:

$$\frac{dP_g^c}{dz} \approx \frac{dP_g^b}{dz} \tag{4.13}$$

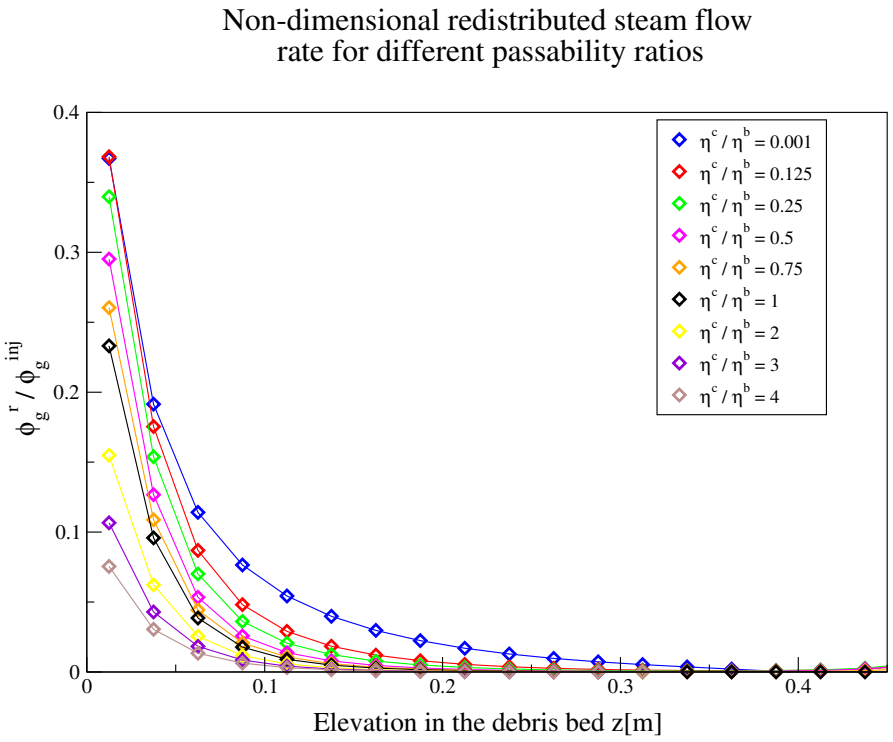

Figure 4.11: Non-dimensional redistributed steam flow rate as function of elevation for different center-to-bypass passability ratios

expanding it using Eq. 4.12:

$$\rho_g g + \frac{\mu_g}{\kappa^c} U_g^c + \frac{\rho_g}{\eta^c} (U_g^c)^2 = \rho_g g + \frac{\mu_g}{\kappa^b} U_g^b + \frac{\rho_g}{\eta^b} (U_g^b)^2 \tag{4.14}$$

Eq. 4.14 renders a quadratic equation relating v_g^c and v_g^b. Substituting for v_g^c using Eq. 4.11, it reduces to a quadratic equation in v_g^b of the form:

$$(v_g^b)^2 + r\, v_g^b + s = 0 \tag{4.15}$$

This formulation allows calculating the steam velocity in the center v_g^c and the bypass v_g^b for a given steam injection flow rate and respective sizes of the central and lateral debris beds. The solution of Eq. 4.15 has the form:

$$v_g^b = +\frac{1}{2} r \;\pm\; \frac{1}{2} \sqrt{r^2 - 4\, s} \tag{4.16}$$

then substituting for v_g^b in Eq. 4.11 allows calculating v_g^c:

$$v_g^c = -\frac{1}{2} \xi\, r \;\pm\; \frac{1}{2} \xi \sqrt{r^2 - 4\, s} + v_g^{inj} \frac{\varepsilon^o}{\varepsilon^c} \tag{4.17}$$

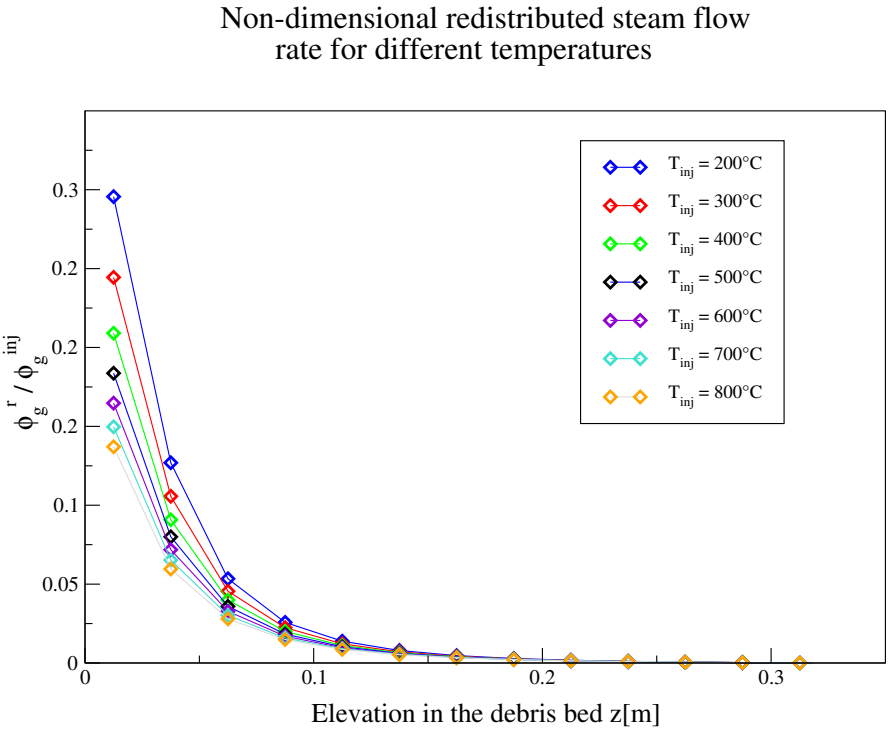

Figure 4.12: Non-dimensional steam flow rate redistributed into the bypass as function of elevation for different temperatures

where

$$r = \frac{2\xi v_0 + v_1\xi + v_1 F_\kappa}{\xi^2 - F_\eta} \qquad and \qquad s = \frac{v_0^2 + v_1 v_0}{\xi^2 - F_\eta} \tag{4.18}$$

with

$$F_\eta = \frac{\eta^c}{\eta^b} \qquad (passability\ contrast) \tag{4.19}$$

$$F_\kappa = \frac{\kappa^c}{\kappa^b} \qquad (permeability\ contrast) \tag{4.20}$$

$$v_0 = v_g^{inj}\frac{\varepsilon^o}{\varepsilon^c} \qquad and \qquad v_1 = \frac{\mu_g \eta^c}{\rho_g \kappa^c} \tag{4.21}$$

In the considered study:

$$\begin{aligned} &\varepsilon^o = 1 && (empty\ zone) \\ &F_\varepsilon = 1 && (\varepsilon^c = \varepsilon^b = \varepsilon,\ \ same\ porosity) \end{aligned} \tag{4.22}$$

The modeled steam velocities in the center and the bypass are compared against the

Icare-Cathare single phase flow calculations and presented in Fig. 4.13 which represents the ratios of the center and bypass velocities to the injection velocity v_g^c/v_g^{inj} and v_g^b/v_g^{inj} as function of the injection velocity. At high steam injection velocities, the quadratic term in the pressure drop equation Eq. 4.12 becomes dominant and it can be then transformed into:

$$-\frac{dP_g}{dz} = \rho_g g + \frac{\rho_g}{\eta} U_g^2 \tag{4.23}$$

In this case, the steam velocities in the center and the bypass are simply related by:

$$U_g^c = U_g^b \sqrt{F_\eta} \tag{4.24}$$

Following the similar procedure in derivation, the absolute velocities are determined to be:

$$v_g^b = \frac{v_g^{inj}}{\sqrt{F_\eta} + \frac{S^b}{S^c}} \tag{4.25}$$

$$v_g^c = \frac{v_g^{inj}\sqrt{F_\eta}}{\sqrt{F_\eta} + \frac{S^b}{S^c}} \tag{4.26}$$

Therefore, at high injection velocities the asymptotic for the velocity ratios v_g^c/v_g^{inj} and v_g^b/v_g^{inj} are given by:

$$\frac{v_g^b}{v_g^{inj}} = \frac{1}{\sqrt{F_\eta} + \frac{S^b}{S^c}} \tag{4.27}$$

$$\frac{v_g^c}{v_g^{inj}} = \frac{\sqrt{F_\eta}}{\sqrt{F_\eta} + \frac{S^b}{S^c}} \tag{4.28}$$

they are shown in Fig. 4.13.

Moreover, the model can be used to study the sensitivity of the flow redistribution to many factors. For instance, varying the particles diameter in the bypass will change the passability and permeability contrast between the central and lateral beds. Fig. 4.14 represents the modeled velocities ratios to the injection velocity as function of the center-to-bypass passability ratio (η^c/η^b).

The model provided very good qualitative and quantitative results in comparison with the code calculations. The slight deviations from the code calculations which appear more in the bypass velocity curves are due to assuming a constant steam density in the model in radial direction whereas in the code the density is recalculated according to the local pressure state of each mesh.

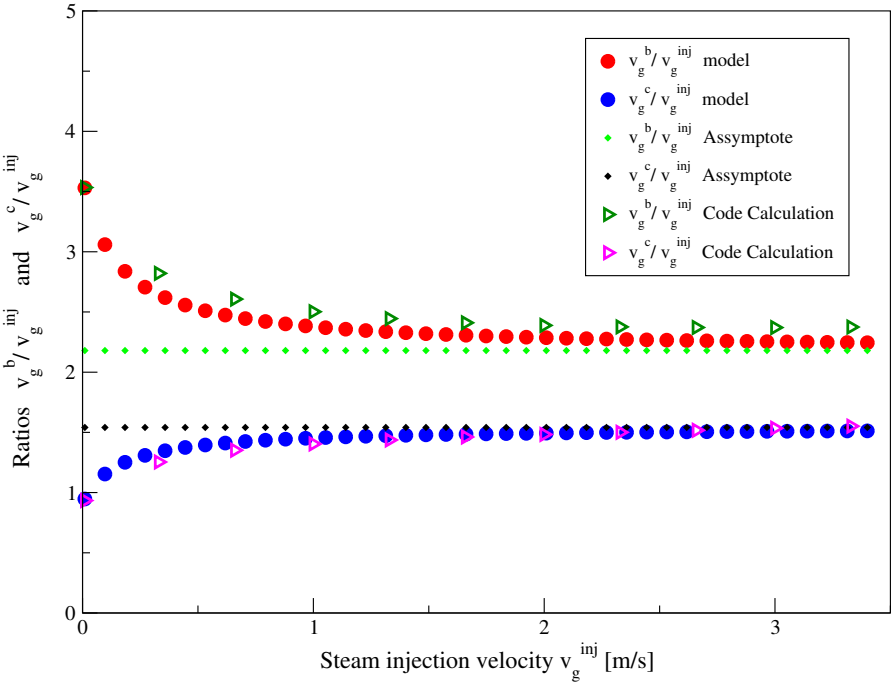

Figure 4.13: Center and bypass steam velocity ratios to injection velocity as function of v_g^{inj}

4.3 Two phase flow with phase change: redistribution

4.3.1 System description

Having investigated the redistribution of the single phase steam flow into the more permeable zone (bypass) in the debris bed system, the two phase flow redistribution in porous media is to be studied. The debris bed system has the same geometry considered in the previous section, based on the PEARL experiment setup (described in Chapter 3 and in [Chikhi 2015b]).

4.3.2 Inlet flow rate

The development of the analytical model starts by writing the mass and energy balance equation for the fluid and the solid particles, in a frame of reference moving at the quench front velocity v^{qf}, between the elevations $(z_0,\ z_1)$ and $(z_1,\ z_2)$. z_0 is

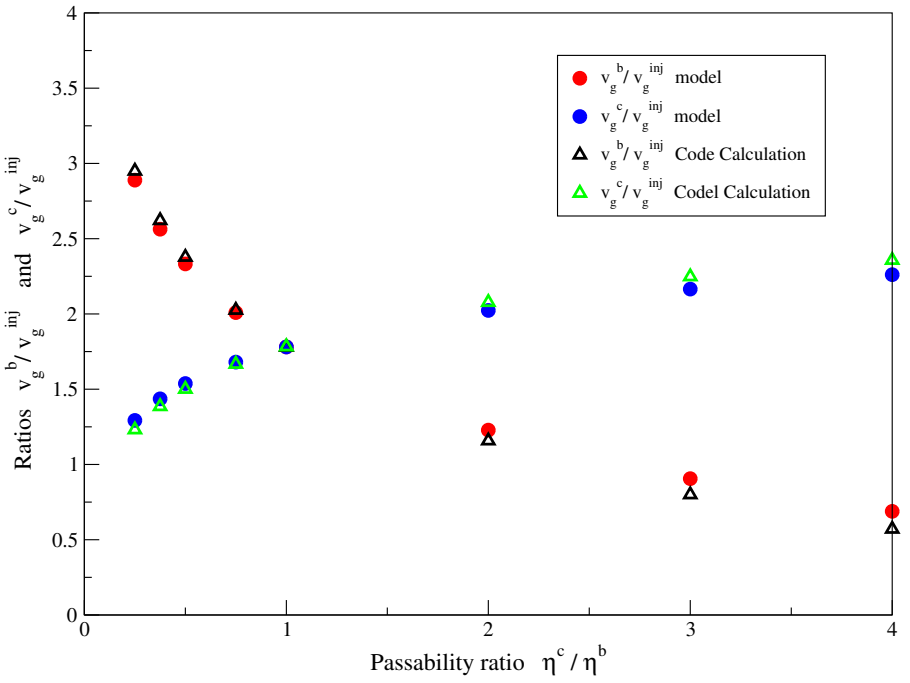

Figure 4.14: Center and bypass steam velocities ratios to injection velocity as function of the passability ratio $\frac{\eta^c}{\eta^b}$

at the debris bed inlet level, z_1 is right below the quench front level, and z_2 is the end of the two phase zone as shown in Figure 4.15.

First, water is injected into the system from bottom and it advances upwards. Below the quench front level, $z = z_1$, the flow is purely liquid and, for a given elevation, the pressure in the center is approximately equal to that in the bypass. This assumption was also demonstrated by Icare-Cathare calculations. So we can write:

$$\frac{\partial {P_l}^c}{\partial z}(z_1) \approx \frac{\partial {P_l}^b}{\partial z}(z_1) \tag{4.29}$$

The Reynolds number for this flow in the central porous layer is defined as:

$$Re_l^c = \frac{\rho_l v_l^{inj} d_p^c}{\mu_l (1-\varepsilon^c)} \tag{4.30}$$

For an injection velocity v_l^{inj}=1.388x10^{-3} m/s, Re^c=24.3, d_p^c=4mm and ε^c=0.4, whereas for the bypass zone Re^b=48.6, with d_p^b=8mm and ε^b=0.4. Hence, the inertial

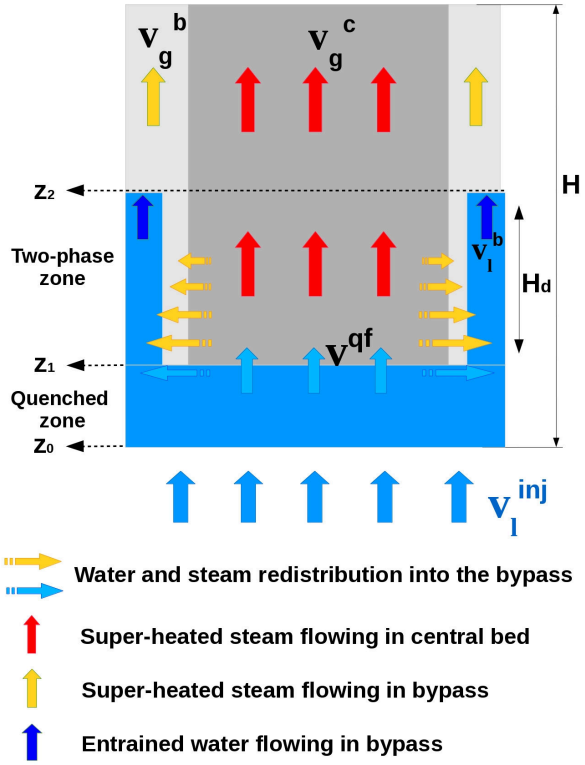

Figure 4.15: Two phase flow redistribution

terms should be included. Eq. 4.29 is thus expanded using the single-phase Darcy-Forchheimer equation:

$$-\rho_l g - \frac{\mu_l}{\kappa^c} U_l^{cin} - \frac{\rho_l}{\eta^c}(U_l^{cin})^2 = -\rho_l g - \frac{\mu_l}{\kappa^b} U_l^{bin} - \frac{\rho_l}{\eta^b}(U_l^{bin})^2 \tag{4.31}$$

thus arriving at a quadratic equation relating the inlet velocity in the center U_l^{cin} to that in the bypass U_l^{bin}.

On the other hand, writing the mass balance equation between the injection level and this level, we obtain:

$$\varepsilon^c S^c \rho_l v_l^{cin} + \varepsilon^b S^b \rho_l v_l^{bin} = \varepsilon^0 (S^b + S^c) \rho_l v_l^{inj} \tag{4.32}$$

with

$$U_l^{cin} = \varepsilon^c v_l^{cin} \qquad and \qquad U_l^{bin} = \varepsilon^b v_l^{bin} \tag{4.33}$$

Substituting Eq. 4.32 into the quadratic Eq. 4.31, we can then explicitly relate each of $v_l^{b\,in}$ and $v_l^{c\,in}$ to the injection velocity v_l^{inj}.

4.3.3 Quench front velocity

The quasi-steady propagation of the quench front is assumed upon the observations made in the PEARL experiments where the quench front velocity was quasi-constant as well as the steam production rate ([Chikhi 2015b], [Chikhi 2017]). However, some other dynamic processes occur quickly in the beds and they are regarded as transient effects corresponding to: 1- the arrival of the quench front at the bottom superheated debris bed and 2- its exit at the top of the debris bed at the last phase of the quenching process. The quasi-constant steam production rate during reflooding a superheated debris bed was also observed by [Tutu 1984b] and [Tung 1983].

Proceeding by writing the mass balance equation for the fluid between elevations z_1 and z_2 in a relative frame of reference moving at the quench front velocity v^{qf}:

$$\begin{aligned}&\alpha_1^c\varepsilon^c S^c\rho_{g1}(v_{g1}^c - v^{qf}) + (1-\alpha_1^c)\varepsilon^c S^c\rho_l(v_{l1}^c - v^{qf}) + (1-\alpha_1^b)\varepsilon^b S^b\rho_l(v_{l1}^b - v^{qf})\\ &= \alpha_2^c\varepsilon^c S^c\rho_{g2}(v_{g2}^c - v^{qf}) + \alpha_2^b\varepsilon^b S^b\rho_g(v_{g2}^b - v^{qf}) + (1-\alpha_2^b)\varepsilon^b S^b\rho_l(v_{l2}^b - v^{qf})\end{aligned} \tag{4.34}$$

in which the subscripts 1 and 2 refer to the elevations z_1 and z_2 respectively. With α_2^c=1 (exiting as pure steam from the center), and α_1^b=α_1^c=0 (at the quench front level, only liquid is entering into the bypass from the bottom, and no boiling below the quenched level in the center). The mass balance can be then written as:

$$\begin{aligned}&\varepsilon^c S^c\rho_l(v_{l1}^c - v^{qf}) + (1-\alpha_1^b)\varepsilon^b S^b\rho_l(v_{l1}^b - v^{qf})\\ &= \varepsilon^c S^c\rho_{g2}(v_{g2}^c - v^{qf}) + \alpha_2^b\varepsilon^b S^b\rho_g(v_{g2}^b - v^{qf}) + (1-\alpha_2^b)\varepsilon^b S^b\rho_l(v_{l2}^b - v^{qf})\end{aligned} \tag{4.35}$$

The steam redistributed from the center into the bypass progresses in the bypass and exits at its outlet together with the entrained water. The steam saturation in the bypass is α^b and the liquid saturation is its complementary (1-α^b). Writing the mass balance equation over a control volume in the bypass between the quench front level z_1 and the top of the redistribution level z_2. Over a relative frame moving with the quench front velocity v^{qf}, it gives:

$$\sum \phi_{in} = \sum \phi_{out} \tag{4.36}$$

$$\phi_l^{b\,in} + \phi_g^{cb} = \phi_l^b + \phi_g^b \tag{4.37}$$

Assuming that the redistributed steam from the center into the bypass above the quench front is flowing out of the bypass, we can set it equal to the flow rate exiting from the bypass at z_2

$$\phi_g^{cb} = \phi_g^b \tag{4.38}$$

we can then relate the water flow rates in the bypass at z_1 and z_2, in a reference frame moving with v^{qf}. Thus we can write:

$$\varepsilon^b S^b \rho_l (v_{l1}^b - v^{qf}) = (1 - \alpha_2^b)\varepsilon^b S^b \rho_l (v_{l2}^b - v^{qf}) \tag{4.39}$$

Hence, Eq. 4.35 reduces to:

$$\varepsilon^c S^c \rho_l (v_{l1}^c - v^{qf}) = \varepsilon^c S^c \rho_{g2} (v_{g2}^c - v^{qf}) + \alpha_2^b \varepsilon^b S^b \rho_{g2} (v_{g2}^b - v^{qf}) \tag{4.40}$$

Following that, writing the energy balance equation between elevations z_1 and z_2 in a frame of reference moving at the quench front velocity v^{qf}, with the saturation temperature T_{sat} as a reference temperature:

$$\begin{aligned}
&\varepsilon^c S^c \rho_l (v_{l1}^c - v^{qf}) h_l^{sat} = (1 - \varepsilon^c) S^c \rho_s (v_{s2}^c - v^{qf}) c_{ps} \Delta T_s^c + (1 - \varepsilon^b) S^b \rho_s (v_{s2}^b - v^{qf}) c_{ps} \Delta T_s^b \\
&+ \varepsilon^c S^c \rho_{g2} (v_{g2}^c - v^{qf})(h_{g2}^{sat} + c_{pg2} \Delta T_g^c) + \alpha_2^b \varepsilon^b S^b \rho_{g2} (v_{g2}^b - v^{qf})(h_{g2}^{sat} + c_{pg2} \Delta T_g^b)
\end{aligned} \tag{4.41}$$

with $v_{s2}^b = v_{s2}^c = 0$ (fixed solid), and assuming that the superheated steam exits at the same temperature from the center and the bypass ($\Delta T_g^c = \Delta T_g^b = \Delta T_g$). Eq. 4.41 can be reformed and written as:

$$\begin{aligned}
&[\varepsilon^c S^c \rho_{g2} (v_{g2}^c - v^{qf}) + \alpha_2^b \varepsilon^b S^b \rho_{g2} (v_{g2}^b - v^{qf})](h_g^{sat} + c_{pg2} \Delta T_g) \\
&= \varepsilon^c S^c \rho_l (v_{l1}^c - v^{qf}) h_l^{sat} + (1 - \varepsilon^c) S^c \rho_s v^{qf} c_{ps} \Delta T_s^c + (1 - \varepsilon^b) S^b \rho_s v^{qf} c_{ps} \Delta T_s^b
\end{aligned} \tag{4.42}$$

Substituting Eq. 4.40 into Eq. 4.42 to eliminate the terms referring to elevation z_2:

$$\begin{aligned}
&(h_g^{sat} + c_{pg2} \Delta T_g)[\varepsilon^c S^c \rho_l (v_{l1}^c - v^{qf})] = \varepsilon^c S^c \rho_l (v_{l1}^c - v^{qf}) h_l^{sat} + \\
&+ v^{qf} \rho_s c_{ps} [(1 - \varepsilon^c) S^c \Delta T_s^c + (1 - \varepsilon^b) S^b \Delta T_s^b]
\end{aligned} \tag{4.43}$$

then regrouping the terms associated to v^{qf}, we get:

$$\begin{aligned} &v^{qf}\{\varepsilon^c S^c \rho_l(\Delta h^{sat} + c_{pg2}\Delta T_g) + \rho_s c_{ps}[(1-\varepsilon^c)S^c \Delta T_s^c + (1-\varepsilon^b)S^b \Delta T_s^b]\} \\ &= \varepsilon^c S^c \rho_l v_{l1}^c (\Delta h^{sat} + c_{pg2}\Delta T_g) \end{aligned} \tag{4.44}$$

Then Eq. 4.44 defining the quench front velocity can be written as:

$$\boxed{v^{qf} = \frac{F}{E} = \frac{F_1}{E_1 + E_2}} \tag{4.45}$$

in which the terms F [J/s] and E [J/m] are given by:

$$F_1 = \varepsilon^c S^c \rho_l v_{l1}^c (\Delta h^{sat} + c_{pg2}\Delta T_g) \tag{4.46}$$

and

$$\begin{aligned} E_1 &= \rho_s c_{ps}[(1-\varepsilon^c)S^c \Delta T_s^c + (1-\varepsilon^b)S^b \Delta T_s^b] \\ E_2 &= \varepsilon^c S^c \rho_l (\Delta h^{sat} + c_{pg2}\Delta T_g) \end{aligned} \tag{4.47}$$

For the reactor case, the temperature difference between the formed debris bed in the center and the surrounding intact zone is not usually high. However, in the general case and in some PEARL tests where the temperature difference between the center and the bypass is significant ($\Delta T_g^c \neq \Delta T_g^b$), the considered assumption of temperature equality doesn't hold and a similar derivation is done. In this case, the quench front velocity v^{qf} is defined as:

$$\boxed{v^{qf} = \frac{A}{B} = \frac{A_1 + A_2 + A_3}{B_1 + B_2 + B_3 + B_4}} \tag{4.48}$$

in which the terms A [J/s] and B [J/m] are given by:

$$\begin{aligned} A_1 &= \varepsilon^c S^c \rho_{g2}^c c_{pg2}^c v_{g2}^c \Delta T_g^c \\ A_2 &= \alpha_2^b \varepsilon^b S^b \rho_{g2}^b c_{pg2}^b v_{g2}^b \Delta T_g^b \\ A_3 &= \varepsilon^c S^c \rho_l v_{l1}^c \Delta h^{sat} \end{aligned} \tag{4.49}$$

and

$$\begin{aligned} B_1 &= \rho_s c_{ps}[(1-\varepsilon^c)S^c\Delta T_s^c + (1-\varepsilon^b)S^b\Delta T_s^b] \\ B_2 &= \varepsilon^c S^c \rho_{g2}^c c_{pg2}^c \Delta T_g^c \\ B_3 &= \alpha_2^b \varepsilon^b S^b \rho_{g2}^b c_{pg2}^b \Delta T_g^b \\ B_4 &= \varepsilon^c S^c \rho_l \Delta h^{sat} \end{aligned} \tag{4.50}$$

4.3.4 Water to steam conversion rate

During reflooding, the injected water evaporates and steam is produced and collected downstream the debris bed. In the analysis of reflooding a homogeneous superheated debris bed, ([Tutu 1984b]) and ([Tung 1983]) had proposed a formulation of the water-to-steam conversion rate. [Chikhi 2015b] have later proposed an updated formulation taking into account two specific features of the PEARL experiment which are relevant to the formed debris bed in a damaged reactor core. Following a similar approach, this model is developed to take into account the presence of a lateral layer (bypass) of larger permeability surrounding the central debris bed.

The ratio of the steam production rate to the water injection rate is called the water-to-steam conversion rate γ_{cr}. It is regarded as a measure of the efficiency of reflooding and defined by:

$$\gamma_{cr} = \frac{\phi_g^{out}}{\phi_l^{inj}} \tag{4.51}$$

Having estimated the quench front velocity v^{qf}, we attempt to derive a formulation for the water-to-steam conversion ratio which relates the mass flow rate of steam produced at the outlet to the injected water flow rate by Eq. 4.51 where:

$$\phi_g^{out} = \varepsilon^c S^c \rho_g v_{g2} + \alpha_2^b \varepsilon^b S^b \rho_g v_{g2}^b \tag{4.52}$$

is determined using Eq. 4.40 which can be written as:

$$\varepsilon^c S^c \rho_g v_{g2}^c + \alpha_2^b \varepsilon^b S^b \rho_g v_{g2}^b = \varepsilon^c S^c \rho_l (v_{l1}^c - v^{qf}) + (\varepsilon^c S^c \rho_g + \alpha_2^b \varepsilon^b S^b \rho_g) v^{qf} \tag{4.53}$$

Regrouping the terms associated to v^{qf}, we obtain:

$$\phi_g^{out} = \varepsilon^c S^c \rho_l v_{l1}^c - v^{qf}[\varepsilon^c S^c \rho_l - (\varepsilon^c S^c \rho_g + \alpha_2^b \varepsilon^b S^b \rho_g)] \tag{4.54}$$

For the fluid at the bottom (between z_0 and z_1), writing the mass balance equation gives:

$$\varepsilon^c S^c \rho_l v_{l1}^c + \varepsilon^b S^b \rho_l v_{l1}^b = \rho_l (S^b + S^c) v_l^{inj} = \phi_l^{inj} \tag{4.55}$$

it can be written as:

$$\varepsilon^c S^c \rho_l v_{l1}^c = \phi_l^{inj} - \varepsilon^b S^b \rho_l v_{l1}^b \tag{4.56}$$

substituting it into Eq. 4.54, renders the equation with the injection velocity term appearing:

$$\phi_g^{out} = \phi_l^{inj} - \varepsilon^b S^b \rho_l v_{l1}^b - v^{qf} [\varepsilon^c S^c \rho_l - (\varepsilon^c S^c \rho_g + \alpha_2^b \varepsilon^b S^b \rho_g)] \tag{4.57}$$

by definition the conversion rate is given by:

$$\gamma_{cr} = \frac{\phi_g^{out}}{\phi_l^{inj}} = \frac{\phi_g^{out}}{\rho_l (S^b + S^c) v_l^{inj}} \tag{4.58}$$

Defining the ratio of the quench front velocity v^{qf} to the injection velocity v^{inj} by γ_u:

$$\gamma_u = \frac{v^{qf}}{v_l^{inj}} \tag{4.59}$$

Then, the derived water-to-steam conversion rate γ_{cr} is given by:

$$\gamma_{cr} = 1 - \varepsilon^b S^b \rho_l v_{l1}^b - \gamma_u [(1 - \frac{\rho_g}{\rho_l})(\frac{\varepsilon^c S^c}{S}) - \frac{\alpha_2^b \rho_g \varepsilon^b S^b}{\rho_l S})] \tag{4.60}$$

Defining the relative cross-section ratio of the central bed to the total surface by ψ:

$$\psi = \frac{S^c}{S} = \frac{S^c}{S^c + S^b} \tag{4.61}$$

We can then simply write:

$$\boxed{\gamma_{cr} = 1 - \varepsilon^b S^b \rho_l v_{l1}^b - \frac{\gamma_u}{\rho_l} [(\rho_l - \rho_g) \varepsilon^c \psi - \alpha_2^b \rho_g \varepsilon^b S^b (1 - \psi)]} \tag{4.62}$$

where S is the total cross-section, v_l^{inj} is the water injection velocity, v_{l1}^b is the bypass inlet velocity, and γ_u is the ratio of the quench front velocity to the injection velocity.

4.3.5 Water entrainment in the bypass

Upon water injection and evaporation, steam produced at the quench front level is redistributed radially into the bypass where water may also be entrained. The entrainment is assumed to occur when the velocity of water in the bypass is significantly higher than the quench front velocity; with a least ratio $U_l^b/U^{qf} > 1.5$. This value ensures that the the quench front propagation is 2D, where it is observed to advance faster in the bypass than the center.

Single phase steam flow simulations showed the existence of a length H_d over which this redistribution occurs. For PEARL configuration, it was approximately the same for different injection flow rates (Fig. 4.4). This length H_d corresponds to the elevation z_2 above the quench front level and above which no more steam or water is redirected radially into the bypass. This can be formulated as:

$$\phi_g^{r\,c\to b}(z = H_d) \approx 0 \tag{4.63}$$

where $\phi_g^{r\,c\to b}(z)$ represents the integral steam flow rate redistributed radially, from the central layer to the bypass, up to an elevation z.

At this level, the pressure in the center is approximately equal to that in the bypass. This allows writing an equality of the vertical pressure gradients for the gas phase in the center and the bypass:

$$\frac{\partial P_g{}^{c}}{\partial z} \approx \frac{\partial P_g{}^{b}}{\partial z} \tag{4.64}$$

Expanding this equality using the Darcy-Forchheimer equation renders a quadratic equations relating the gas phase velocities in the center and the bypass by:

$$\rho_g g + \frac{\mu_g}{\kappa^c} U_g^c + \frac{\rho_g}{\eta^c}(U_g^c)^2 = \rho_g g + \frac{\mu_g}{\kappa^b} U_g^b + \frac{\rho_g}{\eta^b}(U_g^b)^2 \tag{4.65}$$

Then relating the flow rate of steam produced to the water injection flow rate, as defined earlier by the conversion rate equation (Eq. 4.51):

$$\gamma_{cr}\, \rho_l\, S\, v_l^{inj} = \rho_g\, S\, v_g^{out} \tag{4.66}$$

$$\gamma_{cr}\, \rho_l\, S\, v_l^{inj} = \alpha^b \rho_g \varepsilon^b S^b v_g^b + \alpha^c \rho_g \varepsilon^c S^c v_g^c \tag{4.67}$$

At this level, it is pure steam exiting the center (α^c=1) at the top of the two-phase zone. Eq. 4.67 is then reformed to relate v_g^c, v_g^b, and v_l^{inj} by the following equation:

$$v_g^c = \frac{\psi \alpha^b \varepsilon^b}{\varepsilon^c(\psi - 1)} v_g^b + \frac{\gamma_{cr}\rho_l}{\rho_g \varepsilon^c (1-\psi)}(v_l^{inj}) \tag{4.68}$$

If the temperatures of the center and the bypass are different, Eq. 4.65 is then written with distinct steam properties as follows:

$$\rho_g^c g \;+\; \frac{\mu_g^c}{\kappa^c} U_g^c \;+\; \frac{\rho_g^c}{\eta^c}(U_g^c)^2 \;=\; \rho_g^b g \;+\; \frac{\mu_g^b}{\kappa^b} U_g^b \;+\; \frac{\rho_g^b}{\eta^b}(U_g^b)^2 \tag{4.69}$$

And hence, the exiting steam velocities v_g^c and v_g^b, are related to the injection velocity v_l^{inj} by the following equation:

$$v_g^c = \frac{\psi \alpha^b \varepsilon^b \rho_g^b}{(\psi - 1)\rho_g^c} \varepsilon^c v_g^b + \frac{\gamma_{cr} \rho_l}{\rho_g \varepsilon^c (1 - \psi)} (v_l^{inj}) \tag{4.70}$$

Combining Eq. 4.68 and Eq. 4.65 reduces to a quadratic equation in v_g^b of the form:

$$(v_g^b)^2 + r_1 \, v_g^b + s_1 = 0 \tag{4.71}$$

This allows determining the steam velocities v_g^b and v_g^c in terms of the injection velocity v_l^{inj} and the system parameters.

The capillary pressure P_c is defined as the pressure difference between the liquid and gas phases:

$$P_c \;=\; P_g \;-\; P_l \tag{4.72}$$

The capillary length for water is defined as:

$$l_c = \sqrt{\frac{\sigma}{(\rho_l - \rho_g) g}} \tag{4.73}$$

where σ is the surface tension. The capillary length for water is approximately 2mm, and considering the bypass particles size (8mm in diameter) are larger than l_c, the capillary effects can be neglected in this case. This allows assuming that the pressure of the gas phase is approximately equal to that of the liquid phase and thus the following equation holds in the bypass:

$$\frac{\partial {P_g}^b}{\partial z} \;\approx\; \frac{\partial {P_l}^b}{\partial z} \;\approx\; \frac{\partial P^b}{\partial z} \tag{4.74}$$

Expanding it using Darcy-Forchheimer equations for two-phase flow, in the general form defined in Chapter 2:

$$\begin{aligned} &\rho_g g \;+\; a_g U_g \;+\; b_g {U_g}^2 \;+\; c_g U_g U_l \;+\; d_g U_l \;+\; e_g {U_l}^2 \\ &= \rho_l g \;+\; a_l U_l \;+\; b_l {U_l}^2 \;+\; c_l U_l U_g \;+\; d_l U_g \;+\; e_l {U_g}^2 \end{aligned} \tag{4.75}$$

provides a quadratic equation in v_l^b (velocity of water in the bypass). It has the form:

$$(v_l^b)^2 - m_l\, v_l^b + n_l = 0 \tag{4.76}$$

in which

$$m_l = \frac{(c_g - c_l)v_g + d_g - a_l}{b_l - e_g} \qquad n_l = \frac{(\rho^l - \rho^g)g + v_g(d_l - a_g) + {v_g}^2(e_l - b_g)}{b_l - e_g} \tag{4.77}$$

The solution $v_l^b(\alpha)$ for Eq. 4.76 is the first relation between the velocity of the entrained water into the bypass v_l^b, the the steam velocity v_l^g, the fluids properties, and physical properties of the medium. It is given by:

$$\boxed{v_l^b(\alpha) \;=\; +\frac{1}{2} m_l\, [1 \pm \sqrt{1 - 4\frac{n_l}{{m_l}^2}}]} \tag{4.78}$$

Only the physical solution is accepted. Negative and non-real solutions are omitted. Determining the physical solution depends on the steam velocity and the coefficients associated to the velocity terms in the Darcy Forchheimer equations.

Table 4.1: PEARL Tests

Test number	Initial temperature (°C)	Injection velocity (m/h)	Power deposition (W/kg)	Pressure (bar)
PA1	400	5	150	1
PA2	700	5	150	1
PA5	400	10	150	1

Writing the equations in this general form, Eq. 4.75 enables testing any proposed variation in the momentum equations, like interfacial friction laws. And allows assessing the sensitivity of the solutions to the law considered.

The PEARL tests experimental results obtained at IRSN ([Chikhi 2015b]) were considered for comparison. The main characteristics of some selected tests are listed in Table 4.1. Adopting the same configuration, the total height of the debris bed is H=0.5 m, the radius of the central bed is R^c=0.225 m whereas the more permeable bypass had a radial thickness of 0.045 m making the total radius of the system R^{ext}=0.27 m. The diameter of the particles in the center is d_p^c=4 mm whereas the

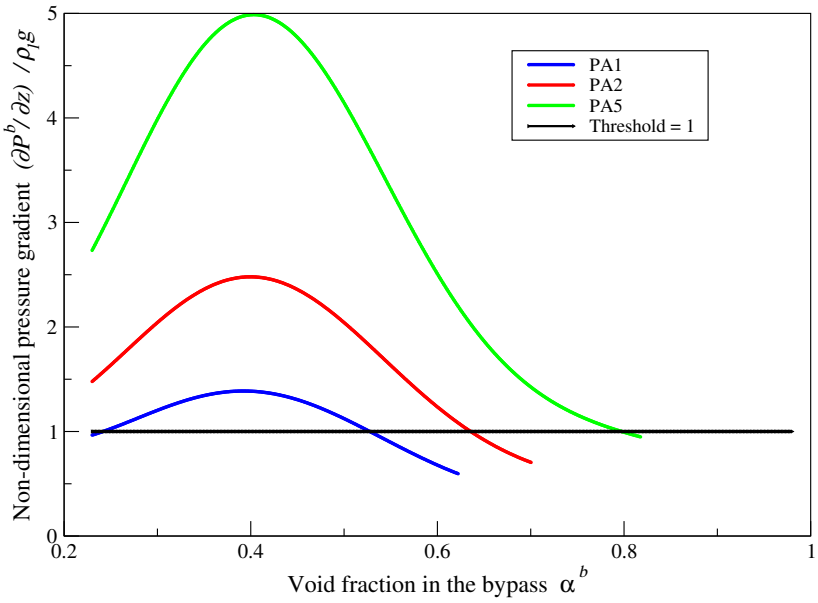

Figure 4.16: Non-dimensional vertical pressure gradient in bypass as function of void fraction α^b

more permeable bypass was composed of particles of larger diameter d_p^b=8 mm. The porosity for both debris layers was set to 0.4.

For water to get entrained and flows upwards in the bypass (i.e. obtaining non-zero solutions for v_l^b), the vertical pressure gradient must be larger than the hydrostatic pressure. The necessary condition for the entrainment of water in the bypass is defined by a threshold. It is represented by the non-dimensional vertical pressure gradient in the bypass ω (Figure 4.16):

$$\omega = [\frac{\partial P^b}{\partial z}]/[\rho_l g] \tag{4.79}$$

The threshold is ω_o=1. Below this threshold the entrainment of water in the bypass is impossible and the progression of water in the bypass is limited to the quench front velocity. The Darcy-Forchheimer form of momentum equations was considered such that the cross-terms $\mathbf{K}_{ij}$, $\mathbf{F}_{ij}$ are non-zero and the adapted interfacial friction law is that of Schülenberg-Müller defined earlier (ref chapter 2). Entrainment occurs when the velocity of water in the bypass is significantly higher than that in the center;

with a least ratio of $U_l^b/U^{qf} > 1.5$ which corresponds to the situations where the pressure gradient is sufficiently larger than the hydrostatic pressure.

For instance, considering three PEARL tests (PA1, PA2, and PA5) with different injection velocities, the quench front velocity and the conversion rate were obtained by the analytical model and the results of the modeled water velocity in the bypass $v_l^b(\alpha)$ provided by Eq. 4.78 (1st solution) are presented in Figure 4.17. It shows the occurrence of water entrainment in the bypass in all cases just as in the reflooding test with a 2-D shaped quench front propagation.

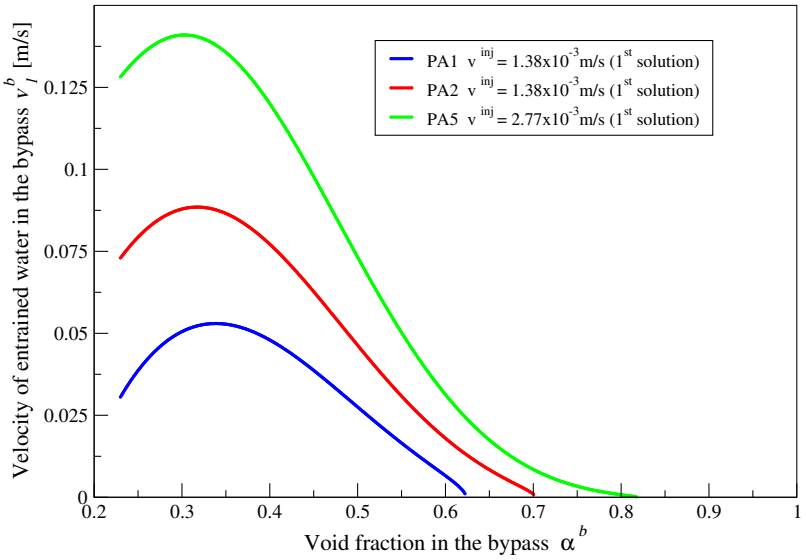

Figure 4.17: Entrained water velocity as function of void fraction $v_l^b(\alpha)$ for different PEARL tests - 1^{st} solution

Alternatively, the velocity of the entrained water is estimated by writing the mass balance equation over a control volume in the bypass between the quench front level z_1 and the top of the redistribution level z_2 as shown in Figure 4.18. The mass balance over the orange contour writes:

$$\sum \phi_{in} = \sum \phi_{out} \tag{4.80}$$

$$\phi_l^{b\,in} + \phi_g^{cb} = \phi_l^b + \phi_g^b \tag{4.81}$$

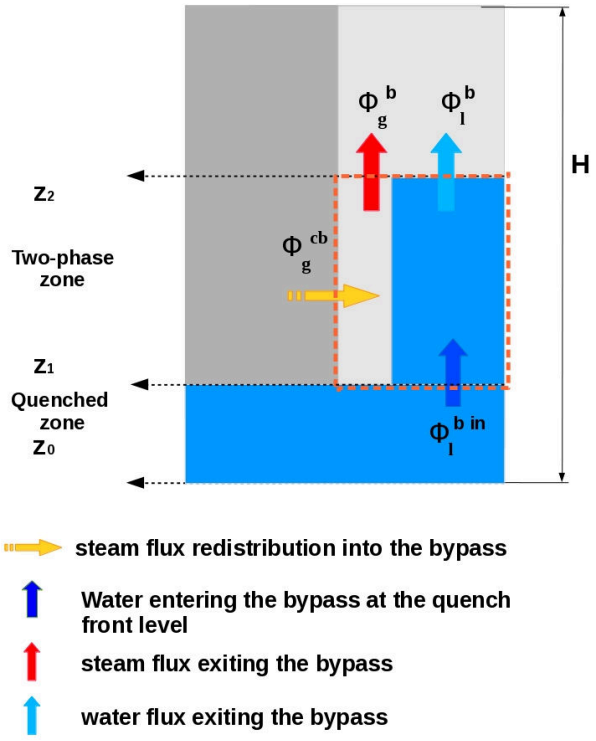

Figure 4.18: Mass balance in the bypass

with

$$\phi_g^{cb} = \phi_g^b \tag{4.82}$$

$$\phi_l^b = (1-\alpha^b)\,\rho_l\,\varepsilon^b\,S^b\,(v_l^b - v^{qf}) \tag{4.83}$$

$$\phi_l^{b\,in} = \rho_l\,\varepsilon^b\,S^b\,(v_l^{b\,in} - v^{qf}) \tag{4.84}$$

where $v_l^{b\,in}$ is previously calculated by Eq. 4.32.

This provides another estimation of the water velocity in the bypass in terms of the void fraction α^b, injection velocity v_l^{inj} and the quench front velocity v^{qf}, defined by:

$$\boxed{v_l^b = \frac{(v_l^{b\,in} - \alpha^b v^{qf})}{1-\alpha^b}} \tag{4.85}$$

This is a second relation for the velocity of entrained water in bypass: $v_l^b(\alpha)$. Figure

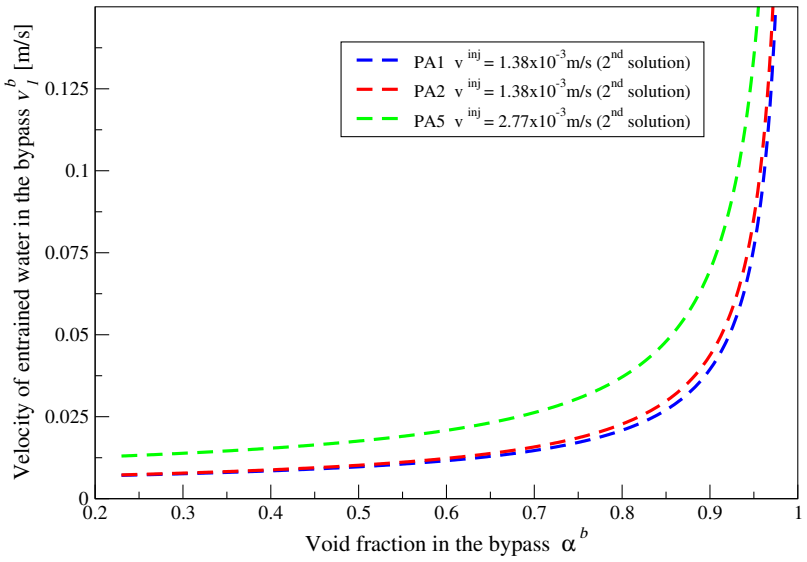

Figure 4.19: Entrained water velocity as function of void fraction $v_l^b(\alpha)$ for different PEARL tests - 2^{nd} solution

4.19 represents the variation of as function of v_l^b as function of the void fraction. An overlay of the two modeled solutions of $v_l^b(\alpha)$ provided by Eq. 4.78 and Eq. 4.85 presented in Figure 4.20 shows that the respective curves intersect at particular solutions whose abscissa α_i (Figure 4.21) are the void fractions in the bypass corresponding to each case, depending on the system characteristics and flow conditions. For the considered cases, it shows the occurrence of water entrainment in the bypass where the velocity of entrained water exceeded the quench front velocity ($U_l^b/U^{qf} > 4$). This is consistent with the observations made upon reflooding tests where a 2-D shaped ($U_l^b > U^{qf}$) quench front propagation was observed.

However, instead of following this methodology of finding the intersection of two solutions for $v_l^b(\alpha)$, Newton-Raphson method could also be applied to solve the same system of equations. In the latter case, we will only obtain the particular solution as a scalar output instead of profiles function of the void fraction, and problems while attempting convergence could also rise. The considered methodology provides a more clear view and helps to identify the behavior of the solutions and its sensitivity to the different input parameters.

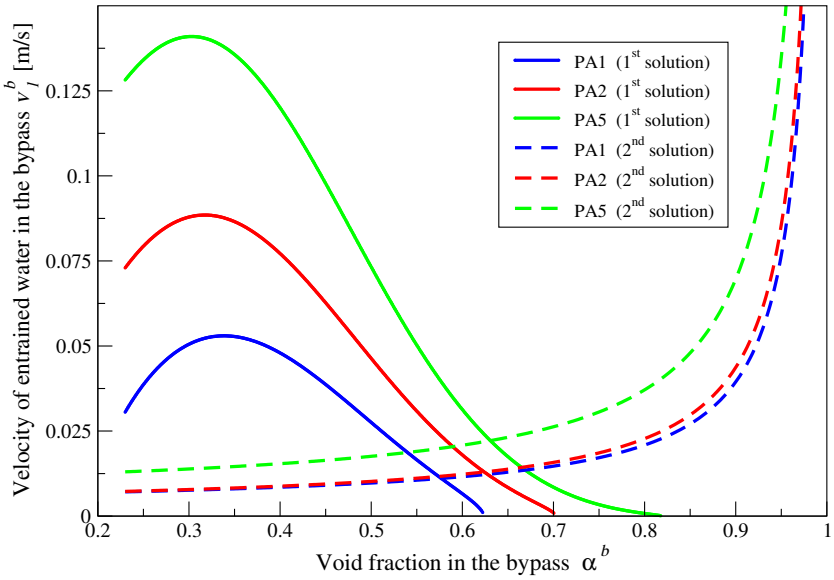

Figure 4.20: Velocity of entrained water in the bypass v_l^b as function of void fraction α^b for different PEARL tests - (intersect of solutions)

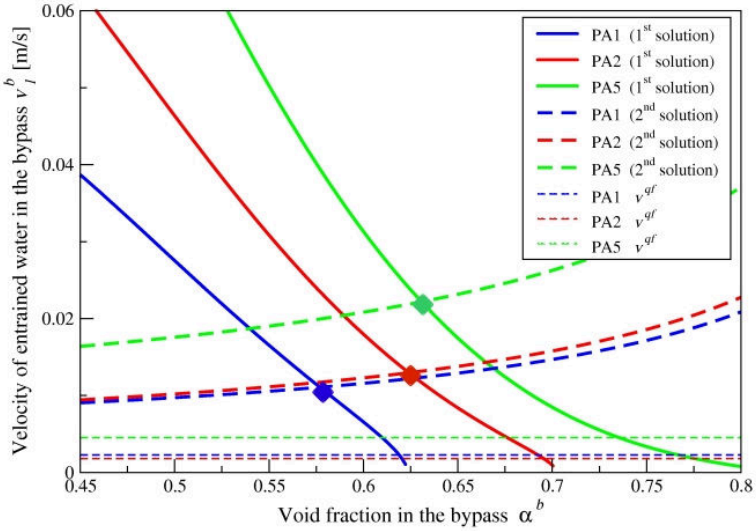

Figure 4.21: Intersection of bypass water velocity curves at the particular solution at abscissa α_i - (Solutions intersect, Zoom-in)

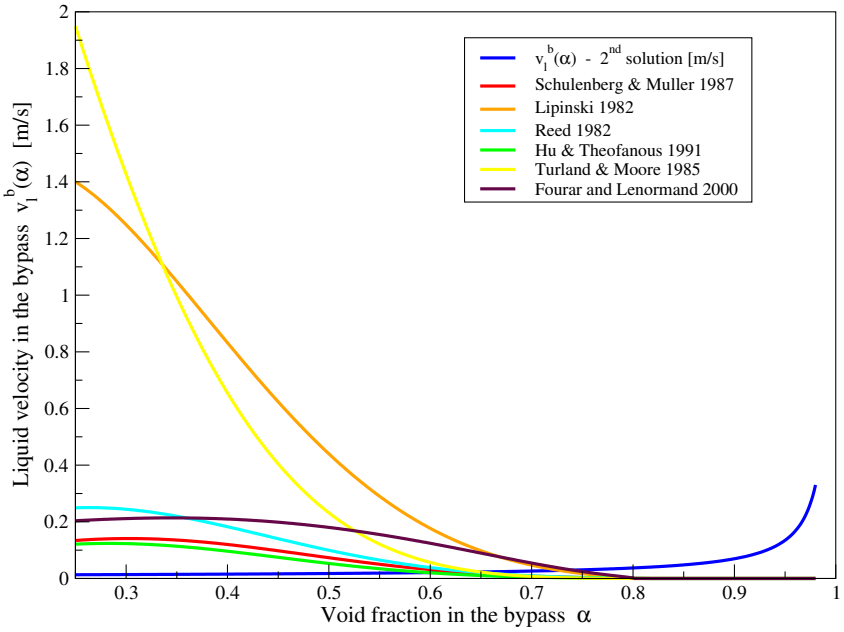

Figure 4.22: Velocity of entrained water in the bypass v_l^b as function of void fraction α^b for different relative permeability and passability correlations - test case PA5, $v_l^{inj} = 2.77 \times 10^{-3} m/s$

4.4 Sensitivity studies

In this section, sensitivity studies concerned in the choice of the correlations of relative permeability and passability found in the literature. Also, the impact of including, and the choice of, an interfacial friction law in the Darcy Forchheimer momentum equations will be studied based on the few existing old models (Tung-Dhir and Schülenberg-Müller) and a recent proposed model by Clavier. Description of the friction laws and the correlations that will be used, are found in Chapter 2.

4.4.1 Relative permeability and passability correlations

Fig. 4.22 and Fig. 4.23 represent a comparison of several correlations implemented in the developed analytical model to calculate the velocity of entrained water in the bypass, in particular for the PA-5 case. It is obvious that the choice of the correlation affects the redistribution behavior. The considered correlations can be divided into groups according to the estimation of the liquid velocity and the behavior over the void fraction domain. Reed, Hu, Turland, and Schülenberg models provided close estimations of the liquid velocity whereas Lipinski and Fourar models overestimated

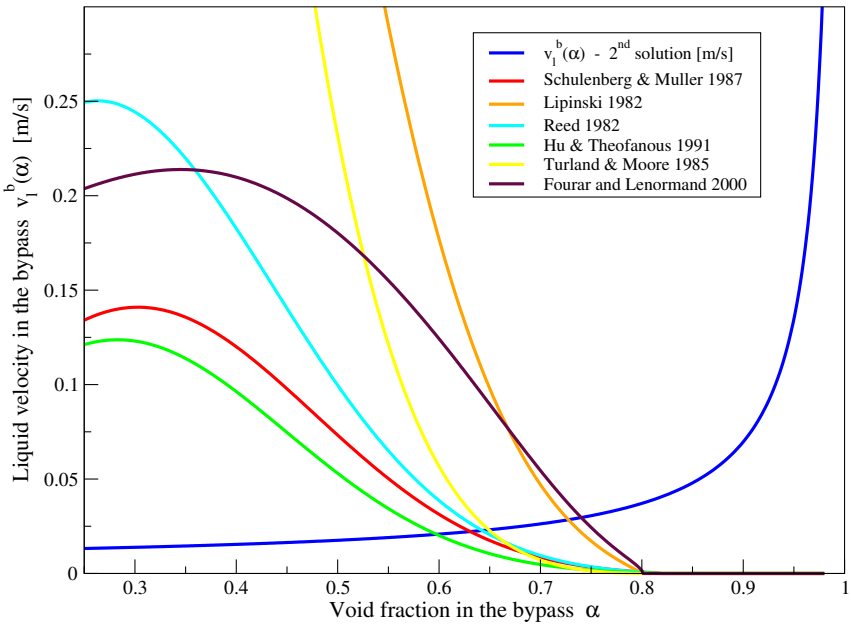

Figure 4.23: Velocity of entrained water in the bypass v_l^b as function of void fraction α^b for different relative permeability and passability correlations - test case PA5, $v_l^{inj} = 2.77 \times 10^{-3} m/s$ (zoom-in)

it. On the other hand, a similar pattern over the void fraction domain is observed for the models of Reed, Hu, Fourar, and Schülenberg. Whereas Turland and Lipinski models estimated higher velocity profiles for low void fractions.

4.4.2 Cross-terms and interfacial friction laws

Considering the Darcy-Forchheimer law defined earlier in Chapter 2:

$$\langle \mathbf{v}_\theta \rangle \;=\; -\frac{\mathbf{K}}{\mu_\theta} \cdot (\nabla \langle p_\theta \rangle^\theta \;-\; \rho_\theta \mathbf{g}) - \; \mathbf{F}(\langle \mathbf{v}_\theta \rangle).\langle \mathbf{v}_\theta \rangle \tag{4.86}$$

For a (liquid-gas) two-phase flow system, the equations obtained theoretically by [Lasseux 2008] have the following structure:

$$\langle \mathbf{v}_l \rangle = -\frac{\mathbf{K_{ll}}}{\mu_l} \cdot (\nabla \langle p_l \rangle^l - \rho_l \mathbf{g}) - \mathbf{F_{ll}} \cdot \langle \mathbf{v}_l \rangle + \mathbf{K_{lg}} \cdot \langle \mathbf{v}_g \rangle - \mathbf{F_{lg}} \cdot \langle \mathbf{v}_g \rangle \tag{4.87}$$

$$\langle \mathbf{v}_g \rangle = -\frac{\mathbf{K_{gg}}}{\mu_g} \cdot (\nabla \langle p_g \rangle^g - \rho_g \mathbf{g}) - \mathbf{F_{gg}} \cdot \langle \mathbf{v}_g \rangle + \mathbf{K_{gl}} \cdot \langle \mathbf{v}_l \rangle - \mathbf{F_{gl}} \cdot \langle \mathbf{v}_l \rangle \tag{4.88}$$

When written with non-zero cross-terms ($\mathbf{K_{lg}}$, $\mathbf{K_{gl}}$, $\mathbf{F_{lg}}$, and $\mathbf{F_{gl}}$), the interfacial friction laws that are found in the literature can be easily implemented in this analytical model when written in the form Eqs. 4.89 and 4.90. Details about embedding an interfacial friction law into those equations are found in Chapter 2, section 2.5.3. This allows us to perform sensitivity studies in an efficient manner faster than the Icare-Cathare calculation which often faced problems achieving convergence when the Schülenberg-Müller friction law was used.

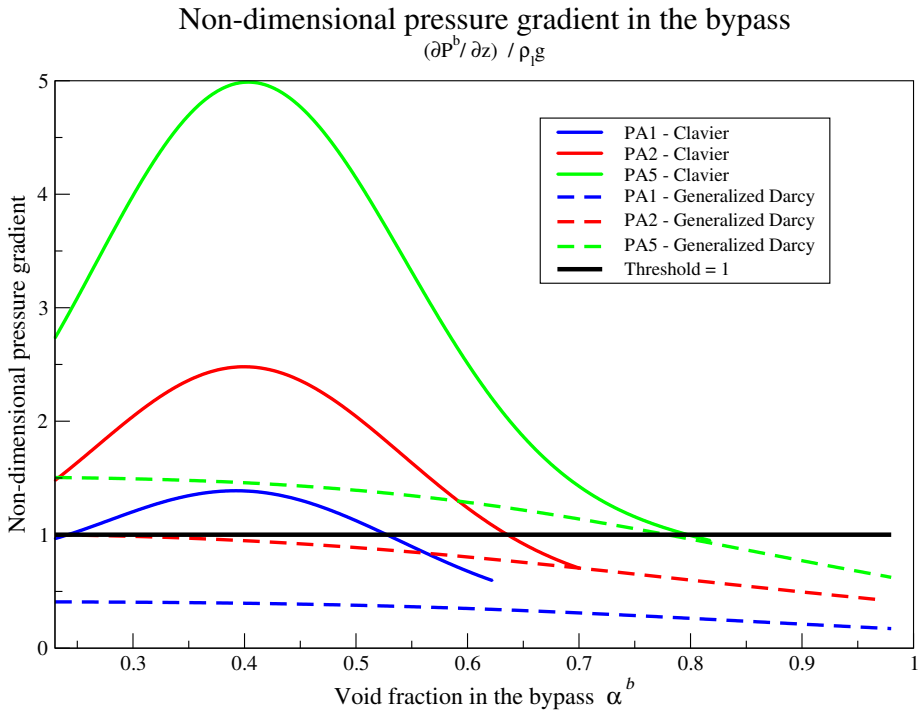

Figure 4.24: Non-dimensional vertical pressure gradient in bypass as function of void fraction α^b , Generalized Darcy Forchheimer without cross-terms (dashed lines) and Clavier model (solid lines)

$$-\frac{dP_g}{dz} = \rho_g g + a_g U_g + b_g {U_g}^2 + c_g U_g U_l + d_g U_l + e_g {U_l}^2 \tag{4.89}$$

$$-\frac{dP_l}{dz} = \rho_l g + a_l U_l + b_l {U_l}^2 + c_l U_l U_g + d_l U_g + e_l {U_g}^2 \tag{4.90}$$

Checking the necessary condition for the entrainment of water in the bypass defined by the defined by, ω, the ratio of the vertical pressure gradient to the hydrostatic

pressure (non-dimensional vertical pressure gradient):

$$\omega = [\frac{\partial P^b}{\partial z}]/[\rho_l g] \tag{4.91}$$

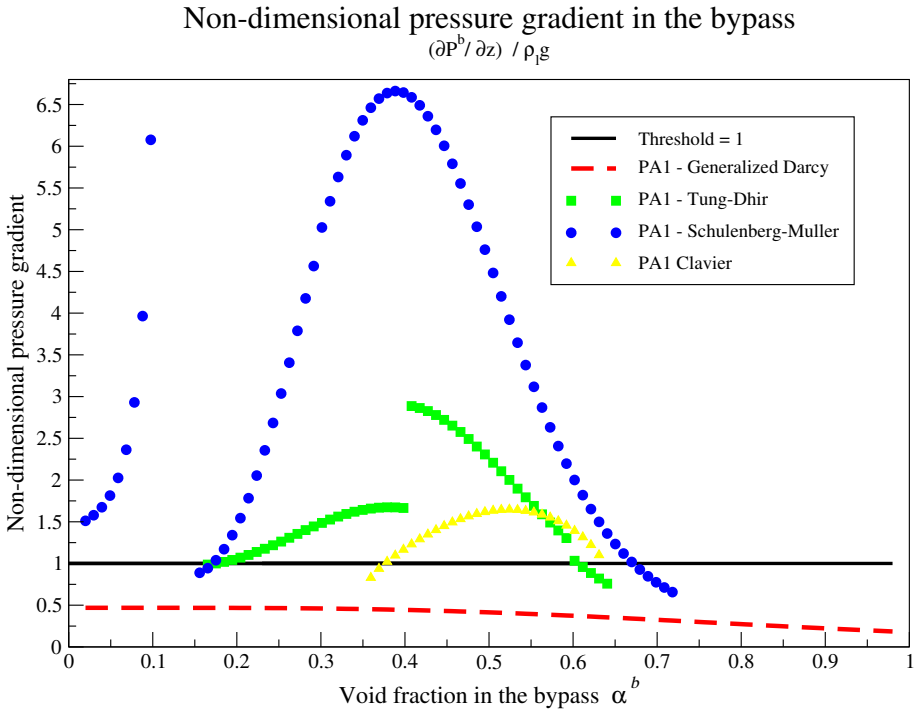

Figure 4.25: Non-dimensional vertical pressure gradient in bypass as function of void fraction α^b , sensitivity to the choice of the interfacial friction law - PA1 test

Figure 4.24 shows the effects of defining the cross-terms in the Darcy-Forchheimer equations, for different PEARL tests (PA1, P12, and PA5) in which water entrainment was identified in the experiments. The dashed lines correspond to the Generalized Darcy Forchheimer form of the momentum equations without cross-terms (i.e. no cross-terms, $\mathbf{K}_{ij}$=0, $\mathbf{F}_{ij}$=0 for i≠j). Whereas solid lines correspond to the Darcy-Forchheimer momentum equations (including cross-terms $\mathbf{K}_{ij}$, $\mathbf{F}_{ij}$ by adapting the model proposed by Clavier described in Chapter 2). The results obtained without the interfacial friction terms ($\mathbf{K_{lg}}$, $\mathbf{K_{gl}}$, $\mathbf{F_{lg}}$, and $\mathbf{F_{gl}}$ set null) couldn't predict well the entrainment behavior (PA1, PA2). This is due to the fact that some the considered cases correspond to the limiting geometric and flow conditions for which the predefined threshold for entrainment occurrence is compromised. Excluding the cross-terms from the momentum equations underestimated the vertical pressure gradient in the bypass in some cases (insufficient for entrainment). For higher injection

flow rates (PA5), the entrainment could be predicted without a friction law, yet it was underestimated. Hence, including non-zero cross-terms is necessary to obtain good estimations.

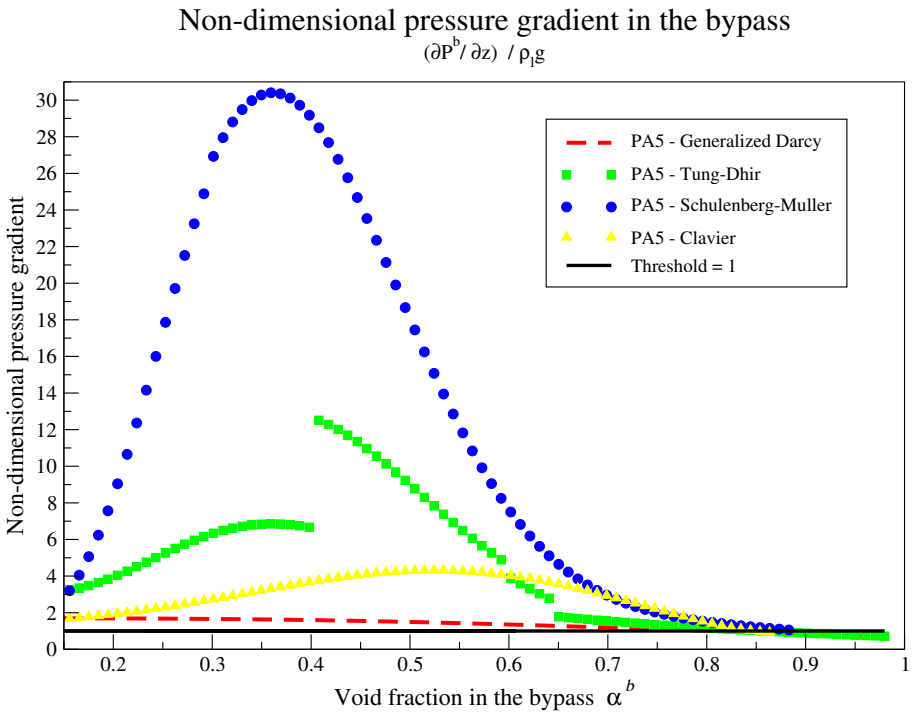

Figure 4.26: Non-dimensional vertical pressure gradient in bypass as function of void fraction α^b, sensitivity to the choice of the interfacial friction law - PA5 test

Moreover, the choice of the cross-terms and the interfacial friction law also affects the description of the entrainment (Figures 4.25, 4.26) and the estimation of the entrained velocity (Figure 4.27). The sensitivity to the choice of the friction law, for the non-dimensional pressure gradient in the bypass ω, is represented in Figures 4.25 and 4.26 corresponding to PA1 and PA5 PEARL test respectively. Those graphs describe the necessary condition for the entrainment occurrence when including an interfacial friction law in the Darcy-Forchheimer momentum equations. The black solid line is the threshold and the red dashed line correspond to the generalized Darcy law with only Forchheimer corrections and no interfacial friction terms. In the experiments, entrainment of water in the bypass was recorded in both PA1 and PA5 tests. However, Figure 4.25 shows that the model will only predict the entrainment behavior if the interfacial friction terms were included. We firstly notice that some of the curves does not cover the whole void fraction range. This is due

to the fact that for some intervals of void fraction, the solutions were either non-real or negative, so they were omitted. Without the interfacial friction terms (red-dashed line), ω was below the threshold and the quenching process in that case is said wrongly described as 1D. The pressure gradient in the bypass was higher when estimated using Schülenberg-Müller law, and it covered a wider void fraction range than Tung-Dhir and Clavier. The latter recorded lower pressure gradients and covered the smallest range over the void fraction. At low void fractions, Schülenberg-Müller showed an asymptotic behavior. However, the solutions for the velocity were generally corresponding to void fractions away from the asymptote, so that behavior did not present a problem. The discontinuity appearing in the curves corresponding to Tung-Dhir law is due to the division of the void fraction domain into several intervals describing the flow regime (bubbly, slug, annular). In each regime, the interfacial friction term is defined up to a distinct function of the void fraction. The difference between those functions lead to having such discontinuities in the curves.

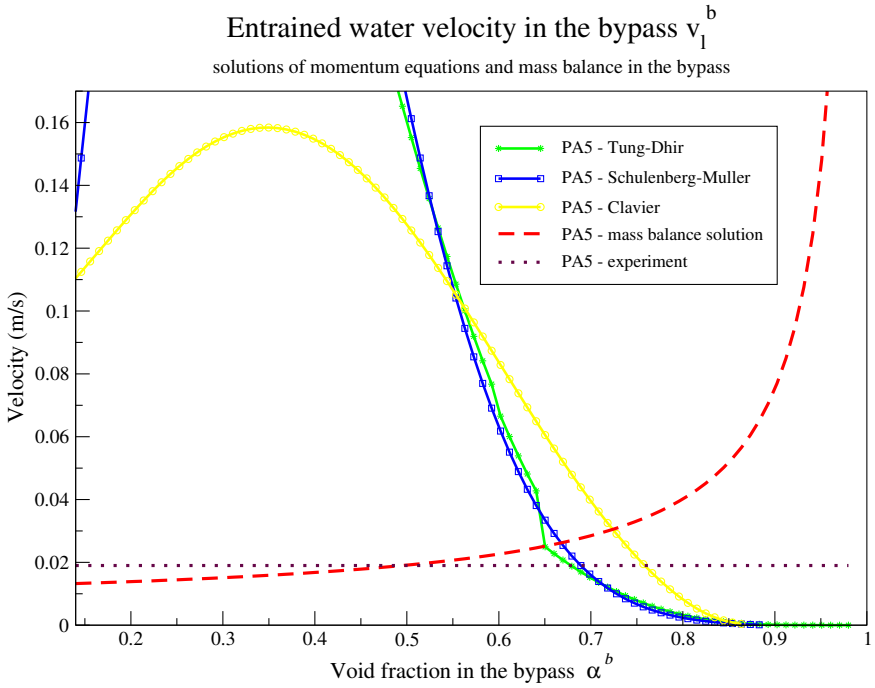

Figure 4.27: Sensitivity to the friction law - PEARL test PA5 entrained velocity

For PA5 test (Figure 4.26), which was conducted at higher injection rate, entrainment was predicted even without including the friction terms, but it was underestimated. ω in that case (red dashed line) was slightly higher than the threshold, but enough to predict entrainment This is observed clearly in Figure 4.27 represent-

ing the sensitivity of the entrained water velocity v_l^b to the choice of the interfacial friction laws. The red dashed line is the v_l^b solution from the mass balance in the bypass. The other curves correspond to the solution of the momentum equations using different friction laws. As described earlier, the particular solution is defined by the intersection of those solutions.

Similar to PA1 case, we also observe here that Schülenberg-Müller estimated higher pressure gradients (Figure 4.26), and the lowest were predicted by Clavier. However, the particular solution for the entrained velocity was obtained highest by Clavier and overestimating the experimental result, whereas Tung-Dhir and Schülenberg-Müller provided very close predictions lower than Clavier and closer to the measurements.

Figure 4.28 compares the entrained water velocities as estimated by the considered interfacial friction laws, the Icare-Cathare calculations, and the experimental measurements for the PEARL tests PA1, PA2, PA5. In those tests, a 2D quench front progression was observed in the experiments and the entrained water in the bypass surpassed the quench front velocity. The Icare-Cathare calculations presented in Chapter 3 demonstrated a lack in the existing models. It was not able to describe the water entrainment behavior for PA1 and PA2 and underestimated it for PA5. This was also observed when using the simplified analytical model without the cross-terms (GDF*: Generalized Darcy Forchheimer law without cross-terms). Using the latter, the analytical model was not able to predict the entrainment of water in the bypass because the necessary condition was not satisfied, which can be observed in Figure 4.24. And in that case, i.e. when the necessary condition for entrainment is not satisfied, the model considers that the quenching is 1D and attributes the quench front velocity in the center to be entrained water velocity in the bypass. For PA5, GDF* estimated well the entrained water velocity. However, the experimental value for PA5 in particular was estimated and not measured.

On the other hand, when an interfacial friction law was used, the prediction of the entrainment behavior was enhanced. Tung-Dhir and Schülenberg-Müller estimations were very close to each other and predicted the entrainment sufficiently. Whereas Clavier's model overestimated it and could not provide a valid solution for PA1 test, so the quench front velocity in the center was attributed to the entrainment velocity in the latter case.

Considering the performance of the interfacial friction laws for the studied case and for this specific configuration of a two-layered debris system. We observe that Tung-Dhir and Schülenberg-Müller tend to provide close predictions of the water entrainment whereas over-estimations were obtained by Clavier model. Clavier's

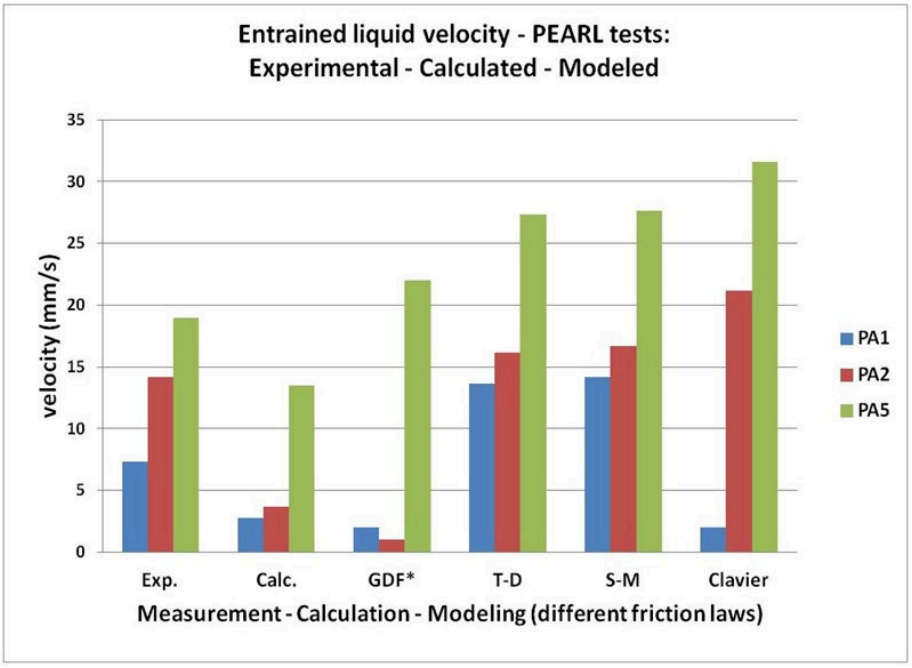

Figure 4.28: Sensitivity to the friction law - entrained velocity estimated by different friction laws *(T-D: Tung-Dhir, S-M: Schülenberg Müller, C: Clavier)*. A comparison against experimental results *(Exp.)* and Icare-Cathare calculations *(Calc.)* for different PEARL tests

model is a rather concise description of the velocity-saturation relationship over the saturation range whereas the model of Tung-Dhir was developed to describe the flow after classifying the flow regimes according to the saturation. Schülenberg-Müller model performed a bit better than the Tung-Dhir model, yet it showed some asymptotic behavior in the low void fraction range in some situations. For certain cases, Clavier's model was not able to provide estimations whereas Schülenberg-Müller succeeded. However, one can conclude that for the considered configuration, in overall, the Schülenberg-Müller model performed the best among the other interfacial friction laws concerning the studied flow in such debris systems.

4.5 Limitations

The model is designed to predict the entrainment behavior in the bypass. Thus its predictions are focused on the situations with 2D quench front propagation. However, it can be used to distinguish between the 1D and 2D cases. Even though, for the 1D cases, the model can still predict the conversion rate and the quench front velocity. Moreover, in the 1D case, the velocity of water in the bypass is usually

close to the quench front velocity. So the model may then assume the bypass water velocity to be equal to the quench front velocity.

The model falls short of being capable to evaluate the dynamics leading to the estimation of the temperature of produced steam at the downstream the debris system. This parameter determines how much of the system initial energy has been consumed to overheat the steam above the saturation temperature. It also affects the estimation of the pressure gradient.

The model is generally designed to provide estimations for flow redistribution over contrasting permeability debris layers. It can provide estimations for very high contrasts, however, when the porosity of the center becomes very low (less than 5%), the reliability of the results are questionable.

4.6 Conclusion

In this study, an investigation of two-phase (water and steam) flow in a heated porous medium composed of two cylindrical layers of contrasting porosity and permeability was conducted. An analytical two-phase model was derived to describe the entrainment behavior of water into the bypass. The criterion for which the entrained water progresses in the bypass faster than the quench front velocity has been examined for different cases. The velocity of the entrained water in bypass was estimated analytically as well as the void fraction in the bypass for the corresponding system configuration and flow conditions.

This simplified analytical model forms a tool to perform fast calculations of two phase flow redistribution in such a porous layers system, with different thickness, porosity and permeability and assess the conditions for water entrainment. It also allows testing different correlations in the variations of the momentum equations for porous media such as relative permeability and passability correlations, interfacial friction laws.

Provided the initial and boundary conditions, the model can estimate the entrainment, quenching speed, and the efficiency of the reflooding. It is thus suitable for probabilistic studies of the efficiency of various safety injection systems.

Good qualitative and quantitative results for two-phase flow redistribution downstream of the quench front as compared to the results obtained in PEARL reflooding tests where it predicts the occurrence of entrainment (advance of water in the by-

pass at a velocity v_l^b higher than the quench front velocity v^{qf}). This means that the model probably catches the physical phenomenon governing the water entrainment. It assumes the redistribution of produced steam into the more permeable bypass, and it estimates the pressure gradient increase. The effect of interfacial friction on the pressure gradient associated with entrainment in the bypass was demonstrated by the model using several friction laws.

The developed model has several advantages. It is written in a rather general form including the Forchheimer correction terms and non-zero cross-terms in the generalized Darcy-Forchheimer momentum equation. It allows testing easily and efficiently any proposed variation of the momentum equation including changes in correlations and friction laws up to quadratic terms. The model allows performing fast evaluations of the efficiency of cooling by computing the fraction of the injected flow rate that participates in cooling. Upscaling to the reactor scale is straightforward, provided the geometry and boundary conditions are respected. Thus the model is very useful to estimate the total quenching time and the maximum temperature that could be reached by the hot debris bed at large scales in accidental conditions. It can be also used to perform sensitivity studies on the physical properties of the particle beds and the fluid, as well as different variations of the momentum equations. For instance, it was shown that the Generalized Darcy law is not able to provide acceptable evaluations whereas considering non-zero cross-terms in the Darcy Forchheimer equations by including an interfacial friction law succeeds in obtaining better results. The interfacial friction laws found in the literature (Tung-Dhir, Schülenberg-Müller, and Clavier) were implemented and tested. Even though it is highly non-linear in void fraction (α^7), in overall, Schülenberg-Müller law provided the best estimations and covered a larger range of validity. The advantage of using this simplified model is its ability to cope with such non-linearity and the ease of manipulation of the friction laws definition. That for instance, represent a difficulty when we deal with a thermal hydraulics code like Icare-Cathare with which the calculations using the Schülenberg-Müller law were not feasible due to divergence of the void fraction out of the possible range. It leaded the calculations to crash; that divergence is suspected to be a result of the high non-linearity in the void fraction.

It is essential to include the cross-terms in order to provide better estimations. The interfacial friction laws present in the literature are based on experimental measurements. However, the model proposed by Clavier was a more rigorous approach to define a more concise form starting from the determination of the 8 unknown terms in the Darcy Forchheimer equations. Further studies are needed in order to find an adequate formulation of the cross-terms.

The momentum equations were based on the generalization of Darcy's law with quadratic corrective Forchheimer terms. Discussion about the choice of the Darcy Forchheimer law was presented in Chapter 2. However, the model can be improved by including cubic correction terms, in the weak inertia flow regime, to the Darcy's law instead of the quadratic terms. This will mainly improve the momentum equations accurate description in the liquid phase since, according to the most likely considered situations of reflooding, the gas phase is mostly flowing in the strong inertia regime where Forchheimer quadratic terms best describe it. The model can be improved to assume different forms of the momentum equations for the liquid and gas phases according to the flow regime.

Further investigations including comparison against PEARL results, and a reactor-scale calculation with parametric studies to precise the effect of the geometrical characteristics of the debris bed and flow conditions on the reflooding process, are presented in the next chapter.

Chapter 5

Model estimations for PEARL and reactor scale

Implementation of the proposed analytical is presented in this Chapter. Estimations for several PEARL tests will be presented and compared to the experimental measurements. It is be followed by a reactor-scale study where a reference configuration is defined, then a parametric study will be presented to assess the impact of some initial and boundary conditions, as well as debris geometry on the behavior of the reflooding process. The investigation concludes with the assessment of the coolability chances depending on the variation of the studied parameters.

Contents

5.1 PEARL modeled results against experiments

5.1.1 PEARL tests

The PEARL tests performed at IRSN were considered, Table 5.1 summarizes the test conditions (Initial temperature of the inner bed T^c, injection velocity v^{inj}, and the Pressure P). Estimations of the quench front velocity and the entrained water velocity in the bypass were provided by the proposed model. A comparison of those estimations against the experimental results for the quench front velocity in the center and the bypass are then presented.

Tests PA1, PA2, PA4, and PA5 correspond to the set of PEARL tests performed earlier. In this preliminary set of experiments, few tests at different temperature and injection velocity were performed. Those tests were investigated with Icare-Cathare calculations and discussed in Chapter 3. More recently, another set of PEARL tests were performed to investigate more thoroughly the effect of injection velocity and pressure on the reflooding process. In this new set, the initial temperature was the same for all tests (700°C). The reference tests is P3-10 (REF), it is conducted at P=3 bars and injection velocity v^{inj}=5m/h. Considering the reference conditions, the pressure and injection velocity were varied for several tests to investigate their impact.

Table 5.1: PEARL Tests Matrix

Test number	Initial temperature (degC)	Injection velocity (m/h)	Pressure (bar)	Flooding mode
PA1	400	5	1	Bottom
PA2	700	5	1	Bottom
PA4	400	2	1	Bottom
PA5	400	10	1	Bottom
P2-6	700	5	2	Bottom
P3-10 (REF)	700	5	3	Bottom
P4-1	700	5	4	Bottom
P3-8	700	7.5	3	Bottom
P3-4	700	10	3	Bottom

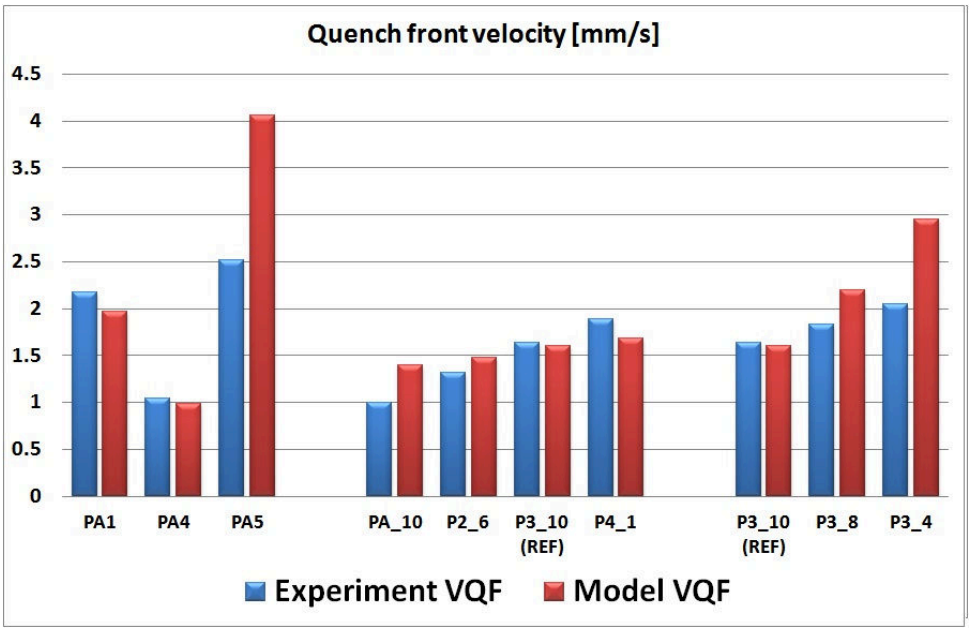

Figure 5.1: Quench front velocity v^{qf}, analytical model against experimental results for different PEARL tests

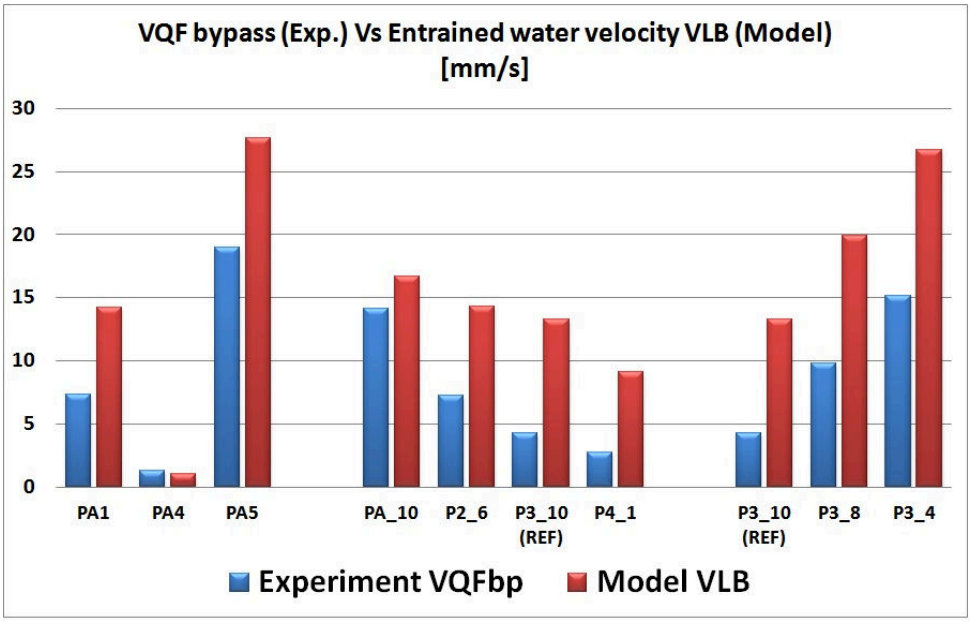

Figure 5.2: Comparison of modeled water entrained velocity v_l^b and the experimental quench front velocity v^{qfb} for different PEARL tests

5.1.2 Quenching and water entrainment

Upon the investigation provided in section 4.4.2 of Chapter 4, concluding that it is necessary to include an interfacial friction law in order to better predict the results, the Schülenberg-Müller friction law was selected for this study. Even though highly non-linear in void fraction, this friction law provided a wider range of applicability and relatively better estimations than the other laws.

The comparison of the quench front velocity v^{qf} in the center is presented in Figure 5.1. The modeled quench front velocity is acceptable as compared to the experimental results. For the set of tests with increasing pressure, the model could catch the slight increase in the quench speed. For the set of tests with different injection velocity P3-10 (REF), P3-8, and P3-4 at v^{inj}= 5m/h, 7.5m/h, and 10m/h respectively, the quench front velocity increases. The model was able to predict this behavior. In general, the modeled estimations were acceptable, but they were overestimated for the tests at highest injection velocity.

In the bypass, the measured quench front velocity v^{qfb} is compared to the estimated velocity of entrained water. We observe that the estimations surpass the quench front velocity v^{qfb}. This could happen for two main reasons:

- While the analytical model estimates an average entrained water velocity which is generally faster than the quench front velocity in the bypass v^{qfb}, the experimental measurements correspond to a particular position where the velocity may not be the average one. In the experiments the measurement of the quench front velocity in the 4.5cm-thick bypass was based on a single thermocouple reading.
- The model is sensitive to small variations of the void fraction in some cases. That is due to the non-linearity of the cross-terms.

5.1.3 Discussion

The results obtained by the tests performed at different injection velocities indicate the entrained water velocity in the bypass increases for the tests at higher injection rates. May this infer that the entrained fraction of the injected flow rate, ϕ_l^b/ϕ^{inj}, in the bypass increases at higher injection rates?. This can be only inferred if the measured velocity represents the superficial velocity in the bypass. In fact, the determination of the quench front position is done by a single thermocouple, (1 in

the radial direction, with 9 thermocouples in total positioned at different elevations) and the bypass is relatively large. So, assuming that the bypass is fully saturated with water (void fraction = 0) at the measurement position can not be fortified based on a single position reading. Moreover, the video records of 2D-quenching PEARL tests, show a flow of water and steam in the bypass much faster than the quench front. The entrainment of water is dragged by a strong radial flow of steam from the center into the bypass. This was observed especially in the tests with strongly curved (2D) quench fronts. Therefore, it is expected that the void fraction is significant rather than having a piston-like entrainment of a fully saturated water column, in a 4.5cm high permeability debris layer with coarse spherical particles (8mm). It is clear that the entrained flow rate increases for high injection flow rates, but we can not infer that their ratio (or the so called, entrained fraction) also increases with increasing injection rates.

In brief, with increasing injection velocity, the increase of the measured water velocity in the bypass does not necessarily imply that the entrained fraction of the injected water also increases. This is due to the fact that the bypass is not fully saturated with water and the void fraction α has to be taken into account in order to determine precisely the fraction of entrained water ϕ_l^b/ϕ^{inj}.

In addition to the observed behavior in the video records, one can also prove that the void fraction in the bypass α^b is not zero by taking a mass balance over a frame of reference moving with the quench front velocity. Computing the mass balance using the experimental results shows that α^b is not zero. Or more simply, considering PA2 test, assuming that the bypass is fully saturated (α^b=0), the entrained fraction would be higher than the injected flow rate! Therefore, the bypass is not fully saturated, α^b is not zero and should be taken into account.

In order to investigate this behavior more precisely, we need to determine the entrained fraction of the injected water flow rate which can not be done by measuring the velocity only. For that, the void fraction measurements, and more than one-thermocouple for each elevation, in the bypass are necessary. Performing tests at higher injection velocities than 10m/h is also necessary. In the parametric study presented in the next section on of a reactor scale configuration, the analytical model shows that, as function of the injection velocity, there exists two trends for the ratio of the entrained velocity to the quench front velocity v_l^b/v^{qf} and that of the entrained velocity to the injection velocity v_l^b/v^{inj}. The fact that the considered injection velocities, in the PEARL experiment, correspond to one of the trend makes it appealing to test if the experiments will prove the validity of the other proposed trend. This task can be fulfilled by performing tests higher than 15 m/h.

5.2 Model estimations for reactor-scale configuration

5.2.1 System description

The system under investigation is a heterogeneous debris bed describing a highly degraded nuclear reactor core of 3.8m diameter and 1m height. Similar to the debris systems described in this thesis, we consider a heterogeneous debris system composed of two coaxial cylindrical beds describing the total diameter of the reactor core. The central debris bed is assumed to have larger cross-section, higher temperature, smaller particles, and smaller porosity than the lateral debris bed which is modeled to describe the presence of intact fuel assemblies surrounding the formed debris bed.

The implementation of the proposed model, in Chapter 4, for such reactor scale calculations is straight forward. In order to assess the coolability chances of a highly degraded nuclear reactor core, the effect of several geometric parameters and thermal hydraulic variables was investigated. In the calculations, geometric parameters and thermal hydraulic variables are varied, each alone at once, and their effect on the main outcomes of the reflooding process is studied. Calculations with simultaneous variation of two or more variables can be also performed, but it was not presented because the main focus is to study the impact of varying each parameter alone.

5.2.2 Reference calculation conditions

All the calculations are based on a reference calculation that is described by a hot debris bed comparable in size and geometry to that formed in the TMI-2 accident. In the reference calculation, the central hot debris bed is assumed to be 1 m height, and covering 85 percent of the total cross-section of the reactor ($\psi = S^c/S$=0.85).

Sphericity of the particles is assumed as in the experimental reflooding tests. The porosity is ε^c=0.42 and it is composed of particles with diameter d_p^c=3 mm. According to the post-accident examination of the TMI debris, the corium fragments were mainly composed of UO2 and ZrO2 with approximate weight percentages of 75% and 20% respectively [Akers 1989], [Nagase 2012]. For this reason, we consider the solid particles to have a density and heat capacity comparable to that of UO2 which represents the main composing material of the formed debris in the core. The density of the solid particles is considered to be ρ_s=8000kg/m^3 following the study of [Akers 1989] upon the post accident examination of TMI formed debris.

The heat capacity c_{ps} is temperature dependent and it is extrapolated from fitting experimental results. It is modeled as:

$$c_{ps} = 316 + 0.2213(T^c - 400) \tag{5.1}$$

where, T^c is the temperature of the debris bed in °C. Among the other materials composing corium, UO2 ,which also represents the largest mass fraction, has the highest melting temperature; it starts to melt at around 2840°C. However, due to the presence of the other materials, the melting temperature of corium is less than that of UO2. The melting temperature of the UO2/ZrO2 compounds estimated from the pseudo-binary phase diagram is approximately 2560°C (around 2830 K). [Nagase 2012] performed an experimental study on a simulated debris (SIMDEBRIS), having a material composition based on the TMI debris composition. In their experiments, they measured the melting temperature of the SIMDEBRIS and found that the value (2840 K) is in very good agreement with that of UO2/ZrO2 mixture, provided the respective fractions of UO2 and ZrO2. They concluded that melting temperature is very slightly influenced by the other minor core materials (less than 10% by weight) presented in the core debris, such as Ag, Fe, Ni, Cr, etc. For this reason, we consider that the debris melting temperature T_{melt} is 2560°C.

Table 5.2: Geometric and thermal-hydraulic conditions for Reactor-scale calculations

Parameter	Notation	Reference value	Units
Height	H	1	m
Radius	Rext	3.8/2	m
Cross-section fraction of central bed	ψ	0.85	
Central bed porosity	ε^c	0.42	
Bypass porosity	ε^b	0.55	
Central bed particle diameter	d_p^c	3	mm
Bypass particle diameter	d_p^b	9	mm
Central bed temperature	T^c	2000	°C
Bypass temperature	T^b	1500	°C
Steam outlet temperature	T_g^o	1500	°C
Injection velocity	v^{inj}	40	m/h
Residual power	Q	200	W/kg
Pressure	P	3	bar

Due to the continuous heating of the debris by the residual power and in the absence

of cooling, this bed is considered to have attained a high temperature of T^c=2000°C. The power deposition due to the residual heat is approximately Q=200 W/kg. For this magnitude of power deposition in the corium mixture, the rate of the debris temperature rise $\dot{\theta}$ is approximately 0.4°C/s.

The lateral debris layer representing the intact fuel assemblies is more permeable than the central bed. It is modeled by a debris bed of porosity ε^b=0.55 and particle diameter d_p^b=8 mm. Those considered values correspond to a permeability comparable to that of intact fuel assemblies.

It is considered that this bypass layer has attained a high temperature, yet lower than the central bed temperature due to several reasons. It is less dense ($\varepsilon^b > \varepsilon^c$, hence the initial energy per unit surface and the residual heat deposition is smaller. Also, the the energy flux in the nuclear reactor is usually smaller at the periphery which favors having lower temperatures than that in the center of the core. The considered bypass temperature is T^b=1500°C. The material has the same physical properties as that in the inner bed.

During a severe accident including the loss of coolant of the reactor core, cooling is restored by the safety injection systems. At the moment of reflooding of the formed hot debris bed, the reactor vessel is depressurized to a range between 1 and 10 bars. For the reference calculation, we consider a pressure of 3 bars. In this case, the saturation temperature is T_{sat}=133°C. In a French 1300 MWe PWR, the safety injection systems deliver a flow rate ranging between 55 l/s (or 200 m^3/h, at P=10 bars) and 360 l/s (or 1300 m^3/hr, at P=1 bar). The capacity of the safety injection systems depends not only on the availability of water in the storage tanks but also on the capacity of the pumps to recirculate the coolant. And the capacity of each pump itself depends on its water feeding and power feeding. The failure of the pump to deliver water into the reactor may occur due to water unavailability or a break depriving it from water feeding, or due to lack of power feeding such as during a station black-out scenario. In this case, the water injection flow rate of the injection system is reduced. The considered injection flow rate is 125 l/s (or 455 m^3/hr). For this flow rate in a 3.8 diameter reactor vessel, the injection velocity is thus v^{inj}=40 m/h (or 0.011 m/s). We consider that pressurized water is injected at 70°C.

During the reflooding process, strong evaporation of water occurs inside the hot debris bed and the bypass. The produced steam flowing downstream the debris is assumed to be superheated to T_g^o=1500°C. For the considered reference case at P=3 bars, the overheated steam properties are extrapolated from existing data at lower temperatures.

The properties defining the reference calculation are summarized in Table 5.2.

5.2.3 Main results of the reflooding process

When investigating the process of reflooding a debris bed, the main results that are of major concern are:

- Conversion ratio γ
- Entrainment in the bypass ${\phi_l}^{b*}$
- Duration of the process t_q
- Mass of steam produced M_{vap}

The efficiency of reflooding is described by the water-to-steam conversion ratio γ defined earlier in Chapter 4. The high conversion ratio described a high-efficiency process of reflooding where the energy of the hot debris is extracted by converting injected water into steam. Some part of the extracted energy is also carried out by the overheating of the steam. Low conversion ratios correspond to the situations where water is injected but only a small portion participates in cooling the hot debris. Recalling the mathematical definition of the conversion ratio, it is computed as:

$$\gamma = \frac{\phi_g^{out}}{\phi_l^{inj}} \tag{5.2}$$

Moreover, in such geometries with a lateral highly permeable bypass, a significant fraction of the injected flow rate bypasses the central hot debris bed. This entrainment behavior has been described in details in Chapters 3 and 4. The quench front propagates in 2D and the entrained fraction of water exits the debris zone without participating in the cooling process. This phenomenon has been observed in the PEARL tests when: the central bed is very hot, the injection velocity is high, the pressure is low. But how much is very hot, or high, or low?. Those criteria are defined with respect to threshold values which are determined by the debris bed geometry and the thermal hydraulics of the reflooding process. For example, for a specific two-layered debris system with certain porosity and particles sizes, and at a certain pressure and debris temperature, there exists a threshold injection flow rate beyond which the entrainment in the bypass takes place. Below that threshold, the quench front is flat and progresses in 1D upwards along the debris layers. Given the

debris composition, geometry, initial and boundary conditions, the model proposed in Chapter 4 can be implemented to determine those thresholds.

The entrained rate of water in the bypass ${\phi_l}^b$ does not participate in the cooling process during reflooding. This bypassing of the hot debris bed reduces the efficiency of reflooding and extends its duration. In certain scenarios, such as very high initial debris temperature, extending the reflooding duration may lead to melting of the debris zones which remain uncovered for a long time. Thus it is favorable to have smaller entrained fractions of the injected flow rate, ${\phi_l}^{b*}$. It is simply defined by:

$$ {\phi_l}^{b*} = \frac{{\phi_l}^b}{\phi^{inj}} \tag{5.3} $$

with

$$ {\phi_l}^b = (1-\alpha^b)\,\varepsilon^b\,S^b\,\rho_l\,v_l^b \tag{5.4} $$

Another main result playing the key role in assessing the coolability of the debris bed is the duration of the reflooding process t_q. The model estimates the quench front velocity, and consequently the total duration elapsed to achieve a total quenching of a debris bed with height H. We are always interested in achieving the highest quench front velocity, or equivalently shorter quenching duration, in order to avoid the start of debris melting in the very hot zones. To achieve a faster quenching, one may intuitively think of increasing the injection flow rate, provided that this option is available. However, this initiative may not be the best option in terms of efficiency and steam production. This will be further discussed in the next section.

It is then important to assess the coolability chances of the reflooding. Among the other features, this is the most important because it determines whether the severe accident may be mitigated or further core degradation due to melting may occur. If the time required for reflooding the debris t_q is less than that needed to reach the melting temperature of the debris composed of corium t_m, the situation may be coolable. Otherwise, if the reflooding requires more time, the debris will attain its melting temperature sooner than the arrival of the quench front at some zones. Melting then occurs and the progress of the severe accident is resumed. In such situations a molten pool of corium is formed inside the reactor core and the molten material will to relocate to the lower zones of the reactor core. To address this problem, the impact of several parameters on the chances of coolability was investigated. In the model, for a debris bed of height H, the quenching duration is computed by:

$$ t_q = \frac{U^{qf}}{\mathrm{H}} \tag{5.5} $$

whereas, the time required to reach melting t_m is determined by the initial temperature of debris and the rate of temperature $\dot{\theta}$ increase due to residual heat. It is computed by:

$$t_m = \frac{T^{melting} - T^c}{\dot{\theta}} \tag{5.6}$$

During the quenching process, the energy deposited in the hot debris is extracted by water evaporation associated with steam production. Steam production may activate the exothermic oxidation of hot Zircaloy and release a significant amount of energy. The heat generated by this reaction is around 1.3 MJ per 1 kilogram of Zirconium. Moreover, this produced mass of steam M_{vap} is accumulated in the reactor core. Excessive steam production and release out of the core in the containment system lead to pressure build-up in the containment. If the containment pressure increases beyond its design pressure, around 7 bars for PWRs, and if the depressurization systems failed to cope with this pressure build-up, then the integrity of the containment is compromised. The mass produced is computed by:

$$M_{vap} = \phi_g^{out} \times t_q \tag{5.7}$$

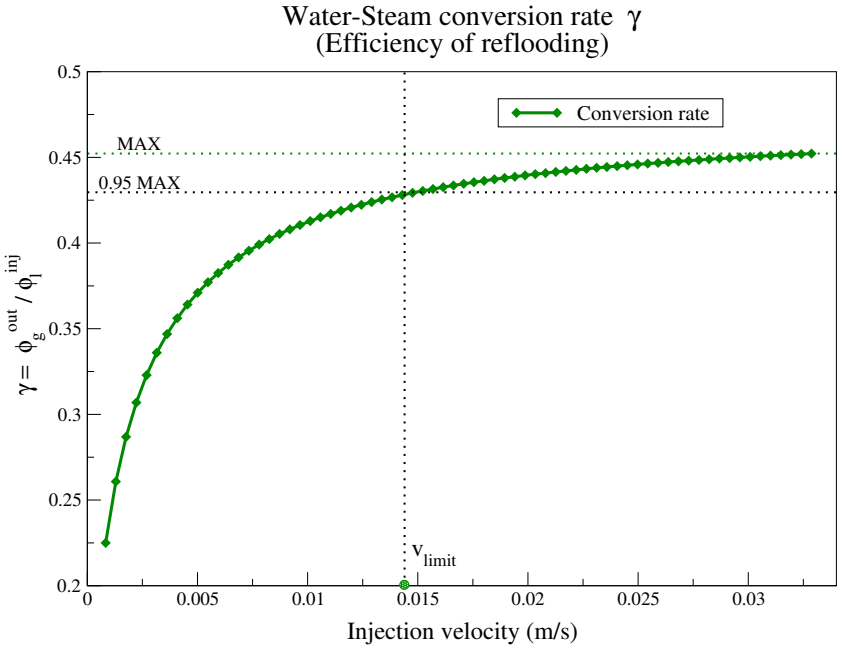

Figure 5.3: Conversion ratio γ as function of injection velocity v^{inj} - Efficiency of reflooding

5.2.4 Impact of injection flow rate

One of the key players in the reflooding process is the coolant injection flow rate. The relationship between the injection rate and the efficiency of reflooding is an important issue from the nuclear safety perspective. In order to obtain a faster quenching, i.e. high quench front velocities, the injection flow rate of water may be increased. Yet, at high injection flow rates, the efficiency of the reflooding process does not increase with further increase of the injected flow rate. This is clearly observed in Figure 5.3 which represents the variation of the water-to-steam conversion rate γ as function of the increasing injection velocity v^{inj}. At low injection velocities, we observe that the efficiency γ increases with increasing v^{inj}. However, at high injection velocities, the efficiency becomes flat and no longer increases with increasing injection flow rate. This indicates that there is an approximate maximum efficiency for the reflooding process for the considered reference calculation. This approximate maximum corresponds to a limiting injection velocity (v_{limit} on the graph). Beyond this limit, the conversion ratio starts to become flat and could only increase by less than 5%.

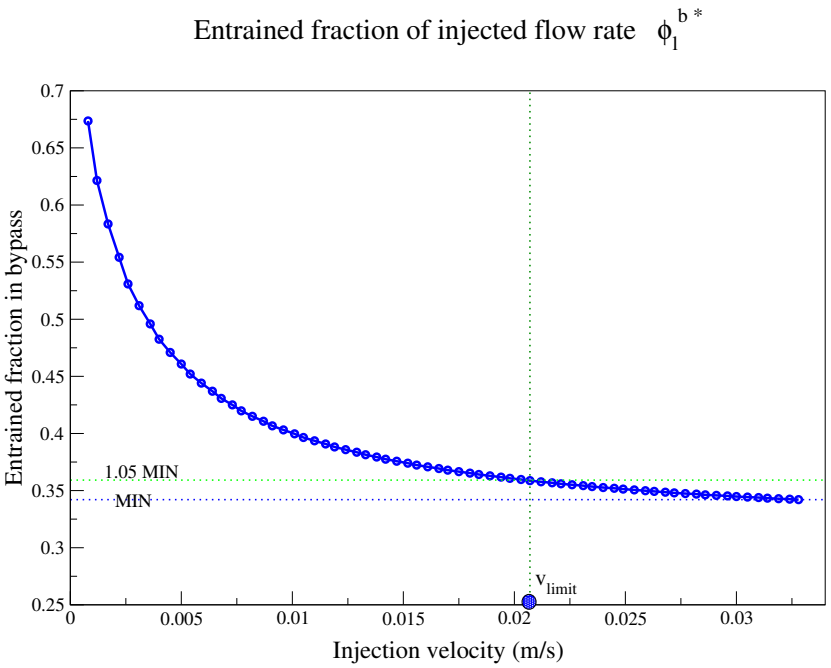

Figure 5.4: Entrained fraction of injected flow rate ϕ_l^{b*} as function of injection velocity v^{inj}

Moreover, the impact of the injection velocity on the entrainment behavior is inves-

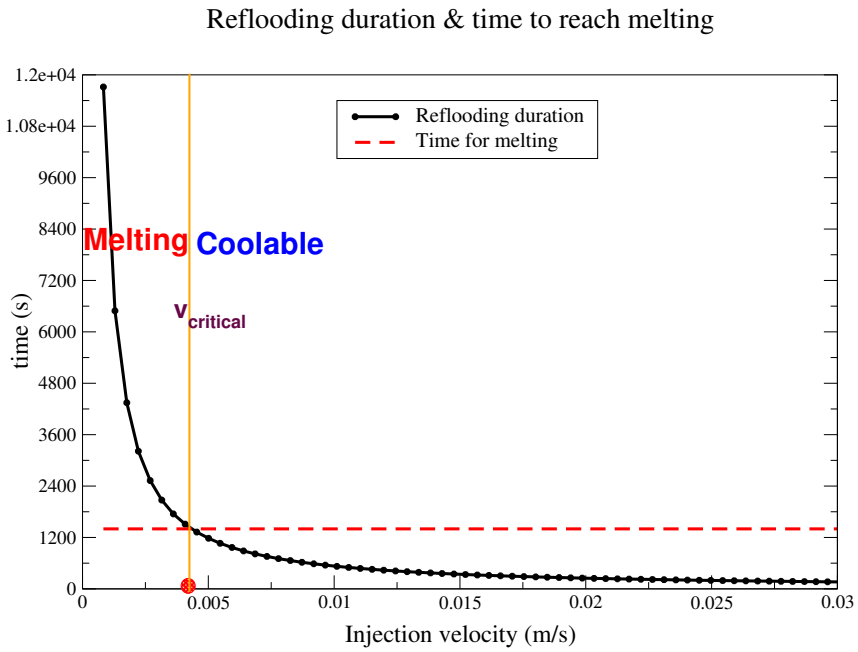

Figure 5.5: Quenching duration (solid lines) and time required to melt (dashed lines) the debris bed as function of injection velocity v^{inj}

tigated. Figure 5.4 represents the variation of the entrained fraction, of injected flow rate in the bypass, as function of the injection velocity. We observe that this fraction ${\phi_l}^{b*}$ decreases as the injection velocity v^{inj} increases, in the low velocity range. However, as the injection velocity becomes very high, the decrease of this fraction is ceased. We observe that the behavior of the entrained fraction as function of v^{inj} is opposite to that of the conversion rate where it has instead reached a minimal value. Yet, both of them become flat at high injection rates. And since we are interested in decreasing the fraction of entrained water flow rate in the bypass, increasing the injection flow rate beyond a limiting velocity (v_{limit} in Figure 5.4) helps in decreasing ${\phi_l}^{b*}$ only within 5% to the approximate minimum.

The mass of steam produced is directly related to the mass flow rate of steam exiting the debris bed and the duration of the quenching process. The model was based on mass and energy balance equations. So, if the initial energy and initial conditions are not changed, the mass of steam produced will remain constant. The initial energy deposited in the debris is extracted by water reflooding. At high injection velocities, high steam flow rate exits the debris system over a short quenching duration. Whereas, low steam flow rate exits the beds over a longer duration if the injection rate is low. In overall, the mass of produced steam M_{vap} remains the same with

varying injection velocity. This is due to fixing the temperature of the superheated steam exiting the beds at 1500°C since the model does not evaluate the dynamics leading to the estimation of the temperature of produced steam. The energy extraction by reflooding is achieved by evaporating water and producing steam. However, if the exiting steam is overheated, portion of the extracted energy has been consumed to overheat the steam. In other words, the overheating of steam is associated with lower steam production and vice versa.

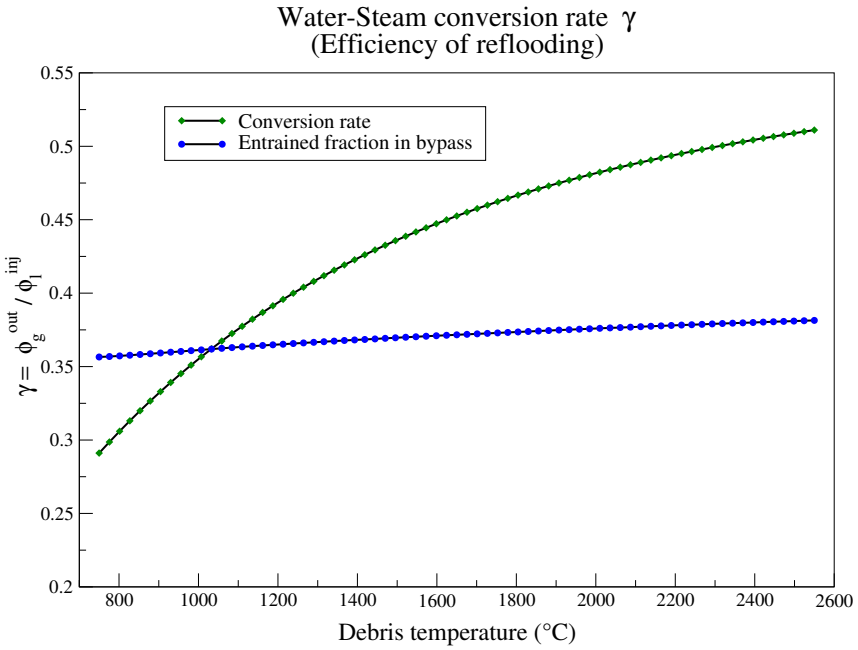

Figure 5.6: Conversion ratio γ and entrained fraction ${\phi_l}^{b*}$ as function of central bed debris temperature T^c

Having investigated the impact on other main results, the impact of the injection flow rate on the quenching duration also agrees with previous indications. Figure 5.5 represents the variation of the total quenching duration t_q and the time needed for the initiation of melting t_m as function of v^{inj}. We observe that increasing the injection rate, in the low velocity range, helps in quenching the debris system faster. But as the injection rate is increased, there exists a limiting injection velocity beyond which the quenching does not go any faster. That is approximately the minimal possible quenching duration for whatever injection flow rate. Moreover, at low injection rates, the considered configuration represents a critical situation. We observe that there is a critical injection velocity $v_{critical}$ defining the coolability criterion. In our case, it is approximately 4x10^{-3} m/s (around 15m/h). At injection velocities lower than

$v_{critical}$, the reflooding consumes a long time, enough for debris to start melting. This regime is also associated with the relatively low conversion ratio (efficiency) and high water entrainment in the bypass. At very low injection rates, the situation becomes drastic where the duration of quenching becomes very long (3.3 hours for an injection velocity of 7.2m/h, i.e. an injection rate of 82 m^3/h).

5.2.5 Impact of central bed temperature

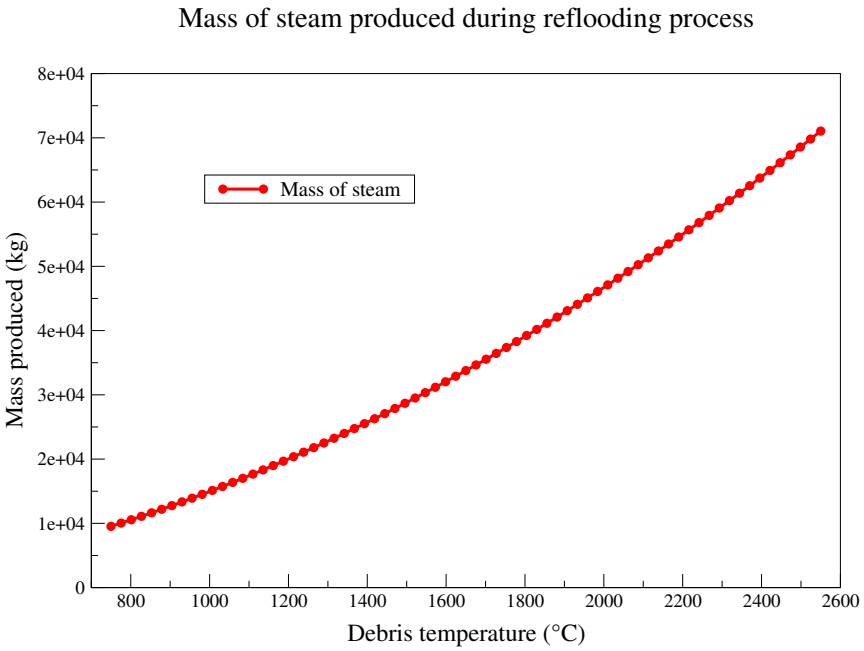

Figure 5.7: Mass of steam produced M_{vap} (kg) as function of central bed debris temperature T^c

Another key player in the reflooding process is the initial temperature of the inner debris bed which contains the greatest portion of the energy stored in the debris bed because it is larger, denser (lower porosity), and hotter than the bypass. The initial temperature T^c of the formed debris bed in an accidental scenario is a critical parameter when assessing the coolability of the debris. Provided that the debris undergoes continuous heating due to the residual power, we can determine the time needed for the initiation of melting of the debris. For the considered reference configuration, the initial temperature of the inner debris bed is varied between low temperatures up to the melting temperature of corium.

In this calculation only, more than one parameter is varied. For instance, it is highly

improbable to have the inner bed at much lower temperatures than a fixed bypass temperature at T^b=1500°C, or produce very hot steam at T_g^o=1500°C. So to conserve the physical reality of the situation, the bypass temperature and the exiting steam temperature are also varied keeping a 500°C difference, below T^c. The impact of those variations on the main results of the reflooding process is then investigated.

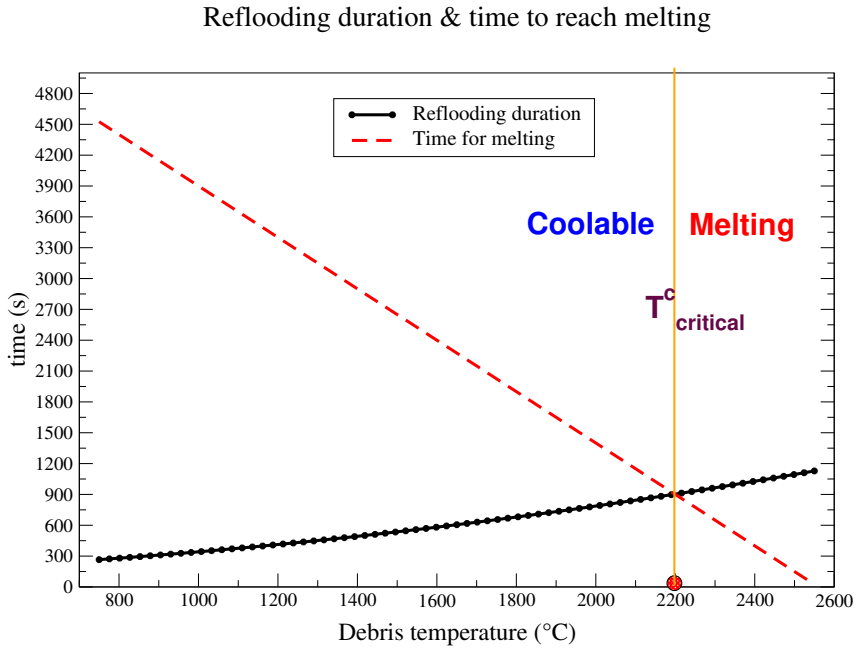

Figure 5.8: Reflooding duration t_q (s) and time need for melting initiation t_m (s) as function of central bed debris temperature T^c

The initial temperature T^c is varied between 750°C and 2550°C. As the temperature increases, the efficiency of the reflooding process increases as shown in Figure 5.6. This behavior reproduces the deduction from PEARL results (PA0, PA1, PA2) conducted at (150°C, 400°C, 700°C), where the conversion ratio records increased with increasing initial temperature (Figure 5.6). The efficiency keeps on increasing but on a slower rate as T^c approaches the highest temperature. The entrained fraction of injected rate ${\phi_l}^{b*}$ also increases, but slightly, for higher initial temperature T^c. On the other hand, the mass of steam produced increases significantly (Figure 5.7) at higher temperatures because in that case the debris is carrying a larger initial energy which has to be extracted.

Checking the coolability criterion with respect to the initial debris temperature, Figure 5.8 shows that the variation t_q and t_m as function of T^c. The time to reach

melting linearly decreases with increasing debris temperature whereas the quenching time increases. The increase in the quenching duration is due to the slowing down of the quench front velocity with higher debris temperatures evaporating larger portions of injected water (γ increases with T^c). For the considered configuration, the critical temperature defining the compromise of coolability because of melting initiation is around $T^c_{critical}$=2200°C. That is only 200°C higher than the that considered for the reference case.

5.2.6 Impact of central bed porosity

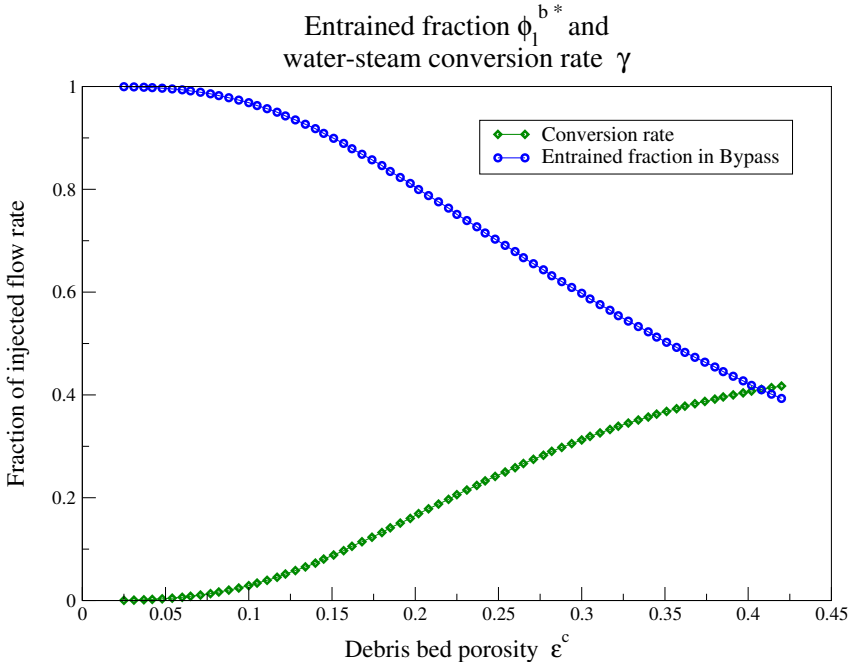

Figure 5.9: Conversion ratio γ and entrained fraction $\phi_l{}^{b*}$ as function of the central bed porosity ε^c

During an accidental scenario leading to the formation of a bed of particulate debris in the reactor core, as described earlier, several factors define the geometric properties of the bed like the porosity and the particle size. For the reference case, we have considered a 30% porosity for the inner hot bed. However, we need to understand the impact of the variation of porosity resulting from different hypothetical accidental conditions. To do that, an investigation on the impact of central bed porosity ε^c was performed. The porosity was considered to range from 42% (which is a typical value for debris beds composing spherical particles), describing a central layer yet

less porous than the lateral bypass, down to a porosity of 2% describing a very dense layer (compact bed).

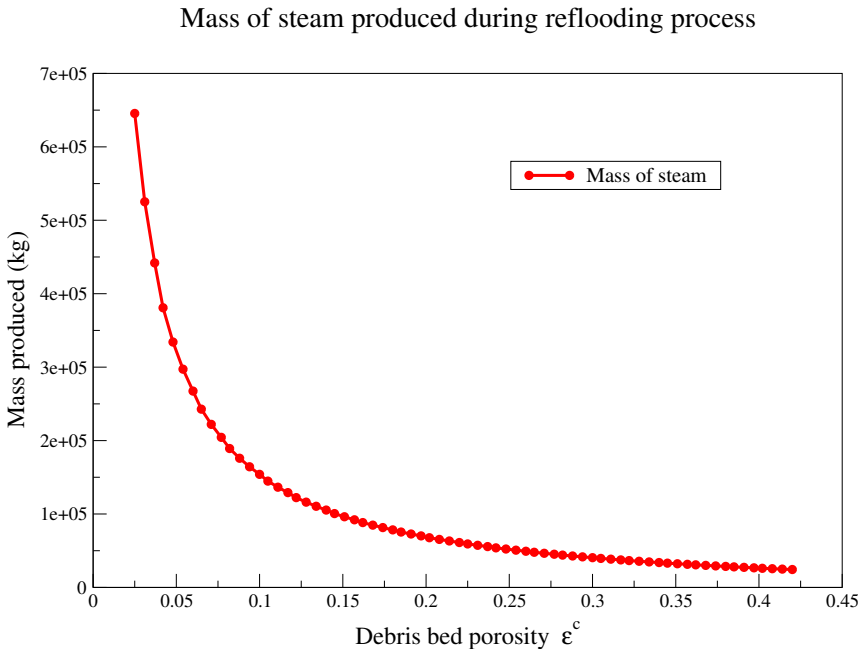

Figure 5.10: Steam production (kg) as function of the central bed porosity ε^c

The impact of varying ε^c on the conversion ratio and entrained fraction ${\phi_l}^{b*}$ is represented in Figure 5.9. It shows that the conversion of water to steam is more feasible when the inner hot bed is more porous. For very compact beds the conversion ratio decreases drastically. This is due to the fact the this porous layer became very dense, with very low permeability limiting the water penetration. In such situations, water will bypass the compact bed. This behavior is also observed in the corresponding variation of the entrained fraction in the bypass ${\phi_l}^{b*}$. For a less porous, and equivalently less permeable, inner bed becomes, larger fractions of injected water are entrained in the bypass. For a very dense debris layer in the center (2

Severe accidents leading to the formation of dense beds may present a critical situation. In fact for very low porosity, the mass of steam produced increases (as shown in Figure 5.10) increases significantly because the initial energy deposited in a denser debris is larger. Moreover, due to the decrease in permeability at low porosity, the limitation of water penetration into the central hot bed, leaves it uncovered for a longer duration. We observe in Figure 5.11 the variation of the reflooding duration and as function of the inner bed porosity. For very compact beds, the quenching

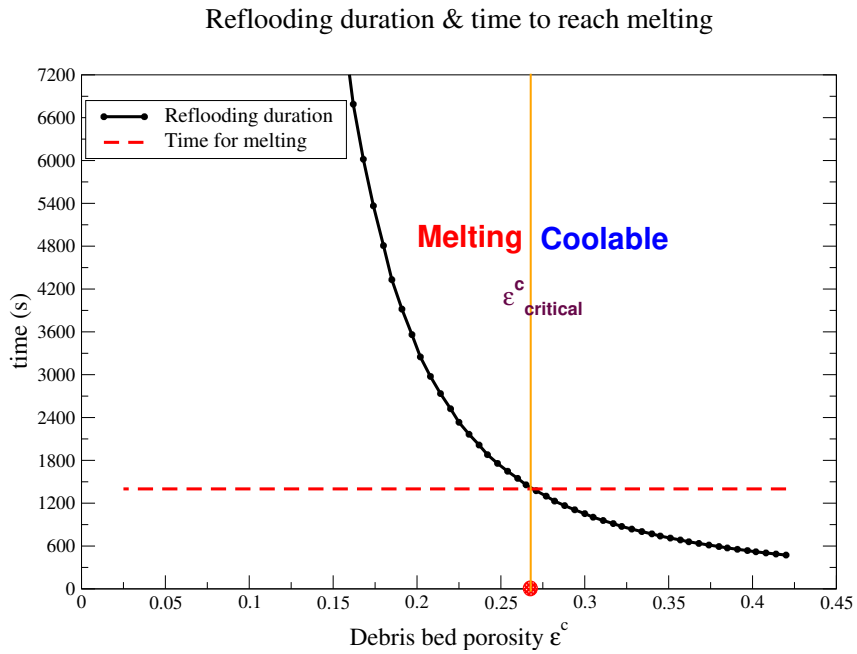

Figure 5.11: Reflooding duration (solid lines) and time to reach melting (red dashed lines) of the debris bed as function of central bed porosity ε^c

speed is poor where the reflooding duration increases significantly. A wider view of the curve is present in Figure A.4 in the appendix A. Considering the time to reach melting, we observe that there is a critical value for the central bed porosity $\varepsilon^c_{critical}$ for which melting, of the yet uncovered debris zones, occurs before the total quenching. For the reference configuration, $\varepsilon^c_{critical}$=0.27, which is 15% denser than the reference configuration (ε^c=0.42). This shows how the considered reference configuration presents a critical situation if the formed debris bed was denser. Further discussion about the sensitivity to the porosity on the impact of varying other parameters like the injection velocity, will be presented in the next section.

5.2.7 Impact of relative cross-section of the inner bed

The size of the formed debris bed inside the reactor core may vary by height and diameter. In the TMI accident, it was very wide and the bypass zone was relatively small. The reference calculation assumes an 85% relative cross-section of the inner debris bed to the whole reactor core cross-section. This means that the radius of the debris bed is around 90% of the external radius of the reactor core. The impact of the size of the inner bed with respect to its cross-section is investigated where the relative cross-sections, ψ, ranging between 2% to 98% were considered. Figure 5.12

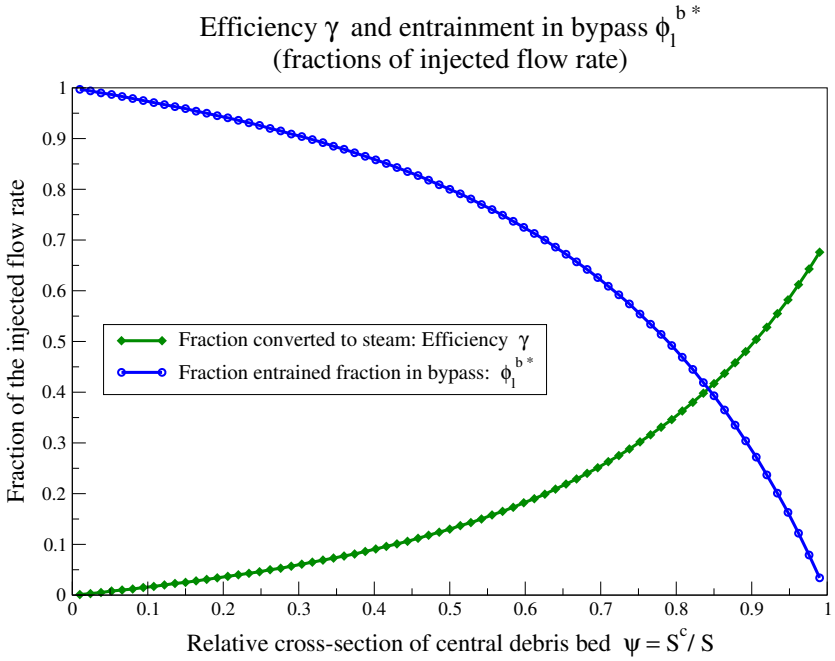

Figure 5.12: Conversion ratio and water entrainment as function of the relative cross-section of the central debris bed ψ

shows the variation of the conversion ratio (efficiency) and the entrained fraction of injected water with respect to the relative cross-section ψ. The conversion rate, efficiency, γ increases with increasing ψ while we observe an opposite behavior for the entrained fraction of water in bypass ϕ_l^{b*}.

For larger inner debris beds (i.e. thinner bypass), by cross-section, less fraction of coolant bypasses the hot bed. This behavior confirms that the presence of the bypass tends to reduce the efficiency of quenching, compared to the case without bypass. i.e. when ψ tend to 1, the bypass is very thin and no entrainment takes place (ϕ_l^{b*} tends to 0); the conversion ratio is then at its maximum ($\gamma \approx 0.7$). Moreover, the mass of steam produced (in Figure 5.13) increases linearly with the increase of the inner bed size and correspondingly the debris mass. The larger the hot debris bed is, the larger the energy to be extracted.

For small inner beds, the conversion ratio is reduced and the larger fractions of water are entrained in the bypass leaving the hot central bed uncovered for longer duration. This increase in the reflooding duration is shown in Figure 5.14 which describes the coolability chances depending on the cross-sectional size of the inner bed ψ. In the reference case, we considered a wide inner bed representing 85% by cross-section.

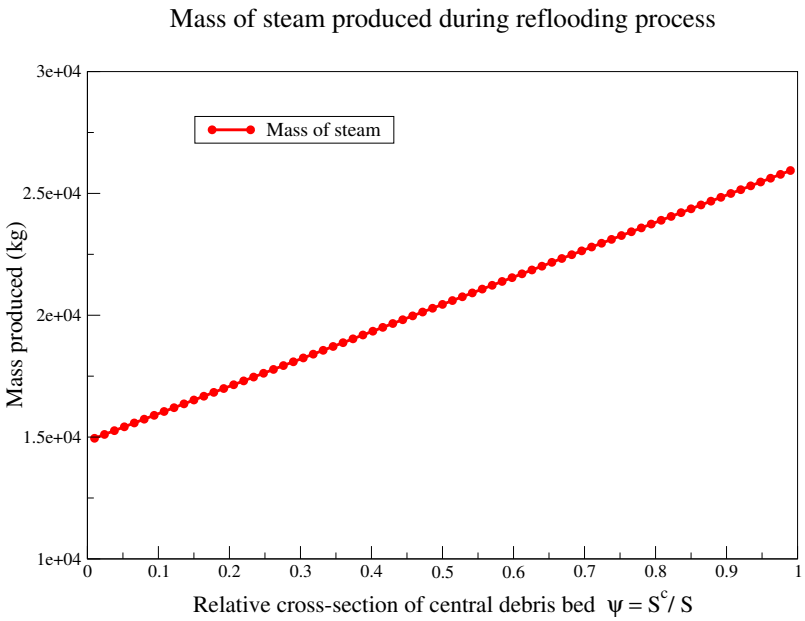

Figure 5.13: Steam produced M_{vap} as function of the relative cross-section of the central debris bed ψ

However, what if the accidental scenario leaded to the formation of an even smaller debris bed, by cross-section? It was obvious that the energy deposited in the debris is less (as shown in steam production variation in Figure 5.13), but that does not necessarily mean that extracting this lower initial energy will be easier. For smaller beds, the efficiency of the reflooding drops while larger fractions get entrained and do not participate in the quenching of the hot central bed. This behavior leads to slower quenching of the debris as shown in Figure 5.14. The quenching duration increases almost linearly for smaller inner beds between psi=0.98 and 0.5; but for lower psi, t_q increases at a higher rate. The critical relative cross-section for the reference case is $\psi_{critical}$=0.46. Debris beds smaller than that will involve melting at some debris zones before the arrival of the quench front.

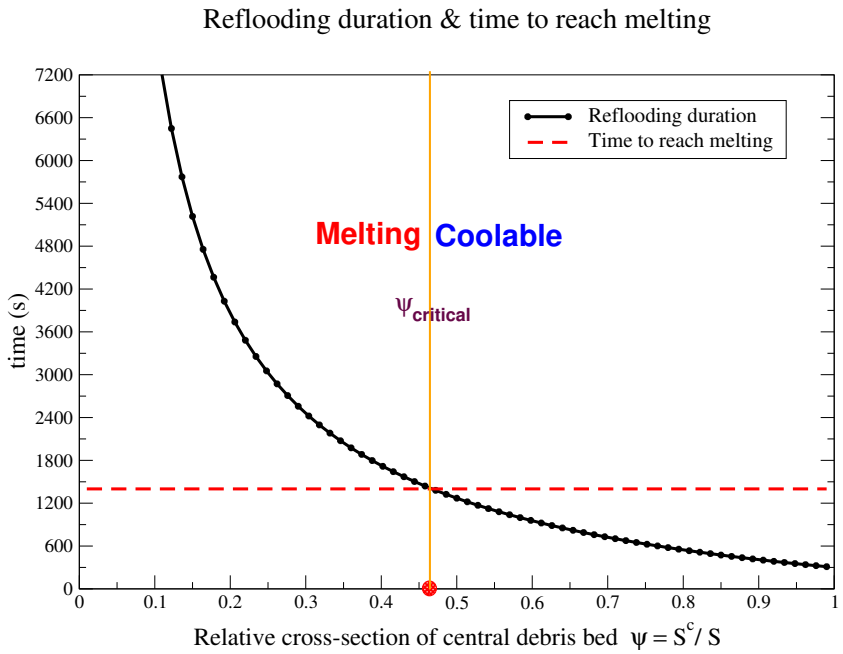

Figure 5.14: Reflooding duration and time to reach melting as function of the relative cross-section of the central debris bed ψ

5.3 Discussion

In the previous section, the impact of several parameters on the behavior of the reflooding process, concerning the main features: the water to steam conversion ratio, the entrained water fraction in the bypass, the steam production, and the coolability criterion, have been investigated. However, that investigation mainly focused on varying one parameter at a time. But to enlarge the scope of our understanding of the reflooding behavior we are also interested in investigating other situations than the considered reference case. In the presented investigation, we sometimes observed that reference value was not very far from the critical value of the investigated parameter, such as the temperature (reference=2000°C, critical=2200°C) or porosity (reference=0.42, critical=0.27), and sometimes farther (such as v^{inj}, reference=40 m/h, critical=15 m/h)). We are interested to in predicting the impact of varying another parameter. For example, how does the change of the initial temperature or porosity affect the trend defining the critical injection velocity? To answer that and go more thoroughly in assessing such situations, some cases were considered for investigation, mainly focusing on the coolability criterion.

5.3.1 Coolability

5.3.1.1 Impact of debris bed height and debris temperature

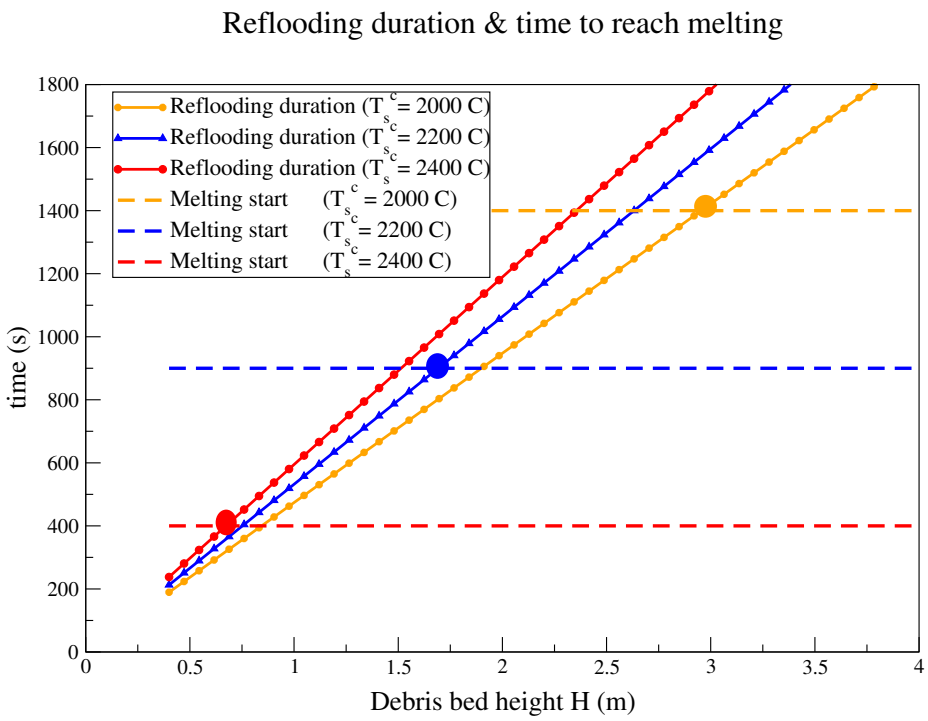

Figure 5.15: Quenching duration (solid lines) and time to reach melting (dashed lines) the debris bed as function of its Height for different initial debris temperatures Ti=2000°C, 2200°C, 2400°C

Considering that the central debris bed has attained a relatively high temperature upon the formation of a debris bed during a severe accident in the reactor core, calculations were performed in order to determine the chances of cooling such a debris bed depending on its hypothetical height inside the core.

For a certain hypothetically formed debris bed in the core of height H, the time required for quenching is determined by the quench front velocity.
Considering an initial temperature of 2000°C, the model estimates the quench front velocity, and consequently the duration of the reflooding process is determined. It was shown coolable for H=1 m. That will not be the case for larger beds. Figure 5.15, represents the time required for quenching and that for reaching the melting temperature as function of the height of the formed debris bed H. The intersection of each two corresponding curves (reflooding and melting), determines the maximum

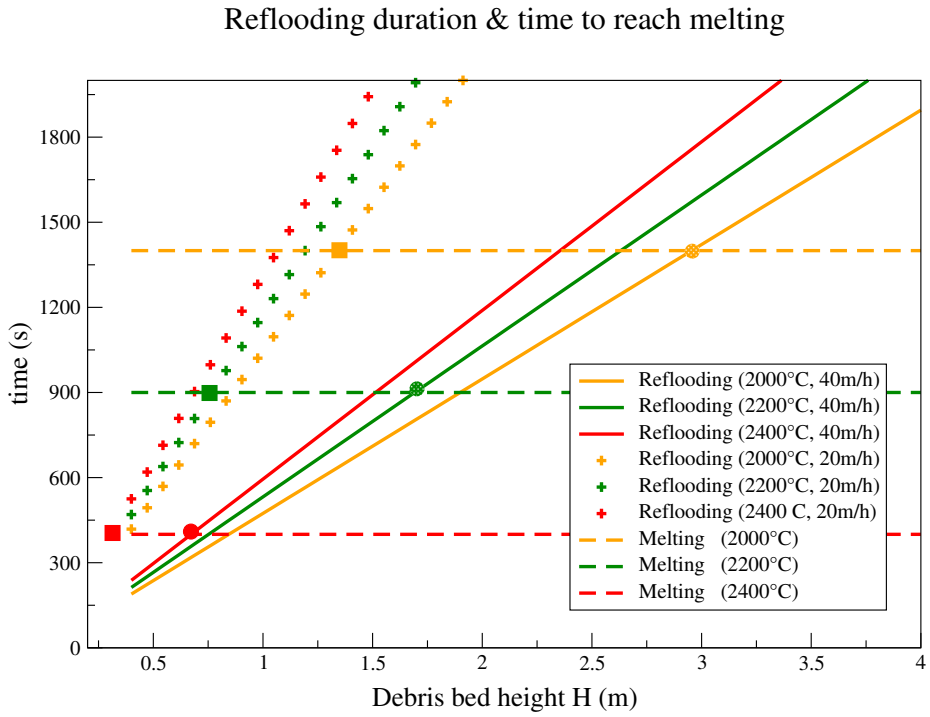

Figure 5.16: Quenching duration (solid lines) and time to reach melting (dashed lines) as function of its Height for different initial debris temperatures Ti=2000°C, 2200°C, 2400°C, and different injection velocities v1=40 m/h and v2=20 m/h

height (or critical height $H_{critical}$) of the debris bed for a coolable situation. Beds larger than that will experience melting stat at the hot zones prior to achieving the total quenching of the debris bed.

In other calculations, we consider that the debris bed has attained higher temperatures prior to the start of reflooding. Two situations with initial temperatures 2200°C and 2400°C were considered. The quench front velocity is estimated by the model and the quenching duration is determined as function of the debris bed height. Figure 5.15 shows the variation of the quenching time and that needed to reach the melting temperature for those situations. We observe that in some situations, the coolability of the debris is compromised. If the debris bed height is larger than a critical height, melting of the debris occurs. The critical bed height decreases with increasing debris temperature T^c. For the reference case with an initial debris temperature of 2000°C, the coolability is compromised if the height of the debris bed is larger than 2.9 m, this corresponds to a duration of 23.3 minutes for the investigated situation. However, if the initial temperature was greater by 200 degrees (case of

2200°C), the coolability is then compromised at an $H_{critical}$=1.7 m only, corresponding to a duration of 15 minutes. At even a higher temperature T^c=2400°C, $H_{critical}$ is further reduced to 0.65m and should be reflooded within 6.7 minutes.

This indicates that the initial temperature of the debris bed formed during a severe accident plays an important role in predicting the coolability chances. The critical height for a coolable debris bed decreases with increasing debris temperature. In the investigated cases, this decrease was sharp because the temperatures are relatively high, close to the melting temperature. For a lower temperature range, the critical height can be shown to decrease with increasing debris temperature as well, but at a slower rate.

5.3.1.2 Impact of debris bed height and a combination of parameters

Considering the failure of the safety injection systems to deliver sufficient injection rates due to water unavailability or a break depriving the pumps from water feeding, or due to lack of power feeding such as during a station black-out scenarios, the water injection rate is then reduced. In this situation, the effect on the coolability is investigated by cutting the injection flow rate of the reference calculation in half. For an injection flow rate at 20 m/h, the quench front progresses slower through the hot debris and the reflood duration increases. Figure 5.16 represents the variation of the reflooding duration and the melting time as function of the debris bed height starting from different initial temperatures and being reflooded at different injection velocities.

Cutting the reference injection velocity by half to 20 m/h, changed the situation drastically. The critical height was reduced by more than half for all the cases. For the reference case at 2000°C initial debris temperature is reduced from 2.9m to 1.3m. For the calculations at higher temperatures, closer to the melting temperature of corium. At 2200°C and 2400°C, cutting the injection rate in half, the debris becomes vulnerable to melting if the bed height is larger than 0.75m rather than 1.7m, and 0.3m rather than 0.65m, respectively. This indicates that the coolability of the debris bed can be drastically compromised if the capacity of delivering the coolant is reduced especially when the debris temperature is higher.

In another example, a combination of parameters are changed: debris height H, porosity ε^c, injection velocity v^{inj}, and the debris temperature T^c. Figure 5.17 shows the coolability criterion considering 3 cases with different conditions. They are named as (T^c, v^{inj}, ε^c). We may observe that:

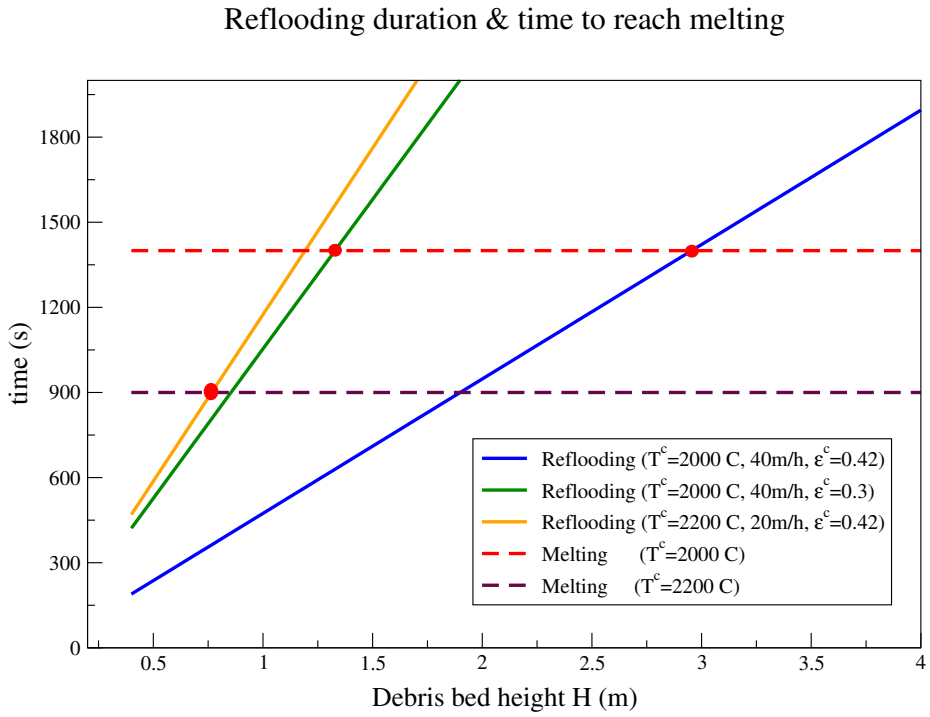

Figure 5.17: Quenching duration (solid lines) and time to reach melting (dashed lines) as function of its Height for different initial debris temperatures T^c, injection velocity v^{inj}, and porosity ε^c

- shifting from the reference case of (2000°C, 40m/h, 0.42)-Blue curve, to another with denser central bed (2000°C, 40m/h, 0.3)-Green curve, reduced the critical bed height from 2.9m to 1.25m.

- shifting to another situation at higher temperature and reflooded at a lower injection rate (2200°C, 20m/h, 0.42)-Orange curve, has also reduced the critical height even further, from 2.9m to 0.75m.

The investigated cases in this section are not generic. The initial and boundary conditions and the geometry and particle size of the debris also play their roles. In such investigations, the determination of a reference case is just indicative. While the need to assess the impact of each parameter is important in order to predict the possible outcomes of the reflooding process, the proposed model can be used to perform this task efficiently.

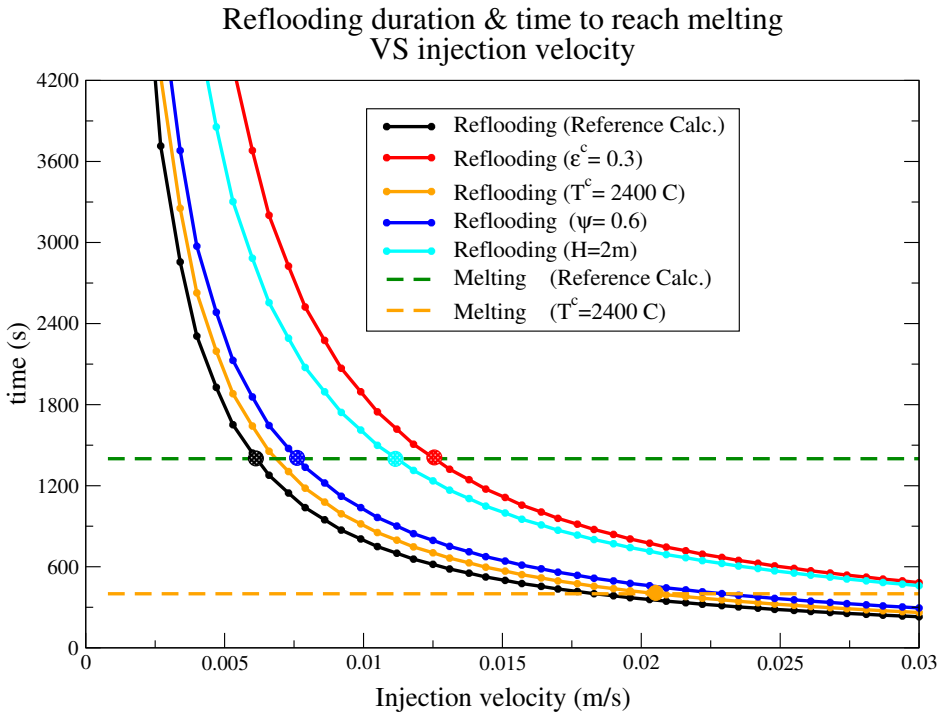

Figure 5.18: Quenching duration (solid lines) and time to reach melting (dashed lines) as function of injection velocity for different initial debris temperatures T^c, porosity ε^c, bed height H, and relative cross-section of inner bed ψ

5.3.1.3 Impact of injection velocity

The impact of the injection velocity on the reflooding process was investigated and it was shown that there exists a minimal critical value $v_{critical}$ necessary to avoid melting of the yet uncovered part of the debris. However, that critical value (around 7.2m/h) corresponds exclusively to the considered configuration with specific initial and boundary conditions. Interested in understanding the behavior in other situations, some parameters were changed. Figure 5.18 represents the variation of the time for quenching t_q and melting t_m, considering different configurations and initial conditions than the reference case. In the figure, the of variation of t_m as function of v^{inj} for the reference case is shown in black curve. The other curves correspond to additionally changing another parameter in favor of the accident progression, as follows:

- Orange curve: Considering a higher initial temperature for the debris (T^c=2400°C, i.e. 400 degrees greater than the reference case), the critical injection velocity $v_{critical}$ is approximately 2.1x10^{-2} m/s. It has increased significantly from

7.2m/h for T^c=2000°C to 75.6 m/h for T^c=2400°C, equivalent to a necessary injection rate around 860 m^3/h.

- Blue curve: Reducing the size of the inner bed by cross-section to psi=0.6, we observe that $v_{critical}$ has also increased, but slightly, to 7.5x10^{-3} m/s, equivalent to 27 m/h and a necessary injection rate around 306 m^3/h.
- Light blue curve: Assuming a larger debris bed by height with H=2 m (double the reference height), $v_{critical}$ increases significantly to 1.15x10^{-2} m/s (or 41.4 m/h at an injection rate of 470 m^3/h).
- Red curve: Considering that the formed inner debris bed was even denser (i.e. lower porosity), ε^c=0.3, we observe the greatest increase among the studied cases where $v_{critical}$ increases to 1.25x10^{-2} m/s (or 45 m/h at an injection rate of 510 m^3/h).

This provides two main deductions. Firstly, this investigation proved that the critical values can not be generalized but rather depend on the considered situation, and the variation of the main reflooding features with respect to a studied parameter will follow a different trend when starting from another value of other parameters. Secondly, considering the impact of additionally changing some parameters, we observe that the critical value is sensitive to some parameters more than others. For instance, we may deduce that coolability is more sensitive to the porosity of the debris and its initial temperature more than its size.

For a larger debris bed by height (H=2m). The initial energy E_H to be extracted from the central bed is:

$$E_H = \int_{T^{sat}}^{T^c} M c_{ps} dT \tag{5.8}$$

with c_{ps} being a linear function of temperature provided in Eq. 5.1, T^{sat}=133°C;

$$E_H = \int_{T^{sat}}^{T^c} M[316 + 0.2213(T^c - 400)]dT \tag{5.9}$$

and M being the debris mass:

$$\begin{aligned} M &= \rho_s V_s = \rho_s \, H \, S^c \, (1 - \varepsilon^c) \\ &= 8000 kg.m^{-3} \times 2m \times 9.63 m^2 \times (1 - 0.42) = 8.945 \times 10^4 kg \end{aligned} \tag{5.10}$$

Hence for the reference case but 2m height debris bed E_H=8.9789x10^{10} J. While for

the reference case but with higher debris temperature T^c=2400°C, E_T=5.1482x10^{10} J. And for the case with a denser central bed, ε^c=0.3, the energy to be extracted is E_ε=5.418x10^{10} J. Even though the initial energy to be extracted is lower for the case of a denser bed and the one with higher initial temperature than that of a larger debris bed (2m height):

$$E_T < E_\varepsilon < E_H \tag{5.11}$$

we observe that the critical injection velocity behaves oppositely and it is highest for the case of a denser bed. This proves how the coolability of the debris is more sensitive to the permeability and the temperature of the debris rather than its size, for a given initial energy, and in some cases even lower initial energy for dense particulate hot beds than larger beds by height. This is an indication of the important effect of limiting the coolant access on the coolability of a formed debris bed during accident scenario.

5.3.2 On entrainment

In the previous section 5.1 investigating the PEARL test, the impact of the injection rate on the entrainment behavior was observed in the tests P3-10, P3-8, and P3-4. Those test performed at same debris temperature (700°C) and pressure P=3 bars, and at water injection velocity: 5 m/h, 7.5 m/h, and 10 m/h respectively. Observing the records of those test with increasing v^{inj}, the entrained water velocity v_l^b in the bypass and its ratio to the injection velocity v_l^b/v^{inj}, they increase with v^{inj}. One can clearly deduce that the entrained flow rate ϕ_l^b is increasing; but may we also deduce that the entrained fraction $\phi_l^{b*} = \phi_l^b/\phi^{inj}$ also increases?. If true, that shows some kind of inconsistency with the results obtained by the proposed analytical model concerning the impact of increasing the injection velocity on the entrained fraction in the bypass ϕ_l^{b*}, as was shown in Figure 5.4 (i.e. with increasing injection rate, the entrained fraction was monotonously decreasing). However, this does not represent an inconsistency for three main reasons:

1. As discussed in section 5.1, the records of entrained velocity can not represent the entrained flow rate without the determination of the void fraction in the bypass α^b. Hence, without void fraction measurements, the increase in the ratio of v_l^b/v^{inj} does not necessarily induce and increase of ϕ_l^b/ϕ^{inj} which should take the water saturation into account.

2. The PEARL debris bed has a different geometry than the reference case at reactor scale. For PEARL, the permeability contrast is C_κ=4, and relative

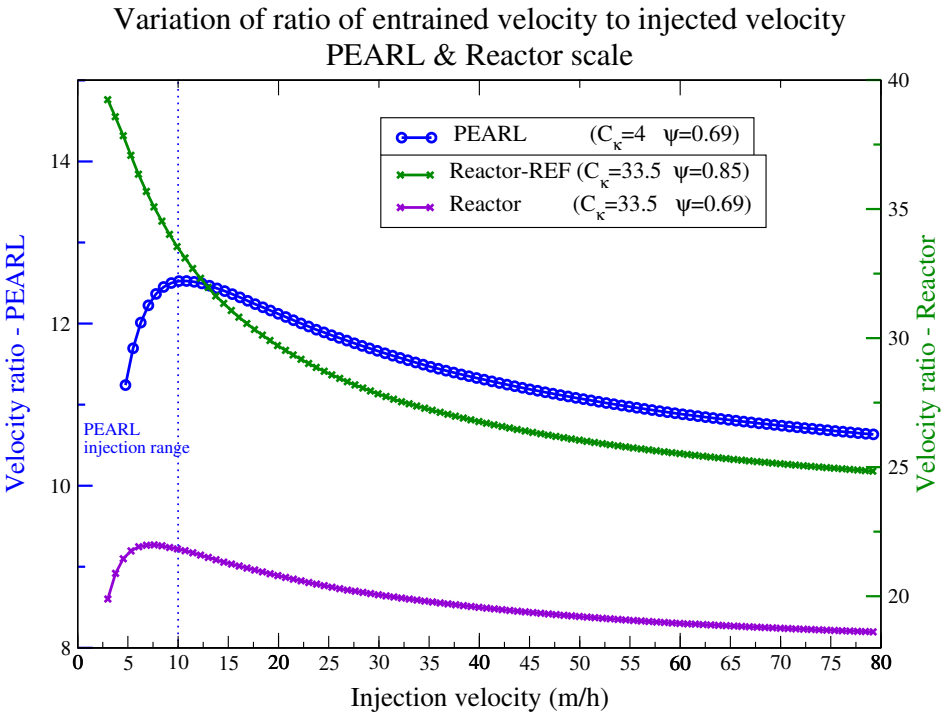

Figure 5.19: Ratio of the entrained water velocity v_l^b/v^{inj} to the injected velocity Vs injection velocity v^{inj}. PEARL scale -(BLUE curve Y-axis left), Reactor - Reference case -(GREEN curve Y-axis right), and Reactor scale (smaller ψ -Violet curve Y-axis right).

cross-section ψ=0.69. While for the reactor scale reference case: C_κ=33.5 and ψ=0.85

3. The thermal-hydraulic conditions are different, and in fact the range of injection velocity used in PEARL tests (5 to 10 m/h) is low and very narrow compared to the range considered in the investigations.

The first reason has been already discussed (section 5.1). Concerning the other two reasons, 3 cases were considered and investigated to develop the reasoning:

1. PEARL scale (T^c=700°C, P=3bars, C_κ=4, ψ=0.69)

2. Reactor scale (Reference case)

3. Reactor scale (Reference case but ψ=0.69)

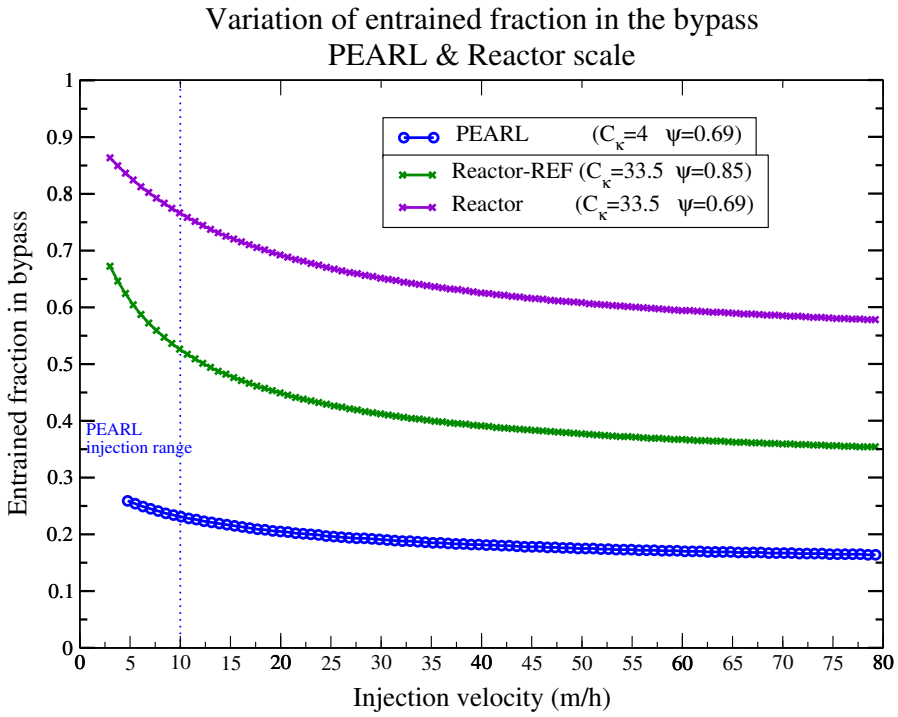

Figure 5.20: Entrained fraction ϕ_l^{b*} Vs injection velocity v^{inj} for PEARL scale - BLUE, Reactor scale (Reference case) -GREEN, and Reactor scale (smaller ψ) - Violet.

The contrast in permeability C_κ is the ratio of the permeability in the bypass to that in the center. Figure 5.19 shows the variation of the ratio of entrained water velocity in the bypass to the injected velocity v_l^b/v^{inj} for the reactor scale cases and PEARL, as function of increasing injection velocity. In PEARL, we observe an increase of the ratio up to an injection velocity around 12 m/h and then it decreases. For the reactor scale, on one hand we only observe a decrease of that ratio in the reference case considered. While on the other hand, when the relative cross-section is smaller as PEARL (ψ=0.69), the behavior seen in PEARL is reproduced, with the maximum at v^{inj}=7 m/h. That behavior included two main trends, an increasing trend of the ratio in a very short and low range of injection velocity and then a monotonous decrease. Hence, the model does reproduce what is measured in PEARL: An increase in the ratio of the entrained velocity to the injection velocity. Yet, to validate the result produced by the model, experimental PEARL tests at higher injection rates have to be conducted. The obvious differences in magnitude between the cases is due to the permeability contrast difference as well as debris temperature (between

reactor scale and PEARL) and because of the difference in ψ between the two case at reactor scale.

Moreover, having reproduced the behavior of v_l^b/v^{inj} recorded in PEARL, we are interested in investigating the behavior of ϕ_l^{b*} and comparing it to that presented earlier in the previous section. Figure 5.20 represents the variation of ϕ_l^{b*} for the three considered cases. We observe that despite the ratio, v_l^b/v^{inj}, of entrained velocity to injected one was increasing for PEARL (case.1 Blue) and reactor scale with ψ=0.69 (case.3 Violet), the entrained fraction of injected flow rate was monotonously decreasing over the whole range of the injection velocity. It did not behave strictly as v_l^b/v^{inj} because it also takes into account the water saturation in the bypass (or 1 - void fraction), which also varies.

The entrained fractions showed a significant difference in magnitude. Between PEARL (case.1) and the Reactor scale (case.2 and case.3), the reason is the difference in the permeability contrast. The reactor scale case considers a permeability contrast 8 times higher than PEARL (33.5 to 4), where the bypass is much more permeable that the center. That was initially considered to represent the presence of a zone with intact fuel assemblies surrounding the formed debris bed. Between the two reactor scale considered cases, for the case with smaller ψ the estimated entrained fraction in the bypass was larger simply because in this case the relative cross-section of the bypass is larger (1-ψ).
In order to investigate the impact of the permeability contrast C_κ more thoroughly, a comparison between PEARL and reactor scale reference case was performed estimating the variation of the fractions distribution of the injection flow rate with injection rate. Figure 5.21 represent the variation of the distribution of the fraction of injected flow rate, namely:

- $\phi_l^{c-inlet}$: inlet fraction into the central bed
- $\phi_l^{b-inlet}$: inlet fraction into the bypass
- ϕ_l^{b*}: entrained fraction in the bypass
- γ: fraction converted to steam

At the bottom of the debris bed, and up to the quench front level, the water flow rate injected into the debris bed composed of two layers of contrasting permeability will be decomposed among the layers into two complementary portions; $\phi_l^{c-inlet}$ into the center and $\phi_l^{b-inlet}$ into the bypass. Afterwards, a water fraction progresses in the center at the quench front speed, a water fraction is entrained in the bypass ϕ_l^{b*},

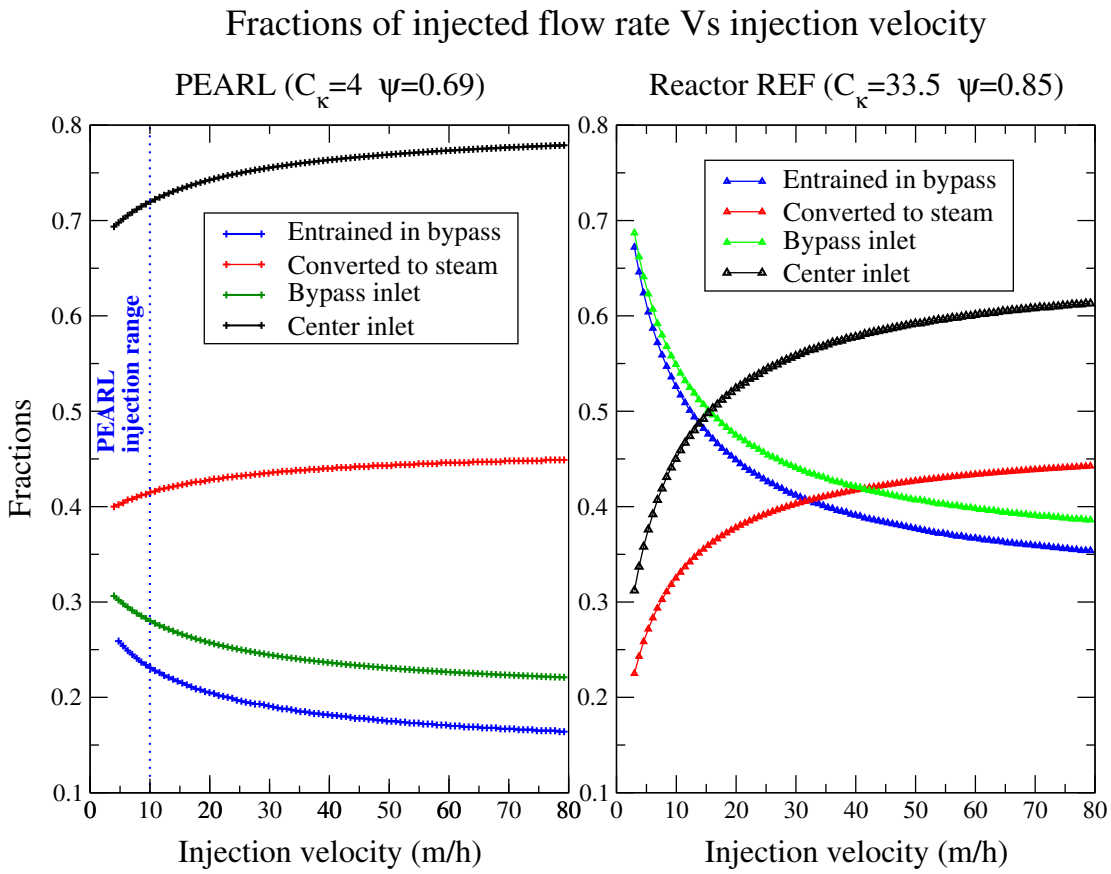

Figure 5.21: Variation of injection flow rate distributed fractions as function of injection velocity v^{inj} for PEARL scale -left, and Reactor scale (Reference case) -right

and another fraction has already evaporated producing a steam γ. The way those fractions are distributed relies on the geometry of the two-layered debris bed, and most importantly the contrast in permeability C_κ. We observe that for the PEARL case, with lower C_κ, in the PEARL tested velocity (i.e. low range: 5 to 10 m/h), the inlet fraction of injected flow rate entering the center is (Black-left) is around 70%. It is higher than that entering the bypass (Green-left), around 30%. To the contrary, in the same injection velocity range (less than 10 m/h), we observe an opposite distribution for the reactor scale reference case. The fraction at the inlet of the central bed is only around 30% with 70% being injected in the bypass. **This shows how the contrast in permeability C_κ induces a redistribution of the injected flow rate among the debris layers. In the considered reference case, 70% of the injected flow were redistributed into the bypass which**

forms only 15% of the total cross-section (1-ψ). And as we observe that the entrained fraction in the bypass trends as the water inlet fraction, we deduce that the contrast in permeability is an important factor describing the water entrainment.

Moreover, the impact of the injection velocity is also observed. At higher v^{inj} we observe a similar trending of $\phi_l^{b-inlet}$ and $\phi_l^{b-inlet}$ between the two cases where $\phi_l^{b-inlet}$ always decreases with increasing v^{inj}, to a certain limit. And $\phi_l^{c-inlet}$ increases with injection velocity, also up to a certain limit beyond which it becomes almost constant. **This indicates that the central debris layer receives larger fractions at higher injected flow rate. Whereas the bypass receives fewer.** That is in favor of quenching, and it is also shown in the variation of the converted-to-steam fraction (for both cases), at higher rates, larger fractions are used to cool down the hot debris. Concerning the impact of C_κ at higher injection rates, we observe that the variations of the distributed fractions in the PEARL case (with C_κ=4) were small compared to the variations in the reactor scale reference case (with C_κ=33.5). In the latter case, we observe a 30% decrease of the inlet flow rate into the bypass from 70% at low injection rates to 30% at high injection rates. To the contrary, this drop was only around 10% in the PEARL case.

5.4 Conclusions

An investigation of the reflooding of a heterogeneous debris bed composed of two coaxial layers of contrasting permeability was conducted. The proposed analytical model was implemented to obtain estimations on the main features of the reflooding process, mainly the conversion ratio, the entrained water fraction, and the coolability of debris. A comparison of the model estimations against PEARL experimental results was presented. The model provided acceptable results for the quench front and the bypass entrained water velocity. The behavior observed in PEARL measurements when changing some boundary conditions was reproduced by the model.

However, the PEARL configuration with its initial and boundary conditions does not fully describe the situation that may arise during an accidental scenario in a nuclear reactor core leading to the formation of a hot bed. The temperature of the debris and the delivered injection flow rates were relatively small. And to understand the behavior of reflooding a debris bed as that formed in a hypothetical accidental scenario, a reference configuration was considered. It was based on the results of the post-accident examination of the TMI unit, and some other conditions that are likely to describe a debris bed formed in that situation. The impact of several parameters,

on the main features of the reflooding process, was investigated. It showed the existence of limiting and critical values of the parameter under investigation. The limiting value represents the value for which increasing or decreasing the parameter will not change the result and will only induce less than 5% increase or decrease, towards the maximum or minimum of the conversion ratio or the entrained water fraction in the bypass. Whereas the critical value represents the necessary condition in order to avoid the melting of the yet uncovered debris zones.

Special attention was given for the PEARL possible deductions, and their compatibility with the modeled results. The model reproduced the main behaviors identified in the PEARL test. An emphasis on the specificity of the PEARL geometry with was made upon the permeability contrast of the debris layers.

The coolability of a heterogeneous debris bed is investigated, but the considered situations for coolability assessment can not be generalized. Each situation has its unique geometry, bed composition, initial and boundary conditions that should be taken into account to predict the coolability chances. However, the behavior of the reflooding process is described and the impact of the initial and boundary conditions, as well as the geometry of the debris bed, is studied. The conclusion about the behavior of the reflooding process and the impact of each of the considered variables can be taken into account when addressing the coolability chances. The proposed model can be implemented to assess rapidly the chances of coolability during the reflooding of a considered debris bed surrounded by a bypass of larger permeability. It can be also used to investigate the effect of initial or boundary condition or bed composition on the coolability of such a debris system with predefined conditions.

For a given initial energy carried by the debris bed, the coolability is more sensitive to the permeability and the temperature of the debris rather than its size, and in some cases even for 10 times lower energy for dense particulate hot beds than longer beds. Limiting the coolant access into the debris bed has a dominant impact on the coolability of a hot debris bed formed during accident scenario.

The contrast in permeability is an important factor describing water entrainment in the bypass. It controls the redistribution of the injected flow rate among the debris layers. In the considered reference case, 70% of the injected flow were redistributed into the bypass which forms only 15% of the total cross-section (1-ψ). But that was the opposite for PEARL.

At higher injection rates, the central debris layer receives larger fractions whereas the bypass receives fewer. The change in the inlet fractions between the low and high

velocity range depends mainly on the permeability contrast. With higher contrasts, a larger difference between the inlet fractions was observed.

The investigated cases are not generic. The initial and boundary conditions, the geometry and particle size of the debris also play a role. The determination of a reference case is just indicative. And the need to assess the impact of each parameter is important in order to predict with confidence the possible outcomes of the accidental scenario. The proposed analytical model is capable of performing those tasks in a relatively short time and predicting the main outcomes of reflooding a superheated heterogeneous debris bed vertically stratified, like the situation of debris bed surrounded by intact assemblies in a highly degraded nuclear reactor core.

Chapter 6

General Conclusion

Contents

In this thesis, we have studied the progression of the quench front in a debris bed, when the latter is surrounded by a more permeable or porous zone. This situation is very likely to occur during reflooding of a strongly degraded reactor core. Indeed, the residual power deposition is not homogeneous, which leads, in most of the accident situations studied, to a more advanced state of degradation in the center. On the contrary, at the periphery, the core is less damaged, which results in lower friction coefficients (permeability, passability). If a partial melting has occurred in the center, one can even end up in a situation where the center is less porous (more compact) than the periphery. In order to study these configurations in an analytical way, they have been simplified in the form of two concentric porous media, the main medium, in the center, being surrounded by a more permeable (and possibly more porous) zone. It is in this geometry that we have studied the progression of water, being injected from below. It is the same configuration that has been studied experimentally on the PEARL facility of IRSN. The results of some PEARL tests were used in this thesis to understand some of the physical phenomena characteristic of this type of system and to validate the proposed modeling. The main conclusions of the thesis work are recalled here, beginning with the physical understanding and then describing the advances made in modeling.

6.1 Conclusions about the physical behavior

When water is injected into a vertically stratified and superheated porous medium, a large flow of steam is generated and distributed between the central debris bed and the peripheral zone. As the pressure drops are lower at the periphery, the surface flow rate of steam is greater than in the center, which results in a large radial flow of steam from the central zone to the periphery. As shown in Chapters 3 and 4, using Icare/Cathare calculations, this transverse redistribution of steam occurs over an area just above the quench front, and covering about a third of the debris bed in most of the cases studied (a few tens of centimeters). Downstream from this zone, there is no more redistribution of steam and no more radial pressure gradient: the pressure is practically uniform between the center and the bypass. For the liquid phase, under certain conditions identified in the thesis (high injection rate, low pressure), there is also a large mass transfer from the center to the periphery, caused by the overpressure in the center and the strong radial flow of steam. However, this redistribution of water occurs over a much smaller zone than the redistribution of steam, only a few centimeters downstream of the quench front. This can be understood easily since it is the area where there is simultaneously a large volume fraction of water (low void fraction) and the maximum overpressure in the center. Beyond this zone, the conditions (high void fraction and lower pressure difference) are not

favorable to a redistribution of water to the bypass, which is obvious in the calculations. However, the primary factor determining the water flow rate in the periphery (bypass) is the distribution of injected water at the inlet of the debris layers which is described by several factors: the contrast in permeability between the layers, the injection flow rate, and the ratio of the inner bed cross-section to the total. Downstream of this zone of radial redistribution of water (for the conditions identified), the bypass is filled both with water at low velocity (of the order of mm/s) and steam at high velocity (of the order of m/s). This results in an increase in the velocity of water in the bypass, which becomes significantly faster than the velocity of the quench front. It is this phenomenon that has been called "2D progression of the quench front" because this progression is faster in the periphery than in the center. When this phenomenon does not occur, the rate of progression of the quench front is the same everywhere and corresponds to what has been called a "1D progression", i.e. a flat quench front. At the scale of the debris bed, the 2D progression results in a water release above the debris bed before the complete cooling of the whole bed. Depending on the conditions, this entrainment of water above the bed can occur very quickly after the start of the cooling, as it has been observed experimentally. This effect has several consequences. On the one hand, it decreases the efficiency of the reflooding because a part of the injected flow circulates only in the peripheral bypass and does not contribute to the cooling of the main bed. This results in a decrease in the conversion rate, as shown in this work (this rate corresponds to the ratio between the flow of steam produced and the flow rate of water injected). On the other hand, it slows down the progress of the quenching front in the main debris bed because the flow of water entering this bed is decreased. However, this effect is not preponderant and, overall, the complete quenching time always decreases when the injected overall flow rate increases. Finally, a final consequence of the water entrainment in the bypass is the accumulation of water above the debris bed during the reflooding, which has the effect of lowering the temperature of the steam produced in the bed (while increasing its flow rate a bit since overheating is converted into additional steam). This effect is beneficial for the safety since it considerably reduces the risks of induced breaks in the primary circuit. These risks are generally associated with the flow of superheated steam in the hot leg and steam generators. It must be emphasized that these complex processes of redistribution of the phases between the center and the periphery and the vertical entrainment of water in the bypass have only been observed in the calculations, i.e. they are the results of the chosen modeling. It is unfortunately not possible to confirm them experimentally because it was not possible to measure velocities or the void fraction in the porous medium. In addition, the radial pressure differences remain small compared to the accuracy of the measurements. It is therefore not possible to make comparisons between the calculations and the experiment for the radial pressure gradient which

is the driving force of these redistributions. Despite this lack of experimental validation by direct comparison with measurements, it is very satisfactory to note that we find, by calculation, the global effects observed in the experiment, namely: a transition between 1D and 2D progression of the quench front when the injection rate increases or the pressure decreases, a decrease in the conversion rate as injection rate increases or pressure decreases and water appears above the bed before the end of the reflooding. In addition, the temperature measurements also make it possible to identify the 1D or 2D progressions by showing either flat or curved front shapes. The calculation allows to find these shapes too. For the reactor situation, the scale, the contrast of permeability and the injection flow rates are different, which changes a little the conclusions compared to the PEARL tests. It was shown that there is a threshold of injection velocity for which the fraction of the injected flow which is diverted through the bypass is maximum. Beyond this threshold, it decreases and tends towards an asymptote. This behavior could not be observed in the experiment because the range of injection velocities was too narrow.

6.2 Conclusions about the modeling

One of the initial objectives of this thesis was to study the impact of porosity variations on the cooling of a debris bed, ie, in a general way, to know how water progresses in an overheated porous medium, heterogeneous in porosity and/or permeability. This objective proved too ambitious because, on the one hand, it was difficult to characterize porosity heterogeneities in a debris bed and, on the other hand, there were no experimental data available. It was therefore restricted to a medium composed of two layers of different permeabilities. On this type of medium, we have been able to benefit from experimental data of the PEARL tests. In this context, we therefore worked mainly on friction terms in momentum equations. Particular attention was paid to the general form of these equations for two-phase flow and the impact of certain terms on the water entrainment phenomena observed in PEARL. One of the important results of this study is the demonstration of the need for "cross" terms, that is, in particular, a term involving the velocity of the gas in the liquid momentum equation. Without this term, the simple pressure gradient generated by the vapor flow in the bypass is insufficient to produce a liquid velocity larger than the quench front velocity, as observed experimentally. For the expression of these cross terms, several models from the literature have been compared. It shows that the Schülenberg and Müller model [Schulenberg 1987] is the most robust of all because it covers a rather large range of void fraction and it provides the best estimations for the velocity of water in the bypass, compared to the experiment. The more recent model of Clavier [Clavier 2015a], although more rigorously established

and validated on the recent experiments CALIDE [Chikhi 2016] proves less robust (its range of applicability does not cover all the conditions met during a reflood), and it overestimated the velocity of the water in the bypass. It has also been shown that the terms of permeability and relative passability in each of the two equations do not play a major role in the velocity of the entrained water. They only play a role in the thickness of the two-phase zone at the quench front. Some studies have also been done on the numerical behavior of the system of equations chosen and the method of resolution. We have thus been able to show that, for this problem of two-dimensional propagation of the quenching front, the solution can be obtained on a relatively coarse mesh, comprising only 3 or 4 meshes in the thickness of the front and that it is independent of possible variations in porosity near the wall. These points give us confidence as to the generic nature of the understanding of the phenomena obtained from the calculations. Nevertheless, it has also been shown that the stability of the resolution is based on the choice of appropriate spatial and temporal discretizations (partially implicite) of the friction terms. This is particularly important for void fraction terms which are highly nonlinear, both in terms of relative passability and permeability, and in cross terms (where they are generally even more nonlinear). This aspect of the numerical study could not be deepened but it seems necessary to find the most adapted discretizations to treat the cross terms. Basically, these strong nonlinearities reflect the fact that the cross terms only play a role over a limited range of the void fraction and are activated on one or several thresholds.

There are important parameters to evaluate the consequences of accident management by injection of water in the core. The 1D reflood is more efficient because all the water is devoted to cool down the debris whereas some of the water is diverted into the bypass and accumulated at the top of the bed for 2D reflood. PEARL tests provided new experimental data about the reflooding of a severely damaged reactor core, numerical simulations of those test were presented and showed acceptable agreement with the experiments. The Icare-Cathare calculations and post-processing of the results are time consuming. There was a need to perform faster calculations and parametric studies as well as testing the several interfacial friction laws present in the literature. That motivated the development of a simplified analytical model describing the main features of the reflooding process.

This simplified analytical model is a tool to perform fast calculations of two phase flow redistribution in such a two-layered debris system, with different cross-sections, porosity and particle size, and it assesses the conditions for water entrainment. It also allows testing different correlations in the variations of the momentum equations for porous media such as relative permeability and passability correlations,

interfacial friction laws. For instance, it was shown that the Generalized Darcy law is not able to provide acceptable evaluations whereas considering non-zero cross-terms in the Darcy Forchheimer equation by including an interfacial friction law succeeds in obtaining better results. It is written in a rather general form including the Forchheimer correction terms and non-zero cross-terms in the generalized Darcy-Forchheimer momentum equation. It allows to test easily and efficiently any proposed variation of the momentum equation including changes in correlations and friction laws up to quadratic terms. The model allows performing fast evaluations of the conversion ratio, water entrainment in the bypass, as well as the quenching speed. Upscaling to the reactor scale is straightforward, provided the geometry and boundary conditions are respected. Thus the model is very useful to estimate the total quenching time and the maximum temperature that could be reached by the hot debris bed at large scales in accidental conditions. It can be also used to perform sensitivity studies on the physical properties of the particle beds and the fluid, as well as different variations of the momentum equations. A parametric study at reactor scale was performed investigating the effect of geometry, size, initial and boundary conditions on the chances of achieving coolability starting from a predefined reference configuration similar to post-LOCA debris configuration.

The model provides good qualitative and quantitative results for two-phase flow redistribution downstream of the quench front as compared to the results obtained in PEARL reflooding tests where it predicts the occurrence of entrainment and a comparable water velocity in all the cases. It can be also used to perform sensitivity studies on the physical properties of the particle beds and the fluid, as well as different variations of the momentum equations. For instance, it was shown that the Generalized Darcy law is not able to provide acceptable evaluations whereas considering non-zero cross-terms in the Darcy Forchheimer equations by including an interfacial friction law succeeds in obtaining better results.

Considering a configuration of a two-layered debris bed formed in a reactor core during a severe accident scenario, a reference calculation with predefined debris bed geometry, and reflooding initial and boundary conditions, is performed. The interfacial friction laws found in the literature (Tung-Dhir, Schulenberg-Muller, and Clavier) were implemented and tested. Even though the Schulenberg-Muller law is highly non-linear in void fraction (α^7), it provided the best estimations in general, and showed a larger range of applicability. The advantage of using this simplified model is its ability to cope with such non-linearity and the ease of manipulation of the friction laws definition. That for instance, represents a difficulty when we deal with a thermal hydraulics code like Icare-Cathare with which the calculations using the Schulenberg-Muller law were not feasible due to divergence of the void fraction

out of the possible range. It leaded the calculations to crash; that divergence is suspected to be a result of the high non-linearity in the void fraction.

Special attention was given for the PEARL possible deductions, and their compatibility with the modeled results. The model reproduced the main behaviors identified in the PEARL test. An emphasis on the specificity of the PEARL geometry with was made upon the permeability contrast of the debris layers. However, the PEARL configuration with its initial and boundary conditions does not fully describe the situation that may arise during an accidental scenario in a nuclear reactor core leading to the formation of a hot bed. The temperature of the debris and the delivered injection flow rates were relatively small. And to understand the behavior of reflooding a debris bed as that formed in a hypothetical accidental scenario, a reference configuration was considered. Implementing the proposed analytical model, the impact of varying each geometric or thermal hydraulic condition on the reflooding process is investigated. The investigation focus on their impact on the main results describing the reflooding process, namely: its efficiency, duration, water entrainment in the bypass, steam production, and the coolability criterion. For each parameter, a limiting value and a critical value were defined. The limiting value represents that for which increasing or decreasing the parameter will can only induce less than 5% increase or decrease, towards the maximum or minimum of the conversion ratio or the entrained water fraction in the bypass. Whereas the critical value represents the necessary condition in order to avoid the melting of the yet uncovered debris zones.

The coolability of a heterogeneous two-layered debris bed was investigated, but the considered situations for coolability assessment cannot be generalized. Each situation has its unique geometry, bed composition, initial and boundary conditions that should be taken into account to predict the coolability chances. However, the behavior of the reflooding process is described and the impact of the initial and boundary conditions, as well as the geometry of the debris bed, is studied. The conclusion about the behavior of the reflooding process and the impact of each of the considered variables can be taken into account when addressing the coolability chances. The proposed model can be implemented to assess rapidly the chances of coolability during the reflooding of a considered debris bed surrounded by a bypass of larger permeability. It can be also used to investigate the effect of initial or boundary condition or bed composition on the coolability of such a debris system with predefined conditions.

For a given initial energy carried by the debris bed, the coolability is more sensitive to the permeability and the temperature of the debris rather than its size, and in some cases even for 10 times lower energy for dense particulate hot beds than longer

beds. Limiting the coolant access into the debris bed has a dominant impact on the coolability of a hot debris bed formed during accident scenario. The contrast in permeability is an important factor describing water entrainment in the bypass. It controls the redistribution of the injected flow rate among the debris layers. In the considered reference case, 70% of the injected flow were redistributed into the bypass which forms only 15% of the total cross-section. For PEARL it was the opposite because of its lower permeability contrast. At higher injection rates, the central debris layer receives larger fractions whereas the bypass receives fewer. The change in the inlet fractions between the low and high velocity range depends mainly on the permeability contrast. With higher contrasts, a larger difference between the inlet fractions was observed.

The investigated cases are not generic. The initial and boundary conditions, the geometry and particle size of the debris also play a role. The determination of a reference case is just indicative. And the need to assess the impact of each parameter is important in order to predict with confidence the possible outcomes of the accidental scenario. The proposed analytical model is capable of performing those tasks in a relatively short time and predicting the main outcomes of reflooding a superheated heterogeneous debris bed vertically stratified, like the situation of debris bed surrounded by intact assemblies in a highly degraded nuclear reactor core.

6.3 Perspectives

At the end of this work, there remain several interesting perspectives to go further in the modeling of two-phase flows in media with heterogeneous porosity and permeability. On the one hand, it would be interesting to use the analytic model developed in a more systematic way to determine thresholds on the size of the bypass or on the permeability of the main debris bed for which the effect of water entrainment and the bypass of the main bed would be maximized. This would better identify potentially very difficult configurations to cool down. On the other hand, always with the analytical model, it would be interesting to deepen the study of the cross terms. From the models of the literature, it would be necessary to compare the ranges of void fraction for which these terms are preponderant, to possibly find analogies between the terms proposed by different authors and to make a synthesis in the form of a model validated over the widest range possible (in void fraction and water and steam velocities). After this first analysis, the establishment of the optimal model would be confirmed by 2D calculations without simplification (Icare/Cathare or MC3D or any other code) whose objective would be to find the results of the PEARL tests but also PRELUDE-2D [Repetto 2013], as well as the tests CALIDE

[Chikhi 2016] and BNL [Tutu 1984b]). Finally, another interesting area for improvement would be the study of the spatial and temporal discretizations of the different friction terms, in particular the cross terms. At present, the quasi-explicit processing of strongly non-linear terms penalizes the calculation time. On the other hand, it remains to determine what the best spatial discretization is. For now, the choice between "centered" or "up-wind" terms or combinations of both is very empirical. A more systematic study of 1D propagation of the quench front should allow improving that. With regard to reactor safety studies, a direct perspective of this work would be to include the analytical model developed in the tools used for PSA-2 studies. Currently PSA-2 models are quite simplistic and consider for example that the conversion rate of water injected into steam is 100% and that it is independent of the parameters such as the geometry of the medium to be cooled or the pressure, which is not justified. It would therefore be quite easy to do better by taking into account the most important physical phenomena underlying the simplified model.

Chapter 6

Conclusion

Dans cette thèse, on s'est intéressé à la progression du front de trempe dans un lit de débris, lorsque ce dernier est entouré d'une zone plus perméable ou plus poreuse. Cette situation est très susceptible de se produire lors du renoyage d'un cœur de réacteur fortement dégradé. En effet, le dépôt de puissance résiduelle n'est pas homogène, ce qui conduit, sur la plupart des situations accidentelles étudiées, à un état de dégradation plus avancée au centre. Au contraire, en périphérie, le cœur est moins endommagé, ce qui se traduit par des coefficients de frottement (perméabilité, passabilité) plus faibles. Si un fusion partielle s'est produite au centre, on peut même aboutir à une situation où le centre est moins poreux (plus compact) que la périphérie. Afin d'étudier ces configurations de manière analytique, elles ont été simplifiées sous forme de deux milieux poreux concentriques, le milieu principal, au centre, étant entouré d'une zone plus perméable (et éventuellement plus poreuse). C'est dans cette géométrie que l'on a étudié la progression de l'eau, celle-ci étant injectée par le bas. C'est la même configuration qui a été étudiée expérimentalement sur le dispositif PEARL de l'IRSN. Les résultats de certains essais PEARL ont été utilisés dans cette thèse afin de comprendre les phénomènes physiques caractéristiques de ce type de système et afin de valider la modélisation proposée. On rappelle ici les principales conclusions des travaux de thèse, en commençant par la compréhension physique puis en décrivant les avancées faites sur le plan de la modélisation.

6.1 Conclusions sur le comportement physique du système étudié

Lors de l'injection d'eau dans un milieu poreux stratifié verticalement et surchauffé, un débit de vapeur important est généré et celui-ci se répartit entre le lit de débris central et la zone périphérique. Comme les pertes de charge sont moins élevées en périphérie, le débit surfacique de vapeur y est plus important qu'au centre, ce qui se traduit par un fort débit radial de vapeur depuis la zone centrale vers la périphérie. Comme on l'a montré aux chapitres 3 et 4, grâce aux calculs Icare/Cathare, cette redistribution transverse de la vapeur se produit sur une zone située juste au dessus du front de trempe, et couvrant environ un tiers du lit de débris dans la plupart

des cas étudiés (soit une bonne dizaine de centimètres). En aval de cette zone, il n'y a plus de redistribution de vapeur et plus de gradient radial de pression: la pression est quasiment uniforme entre le centre et la périphérie. Pour la phase liquide, sous certaines conditions identifiées dans la thèse (débit d'injection élevé, basse pression), il y a également un transfert de masse important du centre vers la périphérie, causé par la surpression au centre et par le fort écoulement radial de vapeur. Cependant, cette redistribution d'eau se produit sur une zone beaucoup plus petite que la redistribution de vapeur, soit seulement quelques centimètres en aval du front de trempe. Cela peut se comprendre assez facilement puisque c'est la zone où il y a simultanément une fraction volumique d'eau importante (faible taux de vide) et le maximum de surpression au centre. Au-delà de cette zone, les conditions (fort taux de vide et faible écart de pression) ne sont pas favorables à une redistribution d'eau vers le bypass, ce qui est évident sur les calculs. En aval de cette zone de redistribution radiale de l'eau (pour les conditions identifées), le bypass est rempli à la fois par de l'eau à faible vitesse (de l'ordre du mm/s) et de la vapeur à vitesse élevée (de l'ordre du m/s). Il en résulte une augmentation de la vitesse de l'eau dans le bypass, celle-ci devenant notablement plus rapide que la vitesse du front de trempe. C'est ce phénomène que l'on a appelé "progression 2D du front de trempe" parce que cette progression est plus rapide en périphérie qu'au centre. Lorsque ce phénomène ne se produit pas, la vitesse de progression du front de trempe est la même partout et correspond à ce qu'on a appelé une "progression 1D", c'est à dire un front de trempe plat. A l'échelle du lit de débris, la progression 2D se traduit par une arrivée d'eau au-dessus du lit de débris avant le refroidissement complet de tout le lit. Selon les conditions, cet entraî nement d'eau au-dessus du lit peut se produire très rapidement après le début du renoyage, comme cela a pu être observé expérimentalement. Cet effet a plusieurs conséquences. D'une part, il diminue l'efficacité du renoyage parce qu'une partie du débit injecté circule uniquement dans le bypass périphérique et ne contribue pas au refroidissement du lit principal. Cela se traduit par une diminution du taux de conversion, comme on l'a montré (ce taux correspond au rapport entre le débit de vapeur produit et le débit d'eau injectée). D'autre part, il ralentit la progression du front de trempe dans le lit de débris principal parce que le débit d'eau entrant dans ce lit est diminué. Cependant, cet effet n'est pas prépondérant et, globalement, le temps de renoyage diminue toujours lorsque le débit global injecté augmente. Enfin, une dernière conséquence de l'entraînement d'eau dans le bypass est l'accumulation d'eau au-dessus du lit de débris pendant le renoyage, ce qui a pour effet d'abaisser la température de la vapeur produite dans le lit (tout en augmentant un peu son débit puisque la surchauffe est convertie en vapeur supplémentaire). Cet effet est bénéfique pour la sûreté puisqu'il réduit considérablement les risques de brèches induites dans le circuit primaire. Ces risques sont généralement associés à la circulation de vapeur d'eau surchauffée dans la branche chaude et les générateurs de

vapeur. Il faut souligner que ces processus complexes de redistribution des phases entre le centre et la périphérie et d'entraînement vertical de l'eau dans le bypass n'ont été observés que sur les calculs, c'est à dire qu'ils sont le résultats de la modélisation choisie. Il n'est malheureusement pas possible de les confirmer expérimentalement parce qu'il n'a pas été possible de mesurer des vitesses ou le taux de vide dans le milieu poreux. Seule l'observation du haut du dispositif montre l'arrivée d'eau avant le refroidissement complet. De plus, les écarts radiaux de pression restent faibles par rapport à la précision des mesures. Il n'est donc pas possible de faire des comparaisons entre les calculs et l'expérience pour le gradient de pression radial qui est le moteur de ces redistributions. Malgré ce manque de validation expérimentale par comparaison directe, il est très satisfaisant de constater que l'on retrouve, par le calcul, les effets globaux observés dans l'expérience, à savoir: une transition entre progression 1D et 2D du front de trempe lorsque le débit d'injection augmente ou que la pression diminue, une diminution du taux de conversion lorsque le débit augmente ou que la pression diminue et une apparition de l'eau au-dessus du lit avant la fin du renoyage. De plus, les mesures de températures permettent également d'identifier les progressions 1D ou 2D en montrant des formes de front de trempe soit plate, soit courbée. Le calcul permet de retrouver ces formes aussi. Pour la situation réacteur, l'échelle, le contraste de perméabilité et les débits d'injection sont différents, ce qui change un peu les conclusions par rapport aux essais PEARL. On a ainsi pu montrer qu'il existe un seuil de vitesse d'injection pour lequel la fraction du débit injecté qui passe par le bypass est maximale. Au-delà de ce seuil, elle diminue puis tend vers une asymptote. Ce comportement n'avait pu être observé expérimentalement à cause de la gamme de vitesses d'injection trop réduite.

6.2 Conclusions sur la modélisation

Un des objectifs initiaux de cette thèse était d'étudier l'impact des variations de porosité sur la refroidissabilité d'un lit de débris, c'est à dire, de façon globale, de savoir comment se propage l'eau dans un milieu poreux surchauffé et hétérogène en porosité et/ou en perméabilité. Cet objectif s'est avéré trop ambitieux parce que, d'une part il était difficile de caractériser les hétérogénéités de porosité dans un lit de débris et, d'autre part, il n'y avait pas de données expérimentales disponibles. On s'est donc restreint aux milieux constitués de deux couches de perméabilités différentes. Sur ce type de milieu, on a pu bénéficier des données expérimentales issues des essais PEARL. Dans ce contexte, on a donc travaillé essentiellement sur les termes de frottement dans les équations de quantité de mouvement. On s'est particulièrement intéressé à la forme générale de ces équations pour un écoulement diphasque et à l'impact de certains termes sur les phénomènes d'entraînement d'eau

observés dans PEARL. Un des résultats importants de cette étude est la démonstration de la nécessité de termes "croisés", c'est à dire, en particulier, d'un terme faisant intervenir la vitesse du gaz dans l'équation de quantité de mouvement du liquide. Sans ce terme, le simple gradient de pression engendré par l'écoulement de vapeur dans le bypass est insuffisant pour produire une vitesse du liquide supérieure à la vitesse du front de trempe et comparable à celle observée expérimentalement. Pour l'expression de ces termes croisés, plusieurs modèles issus de la littérature ont été comparés. Il en ressort que le modèle de Schülenberg et Müller [Schulenberg 1987] est le plus robuste de tous car il couvre une large gamme de taux de vide et il fournit la meilleure de la vitesse de liquide dans le bypass. Le modèle plus récent de Clavier [Clavier 2015a], bien que plus rigoureusement établi et valdié sur les experiences récentes CALIDE [Chikhi 2016] s'avère moins robuste (sa gamme de validité ne couvre pas toutes les conditions rencontrées lors d'un renoyage) mais il fournit une estimation de la vitesse du l'eau dans le bypass un peu haut. On a également montré que les termes de perméabilité et passabilité relatives, dans chacune des deux équations, ne jouent pas un rôle prépondérant sur la vitesse de l'eau entraînée. Ils ne jouent un rôle que sur l'épaisseur de la zone diphasique au niveau du front de trempe. On a également fait quelques études sur le comportement numérique du système d'équations choisi et de la méthode de résolution. On a ainsi pu montrer que, pour ce problème de propagation bi-dimensionnelle du front de trempe, la solution peut être obtenue sur un maillage relativement grossier, ne comprenant que 3 ou 4 mailles dans l'épaisseur du front et qu'elle est indépendante des variations possible de porosité près de la paroi. Ces points sont rassurants quant au caractère générique de la compréhension des phénomènes obtenue à partir des calculs. Néanmoins, on a aussi montré que la stabilité de la résolution repose sur le choix des discrétisations spatiale et temporelle (implicitation partielle) des termes de frottemenent. Ceci est particulièrement important pour les termes en taux de vide qui sont très non-linéaires, aussi bien dans les termes de passabilité et perméabilité relatives que dans les termes croisés (où ils sont même généralement encore plus non linéaires). Cet aspect de l'étude numérique n'a pas pu être approfondi mais il semble nécessaire de trouver les discrétisations les plus adaptées pour traiter les termes croisés. Sur le fond, ces fortes non linéarités traduisent le fait que les termes croisés ne jouent un rôle que sur une gamme limitée du taux vide et s'activent sur un (ou des) seuils.

6.3 Perspectives

A l'issue de ce travail, il reste plusieurs perspectives intéressantes pour aller plus loin dans la modélisation des écoulements diphasiques dans les milieux à porosité et perméabilité hétérogènes. D'une part, il serait intéressant d'exploiter le modèle

analytque développé de façon plus systématique afin de déterminer des seuils sur la taille du by-pass ou sur la perméabilité du lit de débris principal pour lesquels l'effet d'entraînement d'eau et du contournement du lit principal serait maximisé. Cela permettrait de mieux identifier des configurations potentiellement très difficiles à refroidir. D'autre part, toujours avec le modèle analytique, il serait intéressant d'approfondir l'étude des termes croisés. A partir des modèles de la littérature, il faudrait comparer les gamme de taux de vide dans lesquelles ces termes sont prépondérants, trouver éventuellement des analogies entre les termes proposés par différents auteurs et en faire une synthèse sous forme de modèle validé sur la plus large gamme possible (en taux de vide et vitesses d'eau et de vapeur). Après cette première analyse, l'établissement du modèle optimal serait à confirmer par des calculs 2D sans simplification (Icare/Cathare ou MC3D ou autre code) dont l'objectif serait de retrouver les résultats des essais PEARL mais aussi PRELUDE-2D [Repetto 2013], ainsi que les essais CALIDE [Chikhi 2016] et BNL [Tutu 1984b]) Enfin, une autre piste d'amélioration intéressante serait l'étude des discrétisations spatiale et temporelle des différents termes de frottement, en particulier les termes croisés. A l'heure actuelle, le traitement quasi explicite des termes fortement non-linéaires pénalise le temps de calcul. D'autre part, il reste à déterminer quelle est la meilleure discrétisation spatiale. Pour l'instant, le choix entre des termes "centrés" ou "up-wind" ou des combinaisons des deux est très empirique. Une étude plus systématique de propagation 1D du front de trempe devrait permettre d'améliorer cela. Pour ce qui concerne les études de sûreté des réacteurs, une perspective directe de ce travail serait d'inclure le modèle analytique développé dans les outils utilisés pour les EPS2. A l'heure actuelle les modèles EPS2 sont assez simplistes et considèrent par exemple que le taux de conversion de l'eau injectée en vapeur est de 100% et qu'il est indépendant des paramètres tels que la géométrie du milieu à refroidir ou la pression, ce qui n'est pas justifié. Il serait donc assez facile de faire mieux en tenant compte des phénomènes physiques les plus importants identifiés lors de la construction du modèle simplifié.

Appendix A

Appendix

A.1 Figures

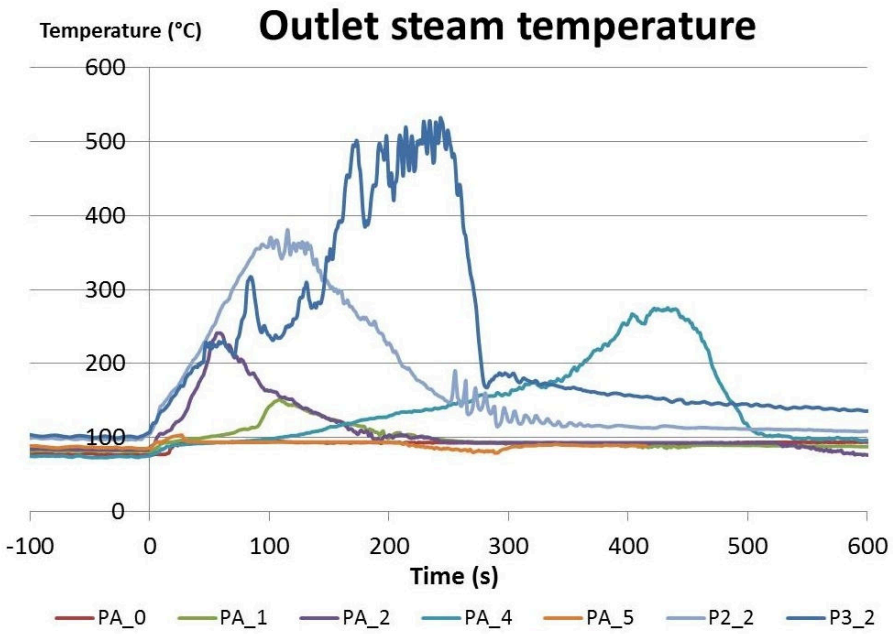

Figure A.1: Measurements of steam temperature at the outlet - PEARL tests

Steam outlet temperature-PEARL tests

Steam flow redistribution Figure A.2 shows the negligible diversion (less than 2%) of the redistributed steam back to the center.

Impact of parameters variation on reflooding process

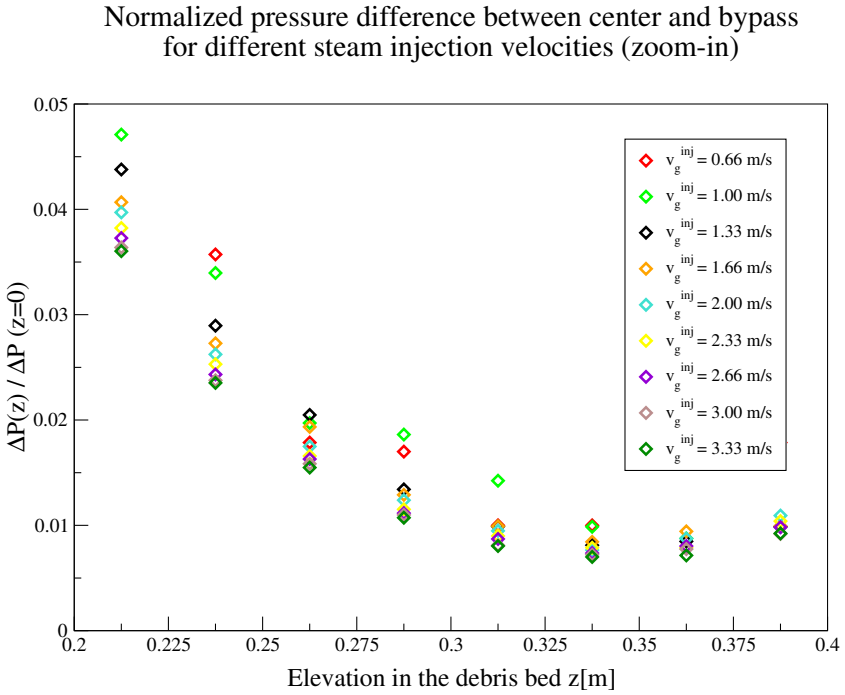

Figure A.2: Normalized pressure difference as function of elevation for different injection velocities (zoom-in)

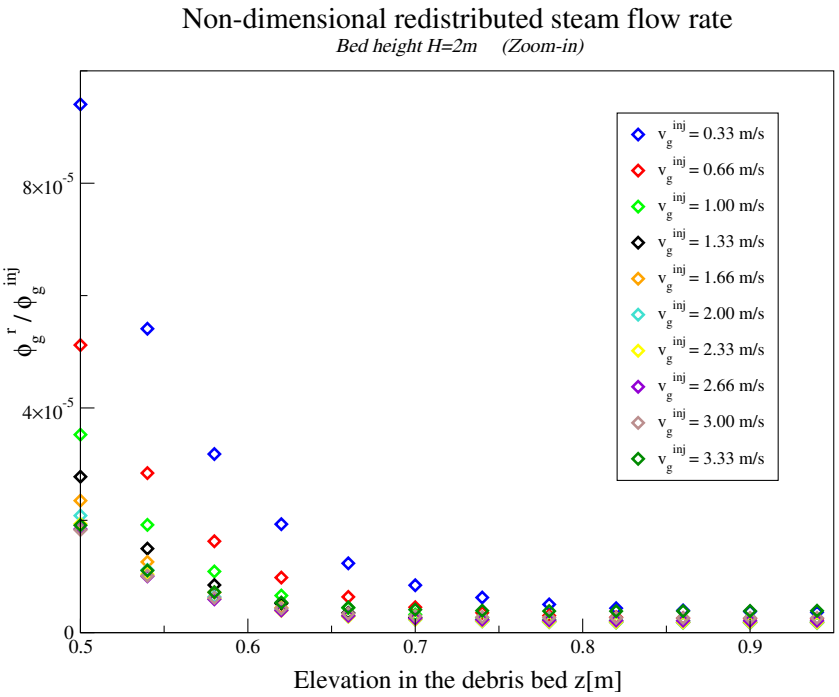

Figure A.3: Non-dimensional redistributed steam flow rate as function of elevation for different injection velocities, H=2m (zoom-in)

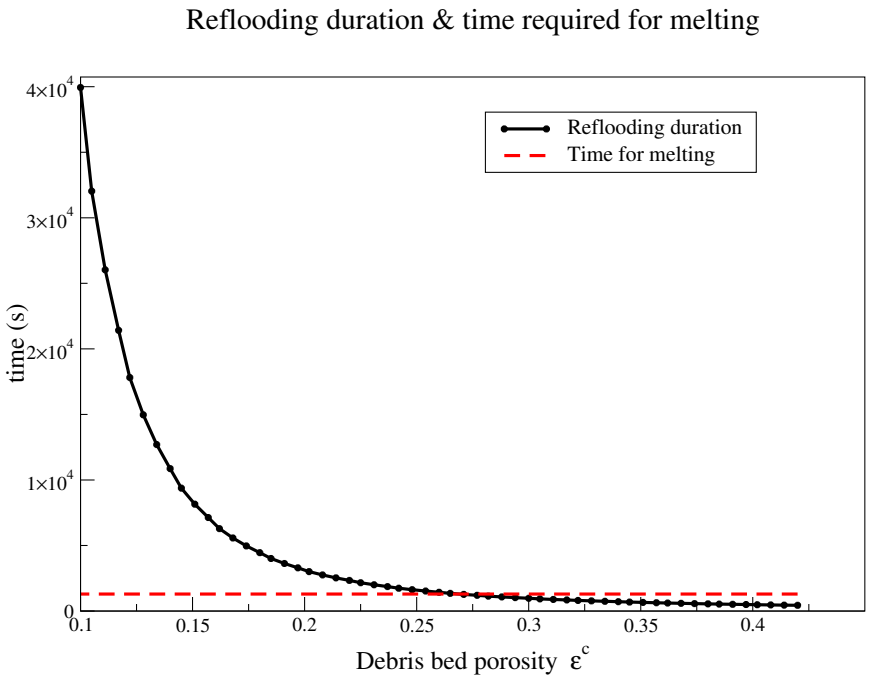

Figure A.4: Reflooding duration (solid lines) and time to reach melting (red dashed lines) of the debris bed as function of central bed porosity ε^c

Bibliography

[Akers 1986] D. Akers, E. Carlson, B. Cook, S. Ploger and J Carlson. *TMI-2 core debris grab samples examination and analysis*. Technical report GEND-INF-075, Sandia National Laboratory, 1986. (Cited on pages viii, 13 and 49.)

[Akers 1989] A. Akers and R.K. McCardell. *Core materials inventory and behavior*. Nuclear Technology, vol. 87, 1989. (Cited on pages viii, 2, 13, 14 and 148.)

[Akers 1994] D. W. Akers, C. M. Allison, M.L. Carboneau, R. R. Hobbins, J. K. Hohorst, S. M. Jensen and S. M. Modro. *Summary of important results and SCDAP/RELAP5 analysis for OECD LOFT experiment LP-FP-2*. NUREG/CR-6160/NEA/CSNI/R(94)3, Idaho National Engineering Laboratory, 1994. (Cited on pages v and 2.)

[Aminian 2007] K. Aminian, S. Ameri and A.G. Yussefabad. *A Simple and Reliable Method for Gas Well Deliverability Determination*. In Eastern regional meeting, Society of Petroleum Engineers, number SPE 111195, Kentucky, USA, October 2007. (Cited on page 31.)

[Anderson 1967] T. B. Anderson and R. Jackson. *A fluid mechanical description of fluidised beds*. Industrial Engineering Chemistry Fund., vol. 6, pages 527–538, 1967. (Cited on page 21.)

[Armstrong 1981] D.R. Armstrong, D.H. Cho, L. Bova, S.H. Chan and G.R. Thomas. *Quenching of a high temperature particle bed*. Transactions of the American Nuclear Society, vol. 39, pages 1048–1049, 1981. (Cited on pages x and 16.)

[Armstrong 1982] D.R. Armstrong, D.H. Cho and L. Bova. *Formation of dry pockets during water penetration into a hot particle bed*. Transactions of the American Nuclear Society, vol. 39, pages 418–419, 1982. (Cited on pages x and 16.)

[Atkhen 2003] K. Atkhen and G. Berthoud. *Experimental and numerical investigations on debris bed coolability in a multidimensional and homogeneous configuration with volumetric heat source*. Nuclear Technology, vol. 142, June 2003. (Cited on pages ix, 15, 16 and 100.)

[Bachrata 2012] A. Bachrata. *Modélisation du renoyage d'un cœur dans le cas d'un rÃ©acteur fortement dÃ©gradÃ©*. PhD thesis, Institut National Polytechnique de Toulouse, 2012. (Cited on pages vi and 3.)

[Bachrata 2013] A. Bachrata, F. Fichot, G. Repetto, M. Quintard and J. Fleurot. *Quench Front Progression in a Superheated Porous Medium: Experimental Analysis and Model Development*. Journal of Energy and Power Engineering, vol. 7, pages 514–523, 2013. (Cited on pages vi, 3 and 43.)

[Balhoff 2010] M. Balhoff, Mikelie A. and Wheeler M.F. *Polynomial filtration laws for low Reynolds number flows through porous media*. Transport in Porous Media, vol. 81, pages 35–60, 2010. (Cited on page 21.)

[Barrère 1990] J. Barrère. *Modélisation des écoulements de Stokes et Navier-Stokes en milieu poreux*. PhD thesis, Université de Bordeaux I, 1990. (Cited on page 29.)

[Béchaud 2001] C. Béchaud, F. Duval, F. Fichot, M. Quintard and M. Parent. *Debris bed coolability using a 3-D two phase model in a porous medium*. In Proceedings of ICONE 9, 9^{th} International Conference on Nuclear Engineering, Nice Acropolis, France, April 2001. (Cited on pages vi, ix, 3 and 15.)

[Bensoussan 1978] A. Bensoussan, J. L. Lions and G. Papanicolaou. Asymptotic analysis for periodic structures. North-Holland, 1978. (Cited on page 21.)

[Bertin 1990] H. Bertin, M. Quintard, V. Coprel and S. Whitaker. *Two-phase flow in heterogeneous porous media III: Laboratory experiments for flow parallel to stratified system*. Transport in Porous Media, vol. 5, pages 543–590, 1990. (Cited on page 45.)

[Bourgeat 1984] A. Bourgeat. *Homogenized behavior of two-phase flows in naturally fractured reservoirs with uniform fractures distribution*. Computer Methods in Applied Mechanics and Engineering, vol. 47, pages 205–216, 1984. (Cited on page 21.)

[Brooks 1966] R. H. Brooks and A. T. Corey. *Properties of porous media affecting fluid flow*. J. Irrig. Drain. Div. Am. Soc. civ. Engrs IR2, vol. 92, pages 61–89, 1966. (Cited on pages 35, 38 and 92.)

[Broughton 1989] J.M. Broughton, P. Kuan, D.A. Petti and E.L. Tolman. *A scenario of the Three Mile Island unit 2 accident*. Nuclear Technology, vol. 87, pages 34–53, 1989. (Cited on pages viii and 13.)

[Buck 2001] M. Buck, W. Schmidt and M. Burger. *Multidimensional modelling of debris bed coolability and quenching*. In First ICARE/CATHARE Seminar, Cadarache, France, November 2001. IRSN. (Cited on pages 37 and 42.)

[Burger 2006] M. Burger, M. Buck, W. Schmidt and W. Widmann. *Validation and application of the WABE code: Investigations of constitutive laws and 2D effects on debris coolability.* Nuclear Engineering and Design, vol. 236, pages 2164–2188, 2006. (Cited on pages 44 and 49.)

[Carman 1937] P.C. Carman. *The Determination of the Specific Surface Area of Powder I.* J. Soc. Chem. Ind., vol. 57, pages 225–234, 1937. (Cited on page 34.)

[Chauveteau 1967] G. Chauveteau and C. Thirriot. *Régimes d'écoulement en milieu poreux et limite de la loi de Darcy.* La Houille Blanche, vol. 1, no. 22, pages 1–8, 1967. (Cited on page 31.)

[Chella 1998] R. Chella, D. Lasseux and M. Quintard. *Multiphase, Multicomponent Fluid Flow in Homogeneous and Heterogeneous Porous Media.* Revue de l'Institut Franï¿½ais du Pétrole, vol. 53, no. 3, pages 335–346, 1998. (Cited on page 22.)

[Chen 2001] Z. Chen, S.L. Lyons and G. Qin. *Derivation of the Forchheimer law via homogenization.* Transport in Porous Media, vol. 44, no. 2, pages 325–335, 2001. (Cited on page 32.)

[Chikhi 2012] Nguyen N.G. Chikhi N. and J. Fleurot. *Determination of the hydrogen source term during the reflooding of an overheated core: Calculation results of the integral reflood test QUENCH-03 with PWR-type bundle.* Nuclear Engineering and Design, vol. 250, pages 351–363, 2012. (Cited on pages viii, 9 and 13.)

[Chikhi 2015a] N. Chikhi. *Programme Renoyage-Rapport de l'essai PA2.* Rapport technique, IRSN-Rapport Pléiade PSN-RES/SEREX/2015-00213, IRSN, 2015. (Cited on pages xxiii, 58, 60 and 71.)

[Chikhi 2015b] N. Chikhi, T. Garcin, F. Foubert, P. March and F. Fichot. *First experimental resutls of large scale debris bed reflood tests in the Pearl facility.* In 16th International Topical Meeting on Nuclear Reactor Thermal Hydraulics (NURETH-16), Chicago, IL, 2015. (Cited on pages x, 16, 58, 100, 115, 118, 121 and 125.)

[Chikhi 2016] N. Chikhi, R. Clavier, J.P. Laurent, F. Fichot and M. Quintard. *Pressure drop and average void fraction measurements for two-phase flow through porous media.* Annals of Nuclear Energy, vol. 94, pages 422–432, 2016. (Cited on pages 44, 183, 187, 192 and 193.)

[Chikhi 2017] N. Chikhi, F. Fichot and A. Swaidan. *Effect of water entrainment on the coolability of a debris bed surrounded by a by-pass: integral reflood experiments and modelling.* Annals of Nuclear Energy, vol. 110, pages 418–437, 2017. (Cited on pages 47, 100 and 118.)

[Cho 1984] D.H. Cho, D.R. Armstrong and S.H. Chan. *On the pattern of water penetration into a hot particle bed.* Nuclear Technology, vol. 65, pages 23–31, 1984. (Cited on pages x and 16.)

[Clavier 2015a] Chikhi N. Fichot F. Quintard M. Clavier R. *Experimental investigation on single-phase pressure losses in nuclear debris beds: identification of flow regimes and effective diameter.* Nuclear Engineering and Design, vol. 292, pages 222–236, 2015. (Cited on pages 44, 182 and 192.)

[Clavier 2015b] R. Clavier. *Étude expérimentale et modélisation des pertes de pression lors du renoyage d'un lit de débris.* PhD thesis, Institut National Polytechnique de Toulouse, 2015. (Cited on pages 30, 33, 34 and 40.)

[Clavier 2017] Chikhi N. Fichot F. Quintard M. Clavier R. *Modeling of inertial multi-phase flows through high permeability porous media: Friction closure laws.* International Journal of Multiphase Flow, vol. 91, pages 243–261, 2017. (Cited on pages 40 and 44.)

[Coindreau 2008] O. Coindreau and F. Fichot. *Specifications fonctionnelles des essais PEARL.* Note Technique DPAM/SEMCA 2008/092, IRSN, 2008. (Cited on pages vii and 13.)

[Coindreau 2013] O. Coindreau, F. Fichot and F. Fleurot. *Nuclear fuel rod fragmentation under accidental conditions.* Nuclear Engineering and Design, vol. 255, pages 68–76, 2013. (Cited on page 48.)

[Coles 1998] M. E. Coles and K.J. Hartman. *Non-Darcy Measurements in Dry Core and the Effect of Immobile Liquid.* In SPE Gas Technology Symposium, number SPE 39977, Canada, 1998. (Cited on page 31.)

[Coulaud 1986] O. Coulaud, P. Morel and J.P. Caltagirone. *Effets non linéaires dans les écoulements en milieu poreux.* Comptes Rendus de l'Académie des Sciences Paris, vol. Série II, no. 6, 1986. (Cited on page 28.)

[Coulaud 1988] Morel P. Coulaud O. and J. P. Catagirone. *Numerical modeling of non-linear effects in laminar flow through a porous medium.* Journal of fluid mechanics, vol. 190, pages 393–407, 1988. (Cited on page 28.)

[Darcy 1856] H. Darcy. Fontaines publiques de la ville de dijon. Libraire des Corps. Imperiaux des Ponts et Chaussees et des Mines, Paris, 1856. (Cited on page 27.)

[De Vries 1979] J. De Vries. *Prediction of Non-Darcy Flow in Porous Media*. Journal of The Irrigation and Drainage Division, vol. 105, no. IR2, pages 147–162, 1979. (Cited on page 28.)

[Décossin 2000] E. Décossin. *Ebullition et Assèchement dans un Lit de Particules avec Production Interne de Chaleur : Premières Expériences et Simulations Numériques en Situation Multidimensionnelle*. Ph.D.,Institut National Polytechnique, Toulouse, Février 2000. (Cited on pages ix and 15.)

[Dhir 1978] V.K. Dhir and G.P. Purohit. *Subcooled film-boiling heat transfer from spheres*. Nuclear Engineering and Design, vol. 47, pages 49–66, 1978. (Cited on pages x and 16.)

[Drai 2010] P. Drai, O. Marchand, F. Fichot, P. Chatelard, O. Coindreau, S. Belon, L.Cloarec and N. Chikhi. *ICARE/CATHARE V2.3 User's Manual and Guidelines*. Rapport technique, IRSN DPAM-SEMCA 2010-028, IRSN, 2010. (Cited on page 68.)

[Dupuit 1863] J. Dupuit. Etudes théoriques et pratiques sur le mouvement des eaux dans les canaux découverts et à travers les terrains perméables. Dunod, Paris, 1863. (Cited on page 29.)

[Duval 2002] F. Duval. *Modélisation du renoyage d'un lit de particules : contribution à l'estimation des propriétés de transport macroscopiques*. PhD thesis, Institut National Polytechnique de Toulouse, 2002. (Cited on pages vi, 3 and 43.)

[Duval 2004] F. Duval, F. Fichot and M. Quintard. *A local thermal non-equilibrium model for two-phase flows with phase change in porous media*. International Journal of Heat and Mass Transfer, vol. 47, no. 3, pages 613–639, 2004. (Cited on pages vi, 3 and 43.)

[Dybbs 1984] A. Dybbs and R.V. Edwards. *A New Look at Porous Media Fluid Mechanics - Darcy to Turbulent*. In J. Bear and M.Y. Corapcioglu, editors, Fundamentals of Transport Phenomena in Porous Media. Martinus Nijhoff, 1984. (Cited on page 28.)

[Ergun 1952] S. Ergun. *Fluid flow through packed columns*. Chem. Eng. Prog., vol. 48, pages 89–94, 1952. (Cited on pages 30, 31, 34 and 37.)

[Firdaouss 1995] M. Firdaouss and J.L. Guermond. *Sur l'Homogénéisation des Equations de Navier-Stokes à Faible Nombre de Reynolds*. Comptes Rendus de l'Académie des Sciences, Série I, vol. 320, pages 245–251, 1995. (Cited on page 29.)

[Firdaouss 1997] Guermond J.L. Firdaouss M. and P. Le Quéré. *Nonlinear corrections to Darcy's law at low Reynolds numbers*. Journal of Fluid Mechanics, vol. 343, pages 331–350, 1997. (Cited on page 29.)

[Forchheimer 1901] P. Forchheimer. *Wasserbewegung durch Boden*. Z. Ver. Deutsch. Ing., vol. 45, pages 1782–1788, 1901. (Cited on pages 29 and 32.)

[Fourar 1998] M. Fourar and R. Lenormand. *A Viscous Coupling Model for Relative Permeabilities in Fractures*. SPE 49006, pages 253–258, 1998. (Cited on page 35.)

[Fourar 2000] M. Fourar and R. Lenormand. *Inertial effects in two-phase flow through fractures*. Oil and Gas Science and Technology, vol. 55, no. 3, pages 259–268, 2000. (Cited on pages 35, 36, 44 and 92.)

[Geertsma 1974] J. Geertsma. *Estimating the coefficient of inertial resistant in fluid flow through porous media*. Society of Petroleum Engineers Journal, pages 445–450, October 1974. (Cited on pages 30 and 31.)

[Ginsberg 1982] T. Ginsberg. *Transient core debris bed heat removal experiments and analysis*. In International Meeting on Thermal Nuclear Reactor Safety, Chicago (USA), August 1982. (Cited on pages x and 16.)

[Ginsberg 1985] T. Ginsberg. *Analysis of influence of steam superheating on packed bed quench phenomena*. In International Meeting on Heat Transfer Conference, Denver (USA), August 1985. (Cited on pages x and 16.)

[Ginsberg 1986] T. Ginsberg, J. Klein, J. Klages, Y. Sanborn, C.E. Schwarz, J.C. Chen and L. Wei. *An experimental and analytical investigation of quenching of superheated debris beds under top-reflood conditions*. Technical report NUREG-CR-4493, Sandia National Labs., 1986. (Cited on pages x and 16.)

[Giorgi 1997] T. Giorgi. *Derivation of the Forchheimer law via matched asymptotic expansions*. Transport in Porous Media, vol. 29, pages 191–206, 1997. (Cited on pages 29 and 32.)

[Gray 1975] W.G. Gray. *A Derivation of the Equations for Multi-Phase Transport*. Chemical Engineering Science, vol. 30, pages 229–233, 1975. (Cited on page 24.)

[Hannoura 1981] A. A. Hannoura and F. B. J. Barends. *Non-Darcy flow, a state of art.* In Proceedings of Euromech 143, pages 37–51, Delft, September 1981. (Cited on page 29.)

[Hardee 1977] H.C. Hardee and R.H. Nilson. *Natural convection in porous media with heat generation.* Nuclear Science and Engineering, vol. 63, pages 119–132, 1977. (Cited on pages ix and 15.)

[Hofmann 1984] G. Hofmann. *On the location and mechanisms of dryout in top-fed and bottom fed particulate beds.* Nuclear Technology, vol. 65, pages 36–45, 1984. (Cited on pages x and 16.)

[Hu 1991] K. Hu and T.G. Theofanous. *On the measurement of dryout in volumetrically heated coarse particle beds.* Int. J. Multiphase Flow, vol. 65, 1991. (Cited on pages x, 16, 35, 37 and 45.)

[IAEA 1995] IAEA. *Guidelines for Accident Analysis of WWER Nuclear Power Plants, Rep. IAEA-EBP-WWER-01.* Technical report, International Aomic Energy Agency, 1995. (Cited on page 7.)

[IAEA 2002] IAEA. *Accident Analysis for Nuclear Power Plants, Safety Reports Series.* Technical report 23, International Aomic Energy Agency, 2002. (Cited on page 7.)

[IAEA 2016] IAEA. *Nuclear Technology Review 2016.* Technical report, International Aomic Energy Agency, 2016. (Cited on page 5.)

[Irmay 1958] S. Irmay. *On the theoretical derivation of Darcy and Forchheimer formulas.* Transactions American Geophysical Union, vol. 39, no. 4, pages 702–707, 1958. (Cited on pages 29 and 32.)

[Janicek 1955] J. D. Janicek and D. L. Katz. *Application of Unsteady State Gas Flow Calculations.* In Proceedings of University of Michigan Research Conference, Michigan, 1955. (Cited on page 31.)

[Jones 1987] S. C. Jones. *Using the Inertial Coefficient, B, To Characterize Heterogeneity in Reservoir Rock.* In Society of Petroleum Engineers of AIME, number SPE 16949, Texas (USA), 1987. (Cited on page 31.)

[Kitch 1985] D.M. Kitch. *Pump Selection and Application in a Pressurized Water Reactor Electric Generating Plant.* In Proceedings of Second International Pump Symposium, pages 47–57, May 1985. (Cited on page 12.)

[Knupp 1995] P.M. Knupp and J.L. Lage. *Generalization of the Forchheimer-extended Darcy flow model to the tensor premeability case via a variational principle*. Journal of Fluid Mechanics, vol. 299, pages 97–104, 1995. (Cited on page 29.)

[Konovalikhin 2000] M.J. Konovalikhin, Z.L. Yang, M. Amjad and B.R. Seghal. *On dry-out heat flux of particle debris beds with a downcomer*. In Proceedings of ICONE 8, 8^{th} International Conference on Nuclear Engineering, Baltimore (USA), April 2000. (Cited on pages x and 16.)

[Lake 1981] L. Lake and G. Hirasaki. *Taylor's dispersion in stratified porous media*. Society of Petroleum Engineers Journal, pages 459–468, 1981. (Cited on page 106.)

[Lasseux 1996] D. Lasseux, Quintard M. and S. Whitaker. *Determination of permeability tensors for two-phase flow in homogeneous porous media : Theory*. Transport in Porous Media, vol. 24, pages 107–137, 1996. (Cited on page 22.)

[Lasseux 2008] D. Lasseux, A. Ahmadi and A. Arani. *Two-Phase Inertial Flow in Homogeneous Porous Media: A Theoretical Derivation of a Macroscopic Model*. Transport in Porous Media, vol. 75, pages 371–400, 2008. (Cited on pages 22, 32, 40 and 132.)

[Lasseux 2011] D. Lasseux, A.A. Abbasian and A. Ahmadi. *On the stationary macroscopic inertial effects for one-phase flow in ordered and disordered porous media*. Physics of Fluids, vol. 23, 2011. (Cited on page 22.)

[Lee 1977] D.O. Lee and R.H. Nilson. *Flow visualization in heat generating porous media*. Technical report SAND76-0614, Sandia National Labs., 1977. (Cited on pages ix and 15.)

[LeRosen 1942] A. L. LeRosen. *Method for the Standardization of Chromatographic Analysis*. Journal of American Chemical Society, no. 64, pages 1905–1907, 1942. (Cited on page 27.)

[Li 2001] D. Li and T. W. Engler. *Literature Review on Correlations of Non-DarcyCoefficient*. In SPE Permian Basin Oil and Gas conference, number SPE 70015, Texas, USA, 15-16 May 2001. (Cited on pages 30 and 31.)

[Li 2012a] L. Li and W. Ma. *Experimental Study on the Effective Particle Diameter of a Packed Bed with Non-Spherical Particles*. Transport in Porous Media, vol. 89, pages 35–48, 01 2012. (Cited on page 26.)

[Li 2012b] L. Li, W. Ma and S. Thakre. *An experimental study on presure drop and dryout heat flux of two-phase flow in packed beds of multi-sized and irregular particles*. Nuclear Engineering and Design, vol. 242, pages 369–378, 2012. (Cited on page 26.)

[Lipinski 1981] R.J. Lipinski. *A One-Dimensional Particle Bed Dryout Model*. Transactions of the American Nuclear Society, vol. 38, pages 386–387, 1981. (Cited on page 35.)

[Lipinski 1982] R.J. Lipinski. *A model for cooling and dryout in particle beds*. Technical report SAND 82-0765, NUREG/CR-2646, Sandia National Labs., 1982. (Cited on page 35.)

[Lipinski 1984] R.J. Lipinski. *A coolability model for post-accident nuclear reactor debris*. Nuclear Technology, vol. 65, pages 53–66, April 1984. (Cited on pages ix, 15, 35, 37 and 45.)

[MacDonald 1979] I. F. MacDonald, M. S. El-Sayed, K. Mow and F. A. L. Dullien. *Flow through porous media: the Ergun equation revisited*. Industrial Engineering Chemistry Fund., vol. 18, pages 199–208, 1979. (Cited on pages 29 and 32.)

[Marle 1967] C. Marle. *Ecoulements Monophasiques en Milieu Poreux*. Revue de L'Institut Francais du Pétrole, vol. XXII, no. 10, pages 1471–1509, 1967. (Cited on page 21.)

[Matheron 1965] G. Matheron. *Les variables régionalisées et leur estimation: une application de la théorie des fonctions aléatoires aux sciences de la nature*. Masson et CIE, 1965. (Cited on page 21.)

[Mayr 1998] P. Mayr, M. Burger, M. Buck, W. Schmidt and G. Lohnert. *Investigations on the Coolability of Debris in the Lower Head with WABE-2D and MESOCO-2D*. OECD/CSNI Workshop on In-Vessel Core Debris Retention and Coolability, March 1998. (Cited on pages ix and 15.)

[McCardell 1990] R.K. McCardell, M.L. Russell, D.W. Akers and C.S Olsen. *Summary of TMI-2 core sample examinations*. Nuclear Engineering and Design, vol. 118, no. 3, pages 441–449, 1990. (Cited on pages viii, 2 and 13.)

[Mei 1991] C.C. Mei and J.L. Auriault. *The Effect of Weak Inertia on Flow through a Porous Medium*. Journal of Fluid Mechanics, vol. 222, pages 647–663, 1991. (Cited on pages 21, 29 and 32.)

[Mei 2010] C. Mei and B. Vernescu. Homogenization methods for multiscale mechanics. September 2010. (Cited on page 21.)

[Muskat 1937] M. Muskat, editor. Flow of homogeneous fluid through porous media. McGraw-Hill, New York, 1937. (Cited on page 31.)

[Nagase 2012] F. Nagase and H. Uetsuka. *Thermal properties of Three Mile Island Unit 2 core debris and simulated debris*. Journal of Nuclear Science and Technology, vol. 49, no. 1, pages 96–102, 2012. (Cited on pages viii, 14, 148 and 149.)

[Naik 1982] A.S. Naik and V.K. Dhir. *Forced flow evaporation cooling of a volumetrically heated porous layer*. International Journal of Heat and Mass Transfer, vol. 25, no. 4, pages 541–551, 1982. (Cited on page 44.)

[Nayak 2005] A. K. Nayak, A. V. Stepanyan and B. R. Sehgal. *Experimental Investigations on the Dryout Behaviour of a Radially Stratified Porous Bed*. In 11th International Topical Meeting on Nuclear Reactor Thermal Hydraulics (NURETH-11), Avignon, France, 2005. (Cited on pages x and 16.)

[Nayak 2006] A. K. Nayak, B. R. Sehgal and A. Stepanyan. *An experimental study on quenching of a radially stratified heated porous bed*. Nuclear Engineering and Design, vol. 236, no. 19-21, pages 2189–2198, October 2006. (Cited on pages x and 16.)

[NEI 2017] NEI. *World Statistics - Nuclear Energy Around the World*. In Nuclear Energy Institute, https://www.nei.org, 2017. (Cited on page 4.)

[NSAC 1980] NSAC. *Analysis of Three Mile Island - Unit 2*. Technical Note by Nuclear Safety Analysis Center NSAC 80-1, Electric Power Research Institute, March 1980. (Cited on pages vii and 13.)

[Nutting 1930] P.G. Nutting. *Physical Analysis of Oil Sands*. Bulletin of American Association of Petroleum Geologists, vol. 14, 1930. (Cited on page 27.)

[Pascal 1980] H. Pascal, G. Ronald and D.J. Kingston. *Analysis of Vertical Fracture Length and Non-Darcy Flow Coefficient Using Variable Rate Tests*. In Society of Petroleum Engineers of AIME, number SPE 9348, Texas (USA), September 1980. (Cited on page 31.)

[Petit 1999] F. Petit, F. Fichot and M. Quintard. *Ecoulement Diphasique en Milieux Poreux : Modèle à Non-Equilibre Local*. Int. J. Therm. Sci, vol. 38, pages 239–249, 1999. (Cited on pages x, 16 and 43.)

[Petti 1989] D.A. Petti. Power burst facility (pbf) severe fuel damage test 1-4: Test results report, volume 88 of *NUREG/CR*. Division of Systems Research, Office of Nuclear Regulatory Research, U.S. Nuclear Regulatory Commission, 1989. (Cited on pages v and 2.)

[Quintard 1994a] M. Quintard and S. Whitaker. *Convection, Dispersion, and Interfacial Transport of Contaminants : Homogeneous Porous Media*. Advances in Water Resources, vol. 17, pages 221–239, 1994. (Cited on page 43.)

[Quintard 1994b] M. Quintard and S. Whitaker. *Transport in Ordered and Disordered Porous Media I: The Cellular Average and the Use of Weighting Functions*. Transport in Porous Media, vol. 14, pages 179–206, 1994. (Cited on page 21.)

[Quintard 1994c] M. Quintard and S. Whitaker. *Transport in Ordered and Disordered Porous Media II: Generalized volume Averaging*. Transport in Porous Media, vol. 14, pages 179–206, 1994. (Cited on page 21.)

[Quintard 1994d] M. Quintard and S. Whitaker. *Transport in Ordered and Disordered Porous Media III: Closure and Comparison Between Theory and Experiment*. Transport in Porous Media, vol. 15, pages 31–49, 1994. (Cited on page 21.)

[Quintard 1994e] M. Quintard and S. Whitaker. *Transport in Ordered and Disordered Porous Media IV: Computer Generated Porous Media for Three-Dimensional Systems*. Transport in Porous Media, vol. 15, pages 51–70, 1994. (Cited on page 21.)

[Quintard 1994f] M. Quintard and S. Whitaker. *Transport in Ordered and Disordered Porous Media V: Geometrical Results for Two-Dimensional Systems*. Transport in Porous Media, vol. 15, pages 183–196, 1994. (Cited on page 21.)

[Quintard 1997] M. Quintard, M. Kaviany and S. Whitaker. *Two-Medium Treatment of Heat Transfer in Porous Media: Numerical Results for Effective Properties*. Advances in Water Resources, vol. 20, no. 2-3, pages 77–94, 1997. (Cited on page 43.)

[Quintard 2000] M. Quintard, B. Ladevie and S. Whitaker. *Effect of Homogeneous and Heterogeneous Source Terms on the Macroscopic Description of Heat Transfer in Porous Media*. In P. Cheng, editor, Symposium on Energy Engineering in the 21st Century, volume 2, pages 482–489, Begell House, New York, Hong Kong, January 2000. (Cited on page 43.)

[Rashid 2013] M. Rashid, S. Rahman, R. Kulenovic, M. Bürger and Laurien E. *Quenching Experiments: Coolability of Debris Bed.* Nuclear Technology, vol. 181, no. 1, pages 208–215, 2013. (Cited on pages x and 16.)

[Rasoloarijaona 1994] M. Rasoloarijaona and J.L. Auriault. *Nonlinear seepage flow through a rigid porous medium.* European Journal of Mechanics, B/Fluids, vol. 13, no. 2, pages 177–195, 1994. (Cited on page 29.)

[Reed 1982] A.W. Reed. *The effect of channeling on the dryout of heated particulate beds immersed in a liquid pool.* PhD thesis, MIT, Cambridge (USA), 1982. (Cited on pages 35, 37 and 92.)

[Reed 1985] A. Reed, K. Boldt, E. Gorham-Bergeron, R. Lipinski and T. Schmidt. *DCC-1/DCC-2 degraded core coolability analysis.* Technical Note NUREG/CR-4390-R3, Sandia National Labs, 1985. (Cited on pages x and 16.)

[Repetto 2011] G. Repetto, T. Garcin, S. Eymery, P. March and F. Fichot. *Experimental program on debris reflooding (PEARL) - results on prelude facility.* In 14th International Topical Meeting on Nuclear Reactor Thermal Hydraulics (NURETH-14), Toronto, Canada, September 2011. (Cited on pages x and 16.)

[Repetto 2013] G. Repetto, N. Chikhi and F. Fichot. *Main outcomes on debris bed cooling from PRELUDE experiments. In 6th European Review meeting on Severe Accident ResearchExperimental program on debris reflooding (PEARL) - results on prelude facility.* In 6th European Review meeting on Severe Accident Research (ERMSAR-2013), 2013. (Cited on pages x, 16, 58, 186 and 193.)

[Saez 1985] A.E. Saez and R.G. Carbonnell. *Hydrodynamic parameters for gas-liquid co-current flow in packed beds.* AIChE Journal, vol. 31, pages 52–62, 1985. (Cited on page 35.)

[Saez 1986a] A.E. Saez, R.G. Carbonnell and J. Levec. *The hydrodynamics of trickling flow in packed beds, Part 1 : Conduit model.* AIChE Journal, vol. 32, no. 3, pages 353–368, 1986. (Cited on page 26.)

[Saez 1986b] A.E. Saez, R.G. Carbonnell and J. Levec. *The hydrodynamics of trockling flow in packed beds. Part II : Experimental observations.* AIChE Journal, vol. 32, no. 3, 1986. (Cited on pages 26 and 44.)

[Sanchez-Palencia 1982] E. Sanchez-Palencia. *On the asymptotics of the fluid flow past an array of fixed obstacles*. International Journal of Engineering Science, vol. 20, no. 12, pages 1291–1301, 1982. (Cited on pages 21 and 28.)

[Schäfer 2006] P. Schäfer, M. Groll and R. Kulenovic. *Basic investigations on debris coolability*. Nuclear Engineering and Design, vol. 236, pages 2104–2116, 2006. (Cited on pages x and 16.)

[Scheidegger 1953] A.E. Scheidegger. *Theoretical models of porous matter*. Producers Monthly, vol. 17, no. 10, pages 17–23, 1953. (Cited on page 30.)

[Scheidegger 1974] A.E. Scheidegger. The physics of flow through porous media. University of Toronto Press, 1974. (Cited on pages 29 and 30.)

[Schmidt 2007] W. Schmidt. *Interfacial drag of two-phase flow in porous media*. Int. J. Multiphase Flow, vol. 33, pages 638–657, 2007. (Cited on pages 34 and 44.)

[Schulenberg 1984] T. Schulenberg and U. Müller. *A Refined Model for the Coolability of Core Debris with Flow Entry from the Bottom*. 6th Information Exchange Meanding on Debris Coolability, Los Angeles, 1984. (Cited on pages 35 and 37.)

[Schulenberg 1987] T. Schulenberg and U. Müller. *An improved model for two-phase flow through beds of coarse particles*. Int. J. Multiphase Flow, vol. 13, no. 1, pages 87–97, 1987. (Cited on pages 34, 37, 42, 182 and 192.)

[Sepold 2004] L.K. Sepold, A. Miassoedov, G. Schanz, U. Stegmaier, M. Steinbrück, J. Stuckert and C. Homann. *Hydrogen generation in reflooding experiments with LWR-type rod bundles (QUENCH program)*. Nuclear Technology, vol. 147, no. 2, pages 202–215, 2004. (Cited on page 9.)

[Skjetne 1999a] E. Skjetne and J. L. Auriault. *High-velocity laminar and turbulent flow in porous media*. Transport in Porous Media, vol. 36, no. 2, pages 131–147, 1999. (Cited on pages 28 and 31.)

[Skjetne 1999b] E. Skjetne and J.L. Auriault. *New insights on steady, non-linear flow in porous media*. European Journal of Mechanics, B/Fluids, vol. 18, no. 1, pages 131–145, 1999. (Cited on page 29.)

[Slattery 1967] J. Slattery. *Flow of viscoelastic fluids through porous media*. American Institute of Chemical Engineers, vol. 13, pages 1066–1071, 1967. (Cited on page 21.)

[Sozen 1990] M. Sozen and K. Vafai. *Analysis of the Non-Thermal Equilibrium Condensing Flow of a Gas Through a Packed Bed.* Int. Journal of Heat and Mass Transfer, vol. 33, no. 6, pages 1247–1261, 1990. (Cited on pages x and 16.)

[Stark 1972] K. P. Stark. *A numerical study of the nonlinear laminar regime of flow in an idealized porous medium.* Fundamentals of transport phenomena in porous media, pages 86–102, 1972. (Cited on page 28.)

[Stenne 2009] N. Stenne, M. Pradier, J. Olivieri, S. Eymery, F. Fichot, P. March and J. Fleurot. *Multi-dimensional reflooding experiments: the PEARL program.* In OECD/NEAEC/SARNET2 Workshop, In Vessel Coolability, Paris (France), October 2009. (Cited on pages x and 16.)

[Swaidan 2017] A. Swaidan, F. Fichot and M. Quintard. *Two phase flow redistribution in a two-layered porous medium with contrasting permeability.* In International symposium of computational heat and mass transfer. CHT-17, number 200, Napoli, Italy, May 2017. (Cited on page 99.)

[Takeda 2013] Ohwada A. Takeda T. and H. Nakamura. *Measurement of non-condensable gas in a PWR small-break LOCA simulation test with LSTF for OECD/NEA ROSA Project and RELAP5 post-test analysis.* Experimental Thermal and Fluid Science, vol. 51, pages 112–121, 2013. (Cited on pages xvii and 9.)

[Tek 1957] M. R. Tek. *Development of a generalized darcy equation.* Transactions of the Metallurgical Society of AIME, vol. 210, pages 376–377, 1957. (Cited on pages 28 and 30.)

[Tek 1962] M. R. Tek and D.L. Katz. *The Effect of Turbulence on Flow of Natural Gas through Porous Media.* Journal of Petroleum Technology transactions of AIME, no. 222, pages 799–806, 1962. (Cited on page 31.)

[Tung 1983] V.X. Tung and V.K. Dhir. *Quenching of a hot particulate bed by bottom quenching.* In ASME-JSME Thermal Engineering Joint Conference, Honolulu, Hawaï¿½, 1983. (Cited on pages 118 and 121.)

[Tung 1988] V.X. Tung and V.K. Dhir. *A hydrodynamic model for two-phase flow through porous media.* Int. J. Multiphase Flow, vol. 14, pages 47–65, 1988. (Cited on pages 34, 38, 39 and 68.)

[Turland 1982] B.D. Turland and K. Moore. *One-Dimensional Models of Boiling and Dryout. Post Accident Debris Colling.* Proc. 5th Post Accident Heat Removal Information Exchange Mtg., Karlsruhe, July 1982. (Cited on page 35.)

[Tutu 1984a] N.K. Tutu, T. Ginsberg and J.C. Chen. *Interfacial drag for two-phase flow through high permeability porous beds*. J. of Heat Transfer, vol. 106, pages 865–870, November 1984. (Cited on page 45.)

[Tutu 1984b] N.K. Tutu, T. Ginsberg, J. Klein, J. Klages and C.E. Schwarz. *Debris bed quenching under bottom flood conditions*. Technical report NUREG/CR-3850, Brookhaven National Labs., 1984. (Cited on pages x, 16, 45, 100, 118, 121, 187 and 193.)

[USNRC 2012a] USNRC. *Emergency Core Cooling Systems*. Westinghouse Technology Systems Manual USNRC HRTD Rev 0406, United States Nuclear Regulatory Commission, 2012. (Cited on page 10.)

[USNRC 2012b] USNRC. *Residual Heat Removal System*. Westinghouse Technology Systems Manual USNRC HRTD Rev 0201, United States Nuclear Regulatory Commission, 2012. (Cited on page 10.)

[Ward 1964] J. C. Ward. *Turbulent flow in porous media*. Journal of the Hydraulics Division - ASCE, vol. 90, no. HY5, pages 1–12, 1964. (Cited on page 29.)

[Whitaker 1967] S. Whitaker. *Diffusion and dispersion in porous media*. American Institute of Chemical Engineers, vol. 13, pages 420–427, 1967. (Cited on page 21.)

[Whitaker 1969] S. Whitaker. *Advances in Theory of Fluid Motion in Porous Media*. Industrial and Engineering Chemistry, vol. 61, no. 12, pages 14–28, 1969. (Cited on page 22.)

[Whitaker 1986a] S. Whitaker. *Flow in Porous Media II: The Governing Equations for Immiscible, Two-Phase Flow*. Transport in Porous Media, vol. 1, pages 105–125, 1986. (Cited on page 21.)

[Whitaker 1986b] S. Whitaker. *Flow in Porous MediaI: A Theoretical Derivation of Darcy's Law*. Transport in Porous Media, vol. 1, pages 3–25, 1986. (Cited on pages 21 and 22.)

[Whitaker 1994] S. Whitaker. *The closure problem for two-phase flow in homogeneous porous media*. Chemical Engineering Science, vol. 49, pages 765–780, 1994. (Cited on page 22.)

[Whitaker 1996] S. Whitaker. *The Forchheimer Equation : a Theoretical Development*. Transport in Porous Media, vol. 25, pages 27–61, 1996. (Cited on pages 22 and 32.)

[Whitaker 1999] S. Whitaker. The method of volume averaging. Kluwer Academic Publishers, The Netherlands, 1999. (Cited on pages 21 and 25.)

[Wodie 1991] J.C. Wodie and T. Levy. *Correction Non Linéaire de la Loi de Darcy.* Comptes Rendus de l'Académie des Sciences. Série II, Mécanique, Physique, Chimie, Sciences de l'univers, Sciences de la Terre, vol. 312, no. 3, pages 157–161, 1991. (Cited on pages 21, 29 and 32.)

[Wright 1968] D. E. Wright. *Nonlinear flow through granular media.* Journal of the Hydraulics Division - ASCE, vol. 4, pages 851–872, 1968. (Cited on page 28.)